Characterisation of Competing Orders in Dielectric Oxides

Nathan James Giles-Donovan

Submitted in fulfilment of the requirements for the
Degree of Doctor of Philosophy

James Watt School of Engineering
College of Science and Engineering
University of Glasgow

November 2021

Abstract

Dielectric oxides exhibit many intriguing properties. For example, ferroic materials are central to developing transducers due to their ability to convert energy owing to the presence of coupled orders. In particular, lead-based perovskite relaxor-ferroelectric single crystal have attracted great attention in recent years, with exceptional piezoelectric and dielectric responses reported. Suitable for high-power industrial and underwater SONAR ultrasonic applications due to their high energy density, the performance of these materials has been linked to compositional disorder and short-range order but the mechanism is not yet well-understood.

In general, coupling and competition of different orders can result in thought-provoking physics and, in this work, this link was investigated by studying the fundamental behaviour of complex ferroelectrics and multiferroics. Polarised neutrons were used to characterise the magnetic ground state of $Cu_3Nb_2O_8$, addressing an issue in the literature regarding the microscopic ordering mechanism. Furthermore, muon techniques were used to study the composition and magnetic structure of the relaxor-multiferroic $Pb(Fe_{1/2}Nb_{1/2})O_3$ which provided insight into the role of disorder and random fields. This work was then extended to study the Mn distribution and valence in doped $Pb(In_{1/2}Nb_{1/2})O_3$ - $Pb(Mg_{1/3}Nb_{2/3})O_3$ - $PbTiO_3$. These materials are indicated to be amongst the highest performance piezoelectric but the microscopic mechanisms are not fully understood.

This raised the question of best practice in material comparison, with unbiased comparison of transduction materials desired. To address this, a new method was developed to quantify the energy density of piezoelectric materials, which was verified *in silico* to be independent of a single use case or application.

Overall, this work extends the understanding of three complex ferroelectric and multiferroic systems using fundamental characterisation methods with a foundation in applications.

Contents

List of Tables

List of Figures

Acknowledgements

I would like to acknowledge the many people who have helped me over the last four years and have contributed to my studies and the success of the thesis.

First and foremost, my most sincere thanks go to my academic supervisors Prof. Sandy Cochran and Dr. Chris Stock. I am grateful for their support, advice, occasional warnings and general encouragement without which I am sure this thesis would not exist. Their expertise has both guided and enabled this work and I will be forever appreciative.

I am indebted to Thales UK for providing me with this opportunity. Thanks must go to my industrial supervisor Dr. Laura Stoica for her help and support both during my industrial placement and otherwise.

Besides my supervisors, I must express my gratitude to the instrument scientists at the ILL and ISIS for enabling the neutron and muon studies in this thesis. I am thankful for the expertise of Drs. Adrian Hillier, Katsu Ishida and Navid Qureshi, and for their assistance in data collection, analysis and interpretation. I would also like to thank those who provided the samples for such studies: Profs. Sang-Wook Cheong and Haosu Luo and their respective groups.

I must also thank Prof. Shujun Zhang and his group for being so welcoming during my visit to Wollongong and for his guidance and advice.

To all my colleagues and friends at the Universities of Glasgow and Edinburgh, I would like to express my upmost appreciation. My gratitude goes to the members, past and present, of the Centre for Medical and Industrial Ultrasonics, the Materials and Devices group and the Stock group. In particular, I must recognise Nicola Fenu and Hannah Rose (as fellow Piezopals) for their ever-present support and collaboration over the past years; and thank Bartas Abaravicius, Arjin Boonruang, Harry Lane, Jana Pásztorová, Jill Savva, Jack Stevenson, Colin Souza, Hannah Thomson, Mihnea Turcanu and the others *unfortunate* enough to share an office with me. The whole team were brilliant colleagues without whom this would have been much less fun.

Finally, I am thankful to my friends and family who supported and believed in me, even if they frequently didn't understand me.

The research contained herein received funding from: EPSRC/Thales UK iCASE award EP/P510506; the STFC and ILL, to support beamtime experiments; the University of Glasgow Mobility Fund, to support my visit to Wollongong; and OnScale, by providing a research myhllicence.

Declaration

I hereby declare that this thesis, entitled *"Characterisation of Competing Orders in Dielectric Oxides"*, submitted in partial fulfilment of the requirements of the University of Glasgow for the degree of Doctor of Philosophy represents my own work. No part of the work referred to in this thesis has been supported in application for another degree or qualification of this university or any other university or institute of learning.

Nathan James Giles-Donovan
18th November 2021

Glossary of Terms

ceramic Polycrystalline material containing many differently orientated grains.

crystal The infinite repetition of identical units of atoms (unit cells) in a periodic way possessing long-range order and translational symmetry.

Curie temperature Temperature at which a system undergoes a phase transition from a disordered state to one with ferroic order, e.g. ferroelectric-paraelectric, ferromagnetic-paramagnetic. A Curie-Weiss law is obeyed above the transition in the disordered state.

domain Regions within a crystal that have similar crystal structures or other properties. Usually results from spontaneous symmetry breaking during a phase transition or other process.

domain engineered A ferroelectric crystal which has been poled by the application of a large electric field along a direction other than the spontaneous polarisation direction. This creates a set of symmetry-related domains in which the polarisation vectors are oriented so as to minimise their angles to the poling direction and has been shown to unlock new piezoelectric modes, e.g. d_{36}, and large piezoelectric coefficients.

electromechanical coupling factor The proportion of the instantaneous work converted from electrical to mechanical energy (and *vice-versa*) and stored in a piezoelectric material. Denoted as k^2.

electrostriction A quadratic coupling between mechanical and dielectric properties present in all materials.

ferroelectric Supporting a spontaneous dielectric polarisation which is reversible under an external field.

ferromagnetic Supporting a spontaneous and macroscopic magnetisation which may persist after removal of an applied field.

Generation I Binary solid solutions of a relaxor component with $PbTiO_3$.

Generation II Ternary solid solutions of two relaxor components with $PbTiO_3$.

Generation III Doped ternary solid solutions of two relaxor components with $PbTiO_3$.

lattice vector Vectors which define the geometry of the unit cell. Typically denoted as $\vec{1}$, $\vec{2}$ and $\vec{3}$ or $\vec{a}$, $\vec{b}$ and $\vec{c}$.

magnetoelectric A coupling between magnetic and dielectric order.

mechanical quality The reciprocal quantity to mechanical losses.

Miller index System for labelling crystallographic planes: a plane is denoted by indices (h,k,l) where h, k and l are proportional to the reciprocal of the intercepts of the plane with the lattice vectors $\vec{a}$, $\vec{b}$ and $\vec{c}$ respectively. They also label points on the reciprocal lattice.

morphotropic phase boundary A phase boundary which arises due to compositional changes.

multiferroic A coupling between ferroic orders, usually magnetism and ferroelectricity. *See* magnetoelectric

muon A fundamental subatomic particle with a mass (105.7MeV/c^2) approximately 200 times that of an electron and an electric charge of either $\pm e$. Can be used to sensitively probe magnetic systems (μ^+) through μSR and compositional heterogeneity (μ^-).

Néel temperature Temperature at which a system undergoes a phase transition from a disordered state to one with antiferromagnetic or other type of magnetic order.

Neumann's principle Provides a link between crystal symmetry and physical properties: crystal point group symmetries must be obeyed by the physical properties of that crystal.

neutron A subatomic particle of approximately the same mass (939.6 MeV/c^2) as a proton and no electric charge. Typically found within the nuclei of atoms, it can also be used to probe condensed matter system's nuclear structure, due to interaction of the scale of crystal typical intra-lattice spacing, and magnetism, due to the neutron's large magnetic moment.

normal ferroelectric A material which supports ferroelectric behaviour and shows a sharp ferroelectric-paraelectric phase transition at the Curie temperature and follows a Curie-Weiss law in the paraelectric phase.

paraelectric Supporting no overall electric polarisation vector.

perovskite A material with chemical formula ABX_3, where A and B represent cations and X anions (typically O), which shares a crystal structure with calcium titanate $CaTiO_3$.

phase transition A qualitative change in the state of a system typically associated with spontaneous symmetry breaking and the emergence of an order parameter.

piezoelectric A linear coupling between mechanical and dielectric properties only present in certain crystal symmetries.

point group Group of symmetry operations that leave the unit cell of a crystal unchanged.

pyroelectric Develops an electric charge homogenously when heated.

relaxor-ferroelectric A material which supports ferroelectric behaviour but shows a frequency dependent, diffuse ferroelectric-paraelectric phase transition and deviates from the Curie-Weiss law in the paraelectric phase. These features are linked to compositional disorder.

relaxor-PT Solid solutions of relaxor components, e.g. PMN, with $PbTiO_3$ which are of interest due to their large piezoelectric effects.

Rochelle salt Sodium potassium tartrate tetrahydrate - $NaKC_4H_4O_6 \cdot 4H_2O$.

single crystal A material which consists of a single unbroken crystal lattice across its entire volume.

transducer A device which converts energy from one form to another, e.g. mechanical to dielectric.

ultrasound Sound or vibrations with a frequency above the human hearing threshold (>20 kHz). Widely used in medical and industrial situations such as diagnostic imaging and SONAR.

unit cell The most fundamental repeating unit of a crystal.

Voigt notation Also known as 'matrix' notation. Allows, through exploitation of the intrinsically symmetric nature of the stress and strain tensors, representation of three dimensional tensors as matrices by pairing indices according to Table 2.2. In this thesis, Voigt indices are denoted with greek letters such that $\mu, \nu, \ldots = 1-6$.

List of Abbreviations

BF bismuth ferrite - $BiFeO_3$

BNT bismuth sodium titanate - $Bi_{1/2}Na_{1/2}TiO_3$

BT barium titanate - $BaTiO_3$

BVP boundary value problem

$c^D_{\mu\nu}$ components of the stiffness at constant electric displacement (stiffened) in Voigt notation

$c^E_{\mu\nu}$ components of the stiffness at constant electric field in Voigt notation

CNO copper niobium oxide - $Cu_3Nb_2O_8$

D_i components of the electric displacement field

$d_{i\mu}$ components of the piezoelectric strain constant in Voigt notation

E_i components of the electric field

$e_{i\mu}$ components of the piezoelectric stress constant in Voigt notation

EPD elasto-piezo-dielectric matrix

ε^S_{ij} components of the dielectric permittivity at constant strain (clamped)

ε^σ_{ij} components of the dielectric permittivity at constant stress (unclamped)

F Helmholtz free energy

FEA finite element analysis

FOM figure of merit

G Gibbs free energy

$g_{i\mu}$ components of the piezoelectric voltage constant in Voigt notation

H enthalpy

$h_{i\mu}$ components of the piezoelectric stiffness constant in Voigt notation

k *see* electromechanical coupling factor

KDP potassium dihydrogen phosphase - KH_2PO_4

LE length extensional mode, also known as the '33' mode.

LF longitudinal field

LNO lithium niobate - $LiNbO_3$

LT low temperature phase in CNO which exists for $T < 24$ K

LTE length-thickness extensional mode, also known as the '31' mode.

LTO lithium tantalate - $LiTaO_3$

Mn:PIN-PMN-PT solid solution of lead indium niobate, lead magnesium niobate and lead titanate doped or modified with Mn - Mn:$Pb(In_{1/2}Nb_{1/2})O_3$ - $Pb(Mg_{1/3}Nb_{2/3})O_3$ - $PbTiO_3$

Mn:PMN-PZ-PT solid solution of lead magnesium niobate, lead zirconate and lead titanate doped or modified with Mn - Mn:$Pb(Mg_{1/3}Nb_{2/3})O_3$ - $PbZrO_3$ - $PbTiO_3$

MPB *see* morphotropic phase boundary

MT middle temperature phase in CNO which exists for 24 K $< T <$ 26.5 K

μ^- negative muon

μ^+ positive muon

μ**SR** muon spin relaxation, also known as muon spin rotation

PFN lead iron niobate - $Pb(Fe_{1/2}Nb_{1/2})O_3$

PIN lead indium niobate - $Pb(In_{1/2}Nb_{1/2})O_3$

PIN-PMN-PT solid solution of lead indium niobate, lead magnesium niobate and lead titanate - $Pb(In_{1/2}Nb_{1/2})O_3$ - $Pb(Mg_{1/3}Nb_{2/3})O_3$ - $PbTiO_3$

PMN lead magnesium niobate - $Pb(Mg_{1/3}Nb_{2/3})O_3$

PMN-PT solid solution of lead magnesium niobate and lead titanate - $Pb(Mg_{1/3}Nb_{2/3})O_3$ - $PbTiO_3$

PMN-PZ-PT solid solution of lead magnesium niobate, lead zirconate and lead titanate - $Pb(Mg_{1/3}Nb_{2/3})O_3$ - $PbZrO_3$ - $PbTiO_3$

PNR polar nano-region

P_i' components of the polarisation created in a SNP experiment

$\tilde{\mathsf{P}}_{ij}$ components of the polarisation matrix

P_{ij} components of the polarisation tensor

PT lead titanate - $PbTiO_3$

PZ lead zirconate - $PbZrO_3$

PZN lead zinc niobate - $Pb(Zr_{1/3}Nb_{2/3})O_3$

PZN-PT solid solution of lead zinc niobate and lead titanate - $Pb(Zn_{1/3}Nb_{2/3})O_3$ - $PbTiO_3$

PZT lead zirconate titanate - $Pb(Ti_xZr_{1-x})O_3$

$Q_{\mathbf{m}}$ *see* mechanical quality factor

RMS root mean square

S_μ components of the strain tensor in Voigt notation

$s^D_{\mu\nu}$ components of the compliance at constant electric displacement (stiffened) in Voigt notation

SDW spin density wave

$s^E_{\mu\nu}$ components of the compliance at constant electric field in Voigt notation

σ_μ components of the stress tensor in Voigt notation

SNP spherical neutron polarimetry

SONAR SOund Navigation And Ranging

TE thickness extensional mode, also known as the 'plate' or 'k_t' mode.

TF transverse field

TRS time reversal symmetry

U total internal energy density

Z atomic number - the number of protons and neutrons in the nucleus of an atom.

ZF zero field

Chapter 1

Introduction

This chapter provides a brief introduction to the thesis. Following a general overview, the motivation, aims and objectives are laid out. Next, the contributions to knowledge contained in this thesis are summarised. Finally, the structure of the thesis and publications arising from this work are outlined.

1.1 General Overview

Dielectric oxides, as a class of materials, are represented in most branches of modern physics and engineering. A classic example of this is the field of piezoelectricity. Whilst piezoelectric materials have been under continuous development for the past 140 years [1], driven both by their wide ranging applicability and unique properties [2], it is the coupling between dielectric properties and mechanical deformation on which many industries rely for their ability to generate and receive ultrasound. Examples include: medical diagnostic imaging [3], therapeutic ultrasound [4, 5], surgical ultrasound [6, 7], underwater acoustics such as SOund Navigation And Ranging (SONAR) [8], ultrasonic cleaning [9], and industrial non-destructive evaluation [10, 11].

Whilst early piezoelectric materials were varied in structure, the current best performing piezoelectric materials are the dielectric oxide perovskite class, with general chemical formula ABO_3 [12]. They include the current standard piezoelectric material $Pb(Ti_xZr_{1-x})O_3$ (PZT), a solid solution between the perovskites $PbZrO_3$ (PZ) and $PbTiO_3$ (PT) [13], which is used in ceramic form and has been shown to exhibit a substantial piezoelectric effect [13]. However, PZT's main strength is the versatility allowed by chemical variations (through the parameter x or other dopants) to obtain materials with a wide range of operating parameters but without serious reduction of the piezoelectric properties [14].

Despite the advantages of the PZT family, development of other piezoelectric materials has actively been pursued and this evolution is illustrated in Figure 1.1. One other emerging class of materials is the relaxor-ferroelectrics [15]. Named in analogy with ferromagnets, a ferroelec-

tric material has a permanent and reversible electric dipole moment [16]. This thesis mostly considers the class of relaxor-ferroelectrics, with some comparison to the so-called normal ferroelectrics. Ferroelectricity was first discovered in Rochelle salt [17] but the prime example of a normal ferroelectric material is the perovskite $BaTiO_3$ (BT) [18]. The prototypical relaxor-ferroelectric is $Pb(Mg_{1/3}Nb_{2/3})O_3$ (PMN) which was first reported in 1961 [19] and again adopts a perovskite structure. It was first noted for its exceptional dielectric properties but its piezoelectric potential was not realised until it was combined, again in solid solution, with PT (similar to PZT), whence it exhibited a piezoelectric coefficient, d_{33}, almost three times that of PZT [20]. Furthermore, whilst the growth of single crystal samples of PZT has been reported [21], it has generally been found to be difficult to produce large single crystal samples due to chemical decomposition of the constituent perovskites during the crystal growth process [22, 23]. However, it has proved relatively simple to grow single crystal specimens of relaxor-PT solid solutions [24].

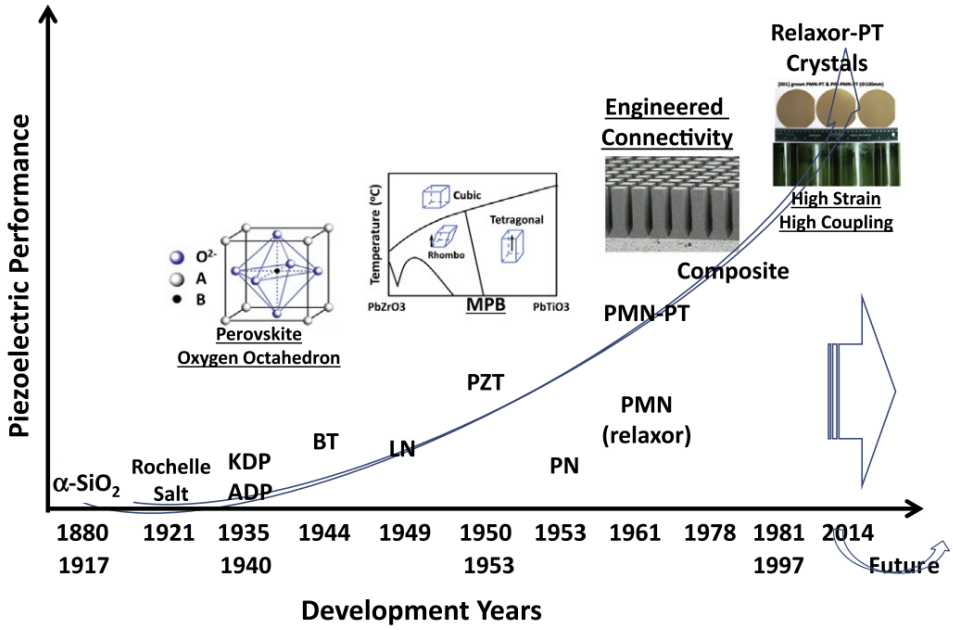

Figure 1.1: The development of piezoelectric materials. The superiority of relaxor-PT single crystal materials over PZT and other early materials is clearly demonstrated. Reprinted from S. Zhang *et al.*, "Advantages and challenges of relaxor-$PbTiO_3$ ferroelectric crystals for electroacoustic transducers - a review," *Prog. Mater. Sci.*, vol. 68, pp. 1–66, 2015, Copyright (2015), with permission from Elsevier.

After decades of dominance by PZT ceramics, relaxor-PT single crystals have attracted much attention in recent years and are now finding applications in commercial ultrasound transducers, with PMN-PT already commercialised in the medical ultrasonic imaging industry [15, 25]. They allow transducers with larger bandwidths and higher sensitivity than PZT based devices [15]. Adding a third constituent perovskite, i.e. PMN-PT becomes $Pb(In_{1/2}Nb_{1/2})O_3$ - $Pb(Mg_{1/3}Nb_{2/3})O_3$

- $PbTiO_3$ (PIN-PMN-PT), increased the upper temperature usage limits and provided greater stability, thus allowing device usage conditions to be broadened with respect to temperature, electric field and mechanical stress [26]. Recently Mn modification of PIN-PMN-PT (denoted as Mn:PIN-PMN-PT) has further reduced the mechanical losses, increasing suitability for high-power application such as ultrasonic surgery devices and underwater SONAR [15].

More generally, perovskites have been shown to display a range of interesting properties including superconductivity and large magneto-resistance and have recently become of interest for photovoltaic applications [27] where promise is shown by both halide and hybrid organic-inorganic perovskites [28, 29].

Indeed the main strength of these materials, not only in piezoelectricity but also in other applications, is the exploitation of multiple simultaneous, and often competing, orders. For example, a material which exhibits both ferromagnetic (or some other form of magnetic ordering) and ferroelectric behaviour is called a multiferroic. Typically, these materials are of interest due to the potential to influence, for example, magnetic properties by the application of an electric field in a magnetoelectric device [30]. However, despite the inherent link between electricity and magnetism shown in the theory, i.e. Maxwell's equations [31], multiferroics are somewhat rare and this has been suggested to be caused by to differing requirements in the crystal's electronic structure [32]. Regardless, where a coupling does occur, it can be seen to arise from a delicate balance between these competing requirements and if this can be understood, more of such materials may be developed.

This work provides further investigation into the fundamental behaviour of complex ferroelectrics and multiferroics with a specific focus on piezoelectric applications. However, a comprehensive understanding of the mechanisms is required to fully exploit these materials and this thesis closes that gap.

1.2 Motivation

Due to the delicate competition between different orders, complex ferroelectrics and multiferroics provide the opportunity for potentially novel structural and magnetic ground states with relaxors [33–36] and skyrmion phases [37] being just several of many examples. A specific case of this is relaxor-PT single crystals, which are emerging as materials with great potential for high-power industrial, surgical and underwater SONAR applications. By exploiting their crystal anisotropy, they allow novel transducer designs. However, methods of crystal growth result from experimentally-developed specifications following a historical lack of theoretical input, which is essential to develop materials with enhanced properties.

Understanding the origins of observed behaviour of relaxor-ferroelectrics is also key to enable exploitation of these materials for use in devices. Historically, SONAR was the driving force behind development of piezoelectric materials (especially during the second world war).

SONAR is most widely associated with military applications, where it can be used for both navigation and object detection, but it can also be used outside military contexts e.g. underwater cartography, construction, maintenance, exploration and to detect underwater life [8]. Due to the long detection ranges involved and the possibility to use optical techniques at very short ranges, SONAR typically uses low frequencies (< 1 MHz) and high power and the properties of relaxor-PT single crystals make them perfect for SONAR transducers [15].

More widely, the performance of a piezoelectric material for a particular application can be quantified by a figure of merit (FOM) [15]. These are typically constructed from relevant material properties, e.g. piezoelectric constant, dielectric constant, and the FOMs for many ultrasonic applications are reviewed by Zhang *et al.* in Ref. [15]. This concept will be explored further in the review of relaxor-PT single crystals in Chapter 6 but, in summary, relaxor-PT single crystals have been shown to exhibit a FOM twice that of standard PZT for SONAR [38–40] and other high-power applications, meriting further study and one of the reasons behind their continued research attention. Furthermore, relaxor-PT single crystals may be suitable for other applications such as tactile sensors and acoustic tweezing due to their superior piezoelectric, dielectric, and compliance when compared to the standard materials.

Another motivation for studying materials with competing orders is for their innate coupling between these orders, which results in transduction properties. Ferroelectrics are well-known to be strongly piezoelectric, converting between mechanical and dielectric energy, whereas the coupling in multiferroics, if at workable temperatures, opens up the ability to create new magnetoelectric devices independently controllable with magnetic and electric fields [30].

This transduction is key in piezoelectric devices and relaxor-PT single crystals are reported to possess high energy density, which may be exploited to give smaller, lighter devices [15]. However, this is hard to quantify historically, making specific comparisons difficult. This issue must be addressed if it is to be used to justify the conversion of devices from PZT to relaxor-PT single crystals. This study could also be used to determine device power limits: whilst there are some studies in the literature regarding power limits of transducers [41], there is a lack of generality, with very limited applications considered.

Furthermore, the high dielectric and piezoelectric performance of relaxor-ferroelectrics has been linked to short-range order resulting from compositional disorder but the mechanism is not well-understood. In the class of mixed perovskites with structure $A(B_xB'_{1-x})O_3$ such as PMN, materials exhibit a random mixture of cations on the B-site and this disorder has been indicated as, at least partially, a reason for their high performance [42]. Indeed, the phase transitions in these materials have also challenged understanding of ferroelectric transitions in the presence of disorder as relaxor-ferroelectrics display characteristic transitions distinct from those of normal ferroelectrics [33]. They show huge dielectric properties over a large temperature range which must be encompassed for full characterisation. Furthermore, the cryogenic temperature region has provided insight into the role short-range order plays in the enhanced performance [43].

Also, given the inherent anisotropy tied to ferroelectricity through supporting a macroscopic electric dipole vector, relaxor-ferroelectrics provide unique systems to study the effects of disorder and random fields.

Hence, complete fundamental characterisation, with a foundation in applications, is needed to realise the potential of dielectric oxides such as relaxor-PT single crystals. This is essential to enabling the continuing development and use of such complex materials, which play a notable role in the modern world.

1.3 Aims and Objectives

The overall aim of this thesis is to further the understanding of complex ferroelectrics and multiferroics. As set out above, these materials not only have wide applicability but also pose intellectually stimulating questions regarding the mechanisms behind their structures and behaviour. This leads to the first of three more specific aims of this thesis:

1. To use condensed matter probes to advance understanding of the fundamental behaviour of complex ferroelectrics and multiferroics and to elucidate the mechanisms by which they emerge.

The potential applications of materials must not be forgotten and should be used to direct research. To this end, the main application considered in this thesis is in ultrasonic devices. Hence, investigation of the transduction properties which arise from the order coupling must be forthright. This leads to the second aim of the thesis which attempts to address a more applied question:

2. To arrive at a universal and comparable metric for the energy density of a piezoelectric material and to understand the different energy conversion mechanisms at play in relaxor-PT single crystals.

Lastly, relaxor-PT single crystals represent the culmination of both competing order effects suitable for more theoretical studies, and applicability in high-power ultrasonics and underwater SONAR. However, much of their behaviour is still not well-understood and this leads to the final aim:

3. To explore the mechanisms behind the high performance of relaxor-PT single crystals with a focus on Mn doping and the cryogenic temperature regime.

In order to realise these aims, the following objectives were set for this work:

- Characterise the structure of multiferroics with neutrons and muons, including looking at both the low temperature magnetic structure and any compositional gradients. This supports Aims 1 and 3.

- Use muon techniques to characterise relaxor-ferroelectrics and assess the feasibility of studying Mn:PIN-PMN-PT. This objective supports Aim 3.
- Explore the electromechanical mechanisms of piezoelectric materials in order to further understand the concept of energy density, allowing Aim 2 to be realised.

1.4 Contributions to Knowledge

This thesis has contributed to the understanding of complex ferroelectric materials in many ways. Specifically these contributions can be summarised as follows:

1. This thesis contains, for the first time, a successful demonstration of the use of spherical neutron polarimetry to characterise the magnetic ground state of the complex multiferroic $Cu_3Nb_2O_8$ (CNO) (N. Giles-Donovan *et al.*, Physical Review B, 2020 [44]; Oral presentation: Fundamentals of Ferroelectrics and Related Materials 2019). This directly addressed and provided a solution to an issue in the literature of CNO regarding the microscopic mechanism behind this magnetic structure. This work is detailed in Chapter 4.
2. By characterising the composition gradient in the near surface region of multiferroic relaxor-ferroelectric $Pb(Fe_{1/2}Nb_{1/2})O_3$ (PFN), insight into the behaviour of the materials in the context of disorder and random fields was gained. Furthermore, the links to magnetic structure were investigated and mechanisms behind this were discussed (N. Giles-Donovan *et al.*, submitted to Physical Review B [45]; Oral presentation: 2020 International Symposium on Applications of Ferroelectrics). This work is detailed in Chapter 5.
3. In order to study the Mn valence and distribution in Generation III (doped ternary) relaxor-ferroelectric single crystals, this thesis also includes an investigation into the feasibility of using the negative muon compositional analysis technique (N. Giles-Donovan *et al.*, in preparation for Acta Crystallographica A [46]). This work is detailed in Chapter 6.
4. In this thesis, a method for quantifying the energy density of piezoelectric materials was developed allowing for an unbiased comparison (Conference Preceedings: 2018 IEEE International Ultrasonics Symposium [47]; Oral presentation: Fundamentals of Ferroelectrics and Related Materials 2021, PIEZO2021: Piezoelectrics for End Users XI; Poster presentation: 2019 International Workshop on Acoustic Transduction Materials and Devices, 2021 IEEE International Ultrasonics Symposium). This work is detailed in Chapter 7.

1.5 Thesis Structure

Chapter 2 provides the background knowledge and literature review necessary for this thesis. This includes the theory behind piezoelectricity, ferroelectricity and magnetic order and the cases where these intermingle. Chapter 3 reviews the experimental methods that were used to gather data for this thesis. This includes details of the experimental setups and facilities where the experiments were performed.

The next four chapters contain the core results of the thesis. They begin with Chapter 4 which details the characterisation of the multiferroic $Cu_3Nb_2O_8$ (CNO) using polarised neutron scattering. Through careful analysis of the results, a new mechanism is proposed which accounts for the magnetic structure and provides insight into the emergence of the electric polarisation.

Chapters 5 and 6 detail the application of muon techniques to study the behaviour of relaxor-ferroelectrics. The near-surface region of $Pb(Fe_{1/2}Nb_{1/2})O_3$ (PFN) is studied in Chapter 5. This study probes both the composition and magnetic structure and links the phenomenology to the presence of random fields. Chapter 6 details attempts at characterisation of Generation III relaxor-PT single crystals with muons. Specifically the valence of the Mn dopant was investigated using negative muon techniques. Theoretically predicted, an experimental feasibility study was conducted into the sensitivity of the method to the valence of Mn using three oxide samples with known Mn oxidation. This was followed by an application of these results in Mn:$Pb(In_{1/2}Nb_{1/2})O_3$ - $Pb(Mg_{1/3}Nb_{2/3})O_3$ - $PbTiO_3$ (Mn:PIN-PMN-PT).

Chapter 7 presents work on quantifying the higher energy density of relaxor-PT single crystals. This starts with a review of energy in a piezoelectric material followed by the development of a generalised, static electromechanical coupling factor. *In silico* validation is provided. This method is then applied to two cases in which comparison of piezoelectric material is important - relaxor-PT single crystals and the development of Pb-free materials.

Finally, Chapter 8 provides a summary of all results and, after the conclusions are laid out, future work is presented.

1.6 Publications Arising

1.6.1 Peer Reviewed

- **N. Giles-Donovan**, N. Qureshi, R. D. Johnson, L. Y. Zhang, S.-W. Cheong, S. Cochran, and C. Stock, "Imitation of spin density wave order in $Cu_3Nb_2O_8$", *Physical Review B*, vol. 102, no. 2, pp. 024414, (2020). DOI: 10.1103/PhysRevB.102.024414.

- N. G. Fenu, X. Li, **N. Giles-Donovan**, M. Lucas, and S. Cochran, "Comparison of high-Q piezocrystal with hard PZT in a bolted Langevin-style transducer for power ultrasonics", *IEEE Transactions on Ultrasonics, Ferroelectrics and Frequency Control*, (submitted).

- **N. Giles-Donovan**, A. D. Hillier, K. Ishida, B. V. Hampshire, B. Roessli, P. M. Gehring, G. Xu, X. Li, H. Luo, S. Cochran, and C. Stock "Depth dependent magnetic clustering in $Pb(Fe_{1/2}Nb_{1/2})O_3$ - (1) Positive and negative muon spectroscopy", *Physical Review B*, (submitted).

- **N. Giles-Donovan**, A. D. Hillier, K. Ishida, L. Stoica, S. Cochran, and C. Stock "Identification of transition metal oxidation states with negative muons in Mn oxides", *Acta Crystallographica A*, (in preparation).

1.6.2 Conference Proceedings

- N. G. Fenu, **N. Giles-Donovan**, X. Li, Z. Liang, A. H. Chibli, H. Luo, C. Stock, S. Zhang, M. Lucas, and S. Cochran, "Progress Towards the Miniaturization of an Ultrasonic Scalpel for Robotic Endoscopic Surgery Using Mn:PIN-PMN-PT High Performance Piezocrystals", *2020 IEEE International Ultrasonics Symposium*, Virtual, 2020. DOI: 10.1109/IUS46767.2020.9251823.

- **N. Giles-Donovan**, N. G. Fenu, C. Stock, S. Zhang, and S. Cochran, "A Measure of Energy Density to Quantify Progress in Pb-free Piezoelectric Material Development", *2021 IEEE International Ultrasonics Symposium*, Virtual, 2021. DOI: 10.1109/IUS52206.2021.9593449.

1.6.3 Conference Presentations

Oral

- **N. Giles-Donovan**, N. Qureshi, S.-W. Cheong, S. Cochran, and C. Stock, "Spin Density Waves and Cycloidal Order in the Multiferroic $Cu_3Nb_2O_8$ Determined with Polarised Neutrons", *Fundamentals of Ferroelectrics and Related Materials 2019*, Embassy Suites, Tampa, FL, USA, 28-30 January 2019.

- **N. Giles-Donovan**, C. Stock, S. Cochran, and L. Stoica, "Subatomic Probes Aid Understanding of Fundamental Piezocrystal Behaviour", *International Symposium on Piezocrystals and Their Applications*, Starling Hotel, École Polytechnique Fédérale de Lausanne, Lausanne, Switzerland, 14 July 2019.

- **N. Giles-Donovan**, A.D. Hillier, A. Berlie , X. Li, H. Luo, S. Cochran, and C. Stock, "Compositional Heterogeneity and its Links to Magnetic Order in the Near Surface Region of $PbFe_{1/2}Nb_{1/2}O_3$ Probed with Muons", *2020 International Symposium on Applications of Ferroelectrics*, Virtual, 19-23 July 2020.

- **N. Giles-Donovan**, N. G. Fenu, C. Stock, S. Zhang, and S. Cochran, "Towards a Method of Quantifying the Higher Energy Density of Relaxor-PT Single Crystals", *Fundamentals of Ferroelectrics and Related Materials 2021*, Virtual, 1-3 February 2021.

- **N. Giles-Donovan**, N. G. Fenu, C. Stock, S. Zhang, and S. Cochran, "Towards a Method of Quantifying the Higher Energy Density of Piezoelectric Single Crystals", *PIEZO2021: Piezoelectrics for End Users XI*, Virtual, 21-24 February 2021.

Poster

- **N. Giles-Donovan**, N. G. Fenu, H. Rose, L. Stoica, C. Stock, and S. Cochran, "Generation II/III Piezocrystal for SONAR Transducers", *Thales UK Academic Showcase*, Reading, UK, 11 November 2018.

- **N. Giles-Donovan**, N. G. Fenu, C. Stock, and S. Cochran, "Towards a Fundamental Understanding of Energy Density for Piezoelectrics", *2019 International Workshop on Acoustic Transduction Materials and Devices*, Pennsylvania State University, PA, USA, 7-9 May 2019.

- **N. Giles-Donovan**, N. G. Fenu, C. Stock, S. Zhang, and S. Cochran, "A Measure of Energy Density to Quantify Progress in Pb-free Piezoelectric Material Development", *2021 IEEE International Ultrasonics Symposium*, Virtual, 11-16 September 2021.

1.6.4 Awards

- ISAF Student Paper Finalist - Lecture, *2020 International Symposium on Applications of Ferroelectrics*, Virtual, 19-23 July 2020.

1.7 Other Publications

- N. G. Fenu, **N. Giles-Donovan**, M. R. Sadiq, and S. Cochran, "Progress towards Piezocrystal and Pb-Free Piezoceramic Performance Prediction for High Power Ultrasound Devices", *2018 IEEE International Ultrasonics Symposium*, Kobe, 2018, pp. 1-4. DOI: 10.1109/ULTSYM.2018.8579653.

- M. Songvilay, **N. Giles-Donovan**, M. Bari, Z.-G. Ye, J. L. Minns, M. A. Green, Guangyong Xu, P. M. Gehring, K. Schmalzl, W. D. Ratcliff, C. M. Brown, D. Chernyshov, W. van Beek, S. Cochran, and C. Stock, "Common acoustic phonon lifetimes in inorganic and hybrid lead halide perovskites", *Physical Review Materials*, vol. 3, no. 9, pp. 093602, (2019). DOI: 10.1103/PhysRevMaterials.3.093602.

- C. Stock, R. D. Johnson, **N. Giles-Donovan**, M. Songvilay, J. A. Rodriguez-Rivera, N. Lee, X. Xu, P. G. Radaelli, L. C. Chapon, A. Bombardi, S. Cochran, Ch. Niedermayer, A. Schneidewind, Z. Husges, Z. Lu, S. Meng, and S.-W. Cheong, "Spin-wave directional anisotropies in antiferromagnetic $Ba_3NbFe_3Si_2O_{14}$", *Physical Review B*, vol. 100, no. 13, pp. 134429, (2019). DOI: 10.1103/PhysRevB.100.134429.

- N. G. Fenu, **N. Giles-Donovan**, X. Li, Z. Liang, A. H. Chibli, H. Luo, C. Stock, S. Zhang, M. Lucas, and S. Cochran, "Progress Towards the Miniaturization of an Ultrasonics Scalpel for Robotic Endoscopic Surgery Using Mn:PIN-PMN-PT", *2020 IEEE International Ultrasonics Symposium*, Virtual/Las Vegas, USA, 7-11 September 2020.

- N. G. Fenu, **N. Giles-Donovan**, M. R. Sadiq, and S. Cochran, "Full Set of Material Properties of Lead-Free PIC 700 for Transducer Designers", *IEEE Transactions on Ultrasonics, Ferroelectrics and Frequency Control*, vol. 68, no. 5, pp. 1797-1807 (2021). DOI: 10.1109/TUFFC.2020.3044790.

- S. Cochran, N. G. Fenu, **N. Giles-Donovan** and H Rose, "Piezocrystals for Power Ultrasonics", *Joint Conference of the IEEE International Frequency Control Symposium and International Symposium on Applications of Ferroelectrics*, Virtual, 19-21 May 2021.

- S. Devireddy, J. Stevenson, N. G. Fenu, **N. Giles-Donovan** and S. Cochran, "High-Power Characterization of d32-Mode Mn:PIN-PMN-PT Piezoelectric Single Crystals at Different Temperatures", *2021 IEEE International Ultrasonics Symposium*, Virtual, 11-16 September 2021. DOI: 10.1109/IUS52206.2021.9593597.

- C. Stock, B. Roessli, P. M. Gehring, J. A. Rodriguez-Rivera, **N. Giles-Donovan**, S. Cochran, G. Xu, P. Manuel, M. J. Gutmann, W. D. Ratcliff, T. Fennell, Y. Su, X. Li and H. Luo, "From paramagentic to glassy dynamics in $Pb(Fe_{1/2}Nb_{1/2})O_3$ - (2) Neutron scattering", *Physical Review B*, (submitted).

References

[1] J. Curie and P. Curie, "Development, via compression, of electric polarization in hemihedral crystals with inclined faces," *Bulletin de la Societe de Minerologique de France*, vol. 3, pp. 90–93, 1880.

[2] J. D. B. Cheeke, *Fundamentals and Applications of Ultrasonic Waves*, 2nd. CRC Press, 2002, ISBN: 9781138077201.

[3] M. Postema, *Fundamentals of Medical Ultrasonics*, 1st. Spon Press, 2011, ch. 7, ISBN: 978-0-203-86350-3.

[4] N. P. K. Ellens and K. Hynynen, "High-intensity focused ultrasound for medical therapy," in *Power Ultrasonics : Applications of High-Intensity Ultrasound*, Woodhead Publishing, 2015, ch. 22, ISBN: 978-1-78242-036-1.

[5] P. D. Mourad, "Therapeutic ultrasound with an emphasis on applications to the brain," in *Ultrasonic Transducers*, Woodhead Publishing, 2012, ch. 17, ISBN: 978-1-84569-989-5.

[6] M. E. Schafer, "Ultrasonic surgical devices and procedures," in *Power Ultrasonics : Applications of High-Intensity Ultrasound*, Woodhead Publishing, 2015, ch. 21, ISBN: 978-1-78242-036-1.

[7] M. Lucas and A. Matheison, "Ultrasonic cutting for surgical applications," in *Power Ultrasonics : Applications of High-Intensity Ultrasound*, Woodhead Publishing, 2015, ch. 23, ISBN: 978-1-78242-036-1.

[8] J. L. Butler and C. H. Sherman, *Transducers and Arrays for Underwater Sound*, 2nd. Springer, 2016, ISBN: 978-3-319-39044-4.

[9] F. J. Fuchs, "Ultrasonic cleaning and washing of surfaces," in *Power Ultrasonics : Applications of High-Intensity Ultrasound*, Woodhead Publishing, 2015, ch. 19, ISBN: 978-1-78242-036-1.

[10] J. Krautkrämer and H. Krautkrämer, *Ultrasonic Testing of Materials*, 4th. Springer-Verlag, 1990, ISBN: 978-3-662-10682-2.

[11] P. McIntire, G. L. Workman, and D. Kishoni, Eds., *Nondestructive Testing Handbook*, 3rd. American Society for Nondestructive Testing, 2007, vol. 7, ISBN: 978-1-57117-105-4.

[12] F. Li *et al.*, "Piezoelectric activity in perovskite ferroelectric crystals," *IEEE Trans. Ultrason. Ferroelectr. Freq. Contr.*, vol. 62, no. 1, pp. 18–32, 2015. DOI: 10.1109/TUFFC.2014.006660.

[13] B. Jaffe, W. J. Cook, and H. Jaffe, *Piezoelectric Ceramics*, 3rd. London: Academic Press, 1971, ISBN: 978-0-12-379550-2.

[14] G. H. Haertling, "Ferroelectric ceramics: History and technology," *J. Am. Ceram. Soc.*, vol. 82, no. 4, pp. 797–818, 1999. DOI: 10.1111/j.1151-2916.1999.tb01840.x.

[15] S. Zhang, F. Li, X. Jiang, J. Kim, J. Luo, and X. Geng, "Advantages and challenges of relaxor-$PbTiO_3$ ferroelectric crystals for electroacoustic transducers - a review," *Prog. Mater. Sci.*, vol. 68, pp. 1–66, 2015. DOI: 10.1016/j.pmatsci.2014.10.002.

[16] C. Kittel, *Introduction to Solid State Physics*, 8th. John Wiley & Sons, Inc., 2005, ch. 16, ISBN: 0-471-41526-X.

[17] J. Valasek, "Piezo-electric and allied phenomena in rochelle salt," *Phys. Rev.*, vol. 17, pp. 475–481, 4 1921. DOI: 10.1103/PhysRev.17.475.

[18] A. von Hippel, R. G. Breckenridge, F. G. Chesley, and L. Tisza, "High dielectric constant ceramics," *Industrial and Engineering Chemisty*, vol. 38, no. 11, pp. 1097–109, 1946. DOI: 10.1021/ie50443a009.

[19] G. A. Smolenskii, V. A. Isupov, A. I. Agranovskaya, and N. N. Krainik, "New ferroelectrics of complex composition," *Sov. Phys. Solid State*, vol. 2, pp. 2651–4, 1961.

[20] S. Zhang and T. R. Shrout, "Relaxor-PT single crystals: Observations and developments," *IEEE Trans. Ultrason. Ferroelectr. Freq. Contr.*, vol. 57, no. 10, pp. 2138–2146, 2010. DOI: 10.1109/TUFFC.2010.1670.

[21] D. Phelan *et al.*, "Single crystal study of competing rhombohedral and monoclinic order in lead zirconate titanate," *Phys. Rev. Lett.*, vol. 105, p. 207 601, 20 2010. DOI: 10.1103/PhysRevLett.105.207601.

[22] S. Zhang and F. Li, "High performance ferroelectric relaxor-$PbTiO_3$ single crystals: Status and perspective," *J. Appl. Phys.*, vol. 111, p. 031 301, 3 2012. DOI: 10.1063/1.3679521.

[23] K. Uchino, "The development of piezoelectric materials and the new perspective," in *Advanced Piezoelectric Materials*, K. Uchino, Ed., Woodhead Publishing, 2017, ch. 1, pp. 1–92, ISBN: 978-0-08-102135-4. DOI: 10.1016/B978-0-08-102135-4.00001-1.

[24] S.-E. Park and T. R. Shrout, "Ultrahigh strain and piezoelectric behavior in relaxor based ferroelectric single crystals," *J. Appl. Phys.*, vol. 82, p. 1804, 1997. DOI: 10.1063/1.365983.

[25] D. Zhou *et al.*, "Fabrication and performance of endoscopic ultrasound radial arrays based on PMN-PT single crystal/epoxy 1-3 composite," *IEEE Trans. Ultrason. Ferroelectr. Freq. Contr.*, vol. 58, pp. 477–484, 2 2011. DOI: 10.1109/TUFFC.2011.1825.

[26] J. Luo, W. Hackenberger, S. Zhang, and T. R. Shrout, "Elastic, piezoelectric and dielectric properties of PIN-PMN-PT crystals grown by bridgman method," *2008 IEEE Int. Ultrason. Symp.*, pp. 261–264, 2008. DOI: 10.1109/ULTSYM.2008.0064.

[27] I. Grinberg *et al.*, "Perovskite oxides for visible-light-absorbing ferroelectric and photovoltaic materials," *Nature*, vol. 503, pp. 18–32, 2013. DOI: doi:10.1038/nature12622.

[28] D. A. Egger *et al.*, "What remains unexplained about the properties of halide perovskites?" *Adv.*, vol. 30, no. 20, p. 1 800 691, 2018. DOI: 10.1002/adma.201800691.

[29] M. Antonietta Loi and J. C. Hummelen, "Hybrid solar cells: Perovskites under the sun," *Nat. Mater.*, vol. 12, pp. 1087–1089, 2013. DOI: 10.1038/nmat3815.

[30] T. Kimura, T. Goto, H. Shintani, K. Ishizaka, T. Arima, and Y. Tokura, "Magnetic control of ferroelectric polarization," *Nature*, vol. 426, no. 6962, pp. 55–58, 2003. DOI: 10.1038/nature02018.

[31] J. Clerk Maxwell, "VIII. a dynamical theory of the electromagnetic field," *Philos. Trans. Roy. Soc. London*, vol. 155, pp. 459–512, 1865. DOI: 10.1098/rstl.1865.0008.

[32] N. A. Hill, "Why are there so few magnetic ferroelectrics?" *J. Phys. Chem. B*, vol. 104, no. 29, pp. 6694–6709, 2000. DOI: 10.1021/jp000114x.

[33] Z. Ye, "Relaxor ferroelectric complex perovskites: Structure, properties and phase transitions," *Key Eng. Mater.*, vol. 155-156, pp. 81–122, 1998. DOI: 10.4028/www.scientific.net/KEM.155-156.81.

[34] Z.-G. Ye, "High-performance piezoelectric single crystals of complex perovskite solid solutions," *MRS Bull.*, vol. 34, no. 4, pp. 277–283, 2009. DOI: 10.1557/mrs2009.79.

[35] R. A. Cowley, S. N. Gvasaliy, S. G. Lushnikov, B. Roessli, and G. M. Rotaru, "Relaxing with relaxors: A review of relaxor ferroelectrics," *Adv. Phys.*, vol. 60, no. 2, pp. 229–327, 2011. DOI: 10.1080/00018732.2011.555385.

[36] C. Stock, M. Songvilay, P. M. Gehring, G. Xu, and B. Roessli, "Broadband critical dynamics in disordered lead-based perovskites," *J. Condens. Matter Phys.*, vol. 32, no. 37, p. 374 012, 2020. DOI: 10.1088/1361-648x/ab86ee.

[37] A. Fert, N. Reyren, and V. Cros, "Magnetic skyrmions: Advances in physics and potential applications," *Nat. Rev. Mater.*, vol. 2, no. 7, p. 17 031, 2017. DOI: 10.1038/natrevmats.2017.31.

[38] X. Huo *et al.*, "Complete set of elastic, dielectric, and piezoelectric constants of $[011]_C$ poled rhombohedral $Pb(In_{0.5}Nb_{0.5})O_3$-$Pb(Mg_{1/3}Nb_{2/3})O_3$-$PbTiO_3$:mn single crystals," *J. Appl. Phys.*, vol. 113, no. 7, p. 074 106, 2013. DOI: 10.1063/1.4792661.

[39] E. Sun, S. Zhang, J. Luo, T. R. Shrout, and W. Cao, "Elastic, dielectric, and piezoelectric constants of $Pb(In_{1/2}Nb_{1/2})O_3$-p$Pb(Mg_{1/3}Nb_{2/3})O_3$-$PbTiO_3$ single crystal poled along $[011]_C$," *Appl. Phys. Lett.*, vol. 97, no. 3, p. 032 902, 2010. DOI: 10.1063/1.3466906.

[40] S. Zhang, J. Luo, W. Hackenberger, and T. R. Shrout, "Characterization of $Pb(In_{1/2}Nb_{1/2})O_3$-$Pb(Mg_{1/3}Nb_{2/3})O_3$-$PbTiO_3$ ferroelectric crystal with enhanced phase transition temperatures," *J. Appl. Phys.*, vol. 104, no. 6, p. 064 106, 2008. DOI: 10.1063/1.2978333.

[41] R. Woollett, "Theoretical power limits of sonar transducers," in *1962 IRE National Convention*, 1962, pp. 90–94. DOI: 10.1109/IRENC.1962.199227.

[42] F. Li, S. Zhang, Z. Xu, and L.-Q. Chen, "The contributions of polar nanoregions to the dielectric and piezoelectric responses in domain-engineered relaxor-$PbTiO_3$ crystals," *Adv. Funct. Mater*, vol. 27, no. 18, p. 1 700 310, 2017. DOI: 10.1002/adfm.201700310.

[43] F. Li *et al.*, "The origin of ultrahigh piezoelectricity in relaxor-ferroelectric solid solution crystals," *Nat. Commun*, vol. 7, p. 13 807, 2016. DOI: 10.1038/ncomms13807.

[44] N. Giles-Donovan *et al.*, "Imitation of spin density wave order in $Cu_3Nb_2O_8$," *Phys. Rev. B*, vol. 102, p. 024 414, 2 2020. DOI: 10.1103/PhysRevB.102.024414.

[45] N. Giles-Donovan *et al.*, "Depth dependent chemical and magnetic disorder in $Pb(Fe_{1/2}Nb_{1/2})O_3$ - (1) positive and negative muon spectroscopy," *Phys. Rev. B*, Submitted.

[46] N. Giles-Donovan, A. D. Hillier, K. Ishida, L. Stoica, S. Cochran, and C. Stock, "Identification of transition metal oxidation states with negative muons in Mn oxides," *Acta Crystallogr. A*, In Preparation.

[47] N. Giles-Donovan, N. G. Fenu, C. Stock, S. Zhang, and S. Cochran, "A measure of energy density to quantify progress in Pb-free piezoelectric material development," in *2021 IEEE Int. Ultrason. Symp.*, 2021, pp. 1–4. DOI: 10.1109/IUS52206.2021.9593449.

Chapter 2

Background and Theory

This chapter provides a technical introduction and background to the material contained within the thesis. As the main application considered here, piezoelectricity is discussed including a review of the development of piezoelectric materials followed by derivation of the piezoelectric constitutive equations via a thermodynamic argument. This section also includes the influence of crystal symmetry on the material properties and more practical considerations such as resonant modes, the electromechanical coupling factor and losses.

Magnetic systems are also reviewed, with the different types of magnetic ordering outlined and classified. Two systems where two or more orders/disorders interact are then introduced being the main topic of study in this work. These are relaxor-ferroelectrics, which show coupling between structural disorder and ferroelectricity, and multiferroics, which show coupling between magnetism and electricity, with the mechanisms outlined.

2.1 Chapter Introduction

Ferroelectrics are a class of materials which exhibit a spontaneous order. In that case, it is an electric polarisation but there exist analogous cases in both magnetism and elasticity [1]. This ordering can be attributed to a loss of symmetry when the material passes through a phase transition. The consideration of symmetry in physics can often provide a short-cut when analysing complex phenomena. Thus, the concept of symmetry in crystals will be examined first, to lay the ground work for the discussion of piezoelectricity, magnetism and structural disorder.

2.2 Crystal Symmetry

A perfect crystal is defined by the infinite repetition of identical units of atoms on a periodic lattice [2]. This periodicity (or long-range ordering) causes the crystal to naturally display some form of translational symmetry. There are 14 admittable crystal lattices known as Bravais lattices

which can be split into seven crystal classes which classify the shape of the unit cell, e.g. cubic, tetragonal, rhombohedral [3–5].

The unit cell of a crystal is the most fundamental repeating unit and it is common to introduce lattice vectors, typically denoted as $\vec{1}$, $\vec{2}$ and $\vec{3}$ or $\vec{a}$, $\vec{b}$ and $\vec{c}$, which define the geometry of the unit cell. Figure 2.1 shows an example of a unit cell of the perovskite structure with chemical formula ABO_3.

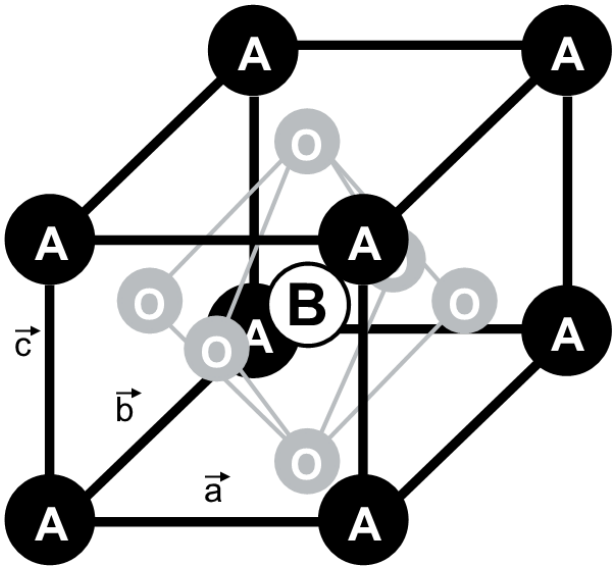

Figure 2.1: Unit cell of the perovskite structure with chemical formula ABO_3.

2.2.1 The Reciprocal Lattice

Being highly periodic, it is natural to try and apply Fourier methods to crystal structures. Consider a function $f(\vec{r})$ defined in three dimensions on a crystal lattice (a physical example could be the electron density which is central to X-ray scattering). This function must obey the translational symmetry of the crystal, $f(\vec{r}) = f(\vec{r}+\vec{L})$, where $\vec{L} = u\vec{a} + v\vec{b} + w\vec{c}$ is a real-space lattice vector. As this function is periodic it may be expressed as a Fourier series

$$f(\vec{r}) = \sum_{\vec{H}} f_{\vec{H}} e^{i\vec{H}\cdot\vec{r}}, \tag{2.1}$$

where $\{\vec{H}\}$ is the set of allowed vectors that are compatible with the symmetry. If the translation property is imposed, the condition on $\vec{H}$ is

$$\vec{H}\cdot\vec{L} = 2\pi n, \tag{2.2}$$

where n is an integer. This is conventionally enforced by constructing the reciprocal lattice. Like the real-space crystal lattice, this can be described by three unit vectors ($\vec{a}^*$, $\vec{b}^*$ and $\vec{c}^*$) which define the unit cell of the reciprocal lattice and satisfy

$$\begin{aligned}
&\vec{a}\cdot\vec{a}^* = 2\pi, && \vec{b}\cdot\vec{a}^* = 0, && \vec{c}\cdot\vec{a}^* = 0,\\
&\vec{a}\cdot\vec{b}^* = 0, && \vec{b}\cdot\vec{b}^* = 2\pi, && \vec{c}\cdot\vec{b}^* = 0,\\
&\vec{a}\cdot\vec{c}^* = 0, && \vec{b}\cdot\vec{c}^* = 0, && \vec{c}\cdot\vec{c}^* = 2\pi.
\end{aligned} \tag{2.3}$$

In this way, the reciprocal lattice vectors, $\vec{H}$, may be expressed in terms of the starred unit vectors. Once these are known, it is easy to construct Fourier representations for any crystal, something that is essential for the understanding of scattering phenomena, as will be explored in more detail in the next chapter. This can be easily motivated by considering the planes in a crystal. These may be described in terms of Miller indices [2] notation that will be followed in this thesis. Briefly, a plane is denoted by indices (h,k,l) where h, k and l are equal to the reciprocal of the intercepts of the plane with the lattice vectors $\vec{a}$, $\vec{b}$ and $\vec{c}$ respectively. Bars denote negative Miller indices and a zero index indicates that the plane does not intersect the associated lattice vector i.e. the intercept is said to be 'at infinity'.

As a plane corresponds to an infinite real-space structure, the reciprocal-space counterpart must be a point - indeed, a point on the reciprocal lattice. This allows the reciprocal lattice to be expressed as the collection of all $\vec{H} = h\vec{a}^* + k\vec{b}^* + l\vec{c}^*$ which form a periodic lattice.

2.2.2 Point Groups

For a given crystal, the point group is the set of operations (closed under multiplication and compatible with the translational symmetry of the lattice) under which the structure of the unit cell, and hence the crystal, is unchanged. Basic point group symmetry operations include rotations, reflections and inversions [6]. All groups contain an identity element (E) and combinations of these operations give 32 different symmetry groups which are physically realisable in a three dimensional crystal [3]. When these point groups are combined with the translation symmetry of the 14 Bravais lattices, they form the 230 crystal space groups [7].

Rotations about an axis may be described in terms of how many operations are required to reach 360°. In this thesis, the rotation axis will be denoted by a superscript and the sense (i.e. clockwise or anticlockwise) by subscript $+$ or $-$ respectively. For example, a $4^{(3)}$ symmetry describes a four-fold rotational symmetry and requires four operations to reach 360°, hence denoting 90° rotations around the $\vec{3}/\vec{c}$ axis. Reflections, σ_P, may be described in terms of a reflection plane P. Finally, inversion I must be defined with respect to an inversion centre through which the operation is performed.

The importance of symmetry in crystals is reinforced by Neumann's principle which states [8]

"Any type of symmetry which is exhibited by the point group of the crystal is possessed by every physical property for the crystal."

Neumann's principle may be seen as a specific case of Curie's later, more general principle [9] and so, by understanding the symmetry of the crystal, the behaviour can also be predicted. This is a very powerful concept used throughout this thesis.

2.3 Piezoelectricity and Ferroelectricity

The piezoelectric effect is the generation of a mechanical deformation in a material when exposed to an electric field or *vice-versa*. It was first discovered in 1880 when brothers Jacques and Pierre Curie observed that materials with certain crystal asymmetries developed an electric potential when compressed, later dubbed the direct piezoelectric effect [10]. The following year, Gabriel Lippmann predicted the existence of the converse piezoelectric effect [11]. This was done using thermodynamic theory and showed that the application of an electric field to one of the Curies' piezoelectric materials should produce a mechanical strain. This was soon verified by the brothers [12]. The concept of piezoelectricity is illustrated in Figure 2.2.

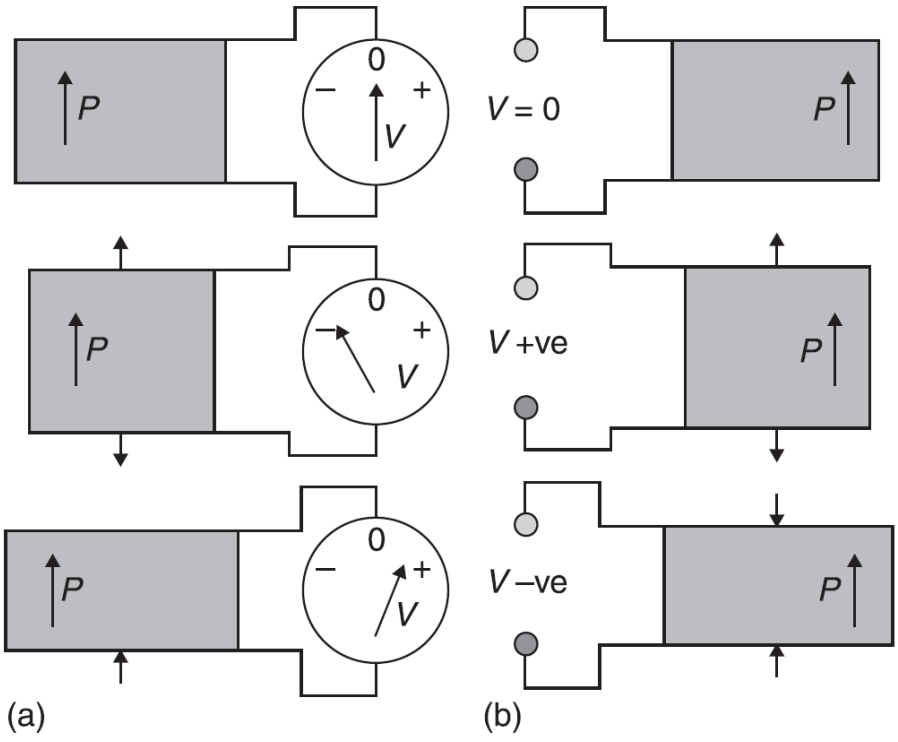

Figure 2.2: The direct (a) and converse (b) piezoelectric effect. Reprinted from S. Cochran, "Piezoelectricity and basic configurations for piezoelectric ultrasonic transducers," in *Ultrasonic Transducers*, Woodhead Publishing, 2012, ch. 1, Copyright (2012), with permission from Elsevier.

Typically piezoelectricity is defined as the linear coupling between electricity and mechanics. As will be demonstrated in the next section, it is only present in certain types of materials. However, there is always the quadratic analogue - electrostriction - which causes a strain to develop that is quadratic in polarisation [14]. As a non-linear component, this can often be neglected to first order in piezoelectric materials.

2.3.1 Piezoelectric Symmetries

In order to support a macroscopic electric polarisation and hence piezoelectricity, a crystal must not exhibit an inversion centre (following Neumann's principle, a inversion would force the polarisation vector to be equal to its inverse and hence be zero in magnitude). There are 21 non-centrosymmetric point groups of which 20 are piezoelectrically active (excluding the cubic group 432 as, though lacking an inversion centre, the symmetry is still too high to allow a polarisation) [15]. Of these piezoelectric groups, there is a further subclass of ten point groups that display a unique polar axis (i.e. invariant under *all* symmetry operations) and hence a spontaneous electric polarisation (that is in the absence of electric field, mechanical stress or other stimuli) [16]. If this spontaneous polarisation changes with temperature then the crystal is said to be pyroelectric. This is where the change in temperature causes the development of a charge on the ends of the crystal (through affecting the size of the electric dipole moment). Furthermore, if this spontaneous polarisation is reversible under the application of an electric field, then the crystal is said to be ferroelectric [16]. Throughout this chapter, piezoelectrics will be used as an umbrella term to represent the whole class of piezoelectric materials including the sub-class of ferroelectrics, as much of the same mathematics is used in their description.

The most relevant point group symmetries for this thesis are those displayed by ferroelectric perovskites. These are 4*mm* (crystal class: tetragonal), *mm*2 (crystal class: orthorhombic) and 3*m* (crystal class: rhombohedral). All symmetry elements in these groups are listed in Table 2.1 where the rotation axis is necessarily taken to be the poling direction.

Table 2.1: Symmetry elements for the point groups of ferroelectric perovskites [17]. Rotation axes are about the polar axis.

Point Group	Crystal Class	Polar Axis	Symmetry Elements
4*mm*	Tetragonal	<100>	E, 4^+, 4^-, 2, $\sigma_{(100)}$, $\sigma_{(010)}$, $\sigma_{(110)}$, $\sigma_{(\bar{1}10)}$
*mm*2	Orthorhombic	<110>	E, 2, $\sigma_{(100)}$, $\sigma_{(010)}$
3*m*	Rhombohedral	<111>	E, 3^+, 3^-, σ_{d1}, σ_{d2} , σ_{d3}

* d1, d2 and d3 denote the three equiangular planes perpendicular to <111>

2.3.2 Brief Historical Review of Piezoelectric Material Development

The Curie brothers' ground-breaking discovery in 1880 [10] fired the developmental starting pistol for piezoelectric materials. Their experiments as well as the early development of piezoelectrics are well catalogued by Katzir [18]. Briefly, the Curies studied crystals (which included tourmaline and quartz amongst others) and concluded that compression resulted in an electric charge developing across the material. As an aside, the Curies were initially investigating pyroelectricity and, as such, actually concluded that the effect of compression was like that of cooling whereas that of decompression was like heating, in terms of the sign of the produced charge.

With Lippmann's prediction [11] of the reciprocal relation and the brothers' confirmation [12], many models for piezoelectricity were proposed. Lippmann's theory relied on the conservation laws of charge and energy and provided a phenomenological description whereas the Curie brothers had an approach which involved 'polarised molecules' (although they were not referred to as such) and built upon the contemporary theories of pyroelectricity [19] (also see [20]). These studies myhlalong with numerous others culminated in the first 'complete' theory of piezoelectricity set out by the theoretician Voigt in 1890 [21] (again see [20] for a summary). This theory had a basis in symmetry which underlines the importance of this concept for piezoelectrics and is somewhat formalised by the Curie principle [9].

The development of piezoelectric materials was closely associated with that of ultrasonic technology [22]. With the advancement of maritime technology and the eventual outbreak of the first world war, there was a push to develop underwater ultrasonic technology. This led to the development of the Langevin transducer in 1917 in collaboration with the French navy [23] - a design which is still used to this day. The initial design used quartz but the performance was limited by its small piezoelectric effect. This led to the search for a higher performance material by US researchers, identifying Rochelle salt as a suitable alternative. It had much better electromechanical properties than quartz and proved easy to grow in large crystals [24]. A history of Rochelle salt is given by Busch [25]. Despite its advantages, the fact that Rochelle salt is water soluble put an end to its use as the material of choice in underwater devices and a new solution was required. However, Rochelle salt is still noteworthy for being the first to be reported to be ferroelectric by Valasek in 1921 [26].

During the interwar period many other piezoelectric materials were tried, most of which have faded into the annals of history. One noteworthy exception is KH_2PO_4 [27] which was 'designed' based on Mueller's 'interaction' theory of Rochelle salt rather than serendipitously discovered [28]. This theory is nicely set out in more familiar 'Landau' style by Mueller [29]) and a personal account of the discovery can be read here [30]. However, none of these compared to the perovskite $BaTiO_3$ (BT) which was independently discovered by four different countries (USA, UK, Russia and Japan) at the start of the second world war. The reader is invited to refer to the review by Kanzig [31] as well as the summary by Uchino [32]. BT also saw the

generalisation of Mueller's 'interaction' argument to a full Landau theory approach by Devonshire in 1949 [33] as detailed in Section 2.4.3. Another development came with the confirmation of piezoelectricity in polycrystalline ceramic BT in 1948 by Mason [34], which allowed easy and consistent manufacturability for transducer applications. Whilst BT had large piezoelectric coefficients and did not suffer from water solubility like Rochelle salt, it still had the issue of a relatively low ferroelectric to paraelectric transition temperature - the Curie temperature at $\approx 120^{\circ}$C - which limited applicability and caused ageing issues, with performance rapidly degrading over time. Again an alternative was desired and staying within the family of perovskites would prove to be the solution.

By the 1950s, Pb-based perovskites had become the material of choice for piezoelectric applications. This dominance started with the discovery of high piezoelectric coefficients in the solid solution formed by $PbZrO_3$ (PZ) and $PbTiO_3$ (PT) dubbed $Pb(Ti_xZr_{1-x})O_3$ (PZT) by Jaffe *et al.* [35] following studies by Japanese groups such as Shirane *et al.* [36] and Sawaguchi [37]. The development of PZT continued in the Clevite Corporation (Cleveland, Ohio, USA); much of this and the characteristics of PZT are summarised in the definitive textbook by Jaffe, Cook and Jaffe [38].

In short, the high piezoelectric performance of PZT is due to the presence of the morphotropic phase boundary (MPB) shown in Figure 2.3 as the near-vertical line at $\approx$50% PT. Whilst 'morphotropic' strictly should apply to phase transitions induced by changes in composition, in the field of ferroelectrics the term MPB usually refers to the transition between the tetragonal and rhombohedral ferroelectric phases, though typically still as a result of varying the composition [39]. Near the MPB, the crystal structure undergoes an abrupt change which results in local maxima of the dielectric and electromechanical properties. The presence of the MPB in PZT ensures that, nearby, the piezoelectric coefficient is large but the real strength is that the phase boundary remains relatively stable against temperature, reflected in the vertical orientation of the MPB [39]. Furthermore, a monoclinic phase was discovered at the MPB in PZT in 1999 by Noheda *et al.* [40] and this was later confirmed in theoretical studies [41]. This has been indicated to increase the strength of the piezoelectric effect and will be discussed further in the context of relaxor-ferroelectric materials in Chapter 6.

The superior Curie temperature of PZT is also shown in Figure 2.3, with $T_C > 200^{\circ}$C and $T_C \approx 375^{\circ}$C near the MPB - a vast improvement over BT. Another strength of PZT is its versatility under doping with a large range of properties achievable [42]. However, PZT is difficult to grow as a single crystal [43]. Nevertheless, its advantages have ensured that polycrystalline PZT has become the main 'workhorse' material for piezoelectric transducer applications [44].

Protected by their patent, Clevite remained the primary manufacturer of PZT apart from the exception of the Murata Manufacturing Company Ltd. (Kyoto, Japan), which also produced PZT under license. However, most other companies were not content with this agreement and so their attention turned to other materials, specifically the development of ternary PZT systems

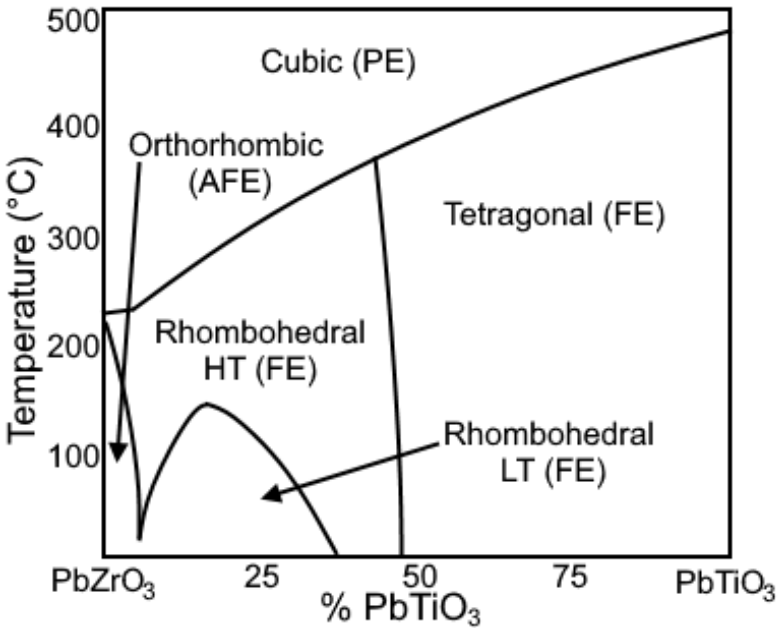

Figure 2.3: A schematic phase diagram for $Pb(Ti_xZr_{1-x})O_3$ (PZT). Shows the high temperature paraelectric (PE) phase and the low temperature ferroelectric (FE) and antiferroelectric (AFE) phases after Jaffe *et al.* [38].

by mixing PZT with other perovskites [22].

Whilst the US and Japan were primarily concerned with PZT based ceramic production, the Russian group of Smolenskii was investigating a new class of compounds with huge dielectric permittivities - the relaxor-ferroelectrics. Their studies concerned the prototypical relaxor-ferroelectrics $Pb(Mg_{1/3}Nb_{2/3})O_3$ (PMN) [45] and $Pb(Zn_{1/3}Nb_{2/3})O_3$ (PZN) [46]. These materials retain an averagely cubic structure down to low temperatures and so are unable to be piezoelectrically active by symmetry [47]. However, when combined in a solid solution with PT, akin to PZT, piezoelectric coefficients up to an order of magnitude larger than PZT can be achieved [48]. The development of these materials, as well as a technical overview, is covered in more detail in Sections 2.6 and 6.3 respectively. A historical review of their early development against PZT is also given by Uchino [22] along with review articles by Zhang *et al.* [49] and Cowley *et al.* [50].

Whilst this thesis primarily concerns Pb-based relaxor-ferroelectric materials, a brief mention of the recent development of Pb-free materials is also warranted. Following the emergence of PZT in the 1950s, development of Pb-free materials continued, somewhat subdued, in parallel, such as for $LiNbO_3$ (LNO) which, despite its chemical formula, is not a perovskite [51]. LNO was discovered to be ferroelectric in 1949 by Matthias and Remeika [52] and showed a very high Curie temperature but was no match for PZT with regard to the most sought after FOMs. However LNO single crystals have since been commercialised in, amongst others, acoustic wave filter applications [22].

There has been a resurgence of interest in Pb-free piezoelectric materials since the millennium because of the toxicity of Pb and fears that contamination of the natural environment may

cause irreversible damage [53]. Indeed, the European Restrictions on Hazardous Substances regulations (RoHs-2002 and RoHS 2-2011) have imposed a 0.1% limit on Pb content by weight. This was also accompanied by similar legislation in Japan and China [54]. Regardless, the difficulty in replacing Pb-based piezoelectric materials is due to their historically poor performance. Promising candidate materials include the alkali niobate family (such as LNO) [55], the mixed relaxor-ferroelectric $Bi_{1/2}Na_{1/2}TiO_3$ (BNT) system [56–58], as well as systems derived from the aforementioned BT [59, 60]. Another interesting Pb-free candidate is the $BiFeO_3$ (BF) system which shows multiferroic behaviour and is well-studied [61, 62].

Whilst their performance is still inferior to Pb-based materials, PZT in particular, Pb-free materials have started to become commercialised in ultrasonics. The issues behind their lack of performance are reviewed by Koruza *et al.* [63] but many prototype devices are being developed in applications such as energy harvesting [64] and ultrasonics actuators [57, 59, 65]. The development of Pb-free materials and their properties and applications are more conclusively reviewed in the books by Wu [54] and Uchino [22] as well as the many review articles referenced here. The question of Pb-based/Pb-free material comparison will be addressed more in Chapter 7.

2.4 Physics of Piezoelectrics

This section will provide a brief technical summary of the physical mechanisms that apply in piezoelectric materials, as a foundation for all other topics discussed in this thesis. This chapter, and indeed the remainder of the thesis, will use index notation to represent tensor and vector properties.

Unless otherwise stated, Einstein summation convention is assumed, where repeated indices are implicitly summed over [66]. Here Latin indices represent three dimensions and so $i, j, k, \ldots = 1, 2, 3$. Furthermore, reduced 'matrix' (or Voigt) notation will also be used [67]. By exploiting the intrinsically symmetric nature of the stress and strain tensors, a simpler representation can be formed by pairing indices. Greek letters will be used here to denote Voigt indices such that $\mu, \nu, \ldots = 1 - 6$. In this representation the 'new' directions (4, 5 and 6) can be seen as representing shears - 4 is shearing about direction 1, 5 is shearing about direction 2 and 6 is shearing about direction 3. For this to hold, the conversion rules in Table 2.2 are introduced.

2.4.1 Constitutive Equations

The behaviour of a piezoelectric material can be fully described by a set of constitutive equations [13]. These equations link together the electric properties D_i (electric displacement) and E_i (electric field) with the mechanical properties σ_μ (stress) and S_μ (strain). In order to unambiguously describe the material's behaviour, any electromechanical pair of these properties

Table 2.2: Conversion between Cartesian index and reduced 'matrix' or Voigt notation [67].

Cartesian	**Voigt/Matrix**
f ij	μ
11	1
22	2
33	3
23 or 32	4
13 or 31	5
12 or 21	6

(e.g. D_i and S_μ) may be written as functions of the other pair. Hence, there are four equivalent formulations of constitutive equations.

In a non-piezoelectric material the mechanical and electric behaviour, denoted by superscripts $^{(M)}$ and $^{(E)}$ respectively, are independent and so may be treated separately. Thus the thermodynamics of each remains disparate. However, in a piezoelectric material this is not the case, and so this coupling must be reflected in any thermodynamic theory. Technically, in order to provide a complete treatment, the temperature should also be considered and this gives rise to phenomena such as pyroelectricity and thermal expansion [67]. However, these will be neglected here as the focus is on the coupling between elasticity and electricity with the temperature assumed constant.

A Thermodynamic Argument

From conventional elasticity theory, the mechanical energy density is the work done against the stress forces inside the material. Introducing σ_μ and S_μ, this energy density is given in differential form by [68]

$$dU^{(M)} = \sigma_\mu dS_\mu. \tag{2.4}$$

Furthermore, the differential dielectric energy density is given by [69]

$$dU^{(E)} = E_i dD_i. \tag{2.5}$$

Hence, in a piezoelectric material the total internal energy density will be the sum of the mechanical and electrical energy densities

$$dU = dU^{(M)} + dU^{(E)} = \sigma_\mu dS_\mu + E_i dD_i. \tag{2.6}$$

Equation 2.6 is the equivalent of the first law of thermodynamics for a piezoelectric material and is the starting point for the study of energy density in Chapter 7. Furthermore, writing the energy density in this form clearly displays the *natural variables* of U as S_μ and D_i such that $U = U(S_\mu, D_i)$. This follows from the laws of partial differentiation [70] and also allows

identification of

$$E_i = \frac{\partial U}{\partial D_i}, \tag{2.7}$$

$$\sigma_\mu = \frac{\partial U}{\partial S_\mu}, \tag{2.8}$$

where the partial derivatives are implicitly defined so that the other thermodynamic variables are fixed. Identification of the natural variables of U then allows expansion of σ_μ and E_i as $\sigma_\mu(S_\nu, D_i)$ and $E_i(S_\mu, D_j)$ to give [71]

$$dE_i = \frac{\partial E_i}{\partial S_\mu} dS_\mu + \frac{\partial E_i}{\partial D_j} dD_j, \qquad d\sigma_\mu = \frac{\partial \sigma_\mu}{\partial S_\nu} dS_\nu + \frac{\partial \sigma_\mu}{\partial D_i} dD_i. \tag{2.9}$$

These are the differential forms of the piezoelectric constitutive equations formulated in terms of S_μ and D_i and explicitly show the piezoelectric coupling. If the rest state of the material is defined in the absence of any stress, strain, electric field or electric displacement then it follows that the constitutive equations must be at least linear [72]. Furthermore, as piezoelectricity includes only the *linear* part of the coupling between elasticity and electricity [73], Equation 2.9 can be integrated to give linear constitutive equations

$$E_i = \frac{\partial E_i}{\partial S_\mu} S_\mu + \frac{\partial E_i}{\partial D_j} D_j, \qquad \sigma_\mu = \frac{\partial \sigma_\mu}{\partial S_\nu} S_\nu + \frac{\partial \sigma_\mu}{\partial D_i} D_i. \tag{2.10}$$

Finally, Equations 2.7 and 2.8 may be substituted to arrive at

$$E_i = \frac{\partial^2 U}{\partial D_i \partial S_\mu} S_\mu + \frac{\partial^2 U}{\partial D_i \partial D_j} D_j, \qquad \sigma_\mu = \frac{\partial^2 U}{\partial S_\mu \partial S_\nu} S_\nu + \frac{\partial^2 U}{\partial S_\mu \partial D_i} D_i, \tag{2.11}$$

where the material constants have been expressed as second differentials of the potential U. These are the constitutive equations in what will be referred to as the *strain-displacement* formulation (named for the natural variables of the associated potential). Comparison with conventional theory of elastic and dielectric materials allows identification [74] of the elastic stiffness at constant electric displacement

$$c^D_{\mu\nu} = \frac{\partial^2 U}{\partial S_\mu \partial S_\nu}, \tag{2.12}$$

and inverse dielectric permittivity at constant strain

$$(\varepsilon^S)^{-1}_{ij} = \frac{\partial^2 U}{\partial D_i \partial D_j}, \tag{2.13}$$

whilst the mixed derivative defines the piezoelectric stiffness constant

$$h_{i\mu} = -\frac{\partial^2 U}{\partial D_i \partial S_\mu}. \tag{2.14}$$

One advantage of this derivation is that the reciprocity of the piezoelectric effect is clearly shown here as $\frac{\partial E_i}{\partial S_\mu} = \frac{\partial \sigma_\mu}{\partial D_i}$. As such, it can be expected that the stress produced by the presence of an electric displacement has the same coefficient as the electric field produced by a strain - $h_{i\mu}$. This is similar to the reasoning used by Lippmann in his derivation of the converse piezoelectric effect in 1881 [11].

Equivalent Formulations

Thermodynamic potentials with other combinations of natural variables can be constructed using the Legendre transform [75]. These are

$$H \equiv U - E_i D_i, \tag{2.15}$$

$$F \equiv U - \sigma_\mu S_\mu, \tag{2.16}$$

$$G \equiv U - \sigma_\mu S_\mu - E_i D_i, \tag{2.17}$$

which are referred to as the *enthalpy*, *Helmholtz free energy* and *Gibbs free energy* respectively, in analogy with classical thermodynamic theory [71, 76]. Expanding these relations into differential form gives

$$dH = \sigma_\mu dS_\mu - D_i dE_i, \tag{2.18}$$

$$dF = -S_\mu d\sigma_\mu + E_i dD_i, \tag{2.19}$$

$$dG = -S_\mu d\sigma_\mu - D_i dE_i, \tag{2.20}$$

thus allowing the natural variables to be established as $H = H(S_\mu, E_i)$, $F = F(\sigma_\mu, D_i)$ and $G = G(\sigma_\mu, E_i)$. Each of these potentials will result in a different but equivalent formulation of the piezoelectric constitutive equations. The full set of constitutive equations is then given by

$$D_i = \varepsilon_{ij}^S E_j + e_{i\mu} S_\mu \qquad \sigma_\mu = c_{\mu\nu}^E S_\nu - e_{i\mu} E_i \tag{2.21}$$

$$D_i = \varepsilon_{ij}^\sigma E_j + d_{i\nu} \sigma_\nu \qquad S_\mu = s_{\mu\nu}^E \sigma_\nu + d_{i\mu} E_i \tag{2.22}$$

$$E_i = -g_{i\mu} \sigma_\mu + (\varepsilon^\sigma)_{ij}^{-1} D_j \qquad S_\mu = s_{\mu\nu}^D \sigma_\nu + g_{i\mu} D_i \tag{2.23}$$

$$E_i = -h_{i\mu} S_\mu + (\varepsilon^S)_{ij}^{-1} D_j \qquad \sigma_\mu = c_{\mu\nu}^D S_\nu - h_{i\mu} D_i \tag{2.24}$$

where ε_{ij}^S and ε_{ij}^σ are the dielectric permittivity at constant strain (clamped) and stress (unclamped) respectively; $c_{\mu\nu}^E$ and $s_{\mu\nu}^E = (c_{\mu\nu}^E)^{-1}$ are the stiffness and compliance at constant electric field respectively; $c_{\mu\nu}^D$ and $s_{\mu\nu}^D = (c_{\mu\nu}^D)^{-1}$ are the stiffness and compliance at constant electric displacement respectively (often referred to as the stiffened parameters); $e_{i\mu}$ is the piezoelectric stress constant; $d_{i\mu}$ is the piezoelectric strain constant; $g_{i\mu}$ is the piezoelectric voltage constant; and $h_{i\mu}$ is the piezoelectric stiffness constant [13].

2.4.2 Elasto-Piezo-Dielectric Matrix

The piezoelectric constitutive equations may be succinctly written in matrix form [13]. For example, Equation 2.21 may be written as

$$\begin{pmatrix} \sigma_1 \\ \sigma_2 \\ \sigma_3 \\ \sigma_4 \\ \sigma_5 \\ \sigma_6 \\ D_1 \\ D_2 \\ D_3 \end{pmatrix} = \left(\begin{array}{cccccc|ccc} c_{11}^E & c_{12}^E & c_{13}^E & c_{14}^E & c_{15}^E & c_{16}^E & -e_{11} & -e_{21} & -e_{31} \\ c_{21}^E & c_{22}^E & c_{23}^E & c_{24}^E & c_{25}^E & c_{26}^E & -e_{12} & -e_{22} & -e_{32} \\ c_{31}^E & c_{32}^E & c_{33}^E & c_{34}^E & c_{35}^E & c_{36}^E & -e_{13} & -e_{23} & -e_{33} \\ c_{41}^E & c_{42}^E & c_{43}^E & c_{44}^E & c_{45}^E & c_{46}^E & -e_{14} & -e_{24} & -e_{34} \\ c_{51}^E & c_{52}^E & c_{53}^E & c_{54}^E & c_{55}^E & c_{56}^E & -e_{15} & -e_{25} & -e_{35} \\ c_{61}^E & c_{62}^E & c_{63}^E & c_{64}^E & c_{65}^E & c_{66}^E & -e_{16} & -e_{26} & -e_{36} \\ \hline e_{11} & e_{12} & e_{13} & e_{14} & e_{15} & e_{16} & \varepsilon_{11}^S & \varepsilon_{12}^S & \varepsilon_{13}^S \\ e_{21} & e_{22} & e_{23} & e_{24} & e_{25} & e_{26} & \varepsilon_{21}^S & \varepsilon_{22}^S & \varepsilon_{23}^S \\ e_{31} & e_{32} & e_{33} & e_{34} & e_{35} & e_{36} & \varepsilon_{31}^S & \varepsilon_{32}^S & \varepsilon_{33}^S \end{array}\right) \begin{pmatrix} S_1 \\ S_2 \\ S_3 \\ S_4 \\ S_5 \\ S_6 \\ E_1 \\ E_2 \\ E_3 \end{pmatrix}. \tag{2.25}$$

This defines the elasto-piezo-dielectric (EPD) matrix in the *strain-field* formulation. Knowledge of this matrix allows the material's behaviour to be fully defined. In general, Equation 2.25 shows that the EPD matrix has 81 components. However, this number can be greatly reduced by considering the symmetry of the material, as shown using the following argument [77]:

The thermodynamic potentials may generally be expanded in the natural variables of a system and, as previously argued, the lowest non-trivial terms in the potentials must be quadratic (this ensures linear constitutive equations). For example, considering the enthalpy function (the thermodynamic potential associated with the strain-field formulation), by this logic it may be expressed as

$$H(S_\mu, E_i) = \frac{1}{2}\Phi_{ijkl}S_{ij}S_{kl} + \frac{1}{2}X_{ij}E_iE_j + \Psi_{ijk}E_iS_{jk} + \cdots, \tag{2.26}$$

where the use of Voigt notation is temporarily suspended. The enthalpy must be a scalar and so Φ_{ijkl}, X_{ij} and Ψ_{ijk} may be identified as a fourth, second and third rank tensor respectively.

It follows from Neumann's principle that any thermodynamics potential must respect the symmetry of the situation and so be invariant under any symmetry transformations. Hence, it must be expressible as a linear combination of all symmetry obeying invariant quantities [77] and so, by constructing all such second-order invariants, a form for the coefficients Φ_{ijkl}, X_{ij} and Ψ_{ijk} can be easily computed. The natural variables of H are S_μ and E_i, hence, the complete list of second-order invariants in 4*mm* symmetry is

$$\begin{aligned} &S_{ii}S_{jj}, \quad S_{ij}S_{ji}, \quad S_{33}^2, \quad S_{ii}S_{33}, \quad S_{3i}S_{3i}, \quad S_{12}S_{12}, \\ &E_iE_i, \quad E_3^2, \\ &E_3S_{33}, \quad E_3S_{ii}, \quad E_iS_{3i}. \end{aligned} \tag{2.27}$$

These quantities are invariant under the four-fold rotation and reflections in the mirror planes of 4*mm* [17]. This means that, in order to fully describe the anisotropic behaviour of a material with 4*mm* symmetry, six independent elastic, two independent dielectric and three independent piezoelectric constants are needed. As an aside, this argument can also be used to see why all materials display the higher order phenomena of electrostriction (quadratic electromechanical coupling) [14, 71]. This is because third order invariants of the form $S_{ij}E_iE_j$ are *always* present in the potential expansion whereas second order coupling in Equation 2.27 is only present for certain symmetries (such as here in 4*mm*).

Therefore, the coefficients Φ_{ijkl}, X_{ij} and Ψ_{ijk} may be written as

$$\begin{aligned} \Phi_{ijkl} = {} & a\delta_{ij}\delta_{kl} + \frac{b}{2}(\delta_{ik}\delta_{jl} + \delta_{il}\delta_{jk}) + c\delta_{i3}\delta_{j3}\delta_{k3}\delta_{l3} + \frac{d}{2}(\delta_{ij}\delta_{k3}\delta_{l3} + \delta_{kl}\delta_{i3}\delta_{j3}) \\ & + \frac{e}{4}(\delta_{i3}\delta_{jl}\delta_{k3} + \delta_{il}\delta_{j3}\delta_{k3} + \delta_{i3}\delta_{jk}\delta_{l3} + \delta_{ik}\delta_{j3}\delta_{l3}) \\ & + \frac{f}{4}(\delta_{i1}\delta_{j2}\delta_{k1}\delta_{l2} + \delta_{i1}\delta_{j2}\delta_{k2}\delta_{l1} + \delta_{i2}\delta_{j1}\delta_{k1}\delta_{l2} + \delta_{i2}\delta_{j1}\delta_{k2}\delta_{l1}), \end{aligned} \tag{2.28}$$

$$X_{ij} = g\delta_{ij} + h\delta_{i3}\delta_{j3}, \tag{2.29}$$

$$\Psi_{ijk} = k\delta_{i3}\delta_{j3}\delta_{k3} + l\delta_{i3}\delta_{jk} + \frac{m}{2}(\delta_{ij}\delta_{k3} + \delta_{ik}\delta_{j3}). \tag{2.30}$$

where δ_{ij} is the Kronecker delta (defined such that δ_{ij} is unity if $i = j$ and zero otherwise) [78]. Care must be taken to express these in appropriately symmetrised form. For example, the term $\frac{1}{2}\Phi_{ijkl}S_{ij}S_{kl}$ is clearly invariant under $i \leftrightarrow j$, $k \leftrightarrow l$ and $i, j \leftrightarrow k, l$ requiring $\Phi_{ijkl} = \Phi_{jikl}$, $\Phi_{ijkl} = \Phi_{ijlk}$ and $\Phi_{ijkl} = \Phi_{klij}$ respectively. This follows from the properties of the strain tensor [67].

Furthermore, by considering derivatives of H,

$$c^E_{ijkl} = \frac{\partial^2 H}{\partial S_{ij}\partial S_{kl}} = \Phi_{ijkl}, \tag{2.31}$$

$$\varepsilon^S_{ij} = \frac{\partial^2 H}{\partial E_i \partial E_j} = X_{ij}, \tag{2.32}$$

$$e_{ijk} = -\frac{\partial^2 H}{\partial E_i \partial S_{jk}} = -\Psi_{ijk}. \tag{2.33}$$

This allows the form of the EPD matrix for $4mm$ (reintroducing Voigt notation) to be written as

$$\left(\begin{array}{cccccc|ccc} c^E_{11} & c^E_{12} & c^E_{13} & 0 & 0 & 0 & 0 & 0 & -e_{31} \\ c^E_{12} & c^E_{11} & c^E_{13} & 0 & 0 & 0 & 0 & 0 & -e_{31} \\ c^E_{13} & c^E_{23} & c^E_{33} & 0 & 0 & 0 & 0 & 0 & -e_{33} \\ 0 & 0 & 0 & c^E_{44} & 0 & 0 & 0 & -e_{15} & 0 \\ 0 & 0 & 0 & 0 & c^E_{44} & 0 & -e_{15} & 0 & 0 \\ 0 & 0 & 0 & 0 & 0 & c^E_{66} & 0 & 0 & 0 \\ \hline 0 & 0 & 0 & 0 & e_{15} & 0 & \varepsilon^S_{11} & 0 & 0 \\ 0 & 0 & 0 & e_{15} & 0 & 0 & 0 & \varepsilon^S_{11} & 0 \\ e_{31} & e_{31} & e_{33} & 0 & 0 & 0 & 0 & 0 & \varepsilon^S_{33} \end{array}\right), \tag{2.34}$$

where $c^E_{11} = a+b$, $c^E_{12} = a$, $c^E_{13} = a+\frac{d}{2}$, $c^E_{33} = a+b+c+d+e$, $c^E_{44} = \frac{b}{2}+\frac{e}{2}$, $c^E_{66} = \frac{b}{2}+\frac{f}{2}$, $\varepsilon^S_{11} = g$, $\varepsilon^S_{33} = g+h$, $e_{31} = -l$, $e_{33} = -k-l-m$, $e_{15} = -\frac{m}{2}$.

The structure of the EPD matrix wholly encompasses the symmetry of the material and, therefore, can be used to predict its behaviour. This shows the power of the thermodynamic argument, where the whole array of material behaviour emerges as a result of the combination of mechanical and elastic energy densities and using the principle that the resulting potential should respect the material's symmetry. The EPD matrix is regularly used to describe behaviour in ultrasonic and material science applications and will be further used in Chapter 7 to analyse the material's response in the context of energy conversion mechanisms.

2.4.3 Devonshire Theory

Another strength of considering the free energy of a system is its ability to describe phase transitions phenomenologically though Landau theory [79]. The classic 'normal' ferroelectric perovskite is BT. It was reported as ferroelectric in 1945 [31] and undergoes three phase transitions: Below -90°C, BT has a rhombohedral structure; between -90°C and 5°C, the crystal is orthorhombic; and, finally, forms a tetragonal structure until undergoing a paraelectric-ferroelectric transition at 123°C [80]. Above this transition, BT is a perfect cubic perovksite.

These transitions were first reported during the latter half of the 1940s [81–83] culminating in a phenomenological Landau model being proposed by Devonshire in 1949 [33]. By expressing the free energy as an even power series that obeys symmetry in polarisation, and later strain, the observed sequence of phases was reproduced [33]. Devonshire later went on to use this theory to derive relations between material constants [84].

With a rise in use of PZT during the 1980s, there was a push to construct a Devonshire expansion. This proved more difficult than BT due to the more complex behaviour of PZT and the lack of single crystal data [43]. From the phase diagram of PZT (Figure 2.3), several phases are present: at low temperatures and percentage of Ti a second rhombohedral phase appears characterised by a tilting of the oxygen octahedra; and, with almost no Ti, there is a rise in antiferroelectric behaviour [85].

These required many more terms to be included in the free energy expansion proposed by Haun *et al.* in a series of five papers in 1989 [86–90]. A tilt angle for the oxygen octahedra had been first included in a one dimensional case by Halemane *et al.* in 1985 [91]. This theory reproduces the observed phases and was also used to construct expressions for physical constants and properties. The results gained from this (assumed to be a single domain sample) were then used to give a greater understanding of properties of PZT that arise from its polycrystalline nature. For example, the large electromechanical anisotropy that occurs in PZT ceramics, but not in single crystals, was explained as where the intrinsic (e.g. lattice deformations) and extrinsic (e.g. domain wall movement near the grain boundaries in polycrystalline samples) contributions. The intrinsic effects are dominant in single crystals but extrinsic effects contribute 20 - 60% to the material properties in ceramics [92]. The separation of these effects was a major motivation for the treatment [90].

2.4.4 Relations between Material Properties

Through mutual substitution of Equations 2.21 - 2.24, the relations between the material properties present in the various formulations of the piezoelectric constitutive equations can be derived and they are reproduced here for convenience [48].

In a general material the four piezoelectric coefficients are related by

$$e_{i\mu} = \varepsilon^S_{ij} h_{j\mu} = d_{i\nu} c^E_{\mu\nu}, \tag{2.35}$$

$$d_{i\mu} = \varepsilon^\sigma_{ij} g_{j\mu} = e_{i\nu} s^E_{\mu\nu}, \tag{2.36}$$

$$g_{i\mu} = (\varepsilon^\sigma)^{-1}_{ij} d_{j\mu} = h_{i\nu} s^D_{\mu\nu}, \tag{2.37}$$

$$h_{i\mu} = (\varepsilon^S)^{-1}_{ij} e_{j\mu} = g_{i\nu} c^D_{\mu\nu}. \tag{2.38}$$

Furthermore, the stiffened $c^D_{\mu\nu}$ and $s^D_{\mu\nu}$ are related to the unstiffened parameters c^E and s^E by

$$c^D_{\mu\nu} = c^E_{\mu\nu} + (\varepsilon^S)^{-1}_{ij} e_{i\mu} e_{j\nu} = c^E_{\mu\nu} + \varepsilon^S_{ij} h_{i\mu} h_{j\nu}, \tag{2.39}$$

$$s^D_{\mu\nu} = s^E_{\mu\nu} - (\varepsilon^\sigma)^{-1}_{ij} d_{i\mu} d_{j\nu} = s^E_{\mu\nu} - \varepsilon^\sigma_{ij} g_{i\mu} g_{j\nu}, \tag{2.40}$$

and the clamped permittivity ε^S_{ij} is given by:

$$\varepsilon^S_{ij} = \varepsilon^\sigma_{ij} - d_{i\mu} d_{j\nu} c^E_{\mu\nu}. \tag{2.41}$$

2.4.5 Piezoelectric Equations of Motion

The general behaviour of a piezoelectric material can be fully described by the displacement vector, u_i, and the quasi-static electric potential, ϕ. This potential maybe introduced under the magnetostatic approximation where, because the speed of sound is much less the speed of light, any induced magnetic fields may be treated as static and so the electric field may be taken as irrotational [93]. Due to the piezoelectric coupling, both a mechanical equation of motion (Newton's 2nd Law) and an electric equation of motion (Gauss' Law) are required to fully describe the behaviour of the material [77]:

$$\rho \frac{\partial^2 u_i}{\partial t^2} = f_i + \frac{\partial \sigma_{ij}}{\partial x_j}, \tag{2.42}$$

$$\frac{\partial D_i}{\partial x_i} = \rho_e, \tag{2.43}$$

where f_i and ρ_e correspond to an external force and charge density respectively (Voigt notation is suppressed for Equation 2.42 only). Substitution of Equation 2.21 then gives

$$\rho \frac{\partial^2}{\partial t^2} u_i - c^E_{ijkl} \frac{\partial^2}{\partial x_j \partial x_k} u_l = f_i + e_{kij} \frac{\partial^2}{\partial x_j \partial x_k} \phi, \tag{2.44}$$

$$\varepsilon^S_{ij} \frac{\partial^2}{\partial x_i \partial x_j} \phi = -\rho_e + e_{ijk} \frac{\partial^2}{\partial x_i \partial x_j} u_k. \tag{2.45}$$

Equation 2.44 takes the form of a wave equation with two sources: one represents the external force density whilst the other corresponds to the piezoelectric coupling. Similarly, Equation 2.45 takes the form of Poisson's equation with source terms corresponding to external charge density and piezoelectric coupling. These equations are generally difficult to solve and so a numerical solution is usually the most convenient option, through a method such as finite element analysis.

2.4.6 Piezoelectric Modes

Resonance is a well known phenomenon in oscillating systems. The simplest occurrence of resonance is in the one dimensional damped simple harmonic oscillator under the influence of a periodic forcing term, $F_0 e^{i\omega t}$ [94]. One definition of resonance is the frequency that corresponds to the maximum response amplitude, which occurs at the frequency $\omega^2 = \omega_0^2 - \frac{\gamma^2}{2}$, where γ gives the mass normalised damping coefficient and ω_0 is the natural frequency of the system i.e. the square root of the mass normalised spring constant [95]. Alternatively, the resonance may be defined when the driving force delivers the greatest possible power to the system [95]. In a mechanical oscillator this occurs when the force is always acting in the same direction as the velocity - so when the phase difference is $\pi/2$ or $\omega = \omega_0$. These two frequencies are typically very close together but only coincide in the absence of damping.

Resonance can also occur in electrical circuits, with the best known example being the *RLC* circuit [96]. This circuit is described by the same differential equation as simple harmonic motion and so an analogous set of properties may be defined, with the inductance in the role of mass, capacitance as the inverse of the spring constant, resistance as the damping and the external voltage as the driving force. An electrical resonance may be found by considering the minimum of the electrical impedance as this will correspond to the maximum current, which plays the role of velocity in the mechanical analogy. In a piezoelectric material there exists coupling between the elastic and dielectric properties and so the material must exhibit *both* mechanical and electrical resonances.

Geometry can be used to isolate resonant behaviour. For example, a bar of length ten times the width will resonate in the so-called length extensional (LE) mode whilst a plate of width ten times the thickness will resonate is the so-called thickness extensional (TE) mode [73]. These modes are illustrated in Figure 2.4(a) and (b) respectively and, whilst the motion is similar, they are actually very distinct. One example of this is when considering the proportion of energy that is converted and stored (this will be covered in the next section). A summary of common piezoelectric modes is included in Table 2.3 which also shows their geometric conditions. Whilst the frequency of resonance is based on material properties, the isolation of resonant behaviour is linked purely to sample geometry and this coupling will obscure the pure material response at these frequencies.

Typically, ultrasonic devices are driven at or near a resonance frequency in order to maximise the output with the geometry chosen to simplify the piezoelectric response. This is key in actuating application such as active SONAR and high-power ultrasonic cutting. Of course, the resonance may also be used to increase the sensitivity (volt per displacement) and this is more relevant for receive applications such as passive SONAR and imaging. However, in a piezoelectric material, every resonance is followed by an antiresonance. An antiresonance is not present in the driven simple harmonic oscillator but can be found when this oscillator is coupled to another. As these two oscillators exert a force on each other, there exists a frequency when

the driving force is cancelled out by the reaction force of the other oscillator. In the converse of a resonance, this results in the displacement of the driven oscillator becoming minimum. Again, an antiresonance may also occur in electrical systems - this corresponds to a minimum of electric current and so can be identified by a maxima in the electrical impedance.

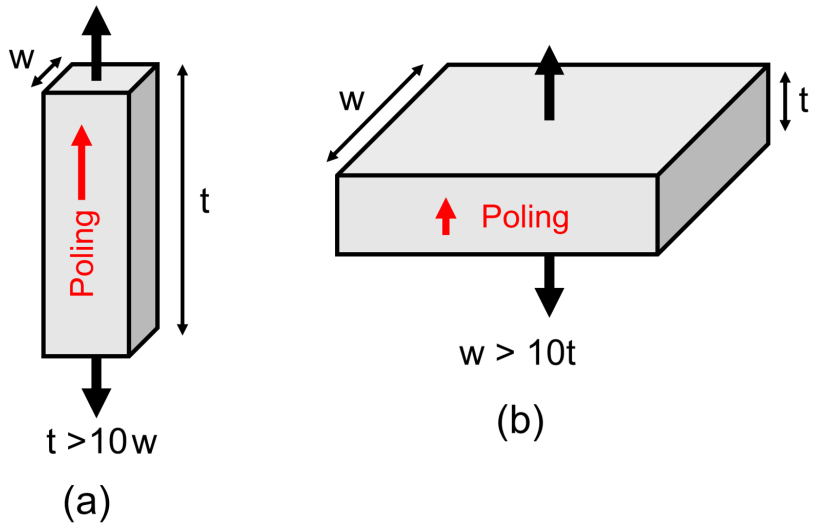

Figure 2.4: A schematic diagram showing the length extensional (a) and thickness extensional (b) geometries.

Table 2.3: Common piezoelectric modes. The table shows their geometric constraints and typical resonant behaviour along with the appropriate electromechanical coupling factor. Geometric constraints from [97].

Mode Name	**Geometry** Constraints*	Diagram	**Electromechanical Coupling Factor**
Length extensional	$t > 10w_1, t >$ 10w2		$k_{33} = \frac{d_{33}}{\sqrt{s_{33}^E \varepsilon_{33}^\sigma}}$
Length-thickness extensional	$w_1 > 10t$, $w_2 > 3t$	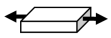	$k_{31} = \frac{d_{11}}{\sqrt{s_1^E \varepsilon_{33}^\sigma}}$
Face shear	$w_1 = w_2 > 10t$		$k_{36} = \frac{d_{36}}{\sqrt{s_{66}^E \varepsilon_{33}^\sigma}}$
Thickness extensional	$w_1, w_2 > 10t$		$k_t = \frac{e_{33}}{\sqrt{c_{33}^D \varepsilon_{33}^\sigma}}$
Length shear	$w_1, w_2 > 10t$	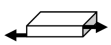	$k_{15} = \frac{e_{15}}{\sqrt{c_{55}^D \varepsilon_{11}^\sigma}}$

* w_1, w_2 = widths of sample, t = thickness of sample

Piezoelectrics are both complex mechanical and electrical systems and so exhibit a large number of resonance and antiresonance pairs. Together these are said to form a piezoelectric mode; the next two sections will briefly explore two important parameters of a mode.

2.4.7 Electromechanical Coupling Factor

The proportion of the instantaneous work converted from electrical to mechanical energy (and *vice-versa*) and stored in a piezoelectric material is given by the electromechanical coupling factor (k^2). Mathematically this is written as

$$k^2 = \frac{\text{converted energy}}{\text{input energy}}. \tag{2.46}$$

Clearly, $0 \leq k^2 \leq 1$ and, practically, it is useful to conceptualise k^2 in the role of a 'piezo-efficiency'. This can be visualised in Figure 2.5, where a work diagram is presented for the LE mode. The square of the electromechanical coupling factor is then given by the ratio of the energy contained inside the cycle, labelled W_1 in Figure 2.5, to the whole area, $W_1 + W_2$ in Figure 2.5. However, the concepts of converted/stored energy and the electromechanical coupling are expanded upon in Chapter 7 and more rigorous distinction will be made there.

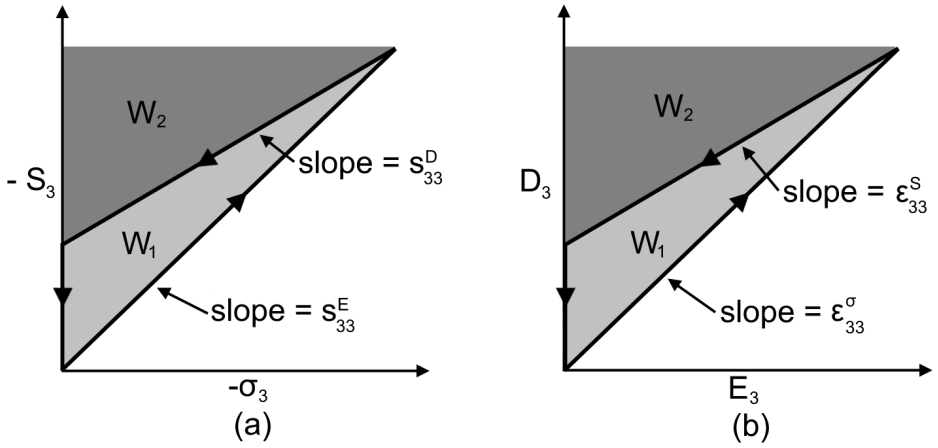

Figure 2.5: Graphic illustration of the electromechanical coupling factor k_{33} for conversion between mechanical to electrical work (a) and electrical to mechanical work (b) after Meitzler *et al.* [73].

The electromechanical coupling factors associated with the common modes are given in Table 2.3 where one penalty for such a simple definition is that a different k must be used for each mode. For example, the TE mode has a lower electromechanical coupling, k_t, than the LE mode, k_{33}, and this can be seen theoretically [98]:

Consider a bar of piezoelectric material with the small faces electroded and subjected to a normal force such that $\sigma_{33} = F$ where F is the normal force per unit area. The equations

of motion can be solved under this assumption and used to calculate energies. By applying the boundary conditions that all normal stresses are zero on the non-electroded surfaces, it is deduced that $S_1 = S_2$, S_3 and D_3 are the only non-zero components of S and $\vec{D}$. If the electrodes are shorted, the potential on each must be the same which implies that $E_3 = 0$. This gives $S_1 = S_2 = s_{13}^E F$, $S_3 = s_{33}^E F$ and $D_3 = d_{33} F$ and hence the work done is

$$W_s = \frac{1}{2} s_{33}^E F^2. \tag{2.47}$$

When the electrodes are open, there is no net charge so $D_3 = 0$, although this is a somewhat idealised assumption. Hence, $S_3 = s_{33}^E \left(1 - \frac{d_{33}^2}{\varepsilon_{33}^\sigma s_{33}^E}\right) F$ so the only term that survives in the energy is the mechanical one

$$W_o = \frac{1}{2} s_{33}^E \left(1 - \frac{d_{33}^2}{\varepsilon_{33}^\sigma s_{33}^E}\right) F^2. \tag{2.48}$$

In an experiment, a mechanical load is applied and a voltage is measured by the connection of an electrical circuit. This corresponds to the shorted case considered above. However, this process can also be split into two steps:

1. The force is applied under open circuit conditions. This steps stores mechanical energy in the material with the amount corresponding to W_o.

2. The circuit is closed under constant force. This step corresponds to the extraction of any electrical energy stored in the material into the circuit. Due to conservation of energy this must be equal to the difference between W_s and W_o.

Hence, for the geometry of this mode, $k^2 \equiv k_{33}^2$ can be calculated as

$$k_{33}^2 = \frac{W_s - W_o}{W_s} = \frac{s_{33}^E F^2 - s_{33}^E \left(1 - \frac{d_{33}^2}{\varepsilon_{33}^\sigma s_{33}^E}\right) F^2}{s_{33}^E F^2} = \frac{d_{33}^2}{\varepsilon_{33}^\sigma s_{33}^E}, \tag{2.49}$$

and a similar analysis of a TE plate can be performed and a coupling constant derived. The steps are the same and are not be repeated here but $k^2 \equiv k_{\mathrm{t}}^2$ can be calculated as [98]

$$k_{\mathrm{t}}^2 = \frac{W_s - W_o}{W_s} = \frac{\frac{F^2}{2c_{33}^E}\left(1 - \frac{1}{1+k_{33}^2}\right)}{\frac{F^2}{2c_{33}^E}} = \frac{k_{33}^2}{1+k_{33}^2} = \frac{e_{33}^2}{c_{33}^D \varepsilon_{33}^S}. \tag{2.50}$$

This shows that k_{t} must always be less than k_{33} implying that the TE mode is less able to convert and store than the LE regardless of their similar motion. Whilst, k^2 is always built out of material properties, and is commonly considered a material property itself, this link to sample geometry (via the mode dependence and definitely not a material property) is unsettling. This issue will also be examined further in Chapter 7.

The effective electromechanical coupling factor of any resonance mode may be determined from the electrical impedance curve in the vicinity of that mode by the following [73]

$$k_{\text{eff}}^2 = \frac{f_a^2 - f_r^2}{f_a^2}, \tag{2.51}$$

where f_r and f_a are the associated resonance and antiresonance frequencies respectively. This relation inherently ties k to the bandwidth of the mode, given by the frequency spacing between f_r and f_a, noting that in this region, the piezoelectric material is deviating from its overall capacitive trend as illustrated in Figure 2.6.

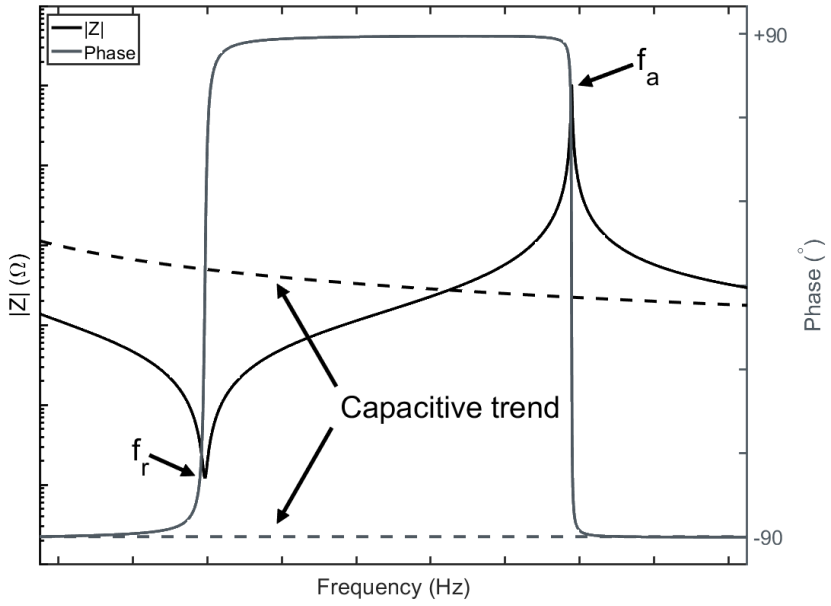

Figure 2.6: Typical piezoelectric mode shape in electrical impedance and phase. The resonance and antiresonance frequencies, f_r and f_a respectively, are indicated as is the overall capacitive trend (dashed lines).

2.4.8 Losses

Understanding of losses in piezoelectric materials is key, especially in high-power applications such as in many SONAR systems. Like the material properties, these losses can be split into three different types: dielectric, mechanical and piezoelectric. Mathematically, this can be expressed by extending the material properties to be complex numbers of the following form [99]

$$\tilde{m} = m(1 - i\tan\psi), \tag{2.52}$$

where m stands for any material property and the tilde denotes its complex nature. Then the

angle ψ (or its tangent) measures how much $\tilde{m}$ deviates from its conventional (real) counterpart m.

The motivation for introducing a complex representation of material properties follows as an extension of the standard ultrasonic attenuation treatment which may be summarised as [100, 101]:

Loss mechanisms may be introduced though the addition of a suitable term to the constitutive equations. For example, when considering ultrasound propagating in human tissue, viscous damping is the dominant loss mechanism [102] and the stress correction is of the form

$$\eta_{ijkl}\frac{dS_{kl}}{dt} = -i\omega\eta_{ijkl}S_{kl}, \tag{2.53}$$

where η_{ijkl} is the material's viscosity tensor and the equality holds for periodic displacements. Then, upon solving the relevant equation of motion (wave equation), it can be shown that the introduction of the losses via the complex mechanical properties leads to an exponentially damped plane wave [100]. Furthermore, in this case, the lossy attenuative behaviour may equally be accounted for by simply allowing the material property c_{ijkl} to become complex with imaginary part $-i\omega\eta_{ijkl}$. This principle works well in general and may be applied beyond this case - the lossy behaviour of the solution is purely a consequence of introducing complex material properties which, in turn, represent some underlying loss mechanism. However, by applying this principle to a generic material, the losses are only treated on a phenomenological level and, unless care is taken, the connection to the loss mechanism is lost [103, 104].

In piezoelectric materials, implementation of this principle leads to the definition of the three loss tangents

$$\tilde{s} = s(1 - i\tan\gamma), \tag{2.54}$$

$$\tilde{\varepsilon} = \varepsilon(1 - i\tan\delta), \tag{2.55}$$

$$\tilde{d} = d(1 - i\tan\theta), \tag{2.56}$$

following the notation of Liu *et al.* where $\tan\gamma$, $\tan\delta$ and $\tan\theta$ represent the elastic, dielectric and piezoelectric losses, respectively [99]. This approach was first reported by Holland after other studies had concluded that conventional elastic and dielectric loss models were insufficient [105]. The description in Equations 2.54 - 2.56 is illustrative only - in a real case, the complex nature must, of course, be extended to *all* components of the EPD matrix. These loss tangents may be physically interpreted as the phase lag between the two variables they connect [106].

For most functional device-based applications, a phenomenological approach (such as this complex model or by direct inclusion of damping terms into the equation of motion) is sufficient to account for losses and allows for excellent agreement between simulations and real devices. However, the mechanisms behind the losses are harder to study due to the complicated way they

interact [107]. Some important mechanisms for ferroelectric losses include lattice deformation (either through polarisation rotation or extension), domain wall motion, grain boundary effects (not in single crystals), interphase boundaries and crystal defects [99]. The presence of losses may also be linked to the hysteretic behaviour of piezoelectrics [108].

The topic of losses in ferroelectric materials is a well-studied one and the reader is referred to the reviews by Liu *et al.* [99] and Uchino *et al.* [104, 108]. A general overview of loss mechanisms is also given in Mason [106].

Quality Factor

Whilst the complex property representation for piezoelectric losses is theoretically convenient, the loss tangents are typically hard to measure accurately in practice - especially the piezoelectric $\tan\theta$ [107, 109]. A more practical method uses quality factors which are defined as being proportional to the ratio of the stored energy over the energy loss within one complete vibration cycle [106]. The quality factors are inversely proportional to the loss tangents - for example, the mechanical quality factor Q_{m} is inversely proportional to $\tan\gamma$ [106]. This establishes quality factors as an alternative way to account for losses in the treatment of piezoelectric materials.

The advantage of quality factors over loss tangents is that the *effective* quality factor is very easy to determine and can, in a similar way to k, be linked to the electrical impedance spectrum at a resonance mode. For any resonance or antiresonance, the effective quality factor is given by the so-called '3 dB rule':

$$Q_{\mathrm{eff}} = \frac{f_0}{f_1 - f_2}, \tag{2.57}$$

where f_0 is either the resonance or antiresonance frequency and f_1 and f_2 are the frequency points corresponding to an impedance value which is 3 dB or $\sqrt{2}$ higher, or lower respectively, than the impedance measured at f_0 [99] This is illustrated in Figure 2.7. This definition of Q_{eff} links it to the sharpness of the resonance or antiresonance feature and makes it very easy to measure. However, it inherently ties Q_{eff} to a specific mode and so cannot be used, in general, to determine losses over all frequencies.

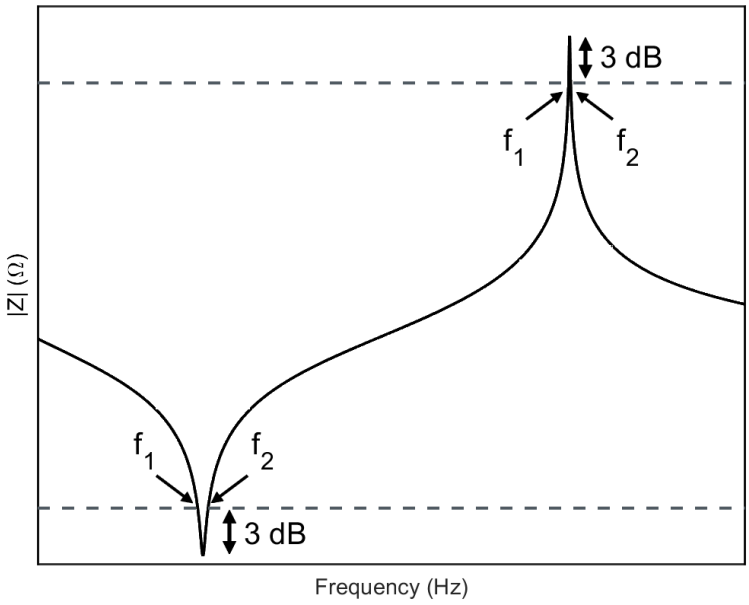

Figure 2.7: The 3 dB method for determining the effective mechanical quality factor. Electrical impedance of a piezoelectric mode is shown along with the 3 dB line for both the resonance and antiresonance.

2.5 Physics of Magnetic Materials

Unlike ferroelectrics, materials with spontaneous and magnetic properties have been known about since the ancient times. However, it was not until 1819 that Ørsted discovered the link between electricity and magnetism [110]. It was this connection that provided the ground work for one of the first great unifications in physics as set out in Maxwell's equations [111]. Furthermore, it is now know that, whilst the magnetic field produced by Ørsted's electrical current is a product of special relativity, the origin of permanent magnetic materials also requires quantum mechanics for a satisfactory explanation. This section provides a brief review of some of the physical mechanisms at play in magnetic materials.

2.5.1 Magnetic Symmetries

Whereas the electric polarisation in a crystal is a *polar* or proper vector, the magnetic moment is an *axial* or pseudo-vector [112]. This can be understood by considering an atomic moment as resulting from a current loop [113], thus illustrating that magnetic moments should behave differently to electric ones. For example, under the effect of a perpendicular mirror plane, the electric polarisation will flip but the magnetic moments will not. This is illustrated in Figure 2.8.

Furthermore, when the magnetic system is in a disordered state, typically at high temperature, the large number of moments present in a macroscopic crystal ensures that, on average, as

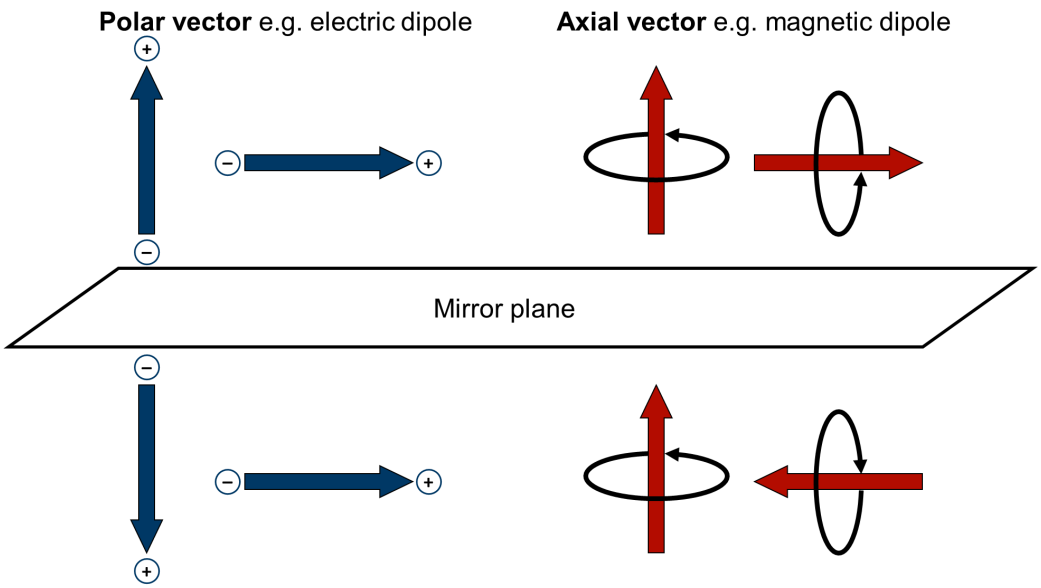

Figure 2.8: Illustration showing the difference between polar vectors, e.g. electric dipoles, and axial vectors, e.g. magnetic dipoles, and their transformation under reflection.

many moments will be pointing up as down. Hence, if all magnetic moments are now flipped then this situation is unchanged. Remembering the current loop model of magnetic moments, flipping the direction of the current will flip the sign of the corresponding moment. With the current being the temporal derivative of the charge, this is 'equivalent' to reversing time. Hence, this symmetry is known as time reversal symmetry (TRS) and is illustrated in Figure 2.9 [112, 114]. So a new symmetry operation can be introduced to represent TRS and will be denoted as E'. If, upon cooling, the crystal magnetically orders, then all moments will not be at random directions and so the system is no longer invariant under TRS. It is also important to note that TRS does not affect the crystal structure itself or any dielectric or piezoelectric properties.

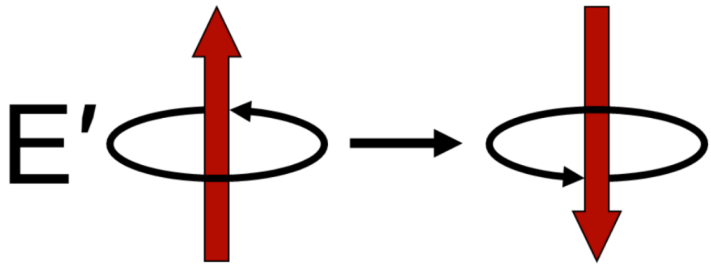

Figure 2.9: Illustration of the effect of TRS, E', on an axial magnetic dipole vector.

The symmetry of magnetic systems can differ from the symmetry of the crystal lattice in which they are embedded. As such, the theory of point groups must be extended to encompass these extra classes. Whilst there are only 32 crystal point groups, there are 122 magnetic point groups. These are formed by various combinations of the crystal point groups with the spin

reversal group $R = \{E, E'\}$ although not all are physically admissible. Magnetic space groups are formed similarly by combining these magnetic point groups with the translational symmetry operations of the lattice. There are 1651 magnetic space groups [115].

2.5.2 Magnetic Ordering

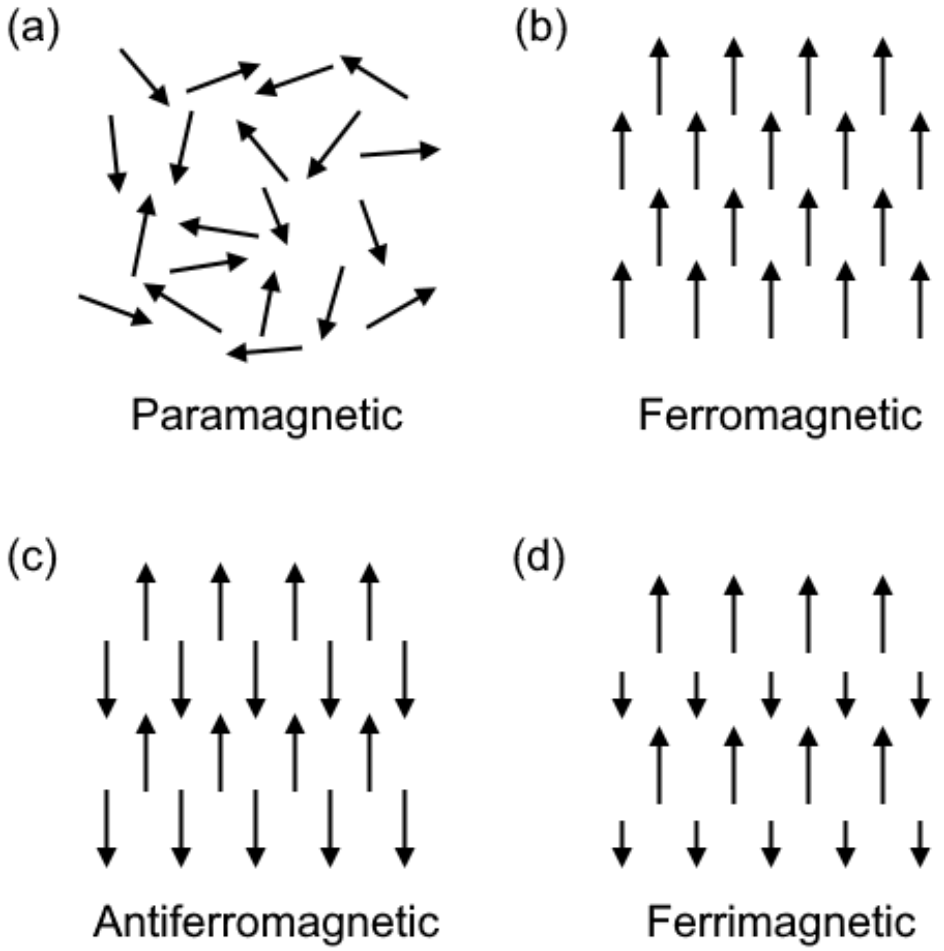

Figure 2.10: Common magnetic ordered structures and the corresponding magnetic dipole configurations.

The most familiar type of magnetic order is ferromagnetism. This is a material in which at least some of the atoms possess a magnetic dipole moment. Typically, at high temperatures, these moments are arranged randomly, called the paramagnetic state, but, upon cooling, will order at some transition temperature, also called the Curie temperature, to produce a spontaneous magnetisation in the sample. These states are shown in Figure 2.10(a) and (b). This magnetisation is caused by the mutual alignment of all moments as originally proposed by Weiss to occur from interaction with an internal 'molecular field' [116]. This field is now known to result from the quantum exchange interaction with the magnetic moments arising from unpaired electrons. One of the simplest variations of this theory is the so-called nearest neighbour inter-

action model [117]. In this case, a magnetic moment is assumed to interact only with the closest neighbouring spins, the number depending on the lattice type. This allows the interaction field at the ith magnetic site to be written as

$$\vec{H}_i = \sum_{\substack{j=\text{nearest} \\ \text{neighbours}}} J_{ij}\vec{m}_j, \tag{2.58}$$

where J_{ij} represents the exchange interaction and is positive for ferromagnetic materials. From elementary magnetic theory, the interaction energy of magnetic moment $\vec{m}_i$ in this field is simply given by

$$U_m \propto \vec{m}_i \cdot \vec{H}_i = \sum_{\substack{j=\text{nearest} \\ \text{neighbours}}} J_{ij}\vec{m}_i \cdot \vec{m}_j, \tag{2.59}$$

and the ordered state occurs when this energy scale matches the thermal energy k_BT where k_B is Boltzmann's constant. As $J_{ij} > 0$, the lowest ordered energy state will occur when neighbouring spins are aligned, giving a positive dot product.

However, the exchange interaction can also be negative, $J_{ij} < 0$. In this case, the lowest energy ordered state corresponds to antiparallel neighbouring spins. This is called antiferromagnetic order and it is illustrated in Figure 2.10(c). In ferromagnetic systems which are typically metallic, the exchange interaction stems from coupling between the outer electrons in the material's band structure. However, antiferromagnets are typically insulators and so the interaction instead is between localised electrons. One mechanism for this is superexchange, where two magnetic cations, e.g. Mn^{2+}, will indirectly couple through the intervening anions such as O^{2-} [118].

Contrary to ferromagnetism, the alternating order in an antiferromagnet results in an overall zero magnetisation. It also means that the material unit cell is effectively doubled. This can be directly seen by the presence of a Bragg peak at wavevector (1/2,1/2,1/2) in magnetic neutron diffraction experiments. The temperature at which antiferromagnetic order sets in is referred to as the Néel temperature. Antiferromagnetism is common in transition metal oxides such as MnO, FeO, CoO and NiO.

Beyond these two simple cases of order exists a myriad of magnetic structures. These include such cases as ferrimagnetism (shown in Figure 2.10(d)), which may be considered a weak case of antiferromagnetism, and spin-spiral ordering which will be revisited in the context of multiferroics.

2.5.3 Propagation Vectors

As is usual in crystallography, consideration of the reciprocal space can further understanding of the magnetic order. Consider a material which is magnetically ordered. Then the configuration of magnetic moments, $\vec{m}_{lj}$ where l labels the unit cell and j the atom number in that cell, can be express as a Fourier series

$$\vec{m}_{lj} = \sum_{\vec{k}} \vec{S}_{\vec{k}j} e^{-i\vec{k}\cdot\vec{L}}, \tag{2.60}$$

where $\vec{k}$ are the 'propagation' vectors, $\vec{S}_{\vec{k}j}$ are the complex Fourier coefficients and $\vec{L}$ is a real-space lattice vector, here pointing to the l^{th} unit cell. Like the reciprocal lattice, the power of this Fourier representation is that it allows an explicit expression of the periodicity of the magnetic order through the values of the propagation vector, $\vec{k}$. It should also be noted that conventionally the propagation vectors are restricted to the first Brillouin zone, the unit cell of the reciprocal lattice, and so the exponential factor above can be seen as a development of Bloch's theorem [119].

A disordered structure will lack any real-space long-range coordination and so must be likewise broad in reciprocal space. This means that disordered magnetic structures, such as a paramagnetic ones, require a near continuous distribution of $\vec{k}$ vectors. Conversely, well-ordered structures require only a single propagation vector as they exhibit long-range order in real-space. Within ordered structures there are three categories of propagation vector:

- 'Null' ($\vec{k} = 0$): From the Fourier expansion, it can be seen that this corresponds to the case where the magnetic structure is identical in all unit cells (independent of l) and so the magnetic translation symmetry is identical to that of the crystal. For Bravais lattices, this case corresponds to a ferromagnetic structure.

- Fraction of reciprocal lattice vector ($\vec{k} = a\vec{H}$): From the definition of $\vec{H}$, the product $\vec{H}\cdot\vec{L}$ is equal to an integer (n_l) multiple of 2π and so this corresponds to the case where the magnetic system has lower symmetry than the crystal. For example, consider the case where $a = \frac{1}{2}$:

  $$\vec{m}_{lj} = \vec{S}_{\frac{1}{2}\vec{H}j} e^{-i\frac{1}{2}\vec{H}\cdot\vec{L}} = \vec{S}_{\frac{1}{2}\vec{H}j} e^{-i\pi n_l} = \vec{S}_{\frac{1}{2}\vec{H}j}(-1)^{n_l} = \vec{m}_{0j}(-1)^{n_l}, \tag{2.61}$$

  and so, in a given unit cell, $\vec{m}_{lj}$ is either identical or opposite to that of the zero cell. This corresponds to an antiferromagnetic structure.

- $\vec{k}$ is arbitrary: In this case the magnetic structure is said to be incommensurate meaning that, after the zero cell, the magnetic translation symmetry will never again coincide with the crystal lattice and so the structure cannot be described by a magnetic space group.

2.6 Relaxor-Ferroelectrics

Now that the basics of dielectric and magnetic order have been set out, two pertinent examples of materials will be reviewed in which two or more orders/disorders are present. This coexistence allows for materials which display novel and exciting properties. The first are relaxor-ferroelectrics which have attracted great attention in recent years, with exceptional piezoelectric and dielectric responses reported [49, 120–124]. They typically consist of mixed perovskites with structure $A(B_xB'_{1-x})O_3$ such as $Pb(Mg_{1/3}Nb_{2/3})O_3$ (PMN) and $Pb(Zn_{1/3}Nb_{2/3})O_3$ (PZN) [50] and exhibit a random mixture of cations on the B-site. This disorder has been indicated as, at least partially, a reason for their high performance [50, 122, 125].

Cross defines *relaxor-ferroelectrics* by three distinguishing features which separate these from 'normal' ferroelectrics [126]:

1. The temperature of the maximum in dielectric permittivity, T_m, increases with frequency.
2. The dielectric hysteresis response slowly reduces as temperature increases.
3. Samples cooled to low temperatures show no evidence of optical anisotropy/X-ray line splitting to longer coherence length probing radiation.

Cross presents evidence that all these conditions are met in PMN, the prototypical relaxor-ferroelectric. However, practically, the distinction is most clearly seen from the first of these features as relaxor-ferroelectrics characteristically display a temperature broadened ferroelectric-paraelectric transition. This is illustrated in Figures 2.11 and 2.12. These figures compare this transition of BT against the relaxor-ferroelectrics PMN [127] and PZN [128] respectively. Figure 2.11 clearly shows a defined sharp peak in the dielectric permittivity of BT above which the Curie-Weiss law

$$\varepsilon \sim \frac{1}{T - T_C}, \tag{2.62}$$

is obeyed. This behaviour is predicted by conventional soft mode theory [129] and the Devonshire theory [71].

In contrast, PMN and PZN, Figure 2.12, show broadened phase transitions with frequency dependent peaks. This cannot be accounted for within the framework of the Devonshire theory, indicating that the peaks do not correspond to a 'traditional' phase transition as in BT and other normal ferroelectrics [128]. Furthermore, the shapes of the peaks also indicate that relaxor-ferroelectrics do not follow the Curie-Weiss law close to T_m [130, 131].

2.6.1 The Smolenskii Model and Superparaelectricity

One of the first models to describe the behaviour of relaxor-ferroelectrics was proposed by Smolenskii *et al.* [45]. It suggested that the B-site disorder was responsible for the broaden-

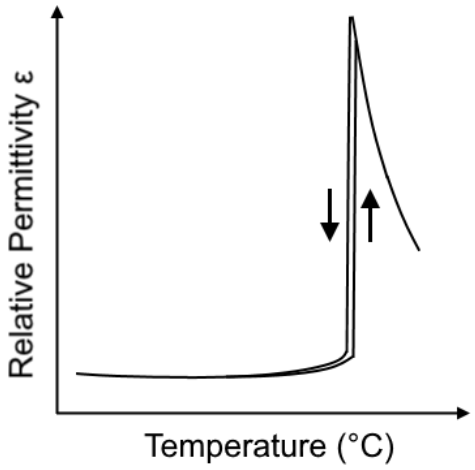

Figure 2.11: Schematic diagram showing the dielectric permittivity, ε, at the paraelectric-ferroelectric phase transition of a 'normal' ferroelectric such as BT. The response shows a sharp peak with Curie-Weiss dependence above.

ing of the phase transition. Due to random fluctuations, some regions will be richer in one B-site ion than the other. This would cause a non-uniform Curie temperature with an *"intimate mix of ferroelectric (polar) and para-electric (non polar) regions"* [126] over a large range of temperatures, as illustrated in Figure 2.13.

Moreover, it can be expected that this effect should result in broadening of the peak and the deviations from the Curie-Weiss law seen in Figure 2.12. The disorder-induced regions will display a distribution of Curie temperatures due to their differing composition [131]. If a Gaussian distribution is taken, then by considering the electrical polarisation in a statistical fashion, the modified Curie law

$$\varepsilon \sim \frac{1}{(T - T_0)^2}, \tag{2.63}$$

is found near the mean transition temperature (T_0). This gives excellent agreement with measured results, shown in Figure 2.14, in many relaxor-ferroelectric compounds [133].

In 1987, Cross proposed an extension to this model termed *superparaelectricity* [126]. Named in analogy with superparamagnetism [134] where small clusters of aligned magnetic moments, unstable due to thermal fluctuations, may be thought of as nano-particles embedded in the paramagnetic base phase.

Cross's argument is summarised thus: The free energy profile, calculated through a Devonshire approach, for a given Smolenskii nano-region, must be of a multiple well structure. The potential barrier between these wells represents the cost of domain reorientation and must scale with the volume of the nano-region because ferroelectricity is a co-operative phenomenon. Hence, for small regions, it can be expected that this barrier is $\sim k_B T$ and, therefore, subject

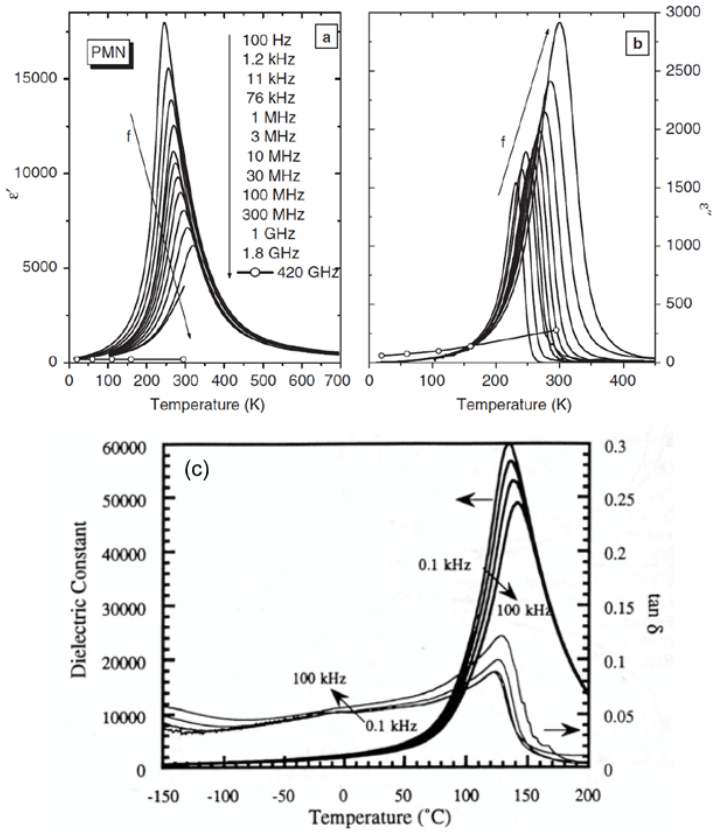

Figure 2.12: The dielectric permittivity and losses ($\tan\delta$) at the paraelectric-ferroelectric phase transition in the relaxor-ferroelectric PMN, (a) and (b) respectively, and (c) PZN. Both show a broadened phase transition with a frequency dependent peak and no Curie-Weiss law in contrast to BT. (a) and (b) reproduced with permission from V. Bovtun *et al.*, "Central-peak components and polar soft mode in relaxor $Pb(Mg_{1/3}Nb_{2/3})O_3$ crystals," *Ferroelectrics*, vol. 298, no. 1, pp. 23–30, 2004; (c) Reproduced with permission from M. L. Mulvihill *et al.*, "Domain-related phase transitionlike behavior in lead zinc niobate relaxor ferroelectric single crystals," *J. Am. Ceram. Soc.*, vol. 80, no. 6, pp. 1462–1468, 1997. Copyright (1997) John Wiley and Sons.

to thermal fluctuations. This process bears a striking resemblance to superparamagnetism, the mechanisms of which are well-understood.

Cross proposed three tests that would support the Smolenskii model and his own theory of superparaelectricity [126]:

1. Are fluctuations in the B-site ion responsible for the diffuse nature of the maximum in dielectric permittivity?

2. Is there direct evidence for a substantial value of root mean square (RMS) polarisation above T_C?

3. Are the polar micro-regions 'flipping' like in a superparamagnet or are they fixed?

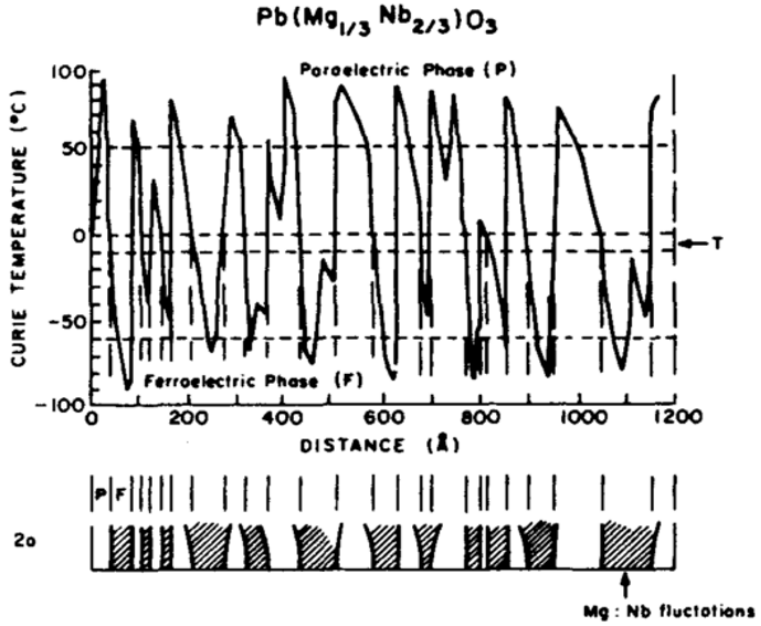

Figure 2.13: Illustration of how a fluctuating Curie temperature (paraelectric-ferroelectric transition) can create polar and non-polar micro-regions in PMN due to B-site (Mg:Nb) disorder. Reproduced with permission from L. E. Cross, "Relaxor ferroelectrics," *Ferroelectrics*, vol. 76, pp. 241–267, 1 1987

Cross presented evidence in favour of these points: Firstly, disorder in the B-site ion would necessarily produce regions rich in either ion and would, therefore, destroy any translational symmetry. However, if a system could be constructed with alternating B-site ions, a translationally invariant super-lattice would be constructed. This alternating state must surely recover 'normal' ferroelectric behaviour due to the recovering of this symmetry. This is supported by studies into $Pb(Sc_{1/2}Ta_{1/2})O_3$ [135, 136] where an annealed sample was compared to a quenched one. The results are summarised in Figure 2.15.

Secondly, the RMS polarisation may be obtained from electrostriction as the strain shows deviation from the expected linear thermal behaviour in the region above the effective T_C [126]. This deviation is indicative of random fluctuations in $\vec{P}$ which must average to zero but will give $\sqrt{\vec{P}^2} \neq 0$. The presence of an RMS polarisation was previously reported in BT by Burns and Dacol who studied the refractive index [137]. This was followed by reporting of similar deviation in PMN and PZN by the same authors [138]. The temperature at which this RMS polarisation emerges upon cooling is referred to as the Burns temperature, T_B, and it marks the upper temperature limit of the deviation from Curie-Weiss behaviour in relaxor-ferroelectrics.

Thirdly, assuming these regions are dynamic, electrostrictive strain can be introduced either by a switching of the already polar micro-regions to an equivalent state or by changing the intrinsic polarisation. As electrostriction is quadratic in polarisation, switching of the micro-regions must give *no* contribution to electrostriction. However, changing the polarisation changes the volume and therefore *must* contribute to electrostriction. Hence, if domain switch-

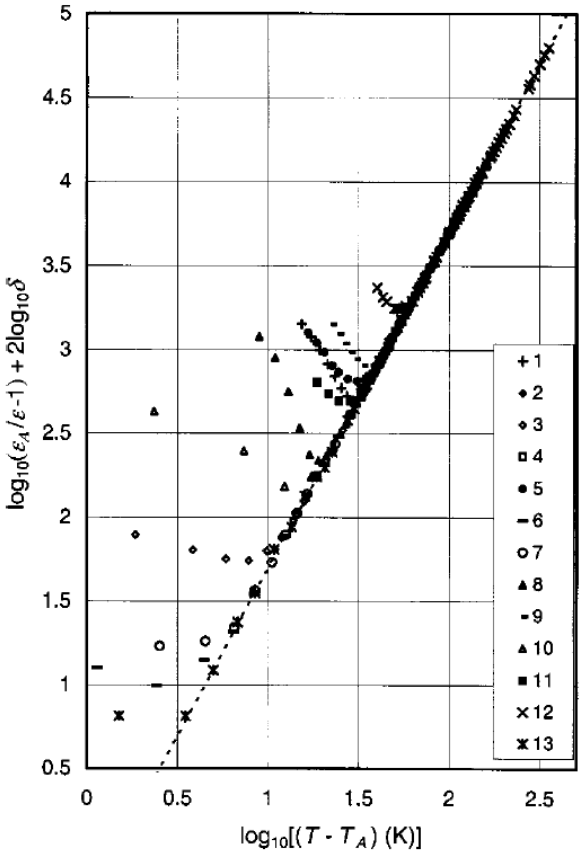

Figure 2.14: Scaling plot for the dielectric permittivity for 13 different relaxor-ferroelectrics. A universal quadratic trend is clearly shown. Reprinted figure with permission from A. A. Bokov *et al.*, "Empirical scaling of the dielectric permittivity peak in relaxor ferroelectrics," *Phys. Rev. B*, vol. 68, p. 052 102, 5 2003. Copyright (2003) by the American Physical Society. The reader is referred to Ref. [133] to find the composition of relaxor-ferroelectrics 1-13.

ing becomes dominant, the induced strain should show anomalously low values [126]. Cross studied $(Ba_{0.4}Sr_{0.6})Nb_2O_6$ with the results shown in Figure 2.16. These support the first strain mechanism and, therefore, that the micro-regions are dynamical.

Furthermore, Viehland *et al.* [139] proposed a model in which correlations between these polar regions result in a frustration of their dynamical nature until they are frozen into a glassy state analogous to a spin glass. This happens at a 'freezing' temperature, T_f, and, as a result, the flipping time given by the Arrhenius equation in superparamagnetism is actually shown to be well-described by an exponential Vogel-Fulcher law [140, 141].

In conclusion, the Smolenskii model of disordered B-site ions accounts for the diffuse transition on a phenomenological level and is capable of predicting the behaviour into the paraeletric phase. The evidence presented by Cross in 1987 [126], further supports this model and also supports the theory that relaxor-ferroelectrics exhibit the electrical analogue to superparamagnetism - superparaelectricity.

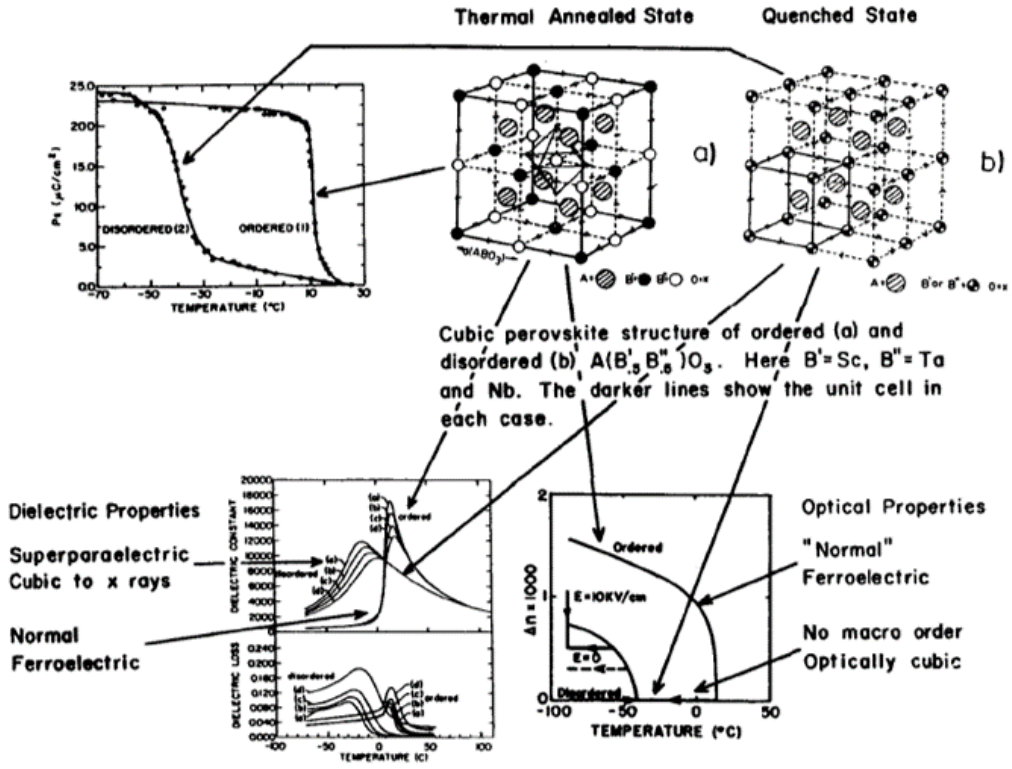

Figure 2.15: Differences between ordered (annealed) and disordered (quenched) $Pb(Sc_{1/2}Ta_{1/2})O_3$. This shows that all the classic relaxor behaviours displayed by the quenched sample disappear upon annealing, supporting Smolenskii's conclusion that relaxor behaviour comes from compositional disorder. Reproduced with permission from L. E. Cross, "Relaxor ferroelectrics," *Ferroelectrics*, vol. 76, pp. 241–267, 1 1987

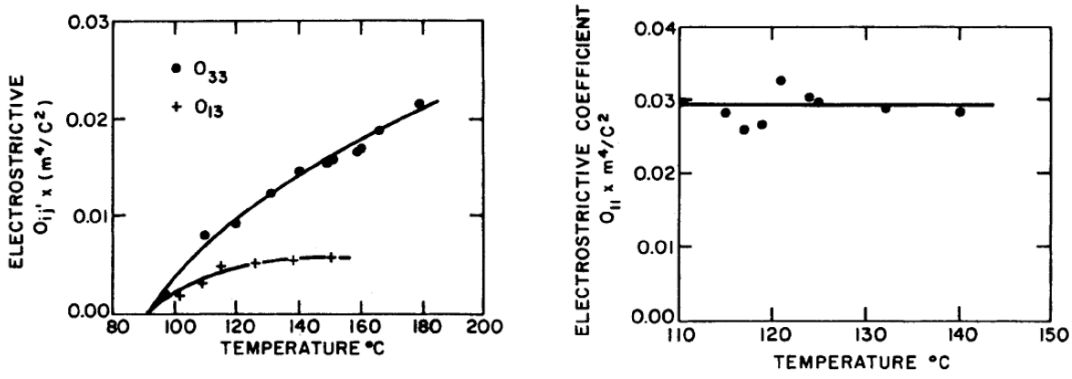

Figure 2.16: Values of electrostriction constants Q_{33}, Q_{31} and Q_{11} in $(Ba_{0.4}Sr_{0.6})Nb_2O_6$ (ferroelectric symmetry 4*mm*). The polar vectors are dominantly orientated along the four-fold axis (direction 3). Hence, switching of micro-regions should be induced by applying a field in direction 3 but not in direction 1. This shows the values of electrostriction constants Q_{33} and Q_{31} going to zero at the Curie temperature whereas Q_{11} remains normal supporting dynamic behaviour of micro-regions. Reproduced with permission from L. E. Cross, "Relaxor ferroelectrics," *Ferroelectrics*, vol. 76, pp. 241–267, 1 1987

2.6.2 Paraelectric-Ferroelectric Transition Temperatures in Relaxors

From the sections above, it is clear that the transition from a paraelectric state to a ferroelectric one is much more complicated in a relaxor-ferroelectric than in, say, BT. It is more accurate to say that there is a temperature range between T_B, i.e. the temperature at which polar micro-regions start to appear and emergence of RMS polarisation upon cooling, at the upper end and the depoling temperature, T_d, i.e. the temperature at which net polarisation emerges upon cooling, at the lower end. This contains many temperatures which are summarised by Davis [128] and describes how the system changes from a paraelectric state to one with long-range ferroelectric order. Most notably, the temperature of maximum permittivity is strongly frequency dependent but does not correspond to an abrupt structural phase transition. This contrasts with a 'normal' ferroelectric which transforms with a well-defined phase transition at one temperature, T_C.

2.6.3 Polar Nano-regions

The nano-regions of Smolenskii and Cross have also been implicated in the high dielectric and piezoelectric properties of relaxor-ferroelectrics [122, 125]. The main evidence for their existence can be seen in refractive index measurements [137] and in the presence of a diffuse scattering component in both neutron and X-ray experiments [142–145]. In a long-range ordered structure, Bragg scattering peaks occur as typically sharp effects, usually with some broadening due to experimental resolution. However, these diffuse regions in relaxor-ferroelectrics appear as a 'smearing' of the Bragg peaks and broadening in reciprocal-space implies short-range real-space correlations.

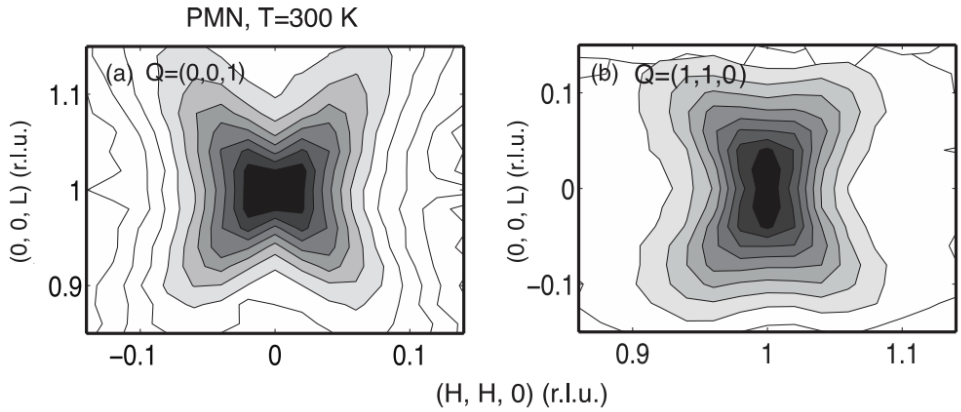

Figure 2.17: Diffuse component of the elastic neutron scattering response seen in PMN. Reprinted figure with permission from C. Stock *et al.*, "Evidence for anisotropic polar nanoregions in relaxor $Pb(Mg_{1/3}Nb_{2/3})O_3$: A neutron study of the elastic constants and anomalous TA phonon damping in PMN," *Phys. Rev. B*, vol. 86, no. 10, pp. 1–18, 2012. Copyright (2012) by the American Physical Society.

The diffuse scattering of PMN is shown in Figure 2.17, where the classic so-called 'butterfly' shape can be easily seen [146]. The butterfly shape shows that the diffuse regions are highly anisotropic, with rods extending along the $\langle 110 \rangle$ directions. This reciprocal space anisotropy is reflective of the existence of both long and short-range correlations in real-space. Furthermore, damping of acoustic phonons shows that these short-range PNRs are also highly anisotropic in real-space [146].

2.6.4 Random Fields

Further building on the Smolenskii disorder, another model proposed for understanding relaxor-ferroelectric behaviour is the random field model. First introduced by Imry and Ma [147], this model introduces a random 'external' field which, in the case of relaxor-ferroelectrics, comes from charge inhomogeneity due to B-site mixing, ionic shifts from the ideal positions and even Pb and O vacancies [148]. These effects lead to imperfections which can be treated as sources of a random electric field embedded in a paraelectric phase [50].

The classic example of a random field approach is the Ising model used to study systems which exhibit co-operative behaviour such as ferromagnetism; the context in which it was originally proposed [149]. This model uses Equation 2.59 but implements a spatially homogeneous nearest-neighbour coupling, i.e. $J_{ij} = J$ is a scalar. Random field effects may be introduced by extending this coupling and modifying the 'external' field to include random contributions with zero mean that are uncorrelated for different sites [150]. This may be motivated by factors such as compositional defects, lattice dislocations and vacancies which can break down the spatial homogeneity of the pure Ising model.

In relaxor-ferroelectrics, the disorder can be modelled as sources of a random field and this model can be used to account for many experimental results. For example, many relaxor-ferroelectrics such as PMN and PZN display a skin effect [151–153] which is a phenomenon familiar from magnetic systems [154, 155]. This effect will be further explored in Chapter 5 in the relaxor-ferroelectric $Pb(Fe_{1/2}Nb_{1/2})O_3$ (PFN).

The random field model applied to relaxor-ferroelectrics is reviewed by Glinchuck [148] and Cowley [50]. The main approach is to consider a self-consistent random field distribution function which is then used to derive average values; many references within Ref. [148] contain methods to try to calculate this function.

Whilst the random field model is able to account for most of the phenomenology of relaxor-ferroelectrics, there remains some question regarding the mixing of relaxors and the inclusions of other ordering mechanisms. These will be addressed in this thesis.

2.7 Multiferroics

The second class of materials which this thesis will explore is known as multiferroics. A multiferroic displays a coupling between two 'ferroic' orders in the same phase, with this usually limited to intertwined magnetic and electrical order i.e. magnetoelectric coupling [62, 156, 157]. As with piezoelectricity, the origin of the magnetoelectric effect may be traced back to Pierre Curie, who posited its existence in 1894 [9], but it was not until the late 1950s/1960s that this prediction was followed by substantial theoretical work [158] which led to the first experimental observation [159].

The coexistence of both electric and magnetic order is not a harmonious one, with magnetic systems requiring partially-filled atomic orbitals and ferroelectric systems favouring filled orbitals [160]. An example of this is the perovskite oxides, e.g. BT or PT, in which ferroelectricity arises through a relative displacement between the B-site ion and the surrounding O octahedra. However, in these cases, the B-site ion is typically Ti^{4+} which lacks electron occupancy in the d orbital which makes magnetic ordering impossible. This also applies to common B-site ions Zr^{4+} and Nb^{5+}. This was referred to as the 'd^0 rule' by Hill [160] and breaking this 'rule' is crucial to allowing simultaneous magnetic and electric orders to develop.

Furthermore, the temperature scales corresponding to both electrical and magnetic order are often disparate, which together indicate that the microscopic origins behind each mechanism must be likewise separate. This competition means that, typically, magnetoelectric coupling is weak. Despite this drawback, coupling of these order parameters would allow hybrid magnetoelectric devices independently controllable using magnetic and electric fields [161] and so alternative systems are desired.

One such candidate is spiral multiferroics [162]. With the extension of the classical multiferroic definition to include any type of magnetic order, large coupling has been found in systems which contain cycloidal magnetic structures such as the rare-earth manganites, e.g. the perovskite $TbMnO_3$ [163–166]. As ferroelectricity is closely linked to helicoidal order since both require noncentrosymmetry [156], chiral magnetic ordering can induce ferroelectricity even if the parent phase forbids it by symmetry, such as in Cr_2BeO_4 [167] or $TbMnO_3$ [161].

The various types of spiral magnetic structures are illustrated in Figure 2.18, with the classic mechanism of induced magnetoelectric effect through a coupling to the spin chirality $\vec{S}_i \times \vec{S}_j$, where i, j are neighbouring spins. This is known as the KNB spin-current model [163] and there exists a strict constraint on the direction of any spontaneous polarization. Where all spins rotate in a common plane, the induced polarization is $\vec{P} \propto \vec{e}_{ij} \times \vec{S}_i \times \vec{S}_j$ where $\vec{e}_{ij}$ is the vector that joins the two neighbouring spins, $\vec{S}_i$, $\vec{S}_j$, and is also in the rotation plane. This results in a polarisation which is constrained to lie in the rotation plane. The KNB model has been verified for many systems such as $MnWO_4$ [168]. However, it cannot fully account for new spiral multiferroics such as $Cu_3Nb_2O_8$, where the electric polarisation is reported to be nearly perpendicular to the rotation plane - a clear violation of the KNB model [169]. This material is studied further in

Chapter 4 and an alternative mechanism is proposed in order to overcome this issue.

Another mechanism which can account for spiral multiferroics is the inverse Dzyaloshinskii-Moriya (D.-M.) effect [170, 171]. The D.-M. interaction is the anitsymmetric magnetic exchange which arises from a second-order perturbation expansion of spin-orbit coupling, a relativistic correction to atomic theory [171, 172]. Considering the case, for simplicity, of two magnetic ions, this interaction produces a perturbative Hamiltonian (quantum mechanical energy operator) of the form [172]

$$\mathcal{H}_{\mathrm{DM}} = \vec{D} \cdot (\vec{S}_1 \times \vec{S}_2), \tag{2.64}$$

where $\vec{D}$ is known as the D.-M. vector and $\vec{S}_1$ and $\vec{S}_2$ are the spins of the two ions. The vector $\vec{D}$ is totally antisymmetric under swapping of the ions and so will vanish when the surrounding symmetry possesses an inversion centre. Furthermore, this interaction plays a large role in the case of magnetic ions with $S = 1/2$, such as Cu^{2+}, as lower order effects will typically vanish [173]. The D.-M. interaction has been linked to non-collinear spin structures such as in high-temperature superconductors [174] and multiferroics such as $BiFeO_3$ [175].

However, this magnetic interaction can induce a shift in the crystal ions due to a competition between magnetic and lattice energies [157]. Whereas in conventional D.-M. interaction reviewed above, a lack of inversion in the structure supports the existence of $\vec{D}$, in the 'inverse' D.-M. interaction, $\vec{D}$ induces an ionic shift which can allow ferroelectricity to manifest. The superexchange interaction between adjacent magnetic ions is typically mediated through O^{2-} ions and the strength of $\vec{D}$ is proportional to the displacement between the magnetic and O ions. As such, the D.-M. vector can cause a shift in the positions of the O ions relative to the magnetic ions, thus inducing an electrical polarisation. This mechanism has been shown to play a large role in multiferroic perovskites [166].

Mixed perovskites have also been reported to show magnetoelectric coupling. For example, $Pb_2(CoW)O_6$ displays both ferromagnetic and ferroelectric order, and $Pb_2(FeTa)O_6$ displays both antiferromagnetic and ferroelectric order [176]. The introduction of ions with partially-filled d orbital has broken the 'd^0 rule' and is what allows the development of magnetism. However, these materials have rather low Curie/Néel temperatures (~ 10 K) which may be attributed to the dilution of the magnetic ions. Despite this, relaxor-ferroelectrics such as $Pb(Fe_{1/2}Nb_{1/2})O_3$ are still of interest and are reported to show strong magnetoelectric coupling [177]. Study of this material will be the focus of Chapter 5: given the context of random electric fields in relaxor-ferroelectrics, investigation of magnetic order might provide some insight into both the coupling and individual ordering mechanisms. Relaxor-ferroelectrics provide unique systems to study the effects of disorder and random fields, due to the inherent anisotropy tied to ferroelectricity [50], and so are an interesting candidate for multiferroic materials.

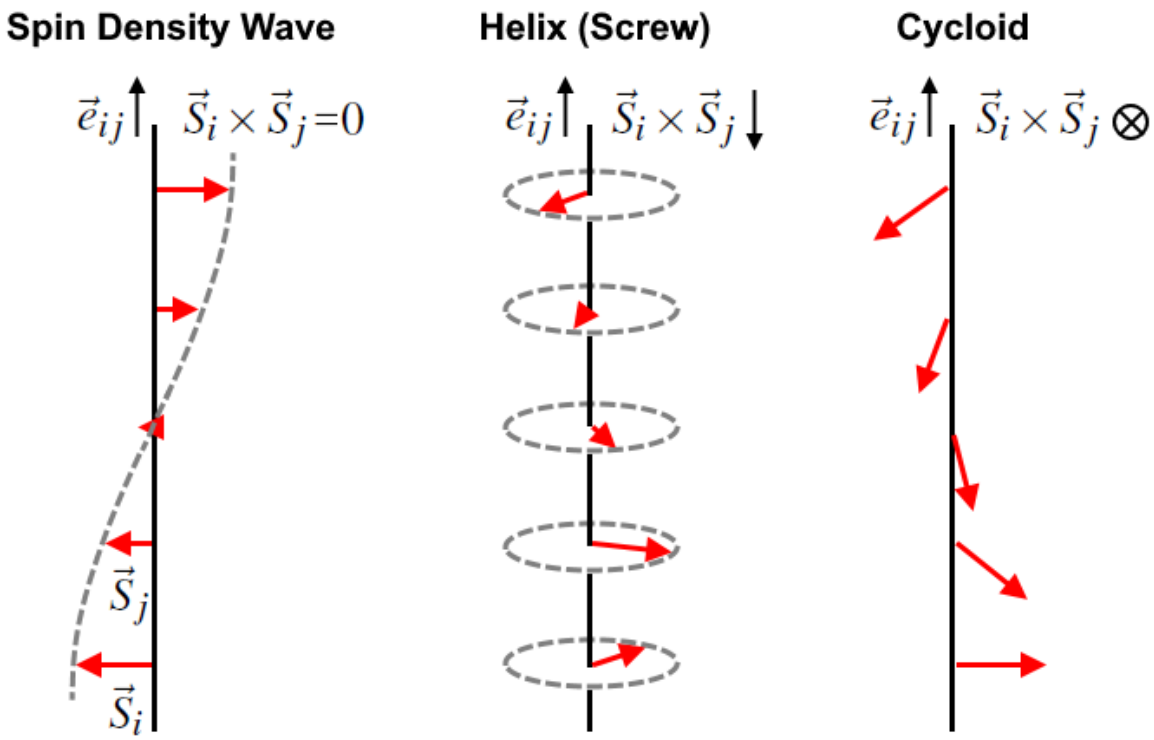

Figure 2.18: Spiral magnetic structures. (left to right) a spin density wave, helix, cycloid. Also shown in the diagrams are the vector $\vec{e}_{ij}$ which joins the two neighbouring spins $\vec{S}_i$, $\vec{S}_j$ and the chirality vector $\vec{S}_i \times \vec{S}_j$.

2.8 Chapter Summary

This chapter has reviewed the base theory behind piezoelectricity, ferroelectricity and magnetism in dielectric oxide materials.

It was shown that the piezoelectric coupling arises from the combination of mechanical and dielectric energy densities and all formulations of the piezoelectric constitutive equations follow through the standard tools of thermodynamics. The importance of crystal symmetry was highlighted and its influence on the structure of the EPD matrix was explicitly computed for 4*mm* material though an invariant argument. An overview of the development of phenomenological (Devonshire) theory was also included as another illustration of the power of the thermodynamic argument. The more practical aspects of piezoelectric materials such as resonant modes, electromechanical coupling and losses were also considered.

An historical overview of the development of piezoelectric materials for ultrasound was undertaken. Following this development, from the Curie brothers in 1880 to the present, highlights the need for new theories to guide the continued evolution of these materials especially in the context of Pb-free piezoelectrics.

The structures of magnetic crystals were then reviewed, with the different types of magnetic ordering classified using the concept of the propagation vector. The extension of point and

space group symmetry to include magnetic structures was also discussed. Two cases where these properties are mixed either with each other or with other orders were then reviewed. The first example is relaxor-ferroelectric materials. They display increased dielectric and piezoelectric properties through the interplay of structural disorder and ferroelectricity. This means that they have further potential to revolutionise the ultrasonic industry with their high electromechanical coupling and piezoelectric coefficients. The second example introduced are multiferroic materials, in which a magnetoelectric coupling exists between electric and magnetic order. The issues that prevent strong coupling in classic multiferroic materials were outlined and two alternative material classes were proposed - study of which will form part of this thesis.

References

[1] V. K. Wadhawan, "Ferroic materials: A primer," *Reson.*, vol. 7, pp. 15–24, 7 2002. DOI: 10.1007/BF02836749.

[2] C. Kittel, *Introduction to Solid State Physics*, 8th. John Wiley & Sons, Inc., 2005, ch. 1, ISBN: 0-471-41526-X.

[3] R. C. Powell, *Symmetry, Group Theory, and the Physical Properties of Crystals*. Springer, 2010, ch. 1, ISBN: 978-1-4419-7598-0.

[4] W. Borchardt-Ott, *Crystallography*, 3rd. Springer-Verlag, 2011, ch. 7, ISBN: 978-3-642-57754-3.

[5] W. Borchardt-Ott, *Crystallography*, 3rd. Springer-Verlag, 2011, ch. 8, ISBN: 978-3-642-57754-3.

[6] W. Borchardt-Ott, *Crystallography*, 3rd. Springer-Verlag, 2011, ch. 6, ISBN: 978-3-642-57754-3.

[7] C. J. Bradley and A. P. Cracknell, *The Mathematical Theory of Symmetry in Solids*. Clarendon Press, 1972, ch. 3, ISBN: 978-0-19-958258-7.

[8] R. R. Birss, *Symmetry and Magnetism*, 2nd. North Holland Publishing Company, 1966, ch. 2, ISBN: 978-0-7204-1453-0.

[9] P. Curie, "Sur la symétrie dans les phénoménes physiques, symétrie d'un champ électrique et d'un champ magnétique," *J. Theor. Appl. Phys.*, vol. 3, no. 1, pp. 393–415, 1894.

[10] J. Curie and P. Curie, "Development, via compression, of electric polarization in hemihedral crystals with inclined faces," *Bulletin de la Societe de Minerologique de France*, vol. 3, pp. 90–93, 1880.

[11] G. Lippman, "Principal of the conservation of electricity," *Ann. Chim. Phys.*, vol. 24, pp. 145–178, 1881.

[12] J. Curie and P. Curie, "Contractions and expansions produced by voltages in hemihedral crystals with inclined faces," *Comptes Rendus*, vol. 93, pp. 1137–1140, 1881.

[13] S. Cochran, "Piezoelectricity and basic configurations for piezoelectric ultrasonic transducers," in *Ultrasonic Transducers*, Woodhead Publishing, 2012, ch. 1, ISBN: 978-1-84569-989-5.

[14] V. Sundar and R. E. Newnham, "Electrostriction and polarization," *Ferroelectrics*, vol. 135, no. 1, pp. 431–446, 1992. DOI: 10.1080/00150199208230043.

[15] J. F. Nye, *Physical Properties of Crystals*, 2rd. Clarendon Press, 1985, ch. 7, ISBN: 0-19-851165-5.

[16] W. Borchardt-Ott, *Crystallography*, 3rd. Springer-Verlag, 2011, ch. 9, ISBN: 978-3-642-57754-3.

[17] C. J. Bradley and A. P. Cracknell, *The Mathematical Theory of Symmetry in Solids*. Clarendon Press, 1972, ch. 2, ISBN: 978-0-19-958258-7.

[18] S. Katzir, *The Beginnings of Piezoelectricity*. Springer, 2006, ISBN: 978-1-4020-4670-4.

[19] J. Curie and P. Curie, "Phénomènes électriques des cristaux hémièdres à faces inclinées," *J. Theor. Appl. Phys.*, vol. 1, no. 1, pp. 245–251, 1882.

[20] S. Katzir, *The Beginnings of Piezoelectricity*. Springer, 2006, ch. 1, ISBN: 978-1-4020-4670-4.

[21] W. Voigt, "Allgemeine theorie der piëzo- und pyroelectrischen erscheinungen an krystallen," *Göttingen Abhandlungen*, vol. 36, pp. 1–99, 1890.

[22] K. Uchino, "The development of piezoelectric materials and the new perspective," in *Advanced Piezoelectric Materials*, K. Uchino, Ed., Woodhead Publishing, 2017, ch. 1, pp. 1–92, ISBN: 978-0-08-102135-4. DOI: 10.1016/B978-0-08-102135-4.00001-1.

[23] D. Zimmerman, "'a more creditable way': The discovery of active sonar, the langevin-chilowsky patent dispute and the royal commission on awards to inventors," *War in History*, vol. 25, no. 1, pp. 48–68, 2018. DOI: 10.1177/0968344516651308.

[24] R. W. Moore, "A method of growing large perfect crystals from solution," *Journal of the American Chemical Society*, vol. 41, no. 7, pp. 1060–1066, 1919. DOI: 10.1021/ja02228a003.

[25] G. Busch, "Early history of ferroelectricity," *Ferroelectrics*, vol. 74, no. 1, pp. 267–284, 1987. DOI: 10.1080/00150198708201307.

[26] J. Valasek, "Piezo-electric and allied phenomena in rochelle salt," *Phys. Rev.*, vol. 17, pp. 475–481, 4 1921. DOI: 10.1103/PhysRev.17.475.

[27] G. Busch and P. Scherrer, "Eine neue seignette-elektrische substanz," *Naturwissenschaften*, vol. 23, p. 737, 1987. DOI: 10.1007/BF01498152.

[28] H. Mueller, "Properties of rochelle salt," *Phys. Rev.*, vol. 47, pp. 175–191, 2 1935. DOI: 10.1103/PhysRev.47.175.

[29] H. Mueller, "Properties of rochelle salt," *Phys. Rev.*, vol. 57, pp. 829–839, 9 1940. DOI: 10.1103/PhysRev.57.829.

[30] G. Busch, "How I discovered the ferroelectric properties of KH_2PO_4," *Ferroelectrics*, vol. 71, no. 1, pp. 43–47, 1987. DOI: 10.1080/00150198708224828.

[31] W. Kanzig, "History of ferroelectricity 1938-1955," *Ferroelectrics*, vol. 74, no. 1, pp. 285–291, 1987. DOI: 10.1080/00150198708201308.

[32] K. Uchino, "The development of piezoelectric materials and the new perspective," in *Advanced Piezoelectric Materials*, K. Uchino, Ed., Woodhead Publishing, 2017, ch. 1, pp. 1–92, ISBN: 978-0-08-102135-4. DOI: 10.1016/B978-0-08-102135-4.00001-1.

[33] A. F. Devonshire, "Theory of barium titanate," *Lond. Edinb. Dublin Philos. Mag. J. Sci.*, vol. 40, pp. 1040–1063, 309 1949. DOI: 10.1080/14786444908561372.

[34] W. P. Mason, "Piezoelectric or electrostrictive effect in barium titanate ceramics," *Phys. Rev.*, vol. 73, pp. 1398–1399, 11 1948. DOI: 10.1103/PhysRev.73.1398.2.

[35] B. Jaffe, R. S. Roth, and S. Marzullo, "Piezoelectric properties of lead zirconate-lead titanate solid-solution ceramics," *J. Appl. Phys.*, vol. 25, no. 6, pp. 809–810, 1954. DOI: 10.1063/1.1721741.

[36] G. Shirane and A. Takeda, "Phase transitions in solid solutions of $PbZrO_3$ and $PbTiO_3$ (i) small concentrations of $PbTiO_3$," *J. Phys. Soc. Jpn.*, vol. 7, no. 1, pp. 5–11, 1952. DOI: 10.1143/JPSJ.7.5.

[37] E. Sawaguchi, "Ferroelectricity versus antiferroelectricity in the solid solutions of $PbZrO_3$ and $PbTiO_3$," *J. Phys. Soc. Jpn.*, vol. 8, no. 5, pp. 615–629, 1953. DOI: 10.1143/JPSJ.8.615.

[38] B. Jaffe, W. J. Cook, and H. Jaffe, *Piezoelectric Ceramics*, 3rd. London: Academic Press, 1971, ISBN: 978-0-12-379550-2.

[39] A.-B. M. A. Ibrahim, R. Murgan, R. M. K. Abd, and J. Osman, "Morphotropic phase boundary in ferroelectric materials," in *Ferroelectrics - Physical Effects*, IntechOpen, 2011, ch. 1, ISBN: 978-953-51-4457-1.

[40] B. Noheda, D. E. Cox, G. Shirane, J. A. Gonzalo, L. E. Cross, and S.-E. Park, "A monoclinic ferroelectric phase in the $Pb(Zr_{1-x}Ti_x)O_3$ solid solution," *Appl. Phys. Lett.*, vol. 74, no. 14, pp. 2059–2061, 1999. DOI: 10.1063/1.123756.

[41] D. Vanderbilt and M. H. Cohen, "Monoclinic and triclinic phases in higher-order devonshire theory," *Phys. Rev. B*, vol. 63, p. 094 108, 9 2001. DOI: 10.1103/PhysRevB.63.094108.

[42] G. H. Haertling, "Ferroelectric ceramics: History and technology," *J. Am. Ceram. Soc.*, vol. 82, no. 4, pp. 797–818, 1999. DOI: 10.1111/j.1151-2916.1999.tb01840.x.

[43] X. Liu *et al.*, "Single-crystal-like materials by the self-assembly of cube-shaped lead zirconate titanate (PZT) microcrystals," *Langmuir*, vol. 21, no. 8, pp. 3207–3212, 2005. DOI: 10.1021/la047655o.

[44] J. A. Gallego-Juarez and K. F. Graf, "Introduction to power ultrasonics," in *Power Ultrasonics : Applications of High-Intensity Ultrasound*, Woodhead Publishing, 2015, ch. 5, ISBN: 978-1-78242-036-1.

[45] G. A. Smolenskii and A. I. Agranovskaya, "Dielectric polarization of a number of complex compounds," *Sov. Phys. Solid State*, vol. 1, pp. 1429–1437, 10 1959.

[46] V. A. Bokov and I. E. Myl'nikova, "Piezoelectric properties of new compound single crystals with perovskite structure," *Sov. Phys. Solid State*, vol. 2, p. 2428, 1961.

[47] D. Phelan *et al.*, "Phase diagram of the relaxor ferroelectric (1 - *x*) $Pb(Mg_{1/3}Nb_{2/3})O_3$ + *x*$PbTiO_3$ revisited: A neutron powder diffraction study of the relaxor skin effect," *Phase Transit.*, vol. 88, no. 3, pp. 283–305, 2015. DOI: 10.1080/01411594.2014.989226.

[48] S. Zhang and F. Li, "High performance ferroelectric relaxor-$PbTiO_3$ single crystals: Status and perspective," *J. Appl. Phys.*, vol. 111, p. 031 301, 3 2012. DOI: 10.1063/1.3679521.

[49] S. Zhang, F. Li, X. Jiang, J. Kim, J. Luo, and X. Geng, "Advantages and challenges of relaxor-$PbTiO_3$ ferroelectric crystals for electroacoustic transducers - a review," *Prog. Mater. Sci.*, vol. 68, pp. 1–66, 2015. DOI: 10.1016/j.pmatsci.2014.10.002.

[50] R. A. Cowley, S. N. Gvasaliy, S. G. Lushnikov, B. Roessli, and G. M. Rotaru, "Relaxing with relaxors: A review of relaxor ferroelectrics," *Adv. Phys.*, vol. 60, no. 2, pp. 229–327, 2011. DOI: 10.1080/00018732.2011.555385.

[51] R. S. Weis and T. K. Gaylord, "Lithium niobate: Summary of physical properties and crystal structure," *Appl. Phys. A*, vol. 37, pp. 191–203, 4 1985. DOI: 10.1007/BF00614817.

[52] B. T. Matthias and J. P. Remeika, "Ferroelectricity in the ilmenite structure," *Phys. Rev.*, vol. 76, pp. 1886–1887, 12 1949. DOI: 10.1103/PhysRev.76.1886.2.

[53] A. J. Bell and O. Deubzer, "Lead-free piezoelectrics-the environmental and regulatory issues," *MRS Bull.*, vol. 43, no. 8, pp. 581–587, 2018. DOI: 10.1557/mrs.2018.154.

[54] J. Wu, *Advances in Lead-Free Piezoelectric Materials*. Springer, 2018, ISBN: 978-981-10-8998-5.

[55] D. Wang, G. Wang, Z. Lu, Z. Al-Jlaihawi, and A. Feteira, "Crystal structure, phase transitions and photoferroelectric properties of $KNbO_3$-based lead-free ferroelectric ceramics: A brief review," *Front. Mater.*, vol. 7, 2020. DOI: 10.3389/fmats.2020.00091.

[56] B.-J. Chu, D.-R. Chen, G.-R. Li, and Q.-R. Yin, "Electrical properties of $Na_{1/2}Bi_{1/2}TiO_3$-$BaTiO_3$ ceramics," *J. Eur. Ceram. Soc.*, vol. 22, no. 13, pp. 2115–2121, 2002. DOI: 10.1016/S0955-2219(02)00027-4.

[57] W. Jo *et al.*, "Giant electric-field-induced strains in lead-free ceramics for actuator applications – status and perspective," *J. Electroceramics*, vol. 29, pp. 71–93, 1 2012. DOI: 10.1007/s10832-012-9742-3.

[58] R. Ranjan, "$Na_{1/2}Bi_{1/2}TiO_3$-based lead-free piezoceramics: A review of structure-property correlation," *Curr. Sci.*, vol. 118, no. 10, pp. 1507–1519, 2020.

[59] J. Gao, D. Xue, W. Liu, C. Zhou, and X. Ren, "Recent progress on $BaTiO_3$-based piezoelectric ceramics for actuator applications," *Actuators*, vol. 6, no. 3, 2017. DOI: 10.3390/act6030024.

[60] W. Liu, L. Cheng, and S. Li, "Prospective of $(BaCa)(ZrTi)O_3$ lead-free piezoelectric ceramics," *Crystals*, vol. 9, no. 3, 201. DOI: 10.3390/cryst9030179.

[61] G. Catalan and J. F. Scott, "Physics and applications of bismuth ferrite," *Adv.*, vol. 21, no. 24, pp. 2463–2485, 2009. DOI: 10.1002/adma.200802849.

[62] N. A. Spaldin and R. Ramesh, "Advances in magnetoelectric multiferroics," *Nat. Mater.*, vol. 18, no. 3, pp. 203–212, 2019. DOI: 10.1038/s41563-018-0275-2.

[63] J. Koruza, A. J. Bell, T. Frömling, K. G. Webber, K. Wang, and J. Rödel, "Requirements for the transfer of lead-free piezoceramics into application," *J. Materiomics*, vol. 4, no. 1, pp. 13–26, 2018. DOI: 10.1016/j.jmat.2018.02.001.

[64] M. Safaei, H. A. Sodano, and S. R. Anton, "A review of energy harvesting using piezoelectric materials: State-of-the-art a decade later (2008–2018)," *Smart Mater. Struct.*, vol. 28, no. 11, p. 113 001, 2019. DOI: 10.1088/1361-665x/ab36e4.

[65] E. Aksel and J. L. Jones, "Advances in lead-free piezoelectric materials for sensors and actuators," *Sensors*, vol. 10, no. 3, pp. 1935–1954, 2010. DOI: 10.3390/s100301935.

[66] A. Einstein, "Grundlage der allgemeinen Relativit atstheorie," *Ann. Phys.*, vol. 4, no. 49, pp. 769–822, 1916.

[67] J. F. Nye, *Physical Properties of Crystals*, 2rd. Clarendon Press, 1985, ISBN: 0-19-851165-5.

[68] L. D. Landau and E. M. Lifshitz, *Theory of Elasticity*, 2nd. Pergamon, 1970, ch. 1, ISBN: 9781299536005.

[69] L. D. Landau and E. M. Lifshitz, *Electrodynamics of Continuous Media*, 1st. Pergamon, 1960, ch. 2, ISBN: 9780750626347.

[70] K. F. Riley, M. P. Hobson, and S. J. Bence, *Mathematical Methods for Physics and Engineering*, 3rd. Cambridge University Press, 2006, ch. 5, ISBN: 978-0-521-67971-8.

[71] A. F. Devonshire, "Theory of ferroelectrics," *Adv. Phys.*, vol. 3, no. 10, pp. 85–130, 1954. DOI: 10.1080/00018735400101173.

[72] W. G. Cady, *Piezoelectricity*, 1st. McGraw-Hill, 1946, ch. 8, ISBN: 9780486828602.

[73] A. H. Meitzler, H. F. Tiersten, A. W. Warner, D. Berlincourt, G. A. Coquin, and F. S. Welsh, *An American National Standard: IEEE Standard on Piezoelectricity*, ANSI/IEEE Std 176-1987, 1987.

[74] J. F. Nye, *Physical Properties of Crystals*, 2rd. Clarendon Press, 1985, ch. 10, ISBN: 0-19-851165-5.

[75] M. E. Glicksman, *Principles of Solidification*. Springer-Verlag New York, 2011, ch. Appendix A, ISBN: 978-1-4419-7344-3.

[76] W. G. Cady, *Piezoelectricity*, 1st. McGraw-Hill, 1946, ch. 11, ISBN: 9780486828602.

[77] J. Yang, *An Introduction to the Theory of Piezoelectricity*. Springer, 1985, ch. 2, ISBN: 0-387-23546-9.

[78] K. F. Riley, M. P. Hobson, and S. J. Bence, *Mathematical Methods for Physics and Engineering*, 3rd. Cambridge University Press, 2006, ISBN: 978-0-521-67971-8.

[79] L. Landau, "On the theory of phase transitions," *Zh. Eksp. Teor. Fiz.*, vol. 7, pp. 19–32, 1937.

[80] G. H. Kwei, A. C. Lawson, S. J. L. Billinge, and S.-W. Cheong, "Structures of the ferroelectric phases of barium titanate," *J. Phys. Chem.*, vol. 97, no. 10, pp. 2368–2377, 1993. DOI: 10.1021/j100112a043.

[81] H. D. Megaw, "Crystal structure of barium titanium oxide and other double oxides of the perovskite type," *Trans. Faraday Soc.*, vol. 42, A224–A231, 1946. DOI: 10.1039/TF946420A224.

[82] M. G. Harwood, P. Popper, and D. F. Rushman, "Curie point of barium titanate," *Nature*, vol. 160, no. 4054, pp. 58–59, 1947. DOI: 10.1038/160058a0.

[83] H. F. Kay, H. J. Wellard, and P. Vousden, "Atomic positions and optical properties of barium titanate," *Nature*, vol. 163, no. 4147, pp. 636–637, 1949. DOI: 10.1038/163636a0.

[84] A. F. Devonshire, "Theory of barium titanate - part II," *Lond. Edinb. Dublin Philos. Mag. J. Sci.*, vol. 42, pp. 1065–1079, 333 1951. DOI: 10.1080/14786445108561354.

[85] X. Tan, C. Ma, J. Frederick, S. Beckman, and K. G. Webber, "The antiferroelectric $\leftrightarrow$ ferroelectric phase transition in lead-containing and lead-free perovskite ceramics," *J. Am. Ceram. Soc.*, vol. 94, no. 12, pp. 4091–4107, 2011. DOI: 10.1111/j.1551-2916.2011.04917.x.

[86] M. J. Haun, E. Furman, S. J. Jang, and L. E. Cross, "Thermodynamic theory of the lead zirconate-titanate solid solution system, part i: Phenomenology," *Ferroelectrics*, vol. 99, pp. 13–25, 1 1989. DOI: 10.1080/00150198908221436.

[87] M. J. Haun, E. Furman, H. A. McKinstry, and L. E. Cross, "Thermodynamic theory of the lead zirconate-titanate solid solution system, part ii: Tricritical behavior," *Ferroelectrics*, vol. 99, pp. 27–44, 1 1989. DOI: 10.1080/00150198908221437.

[88] M. J. Haun, Z. Q. Zhuang, E. Furman, S. J. Jang, and L. E. Cross, "Thermodynamic theory of the lead zirconate-titanate solid solution system, part iii: Curie constant and sixth-order polarization interaction dielectric stiffness coefficients," *Ferroelectrics*, vol. 99, pp. 45–54, 1 1989. DOI: 10.1080/00150198908221438.

[89] M. J. Haun, E. Furman, T. R. Halemane, and L. E. Cross, "Thermodynamic theory of the lead zirconate-titanate solid solution system, part iv: Tilting of the oxygen octahedra," *Ferroelectrics*, vol. 99, pp. 55–62, 1 1989. DOI: 10.1080/00150198908221439.

[90] M. J. Haun, E. Furman, S. J. Jang, and L. E. Cross, "Thermodynamic theory of the lead zirconate-titanate solid solution system, part v: Theoretical calculations," *Ferroelectrics*, vol. 99, pp. 63–86, 1 1989. DOI: 10.1080/00150198908221440.

[91] T. R. Halemane, M. J. Haun, L. E. Cross, and R. E. Newnham, "A phenomenological theory for phase transitions in perovskite ferroelectrics with oxygen octahedron tilts," *Ferroelectrics*, vol. 62, pp. 149–165, 1 1985. DOI: 10.1080/00150198508225989.

[92] F. Li *et al.*, "Piezoelectric activity in perovskite ferroelectric crystals," *IEEE Trans. Ultrason. Ferroelectr. Freq. Contr.*, vol. 62, no. 1, pp. 18–32, 2015. DOI: 10.1109/TUFFC.2014.006660.

[93] S. Imperiale and P. Joly, "Mathematical and numerical modelling of piezoelectric sensors," *ESAIM: M2AN*, vol. 46, no. 4, pp. 875–909, 2012. DOI: 10.1051/m2an/2011070.

[94] D. Halliday, R. Resnick, and J. Walker, *Principles of Physics*, 9th. John Wiley & Sons, Inc., 2011, ch. 15, ISBN: 978-0-470-56158-4.

[95] A. I. Vistnes, *Physics of Oscillations and Waves*. Springer, 2018, ch. 3, ISBN: 978-3-319-72314-3.

[96] D. Halliday, R. Resnick, and J. Walker, *Principles of Physics*, 9th. John Wiley & Sons, Inc., 2011, ch. 31, ISBN: 978-0-470-56158-4.

[97] TASI Technical Software Inc., *PRAP : Piezoelectric Resonance Analysis Program*, Accessed online at https://www.tasitechnical.com/prap/. Accessed 7th October 2021.

[98] J. Yang, *An Introduction to the Theory of Piezoelectricity*. Springer, 1985, ch. 3, ISBN: 0-387-23546-9.

[99] G. Liu, S. Zhang, W. Jiang, and W. Cao, "Losses in Ferroelectric Materials," *Mater. Sci. Eng. R Rep.*, vol. 89, pp. 1–48, 2015. DOI: 10.1016/j.mser.2015.01.002.

[100] B. A. Auld, *Acoustic fields and waves in solids*. John Wiley & Sons, Inc., 1973, vol. 1, ch. 3, ISBN: 0-471-03702-8.

[101] J. D. B. Cheeke, *Fundamentals and Applications of Ultrasonic Waves*, 2nd. CRC Press, 2012, ch. 5, ISBN: 9781138077201.

[102] M. Postema and K. Attenborough, *Fundamentals of Medical Ultrasonics*, 1st. Spon Press, 2011, ch. 4, ISBN: 978-0-203-86350-3.

[103] A. V. Mezheritsky, "Elastic, dielectric, and piezoelectric losses in piezoceramics: How it works all together," *IEEE Trans. Ultrason. Ferroelectr. Freq. Contr.*, vol. 51, no. 6, pp. 695–707, 2004. DOI: 10.1109/TUFFC.2004.1304268.

[104] K. Uchino, Y. Zhuang, and S. O. Ural, "Loss determination methodology for a piezoelectric ceramic: New phenomenological theory and experimental proposals," *J. Adv. Dielectr.*, vol. 1, no. 1, pp. 17–31, 2011. DOI: 10.1142/S2010135X11000033.

[105] R. Holland, "Representation of dielectric, elastic, and piezoelectric losses by complex coefficients," *IEEE Trans. Sonics Ultrason.*, vol. 14, no. 1, 1967. DOI: 10.1109/T-SU.1967.29405.

[106] W. P. Mason, *Physical Acoustics and the Properties of Solids*. Van Nostrand, 1958, ch. 7, ISBN: 9780598457004.

[107] K. Uchino and S. Hirose, "Loss Mechanisms in Piezoelectrics: How to Measure Different Losses Separately," *IEEE Trans. Ultrason. Ferroelectr. Freq. Contr.*, vol. 48, no. 1, pp. 307–321, 2001.

[108] K. Uchino, "High-power piezoelectrics and loss mechanisms," in *Advanced Piezoelectric Materials*, K. Uchino, Ed., Woodhead Publishing, 2017, ch. 17, pp. 647–754, ISBN: 978-0-08-102135-4. DOI: 10.1016/B978-0-08-102135-4.00001-1.

[109] W. Shi, H. N. Shekhani, H. Zhao, J. Ma, Y. Yao, and K. Uchino, "Losses in piezoelectrics derived from a new equivalent circuit," *J. Electroceramics*, vol. 35, pp. 1–10, 1 2015.

[110] H. C. Ørsted, "Experiments on the effect of a current of electricity on the magnetic needle," *Ann. Philos.*, vol. 16, pp. 273–277, 1820.

[111] J. Clerk Maxwell, "VIII. a dynamical theory of the electromagnetic field," *Philos. Trans. Roy. Soc. London*, vol. 155, pp. 459–512, 1865. DOI: 10.1098/rstl.1865.0008.

[112] J.Rodríguez-Carvajal and F. Bourée, "Symmetry and magnetic structures," *EPJ Web of Conferences*, vol. 22, p. 00 010, 2012. DOI: 10.1051/epjconf/20122200010.

[113] L. D. Landau and E. M. Lifshitz, *Electrodynamics of Continuous Media*, 1st. Pergamon, 1960, ch. 4, ISBN: 9780750626347.

[114] R. R. Birss, *Symmetry and Magnetism*, 2nd. North Holland Publishing Company, 1966, ch. 2, ISBN: 978-0-7204-1453-0.

[115] C. J. Bradley and A. P. Cracknell, *The Mathematical Theory of Symmetry in Solids*. Clarendon Press, 1972, ch. 7, ISBN: 978-0-19-958258-7.

[116] P. Weiss, "L'hypothèse du champ moléculaire et la propriété ferromagnétique," *J. Phys.: Theor. Appl.*, vol. 6, no. 1, pp. 661–690, 1907.

[117] P. Weiss, "The application of the bethe-peierls method to ferromagnetism," *Phys. Rev.*, vol. 74, pp. 1493–1504, 10 1948. DOI: 10.1103/PhysRev.74.1493.

[118] D. Jiles, *Introduction to Magnetism and Magnetic Materials*, 3rd. CRC Press, 2016, ch. 9, ISBN: 978-1-4822-3887-7.

[119] C. Kittel, *Introduction to Solid State Physics*, 8th. John Wiley & Sons, Inc., 2005, ch. 7, ISBN: 0-471-41526-X.

[120] Z. Ye, "Relaxor ferroelectric complex perovskites: Structure, properties and phase transitions," *Key Eng. Mater.*, vol. 155-156, pp. 81–122, 1998. DOI: 10.4028/www.scientific.net/KEM.155-156.81.

[121] Z.-G. Ye, "High-performance piezoelectric single crystals of complex perovskite solid solutions," *MRS Bull.*, vol. 34, no. 4, pp. 277–283, 2009. DOI: 10.1557/mrs2009.79.

[122] A. A. Bokov and Z.-G. Ye, "Recent progress in relaxor ferroelectrics with perovskite structure," *J. Mater. Sci.*, vol. 41, pp. 31–52, 2006. DOI: 10.1007/s10853-005-5915-7.

[123] Z.-G. Ye and A. A. Bokov, "Dielectric and structural properties of relaxor ferroelectrics," *Ferroelectrics*, vol. 302, p. 473, 2004. DOI: 10.1080/00150190490455043.

[124] Z.-G. Ye, "Relaxor ferroelectric $Pb(Mg_{1/3}Nb_{2/3})O_3$: Properties and present understanding," *Ferroelectrics*, vol. 184, p. 193, 1996. DOI: 10.1080/00150199608230260.

[125] F. Li *et al.*, "The origin of ultrahigh piezoelectricity in relaxor-ferroelectric solid solution crystals," *Nat. Commun*, vol. 7, p. 13 807, 2016. DOI: 10.1038/ncomms13807.

[126] L. E. Cross, "Relaxor ferroelectrics," *Ferroelectrics*, vol. 76, pp. 241–267, 1 1987. DOI: 10.1080/00150198708016945.

[127] V. Bovtun *et al.*, "Central-peak components and polar soft mode in relaxor $Pb(Mg_{1/3}Nb_{2/3})O_3$ crystals," *Ferroelectrics*, vol. 298, no. 1, pp. 23–30, 2004. DOI: 10.1080/00150190490423057.

[128] M. Davis, "Phase transitions, anisotropy and domain engineering: The piezoelectric properties of relaxor-ferroelectric single crystals," PhD thesis, École Polytechnique Fédérale de Lausanne, 2006.

[129] W. Cochran, "Crystal stability and the theory of ferroelectricity," *Adv. Phys.*, vol. 9, no. 36, pp. 387–423, 1960. DOI: 10.1080/00018736000101229.

[130] K. Uchino, S. Nomura, L. E. Cross, S. J. Jang, and R. E. Newnham, "Electrostrictive effect in lead magnesium niobate single crystals," *J. Appl. Phys.*, vol. 51, no. 2, pp. 1142–1145, 1980. DOI: 10.1063/1.327724.

[131] V. V. Kirillov and V. A. Isupov, "Relaxation polarization of $Pb(Mg_{1/3}Nb_{2/3})O_3$(PMN)-a ferroelectric with a diffused phase transition," *Ferroelectrics*, vol. 5, no. 1, pp. 3–9, 1973. DOI: 10.1080/00150197308235773.

[132] M. L. Mulvihill, L. E. Cross, W. Cao, and K. Uchino, "Domain-related phase transition-like behavior in lead zinc niobate relaxor ferroelectric single crystals," *J. Am. Ceram. Soc.*, vol. 80, no. 6, pp. 1462–1468, 1997. DOI: 10.1111/j.1151-2916.1997.tb03004.x.

[133] A. A. Bokov *et al.*, "Empirical scaling of the dielectric permittivity peak in relaxor ferroelectrics," *Phys. Rev. B*, vol. 68, p. 052 102, 5 2003. DOI: 10.1103/PhysRevB.68.052102.

[134] J. Bowles, M. Jackson, A. Chen, and P. Solheid, "Interpretation of low-temperature. data part 1: Superparamagnetism and paramagnetism," *The IRM Quarterly*, vol. 19, pp. 1–11, 3 2009.

[135] N. Setter and L. E. Cross, "The role of B-site cation disorder in diffuse phase transition behavior of perovskite ferroelectrics," *J. Appl. Phys.*, vol. 51, no. 8, pp. 4356–4360, 1980. DOI: 10.1063/1.328296.

[136] C. G. F. Stenger, F. L. Scholten, and A. J. Burggraaf, "Ordering and diffuse phase transitions in $Pb(Sc_{0.5}Ta_{0.5})O_3$ ceramics," *Solid State Commun.*, vol. 32, no. 11, pp. 989–992, 1979. DOI: 10.1016/0038-1098(79)90812-3.

[137] G. Burns and F. H. Dacol, "Polarization in the cubic phase of $BaTiO_3$," *Solid State Commun.*, vol. 42, pp. 9–12, 1 1982. DOI: 10.1016/0038-1098(82)91018-3.

[138] G. Burns and F. H. Dacol, "Glassy polarization behavior in ferroelectric compounds $Pb(Mg_{1/3}Nb_{2/3})O_3$ and $Pb(Zn_{1/3}Nb_{2/3})O_3$," *Solid State Commun.*, vol. 48, no. 10, pp. 853–856, 1983. DOI: 10.1016/0038-1098(83)90132-1.

[139] D. Viehland, S. J. Jang, L. E. Cross, and M. Wuttig, "Deviation from curie-weiss behavior in relaxor ferroelectrics," *Phys. Rev. B*, vol. 46, pp. 8003–8006, 13 1992. DOI: 10.1103/PhysRevB.46.8003.

[140] W. M. Saslow, "Scenario for the vogel-fulcher "law"," *Phys. Rev. B*, vol. 37, pp. 676–678, 1 1988. DOI: 10.1103/PhysRevB.37.676.

[141] D. Viehland, S. J. Jang, L. E. Cross, and M. Wuttig, "Freezing of the polarization fluctuations in lead magnesium niobate relaxors," *J. Appl. Phys.*, vol. 68, no. 6, pp. 2916–2921, 1990. DOI: 10.1063/1.346425.

[142] I.-K. Jeong *et al.*, "Direct observation of the formation of polar nanoregions in $Pb(Mg_{1/3}Nb_{2/3})O_3$ using neutron pair distribution function analysis," *Phys. Rev. Lett.*, vol. 94, p. 147 602, 14 2005. DOI: 10.1103/PhysRevLett.94.147602.

[143] S. B. Vakhrushev, A. A. Naberezhnov, N. M. Okuneva, and B. N. Savenko, "Determination of polarization vectors in lead magnoniobate," *Phys. Solid State*, vol. 37, pp. 1933–1997, 1995.

[144] K. Hirota, Z.-G. Ye, S. Wakimoto, P. M. Gehring, and G. Shirane, "Neutron diffuse scattering from polar nanoregions in the relaxor $Pb(Mg_{1/3}Nb_{2/3})O_3$," *Phys. Rev. B*, vol. 65, p. 104 105, 2002. DOI: 10.1103/PhysRevB.65.104105.

[145] T. R. Welberry *et al.*, "Single-crystal neutron diffuse scattering and monte carlo study of the relaxor ferroelectric $PbZn_{1/3}Nb_{2/3}O_3$ (PZN)," *J. Appl. Crystallogr.*, vol. 38, no. 4, pp. 639–647, 2005. DOI: 10.1107/S0021889805015918.

[146] C. Stock *et al.*, "Evidence for anisotropic polar nanoregions in relaxor $Pb(Mg_{1/3}Nb_{2/3})O_3$: A neutron study of the elastic constants and anomalous TA phonon damping in PMN," *Phys. Rev. B*, vol. 86, no. 10, pp. 1–18, 2012. DOI: 10.1103/PhysRevB.86.104108.

[147] Y. Imry and S.-K. Ma, "Random-field instability of the ordered state of continuous symmetry," *Phys. Rev. Lett.*, vol. 35, pp. 1399–1401, 21 1975. DOI: 10.1103/PhysRevLett.35.1399.

[148] M. Glinchuk, "Relaxor ferroelectrics: From cross superparaelectric model to random field theory," *British Ceramic Transactions*, vol. 103, pp. 76–82, 2 2004. DOI: 10.1179/096797804225012792.

[149] E. Ising, "Beitrag zur theorie des ferromagnetismus," *Zeitschrift für Physik*, vol. 31, pp. 253–258, 1 1925.

[150] T. Nattermann, "Theory of the random field ising model," 1997, Accessed online at https://arxiv.org/abs/cond-mat/9705295. Accessed 25th April 2017.

[151] K. H. Conlon *et al.*, "Direct observation of the near-surface layer in $Pb(Mg_{1/3}Nb_{2/3})O_3$ using neutron diffraction," *Phys. Rev. B*, vol. 70, p. 172 204, 17 2004. DOI: 10.1103/PhysRevB.70.172204.

[152] C. Stock *et al.*, "Strong influence of the diffuse component on the lattice dynamics in $Pb(Mg_{1/3}Nb_{2/3})O_3$," *J. Phys. Soc. Jpn.*, vol. 74, no. 11, pp. 3002–3010, 2005. DOI: 10.1143/JPSJ.74.3002.

[153] G. Xu, Z. Zhong, Y. Bing, Z.-G. Ye, C. Stock, and G. Shirane, "Ground state of the relaxor ferroelectric $PbZn_{1/3}Nb_{2/3}O_3$," *Phys. Rev. B*, vol. 67, p. 104 102, 10 2003. DOI: 10.1103/PhysRevB.67.104102.

[154] J. P. Hill, T. R. Thurston, R. W. Erwin, M. J. Ramstad, and R. J. Birgeneau, "Transition to long-range order in the three-dimensional random-field ising model," *Phys. Rev. Lett.*, vol. 66, pp. 3281–3284, 25 1991. DOI: 10.1103/PhysRevLett.66.3281.

[155] Q. Feng, Q. J. Harris, R. J. Birgeneau, and J. P. Hill, "Neutron and x-ray scattering studies of field-cooled ordering in the three-dimensional random-field ising model," *Phys. Rev. B*, vol. 55, p. 370, 1 1997. DOI: 10.1103/PhysRevB.55.370.

[156] N. A. Spaldin, S.-W. Cheong, and R. Ramesh, "Multiferroics: Past, present, and future," *Physics Today*, vol. 63, no. 10, pp. 38–43, 2010. DOI: 10.1063/1.3502547.

[157] S.-W. Cheong and M. Mostovoy, "Multiferroics: A magnetic twist for ferroelectricity," *Nat. Mater.*, vol. 6, no. 1, pp. 13–20, 2007. DOI: 10.1038/nmat1804.

[158] I. E. Dzyaloshinskii, "On the magneto-electrical effects in antiferromagnets," *Soviet Physics JETP*, vol. 10, pp. 628–629, 1959.

[159] D. N. Astrov, "The magnetoelectric effect in antiferromagnetics," *Soviet Physics JETP*, vol. 11, pp. 708–709, 1960.

[160] N. A. Hill, "Why are there so few magnetic ferroelectrics?" *J. Phys. Chem. B*, vol. 104, no. 29, pp. 6694–6709, 2000. DOI: 10.1021/jp000114x.

[161] T. Kimura, T. Goto, H. Shintani, K. Ishizaka, T. Arima, and Y. Tokura, "Magnetic control of ferroelectric polarization," *Nature*, vol. 426, no. 6962, pp. 55–58, 2003. DOI: 10.1038/nature02018.

[162] T. Kimura, "Spiral magnets as magnetoelectrics," *Annual Review of Materials Research*, vol. 37, no. 1, pp. 387–413, 2007. DOI: 10.1146/annurev.matsci.37.052506.084259.

[163] H. Katsura, N. Nagaosa, and A. V. Balatsky, "Spin current and magnetoelectric effect in noncollinear magnets," *Phys. Rev. Lett.*, vol. 95, p. 057 205, 5 2005. DOI: 10.1103/PhysRevLett.95.057205.

[164] M. Kenzelmann *et al.*, "Magnetic inversion symmetry breaking and ferroelectricity in $TbMnO_3$," *Phys. Rev. Lett.*, vol. 95, p. 087 206, 8 2005. DOI: 10.1103/PhysRevLett.95.087206.

[165] M. Mostovoy, "Ferroelectricity in spiral magnets," *Phys. Rev. Lett.*, vol. 96, p. 067 601, 6 2006. DOI: 10.1103/PhysRevLett.96.067601.

[166] I. A. Sergienko and E. Dagotto, "Role of the dzyaloshinskii-moriya interaction in multiferroic perovskites," *Phys. Rev. B*, vol. 73, p. 094 434, 9 2006. DOI: 10.1103/PhysRevB.73.094434.

[167] R. E. Newnham, J. J. Kramer, W. A. Schulze, and L. E. Cross, "Magnetoferroelectricity in Cr_2BeO_4," *J. Appl. Phys.*, vol. 49, no. 12, pp. 6088–6091, 1978. DOI: 10.1063/1.324527.

[168] K. Taniguchi, N. Abe, T. Takenobu, Y. Iwasa, and T. Arima, "Ferroelectric polarization flop in a frustrated magnet $MnWO_4$ induced by a magnetic field," *Phys. Rev. Lett.*, vol. 97, p. 097 203, 9 2006. DOI: 10.1103/PhysRevLett.97.097203.

[169] R. D. Johnson *et al.*, "$Cu_3Nb_2O_8$: A multiferroic with chiral coupling to the crystal structure," *Phys. Rev. Lett.*, vol. 107, p. 137 205, 13 2011. DOI: 10.1103/PhysRevLett.107.137205.

[170] I. Dzyaloshinsky, "A thermodynamic theory of "weak" ferromagnetism of antiferromagnetics," *J. Phys. Chem. Solids*, vol. 4, no. 4, pp. 241–255, 1958. DOI: 10.1016/0022-3697(58)90076-3.

[171] T. Moriya, "Anisotropic superexchange interaction and weak ferromagnetism," *Phys. Rev.*, vol. 120, pp. 91–98, 1 1960. DOI: 10.1103/PhysRev.120.91.

[172] K. Yosida, *Theory of Magnetism*. Springer, 1996, ch. 4, ISBN: 3-540-60651-3.

[173] K. Yosida, *Theory of Magnetism*. Springer, 1996, ch. 3, ISBN: 3-540-60651-3.

[174] S.-W. Cheong, J. D. Thompson, and Z. Fisk, "Metamagnetism in La_2CuO_4," *Phys. Rev. B*, vol. 39, pp. 4395–4398, 7 1989. DOI: 10.1103/PhysRevB.39.4395.

[175] A. M. Kadomtseva, A. K. Zvezdin, Y. F. Popov, A. P. Pyatakov, and G. P. Vorob'ev, "Space–time parity violation and magnetoelectric interactions in antiferromagnets," *JETP Lett.*, vol. 79, no. 11, pp. 571–581, 2004. DOI: 10.1134/1.1787107.

[176] W. Brixel, J.-P. Rivera, A. Steiner, and H. Schmid, "Magnetic field induced magnetoelectric effects, $(ME)_H$, in the perovskites Pb_2CoWO_6 and Pb_2FeTaO_6," *Ferroelectrics*, vol. 79, no. 1, pp. 201–204, 1988. DOI: 10.1080/00150198808229431.

[177] Y. Yang, J.-M. Liu, H. B. Huang, W. Q. Zou, P. Bao, and Z. G. Liu, "Magnetoelectric coupling in ferroelectromagnet $Pb(Fe_{1/2}Nb_{1/2})O_3$ single crystals," *Phys. Rev. B*, vol. 70, p. 132 101, 13 2004. DOI: 10.1103/PhysRevB.70.132101.

Chapter 3

Experimental Methods

This chapter provides a brief review of experimental methods used in this thesis. This includes outlining the scientific principles behind each technique and a short description of how they were implemented.

3.1 Chapter Introduction

The work described in this thesis used two main techniques in order to probe the fundamental behaviour of dielectric oxides which are reviewed in this chapter. Sub-atomic condensed matter probes such as neutrons and muons were used and the workings of the various experimental sources of both types of particle are outlined as is their interaction with matter.

3.2 Review of Fundamental Particles

An essential aspect of modern condensed matter physics is the use of sub-atomic probes at large-scale facilities. These facilities are able to provide access to techniques that are not feasible in a lab setting. The most widest used of these probes are probably X-rays, neutrons and muons, with the last two being used in this thesis. As such these are the main focus of this review.

The standard model is one of the most fully tested theories in physics [1]. It sets out the types and roles of all fundamental particles which, together, are understood to make up the universe. It also covers interactions of the fundamental strong and electroweak forces. Historically, the standard model came about as an effort by physicists to provide a classification system for the many subatomic particles discovered in the twentieth century.

Broadly speaking the standard model splits particles into two types - fermions and bosons (named for Fermi and Bose respectively). The distinction between these depends on their spin: Typically measured in units of reduced Planck's constant $\hbar$, spin is a consequence of the inclusion of relativistic theory into quantum mechanics and its existence can be derived purely though symmetry [2].

The full taxonomy of particles within the standard model is not required for this thesis but two important classes of fermion must be discussed. Fermions have half-integer spin (e.g. 1/2, 3/2 etc.) and are subject to rules such as the Pauli exclusion principle. They make up ordinary matter and include objects such as electrons, protons and neutrons. Elementary fermions can be further divided into two classes - quarks and leptons - which both contain six members (or flavours, in the jargon). This distinction is made according to fermions which carry colour charge (allowing interaction with the strong force) i.e. quarks, and those that do not i.e. leptons.

Quarks can either form together in threes, to make baryons such as protons and neutrons, or as a quark-antiquark pair, to make mesons. Antiparticles are identical in every way apart from opposite charge - positive electrical charge to negative and colour charge to anti-colour charge. The most common quarks are the so-called first generation, consisting of up quarks and down quarks. The other quarks are very unstable and, due to their large masses, have short lifetimes $\sim 10^{-8}$ - 10^{-12} s [3]. The extreme of this can be seen in the case of the top quark which has ≈ 187 times the mass of a proton, the most massive quark, and a lifetime of 0.5×10^{-24} s [4].

The six flavours of leptons are electrons, muons and taus (charged) and their respective neutrinos (no charge). Again, as muons and taus have larger mass than electrons, they are also unstable. In the standard model, the three neutrino flavours have no mass but this is now known to be purely a measurement limitation [5]. Conventionally, charged leptons have negative charges ($-e$) and antileptons have positive charges (the antielectron being referred to as a positron).

3.3 Neutron Techniques

Neutrons have been used to probe condensed matter systems since they were found to display Bragg scattering in 1936 [6]. Discovered in 1932 by James Chadwick, they are slightly more massive than a proton but have no charge [7] allowing them to probe deeply into matter in the absence of Coulomb interaction. This means that neutrons are unaffected by an atom's electron cloud and interact only with the nucleus via the strong nuclear force. The likelihood of a neutron to scatter is given by the scattering cross-section. Whereas X-ray scattering is dependent upon electromagnetic interactions with the electron cloud and, therefore, cross-sections increase with atomic number, neutron cross-sections vary in a non-systematic way across the periodic table [8]. Also, the neutron possesses a non-zero magnetic moment (1.913 nuclear magnetons) and can, therefore, scatter off unpaired electrons in an atom through the electromagnetic dipole-dipole interaction. The for most magnetic atoms, the effective magnetic scattering length is comparable to the nuclear scattering length and so the magnetic interactions have a similar strength to nuclear ones [8].

3.3.1 Neutron Sources

Most neutrons are bound within the nuclei of atoms. A lone neutron, being slightly heavier than a proton, will undergo beta decay with a half-life of around 15 minutes. Hence, to use neutrons in scattering experiments, they must be obtained from a specific source. There are many neutron facilities around the world using either one of two methods to produce experimental neutrons:

- **Continuous Source** neutrons are produced by a nuclear reactor. Here the neutrons are produced continuously in time as a by-product of the spontaneous fission of ^{235}U. An example of a continuous source is the Institut Laue-Langevin (ILL, Grenoble, France) which produces 1.5×10^{15} neutrons $\mathrm{s}^{-1}\mathrm{cm}^{-2}$ [9]. These sources are capable of high time-integrated neutron fluxes and so are well-suited to Bragg diffraction type experiments.

- **Pulsed/Spallation Source** neutrons are produced by the bombardment of a heavy target (e.g. Ta, W) by an accelerated proton beam. An example is ISIS (STFC Rutherford Appleton Laboratory, Didcot, UK). Here, a beam of protons is accelerated in a synchrotron and is then directed to be incident onto a target, triggering the expulsion of neutrons. Whilst continuous sources may produce greater time-integrated neutron flux, pulsed sources can provide brighter bursts. They are also better suited to time of flight measurements as they provide better time resolution.

In this thesis, a continuous source of neutrons was used to study the multiferroic $Cu_3Nb_2O_8$ (CNO) in Chapter 4.

3.3.2 Nuclear Interactions

The theory of neutron interaction will now be reviewed. Consider a mono-energetic beam with wavevector $\vec{k}^I$. The rate at which neutrons are scattered into solid angle $d\Omega_f$ in direction $\vec{k}^F$ with final energy between E^F and $E^F + dE^F$ is given by the product of the flux, i.e. the wavevector dependent intensity of neutrons, with the differential cross-section, $\dfrac{d^2\sigma}{d\Omega^F dE^F}$.

Fermi's golden rule combined with the Born approximation provide the basis for the treatment of neutron-nuclear scattering [10]. The Born approximation states that the incoming neutron's quantum wavefunction may be written as a plane wave $\sim e^{i\vec{k}^I\cdot\vec{r}}$ and the outgoing, scattered neutron's wavefunction is a spherical wave $\sim \frac{e^{i|\vec{k}^F|r}}{r}$. This approximation will be used again in Chapter 4. Fermi's golden rule states the differential cross-section corresponding to a transition between two quantum states, labelled with wavevectors $\vec{k}^I$ and $\vec{k}^F$ and quantum numbers λ^I and λ^F, is proportional to the square of the matrix element of the interaction operator, V, which links these two states. This gives the form for the differential cross-section [8]

$$\frac{d^2\sigma}{d\Omega_f dE_f} = \frac{k^F}{k^I}\left(\frac{m_n}{2\pi\hbar^2}\right)^2 \left|\left\langle \vec{k}^I,\lambda^I\middle|V\middle|\vec{k}^F,\lambda^F\right\rangle\right|^2 \delta(\hbar\omega + E^I - E^F), \tag{3.1}$$

where m_n is the mass of the neutron and the Dirac delta function ensures conservation of energy.

However, in a nuclear scattering experiment, rather than measuring a transition from state λ^I to λ^F, the differential cross-section is measured as defined above. This means that the final states in Equation 3.1 must be summed over, whilst keeping the initial state fixed, and then averaged over initial states. This leads to the expression [11]

$$\frac{d^2\sigma}{d\Omega_f dE_f} = \frac{k^F}{k^I}\frac{1}{2\pi\hbar}\sum_{i,j} b_i b_j \int_{\infty}^{\infty} dt \left\langle e^{-i\vec{Q}\cdot\vec{R}_i(0)} e^{i\vec{Q}\cdot\vec{R}_j(t)} \right\rangle e^{-i\omega t}, \tag{3.2}$$

where b_i is the scattering length of nucleus i, i.e. a constant which effectively mediates the strength of neutron-nuclear scattering, $\vec{Q} \equiv \vec{k_f} - \vec{k_i}$ is the momentum transfer or scattering vector, $\vec{R}_i(t)$ is the position of nucleus i at time t (formally $\vec{R}_i(t)$ should be interpreted as a quantum mechanical Heisenberg, i.e. time dependent, operator), and ω is the frequency corresponding to the energy difference as specified by the Dirac delta function. The angled brackets denote a thermal average.

Like in optics, the differential cross-section may be expressed as a sum of coherent and incoherent parts. However, whereas the definition of coherence is typically expressed in terms of phase between scattered particles [12], it makes more sense to consider the question of coherence in neutron scattering more in terms of correlation functions. This is because, in a neutron experiment, the number of neutrons is known and there exists an uncertainty relation between the number and phase operators in the quantised theory [13]. Therefore, the phase of the neutron is not knowable to an arbitrary precision and so an alternative definition is sought.

Consider a system which consists of a single scattering species. The strength of the neutron scattering is mediated by b and this can vary between nuclei due to differences such as nuclear spin states or the presence of isotopes [14, 15]. In this case, the average scattering length will just be given by

$$\bar{b} = \sum_i p_i b_i, \tag{3.3}$$

where p_i are the weights characterising the variation (such that $\sum_i p_i = 1$), and i labels the nuclei. Then, under the assumptions that the different b values are uncorrelated and that the system contains a large number of nuclei, the measured differential cross-section is may be written as the cross-section averaged over the system

$$\begin{aligned}\frac{d^2\sigma}{d\Omega_f dE_f} =& \frac{k^F}{k^I}\frac{1}{2\pi\hbar}(\bar{b})^2\sum_{i,j}\int_{\infty}^{\infty} dt\left\langle e^{-i\vec{Q}\cdot\vec{R}_i(0)}e^{i\vec{Q}\cdot\vec{R}_j(t)}\right\rangle e^{-i\omega t} \\ &+ \frac{k^F}{k^I}\frac{1}{2\pi\hbar}\left[\bar{b^2}-(\bar{b})^2\right]\sum_{i}\int_{\infty}^{\infty} dt\left\langle e^{-i\vec{Q}\cdot\vec{R}_i(0)}e^{i\vec{Q}\cdot\vec{R}_i(t)}\right\rangle e^{-i\omega t} \\ \equiv& \left(\frac{d^2\sigma}{d\Omega_f dE_f}\right)_{coh} + \left(\frac{d^2\sigma}{d\Omega_f dE_f}\right)_{inc}.\end{aligned} \tag{3.4}$$

This explicitly shows the splitting of the differential cross-section into coherent and incoherent parts [10, 14, 16]. From this expression, it can be seen that coherent scattering physically corresponds to the case if all the nuclear scattering lengths were equal to $\bar{b}$, i.e. no variations. Then, the incoherent scattering arises from the random deviations of the scattering lengths from $\bar{b}$. Furthermore, Equation 3.4 shows that coherent scattering depends of the correlations between both the positions of the same nucleus *and* different nuclei at different times and so may give rise to interference effects such as Bragg scattering. The incoherent cross-section only depends of correlations between the same nucleus at different times and so cannot include interference effects.

Finally, observe that the assumption of elastic scattering, i.e. that the initial and final energies are equal, has *not* been imposed in Equation 3.4 and so both the coherent and incoherent scattering cross-sections may be further separated into elastic and inelastic parts. Elastic, coherent scattering contains information about the structure of the system, as described above, and so primarily consist of Bragg scattering. The elastic, incoherent scattering arising from fluctuations, only contributes a constant background and is usually not of interest [17].

However, this is not the case for inelastic scattering where both parts of the scattering cross-section can contain useful information about the sample. The coherent part of inelastic scattering arise from correlated motion of atoms whereas incoherent inelastic scattering arises from atoms independent behaviour [15, 18]. This means that inelastic, coherent scattering contains information about collective and co-operative excitations such as phonons and other modes as these will provide correlated atomic motion on the scale of the whole crystal lattice. On the other hand, inelastic, incoherent scattering arises from phenomena such as local dynamics or particle diffusion. However, this thesis will not explore inelastic scattering and so will now restrict to the case of elastic scattering.

In the case of simple Bragg scattering i.e. coherent elastic scattering from the nuclear structure, this cross-section reduces to

$$\frac{d\sigma}{d\Omega} = N\frac{(2\pi)^3}{v_0}b^2\sum_{\vec{H}}\delta(\vec{Q}-\vec{H}), \tag{3.5}$$

where N is the number of nuclei, v_0 is the volume of the unit cell, and $\{\vec{H}\}$ is the set of vectors

that make up the reciprocal lattice. This inclusion of the Dirac delta function $\delta(\vec{Q}-\vec{H})$ means that the scattering response will be a maximum whenever $\vec{Q}$ is equal to a reciprocal lattice vector; this is an exact restatement of the von-Laue scattering conditions which are identical to Bragg's law [19]. To generalise this expression to the whole lattice it must be multiplied by the nuclear structure factor $F_N(\vec{H})$ which contains information on atomic positions within a unit cell.

Inelastic scattering occurs when momentum and energy are transferred to or from the sample. This can be thought of as either creating or annihilating a phonon, a quantum of lattice vibration defined in an analogous way to a photon with regard to light waves. As these phonons propagate through the material, they provide information about mechanical properties. In this case the scattering response is linked to the imaginary part of the material's dynamic susceptibility through the fluctuation-dissipation theorem [10].

3.3.3 Magnetic Interactions

Due to its magnetic moment, a neutron can also scatter from the magnetic moment of atoms in a crystal via the dipole-dipole interaction with a similar strength to nuclear scattering. However, unlike nuclear scattering, magnetic scattering depends not only on the initial and final wave vectors of the neutron but also on the corresponding neutron spin states. The neutron is sensitive to the so-called magnetic interaction vector, which is the component of the magnetic structure perpendicular to $\vec{Q}$. For unpolarised neutron scattering, this interaction over the whole crystal is given by

$$\vec{M}_{\perp}(\vec{Q}) = \frac{1}{Q^2}\vec{Q}\times\vec{M}^T(\vec{Q})\times\vec{Q}, \tag{3.6}$$

where $\vec{M}^T(\vec{Q})$ is the total magnetic interaction:

$$\vec{M}^T(\vec{Q}) \propto \sum_j f_j(\vec{Q}) e^{i\vec{Q}\cdot\vec{r}_j} \sum_{\vec{k}} \vec{S}_{\vec{k}j} \sum_{\vec{H}} \delta(\vec{Q}-\vec{k}-\vec{H}). \tag{3.7}$$

In this Equation 3.7, $f_j(\vec{Q})$ is the magnetic form factor for atom j i.e. the Fourier transform of the unpaired electron density, $\vec{r}_j$ is the vector to the j^{th} atom, $\vec{k}$ is the magnetic propagation vector as discussed in Section 2.5.3 and $\vec{S}_{\vec{k}j}$ are the Fourier components of the magnetic spins. Again, the inclusion of the Dirac delta function means that magnetic Bragg peaks will occur but now only when $\vec{Q} = \vec{k} + \vec{H}$. Hence, only if $\vec{k} = 0$ do these peaks combine with the ones from nuclear scattering.

As was laid out in the last chapter, the allowed values of $\vec{k}$ are determined by the magnetic structure and $\vec{k} = 0$ corresponds to the case where the magnetic moments are independent of real-space location: the magnetic structure has the same translational symmetry as the crystal lattice so it makes sense that the Bragg peaks should coincide.

3.3.4 Polarised Neutron Scattering

The scattering of a polarised beam of neutrons with a single crystal is governed by the Blume-Maleev equations [20, 21]. The most general technique using polarised neutrons is called spherical neutron polarimetry (SNP). Whereas unpolarised scattering as shown in Section 3.3.3 probes only the magnitude of the interaction vector $|\vec{M}_\perp|^2$, SNP is directly sensitive to its components. This allows a much greater level of accuracy and affords the ability to distinguish between structures which appear similar in an unpolarised study [22–24]. This has been shown in the case of FeAs, using both polarised neutron [25] and X-ray [26] scattering, and $CeRhIn_5$ [27, 28], where the structures were found to be spin density wave and helical arrangement respectively. It is also for this reason that SNP can determine complex magnetic structures as shown in the cases of $CaBa(Co_3Fe)O_7$ [29] and Mn_2GeO_4 [30].

Blume-Maleev Equations

State scattering $\left|\chi^I\right\rangle \rightarrow \left|\chi^F\right\rangle$ can be expressed as a transformation in spin-half space by the 2×2 matrix $S = N + \vec{M}_\perp \cdot \vec{\sigma}$: $\left|\chi^F\right\rangle = S\left|\chi^I\right\rangle$, where $\{\sigma_i\}$ are the Pauli matrices, N corresponds to nuclear scattering, and $\vec{M}_\perp \cdot \vec{\sigma}$ is due to magnetic scattering [20]. Scattering from nuclear spins can be discounted as these are taken to be disordered and any linear terms must average to zero.

The scattering cross-section $d\sigma$ is given by the ratio of the number of particles ($Nd\Omega$) scattered into the solid angle $d\Omega$ in angular direction (θ,ϕ) per unit time to the incident flux, ($|\vec{j}^I|$) [31]:

$$\frac{d\sigma}{d\Omega} = \frac{N}{|\vec{j}^I|}. \tag{3.8}$$

Away from the direction of the incident beam, $\hat{k}^I$, $Nd\Omega = \vec{j}^F \cdot d\vec{A}$ where $\vec{j}^F$ is the resultant flux, which is number of particles scattered into the solid angle $d\Omega$ in angular direction (θ,ϕ) per unit time per unit area. At a distance r, $d\vec{A}$ is given by $r^2\hat{r}d\Omega$ and

$$\frac{d\sigma}{d\Omega} = \frac{1}{|\vec{j}^I|}\vec{j}^F \cdot \hat{r}r^2. \tag{3.9}$$

In a reactor-based neutron experiment, the incident flux is a free particle current:

$$\vec{j}^I = \frac{\hbar\vec{k}^I}{m}. \tag{3.10}$$

$\vec{j}^F$ is derived from the Schrödinger equation [32]:

$$\vec{j} = \frac{\hbar}{m}\mathcal{I}m\Big\{\psi(\vec{r})^\dagger\vec{\nabla}\psi(\vec{r})\Big\}, \tag{3.11}$$

where $\psi(\vec{r})$ is the total wavefunction projected into real space. Given that the wavefunction is a

product of a spatial $|\phi\rangle$ and a spin part $|\chi\rangle$ i.e. $|\psi\rangle = |\phi\rangle \otimes |\chi\rangle$, the total wavefunction is a linear combination of the initial and final states

$$|\psi\rangle = \left|\phi^I\right\rangle \otimes \left|\chi^I\right\rangle + \left|\phi^F\right\rangle \otimes \left|\chi^F\right\rangle. \tag{3.12}$$

Considering the spatial part, this is projected into coordinate space by left multiplication of $\langle\vec{r}|$. Then, the initial and final parts are given according to the Born approximation:

$$\psi(\vec{r}) = \langle\vec{r}|\psi\rangle = \langle\vec{r}|\left(\left|\phi^I\right\rangle \otimes \left|\chi^I\right\rangle + \left|\phi^F\right\rangle \otimes \left|\chi^F\right\rangle\right) = e^{i\vec{k}^I\cdot\vec{r}}\left|\chi^I\right\rangle + \frac{e^{i|\vec{k}^F|r}}{r}\left|\chi^F\right\rangle. \tag{3.13}$$

Substituting this into Equation 3.11 and neglecting cross terms, which average to zero, and higher order terms in $\frac{1}{r}$,

$$\vec{j} = \frac{\hbar\vec{k}^I}{m} + \frac{\hbar|\vec{k}_F|}{m}\frac{\left\langle\chi^F\middle|\chi^F\right\rangle}{r^2}\hat{r}. \tag{3.14}$$

The first term corresponds to the initial flux $\vec{j}^I$ and, therefore, the second term must correspond to the outgoing flux $\vec{j}^F$. Substituting these expressions into Equation 3.9, the cross-section is

$$\frac{d\sigma}{d\Omega} = \frac{1}{|\frac{\hbar\vec{k}^I}{m}|}\frac{\hbar|\vec{k}^F|}{m}\frac{\left\langle\chi^F\middle|\chi^F\right\rangle}{r^2}r^2 = \left\langle\chi^F\middle|\chi^F\right\rangle = \left\langle\chi^I\middle|S^\dagger S\middle|\chi^I\right\rangle = Tr(\rho S^\dagger S), \tag{3.15}$$

where $\rho = \left|\chi^I\right\rangle\left\langle\chi^I\right|$ is the density matrix and elastic scattering dictates that $\vec{k}^I$ and $\vec{k}^F$ have equal magnitudes. This result is also expected from Fermi's golden rule.

In order to arrive at a more useful form for ρ, consider the vector space formed by 2×2 Hermitian matrices, ${\mathcal{M}_\mathcal{H}}^2$. Whilst perhaps the most familiar example of a vector space is the one that contains three dimensional Cartesian vectors, $\mathcal{R}^3$, a more rigorous definition of a vector space is: a set of elements called vectors along with two operations, 'addition' and 'scalar multiplication', that satisfy a set of axioms [33]. Whilst this is not considered here, it is trivial to show that ${\mathcal{M}_\mathcal{H}}^2$ satisfies the axioms of a vector space. As members of this space have four free components, four basis 'vectors' are needed to span this space, with the only requirement being that they are linearly independent. This can be expressed for a basis $\{v_i\}$ as

$$\sum_{i=1}^{4} c_i v_i = 0 \quad \textit{iff} \quad c_i = 0\ \forall i \tag{3.16}$$

In this context, consider a candidate basis formed by the Pauli matrices $\{\sigma_1, \sigma_2, \sigma_3\}$ and the 2×2 identity, $\sigma_0 \equiv \mathbb{I}$. This gives

$$\sum_{i=0}^{3} c_i\sigma_i = \begin{pmatrix} c_0 + c_3 & c_1 + ic_2 \\ c_1 - ic_2 & c_0 - c_3 \end{pmatrix}. \tag{3.17}$$

For the $\{\sigma_i\}$'s to be linearly independent, all elements of this matrix must be equal to zero, which results in four simultaneous equations:

$$c_0 \pm c_3 = 0, c_1 \pm ic_2 = 0, \tag{3.18}$$

which may be recast as the matrix problem

$$\begin{pmatrix} 1 & 0 & 0 & 1 \\ 0 & 1 & i & 0 \\ 0 & 1 & -i & 0 \\ 1 & 0 & 0 & -1 \end{pmatrix} \begin{pmatrix} c_0 \\ c_1 \\ c_2 \\ c3 \end{pmatrix} \equiv A\vec{c} = \begin{pmatrix} 0 \\ 0 \\ 0 \\ 0 \end{pmatrix}. \tag{3.19}$$

For $\{\sigma_i\}$ to be linearly independent, the only solution to this equation must be for $\vec{c} = 0$. An easy way to achieve this is to require that $\det|A| \neq 0$. This ensures that A is not singular and so Equation 3.19 may be left multiplied by an appropriate inverse, leaving only the desired result, $\vec{c} = 0$. In this case, $\det|A| = 4i$ and hence $\{\sigma_i\}$ forms a basis and spans the space of 2×2 Hermitian matrices.

Now, as ρ belongs to ${\mathcal{M}_{\mathcal{H}}}^2$, it can be written in the form

$$\rho = a\mathbb{I} + b_i\sigma_i \tag{3.20}$$

using Einstein summation notation. Noting the following relations for the traces of Pauli matrices

$$\begin{aligned} Tr(\sigma_i) &= 0, \\ Tr(\sigma_i\sigma_j) &= 2\delta_{ij}, \\ Tr(\sigma_i\sigma_j\sigma_k) &= 2i\varepsilon_{ijk}, \\ Tr(\sigma_i\sigma_j\sigma_k\sigma_l) &= 2(\delta_{ij}\delta_{kl} - \delta_{ik}\delta_{jl} + \delta_{il}\delta_{jk}), \end{aligned} \tag{3.21}$$

which as come a consequence of the commutator/anticommutator ($[\sigma_i, \sigma_j] \equiv \sigma_i\sigma_j - \sigma_j\sigma_i = 2i\varepsilon_{ijk}\sigma_k$ and $\{\sigma_i, \sigma_j\} \equiv \sigma_i\sigma_j + \sigma_j\sigma_i = 2\delta_{ij}\mathbb{I}$ respectively), a and b_i can be determined. Furthermore, a and b must be real as ρ is Hermitian. To determine the coefficient a, consider the trace of ρ:

$$Tr(\rho) = Tr(a\mathbb{I} + b_i\sigma_i) = aTr(\mathbb{I}) + b_iTr(\sigma_i) = aTr(\mathbb{I}) = 2a. \tag{3.22}$$

However, this can also be written using an arbitrary basis $\{|u_i\rangle\}$ as:

$$Tr(\rho) = Tr(|\chi^I\rangle\langle\chi^I|) = \langle u_i|\chi^I\rangle\langle\chi^I|u_i\rangle = \langle\chi^I|u_i\rangle\langle u_i|\chi^I\rangle = \langle\chi^I|\chi^I\rangle = 1, \tag{3.23}$$

where closure or completeness of the basis $\{|u_i\rangle\}$ ($|u_i\rangle\langle u_i| = \mathbb{I}$) was used along with the fact that $|\chi^I\rangle$ is normalised by convention. Equations 3.22 and 3.23 thus give

$$a = \frac{1}{2}. \tag{3.24}$$

The components $\{b_i\}$ may be found by considering the polarisation of the neutron beam. This is defined as an average of $\vec{\sigma}$: $P_i^I = \langle\sigma_i\rangle$. Using the density matrix to perform this average gives

$$P_i^I = \langle\sigma_i\rangle = Tr(\rho\sigma_i) = Tr([\frac{1}{2}\mathbb{I} + b_j\sigma_j]\sigma_i) = \frac{1}{2}Tr(\sigma_i) + b_j Tr(\sigma_j\sigma_i) = 2b_j\delta_{ij} = 2b_i. \tag{3.25}$$

Using the expressions for a, b, ρ can be expressed in terms of the incident polarisation:

$$\rho = \frac{1}{2}(\mathbb{I} + \vec{P}^I \cdot \vec{\sigma}). \tag{3.26}$$

This dependence of the density matrix makes sense physically. If, for example, the system is fully polarised in the 'up' direction then all the wavefunction density will be concentrated into the 'up' state. This is reflected in ρ due to the presence of $\vec{P}^I$. Similarly, if the state is unpolarised then ρ is diagonal.

An expression for the final polarisation can be constructed as an average of $\vec{\sigma}$ over the *final* spin state:

$$P_i^F = \frac{\langle\chi^F|\sigma_i|\chi^F\rangle}{\langle\chi^F|\chi^F\rangle} = \frac{Tr(\rho S^\dagger\sigma_i S)}{\frac{d\sigma}{d\Omega}}. \tag{3.27}$$

Importantly, as S is not unitary, the norm of a state is *not* conserved in the scattering process and so this average must be normalised appropriately.

By computing these traces using the properties of the Pauli matrices *viz.* Equation 3.21, the cross-section and final polarisation may be calculated. These are the Blume-Maleev equations [20, 21]

$$\frac{d\sigma}{d\Omega} = Tr(S\rho S^\dagger) = |N|^2 + |\vec{M}_\perp|^2 + N(P_i^I M_{\perp i}^*) + N^*(P_i^I M_{\perp i}) - i\varepsilon_{ijk}P_i^I(M_{\perp j}M_{\perp k}^*), \tag{3.28}$$

$$P_i^F = \frac{1}{\frac{d\sigma}{d\Omega}} Tr(S\rho S^\dagger \sigma_i) = \frac{1}{\frac{d\sigma}{d\Omega}} \left[(|N|^2 - |\vec{M}_\perp|^2)\delta_{ij} + i(N^* M_{\perp k} - N M^*_{\perp k})\varepsilon_{ijk} + M_{\perp i} M^*_{\perp j} + M_{\perp j} M^*_{\perp i} \right] P_j^I + \dots$$
$$+ \frac{1}{\frac{d\sigma}{d\Omega}} \left[N M^*_{\perp i} + N^* M_{\perp i} + i(\vec{M}_\perp \times \vec{M}^*_\perp)_i \right]$$
$$\equiv \mathsf{P}_{ij} P_j^I + P_i',$$
(3.29)

where P is the 'polarisation tensor' and contains information about how the polarisation rotates during the scattering. $\vec{P}'$ corresponds to the polarisation created during the interaction.

When a material has a non-zero propagation vector as in the case studied in this thesis, CNO, magnetic Bragg peaks occur as satellites of the nuclear ones. These will be referred to here (Figures 4.4 and 4.5) as

$$(hkl)\pm \equiv (hkl) \pm \vec{k},$$
(3.30)

For CNO, the propagation vector is $\vec{k} = (0.4876, 0.2813, 0.2029)$ and, therefore, this work considers the case where there is no nuclear contribution. This allows $N = 0$ in Equations 3.28 and 3.29.

The Polarisation Matrix

The 'polarisation matrix', with components $\tilde{\mathsf{P}}_{ij}$, is defined as the ratio of scattered polarisation in the jth direction to an incident polarisation which is in the ith direction. It is conventional to use the so-called 'standard' co-ordinates with $x \parallel$ to the scattering vector $\vec{Q}$, z vertical and y completing a right-handed co-ordinate system. $\tilde{\mathsf{P}}$ can be defined using Equations 3.28 and 3.29 as

$$\tilde{\mathsf{P}}_{ij} = \left\langle \frac{\mathsf{P}_{jk} P_k^I + P_j'}{P_i^I} \right\rangle,$$
(3.31)

where the angled brackets indicate an average over domains. It is important to also note that the cross-section contained within P and $\vec{P}'$ must also be averaged over domains [34]. However, if an initial beam is assumed to be polarised along one axis, Equation 3.31 can be rewritten with *no* Einstein convention as:

$$\tilde{\mathsf{P}}_{ij} = \left\langle \mathsf{P}_{ji} + P_j' \right\rangle.$$
(3.32)

Now, it is useful to consider $\frac{d\sigma}{d\Omega}$, P and $\vec{P}'$ in the 'standard' co-ordinates only as, in this basis, the x component of $\vec{M}_\perp$ is *always* zero [34]:

$$\frac{d\sigma}{d\Omega} = |\vec{M}_\perp|^2 + 2P_x^I \mathcal{I}m\{M_{\perp y}M_{\perp z}^*\}, \tag{3.33}$$

$$\mathsf{P} = \frac{1}{\frac{d\sigma}{d\Omega}} \begin{pmatrix} -|\vec{M}_\perp|^2 & 0 & 0 \\ 0 & |M_{\perp y}|^2 - |M_{\perp z}|^2 & 2\mathcal{R}e\{M_{\perp y}M_{\perp z}^*\} \\ 0 & 2\mathcal{R}e\{M_{\perp y}M_{\perp z}^*\} & |M_{\perp z}|^2 - |M_{\perp y}|^2 \end{pmatrix}, \tag{3.34}$$

$$\vec{P}' = \frac{1}{\frac{d\sigma}{d\Omega}} \begin{pmatrix} -2\mathcal{I}m\{M_{\perp y}M_{\perp z}^*\} \\ 0 \\ 0 \end{pmatrix}. \tag{3.35}$$

Substituting these expression into Equation 3.32 for a single domain structure gives

$$\tilde{\mathsf{P}} = \frac{1}{|\vec{M}_\perp|^2} \begin{pmatrix} -|\vec{M}_\perp|^2 & 0 & 0 \\ A & B & C \\ A & C & -B \end{pmatrix}, \tag{3.36}$$

where $A = -2\mathcal{I}m\{M_{\perp y}M_{\perp z}^*\}$, $B = |M_{\perp y}|^2 - |M_{\perp z}|^2$ and $C = 2\mathcal{R}e\{M_{\perp y}M_{\perp z}^*\}$.

There are two key points to note about this matrix for the purposes of the analysis contained within this thesis. Firstly, $\tilde{\mathsf{P}}_{xx} \equiv -1$ is required for magnetic scattering. Secondly, $\tilde{\mathsf{P}}_{xy} = \tilde{\mathsf{P}}_{xz} \equiv 0$. This point will be discussed in Chapter 4 in the context of the measured matrix elements of CNO which motivated an analysis of the errors in SNP.

Naturally, this expression must be averaged over all domains if present. If the structure is chiral, it may have multiple domains of opposite chirality, with each domain polarising the beam in the opposite way due to the opposing handednesses. This has the results that $\tilde{\mathsf{P}}_{yx}$ and $\tilde{\mathsf{P}}_{zx}$ will cancel out under equal chiral domains. This can also be seen mathematically because these two terms are resultant from a cross-product which is odd under a chiral inversion. Practically, this effect can be offset by, for example, cooling under an electric field to offset the domain population [35].

SNP Example

In order to briefly show the power of SNP, consider an example using a simple magnetic structure adapted from Brown [34]. Consider the tetragonal structure illustrated in Figure 3.1 with magnetic moments in the *a*-*b* plane. Now suppose that this structure magnetically orders along the *c* axis with propagation vector $(0,0,1/2)$. This can occur in two ways:

1. The magnetic structure preserves the four-fold rotational symmetry and so remains tetragonal. In this case the magnetic moments are aligned along $\langle 110 \rangle$, illustrated in Figure 3.1 as structure (1).

2. The magnetic structure breaks the four-fold rotational symmetry, becoming orthorhombic. In this case the magnetic moments are aligned along either $\pm[100]$ or $\pm[010]$ illustrated in Figure 3.1 as structures (2) and (3) respectively. As these structures derive from spontaneous breaking of the four-fold axis, a mixture of structures (2) and (3) will occur.

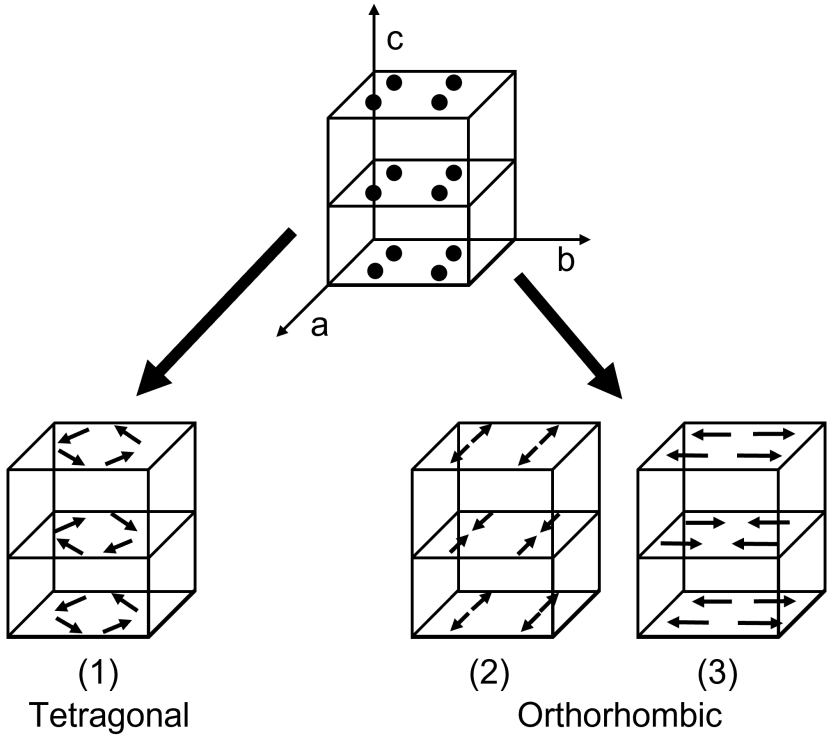

Figure 3.1: A simple tetragonal model. Upon magnetically ordering, it can form any of the three structures shown below.

Now, the unpolarised neutron interaction ($\propto |\vec{M}_\perp|^2$) can be calculated to find

$$|\vec{M}_\perp|^2_{(1)} \propto 1 + \sin^2\phi, \tag{3.37}$$

$$|\vec{M}_\perp|^2_{(2)} \propto 1, \tag{3.38}$$

$$|\vec{M}_\perp|^2_{(3)} \propto \sin^2\phi, \tag{3.39}$$

where ϕ is the angle between the $\vec{Q}$ and the direction $[010]$ and the constant of proportionality is dependent on the magnetic moment length. In this case, a scattering experiment cannot distinguish between structure (1) and an equal mixture of structures (2) and (3). However, now consider the polarisation matrix for the three structures

$$\tilde{\mathsf{P}}_{(1)} = \begin{pmatrix} -1 & 0 & 0 \\ 0 & \frac{\sin^2\phi - 1}{1+\sin^2\phi} & \frac{2\sin\phi}{1+\sin^2\phi} \\ 0 & \frac{2\sin\phi}{1+\sin^2\phi} & \frac{1-\sin^2\phi}{1+\sin^2\phi} \end{pmatrix}, \tag{3.40}$$

$$\tilde{\mathsf{P}}_{(2)} = \begin{pmatrix} -1 & 0 & 0 \\ 0 & -1 & 0 \\ 0 & 0 & 1 \end{pmatrix}, \tag{3.41}$$

$$\tilde{\mathsf{P}}_{(3)} = \begin{pmatrix} -1 & 0 & 0 \\ 0 & 1 & 0 \\ 0 & 0 & -1 \end{pmatrix}. \tag{3.42}$$

The two cases are now easily distinguished by the off-diagonal matrix elements $\tilde{\mathsf{P}}_{yz}$ and $\tilde{\mathsf{P}}_{zy}$. However, these are only dependent on the angle ϕ and so are no longer sensitive to the lengths of the moments, only their directions.

Experimental Realisation

Experimentally, all components of the polarisation matrix can be directly measured using CRYOPAD (Cryogenic Polarisation Analysis Device), Figure 3.2 [36], a method of performing SNP. It consists of a cryostat surrounded by two cylindrical Meissner shields with superconducting coils in between. The Meissner shields ensure the sample space is field free. The coils, along with incoming and outgoing nutators, allow the polarisation vector of the neutron beam to be orientated in any direction. The up-down orientation of the scattered neutron beam is measured using a ^{3}He detector [34]. In this way, the number of neutrons aligned with or against the desired measurement axis, j, $n_j^{(+)}$ and $n_j^{(-)}$ respectively, can be measured for any given initial polarisation direction, i. This gives a means of connecting the intensity with the polarisation matrix

$$\tilde{\mathsf{P}}_{ij} = \frac{n_j^{(+)} - n_j^{(-)}}{n_j^{(+)} + n_j^{(-)}}, \tag{3.43}$$

where it is assumed that the initial beam is fully polarised. This relation provides a direct link between the measured intensity and the polarisation matrix elements. Throughout the rest of this thesis, only the matrix elements $\tilde{\mathsf{P}}_{ij}$ will be used.

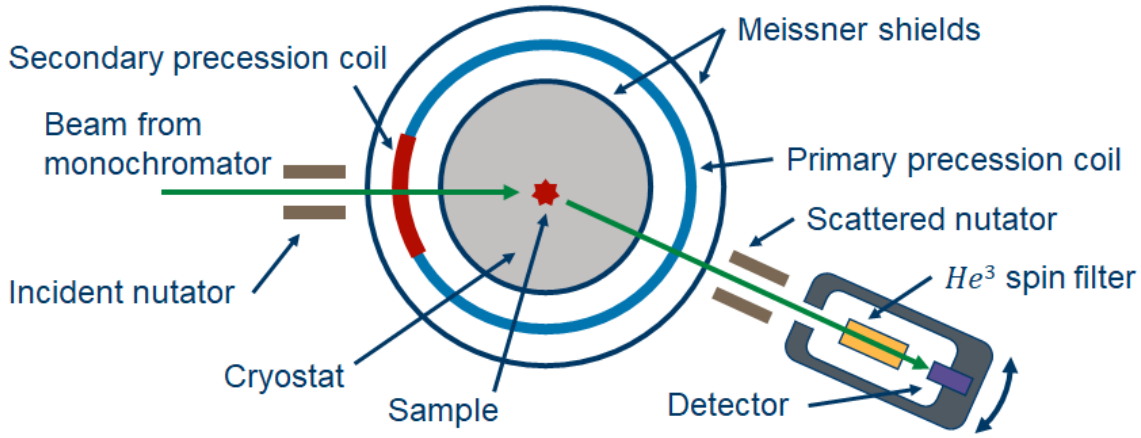

Figure 3.2: The experimental setup of CRYOPAD.

3.4 Muon Techniques

Muon techniques form the basis of Chapters 5 and 6 and are used to study the behaviour of relaxor-ferroelectric samples. In this work both negative and positive muons, μ^- and μ^+, were used to characterise various dielectric oxides non-destructively. Muon science is typically used to study magnetism in materials. The muon possesses a large magnetic moment which means that it is very sensitive to magnetic fields down to $\approx 10^{-5}$ T [37] and has been used to characterise many systems [38].

Another advantage of the muon is that it is a local probe. Unlike the Bragg scattering of neutrons which requires long-range correlations, the muon only interacts with the implantation site. This means that it is uniquely able to probe short-range order or disordered/random magnetic structures [39]. It also has the advantage that a single crystal sample is not always essential and this allows muon experiments to provide information about magnetic order where conventional magnetic neutron diffraction cannot be simply performed, i.e. in a powder sample.

3.4.1 Muon Sources

One source of muons is from cosmic rays in the upper atmosphere. These are generated with an energy of ≈ 4 GeV which corresponds to a long stopping range of about 20 m [40]. This, combined with their low flux and lack of beam polarisation, means cosmic muons are not suitable for probing condensed matter systems. However, they have been used for larger scale tomographic studies [40].

In terms of experimental muons, there are five muon facilities around the world and, as with neutrons, these work by one of two methods. In a 'continuous' source (e.g. PSI, Villigen, Switzerland) muons are produced one-by-one in a cyclotron whereas a 'pulsed' source (e.g. ISIS, STFC Rutherford Appleton Laboratory, Didcot, UK) uses the same setup as a spallation neutron source. However, in this case the target is made from graphite [41]. At ISIS, muons are

produced by the interaction of the accelerated proton beam with this target, consuming approximately 5% of the proton beam. The interaction of the accelerated proton with either a proton or neutron in the target produces a charged pion, albeit of different charges:

$$p^+ + p^+ \rightarrow p^+ + n + \pi^+, \tag{3.44}$$

$$p^+ + n \rightarrow p^+ + p^+ + \pi^-, \tag{3.45}$$

where p^+ refers to a proton, n a neutron and $\pi^\pm$ a pion. The pion is a meson and so consists of two quarks: an up quark and an anti-down quark (π^+) or a down quark and an anti-up quark (π^-). Hence, the π^+ and π^- are antiparticles of one another. Pions have a mass of 139.6 MeV/c^2 and a mean lifetime of 2.603×10^{-8} s.

The main decay channel, probability $\approx$ 99.99%, of charged pions is to a muon ($\mu^\pm$) and muon neutrino (ν_μ)/antineutrino ($\bar{\nu}_\mu$) via the electroweak interaction [42]:

$$\pi^+ \rightarrow \mu^+ + \nu_\mu, \tag{3.46}$$

$$\pi^- \rightarrow \mu^- + \bar{\nu}_\mu. \tag{3.47}$$

Depending on the energy of the pion when it decays, it can produce either 'surface' or 'decay' muons. The former are from pions that form at rest i.e on the *surface* of the target, and are only capable of producing μ^+ due to the re-capture of μ^-, whilst the latter form from pions that *decay* in the beamline and can produce both μ^+ and μ^- [43].

In this thesis, experiments were carried out at the RIKEN-RAL facility, ISIS so a brief overview of the facility is given:

Each spill from the accelerator produces two pulses of charged pions, separated by 320 ns, with each pulse having FWHM of 70 ns [43]. These pions then decay into muons which can be used for experiments. Whereas the other beamlines at ISIS operate at a fixed momentum of 28 MeV/c, the RIKEN-RAL beamline illustrated in Figure 3.3(a) contains an array of magnets which allows the momentum of the muon beam to be tuned to experimental need. The muon intensity as a function of momentum is shown in Figure 3.3(b). These magnets also enable pions to be extracted from the muon target and thus allow the formation of decay muons. Hence, the RIKEN-RAL beamline is capable of production of both μ^+ and μ^- at a range of momenta [43]. Given that the key advantage of muon techniques is that they are local probes, varying the momentum of the muon beam allows the implantation depth to be controlled and thus provides depth dependent analysis. The resolution of implantation depths is typically $\sim$ 10 μm although this can vary with momentum and so should be calculated through simulation for each experiment. This point will be addressed further in Chapter 5 where details of such simulations are given.

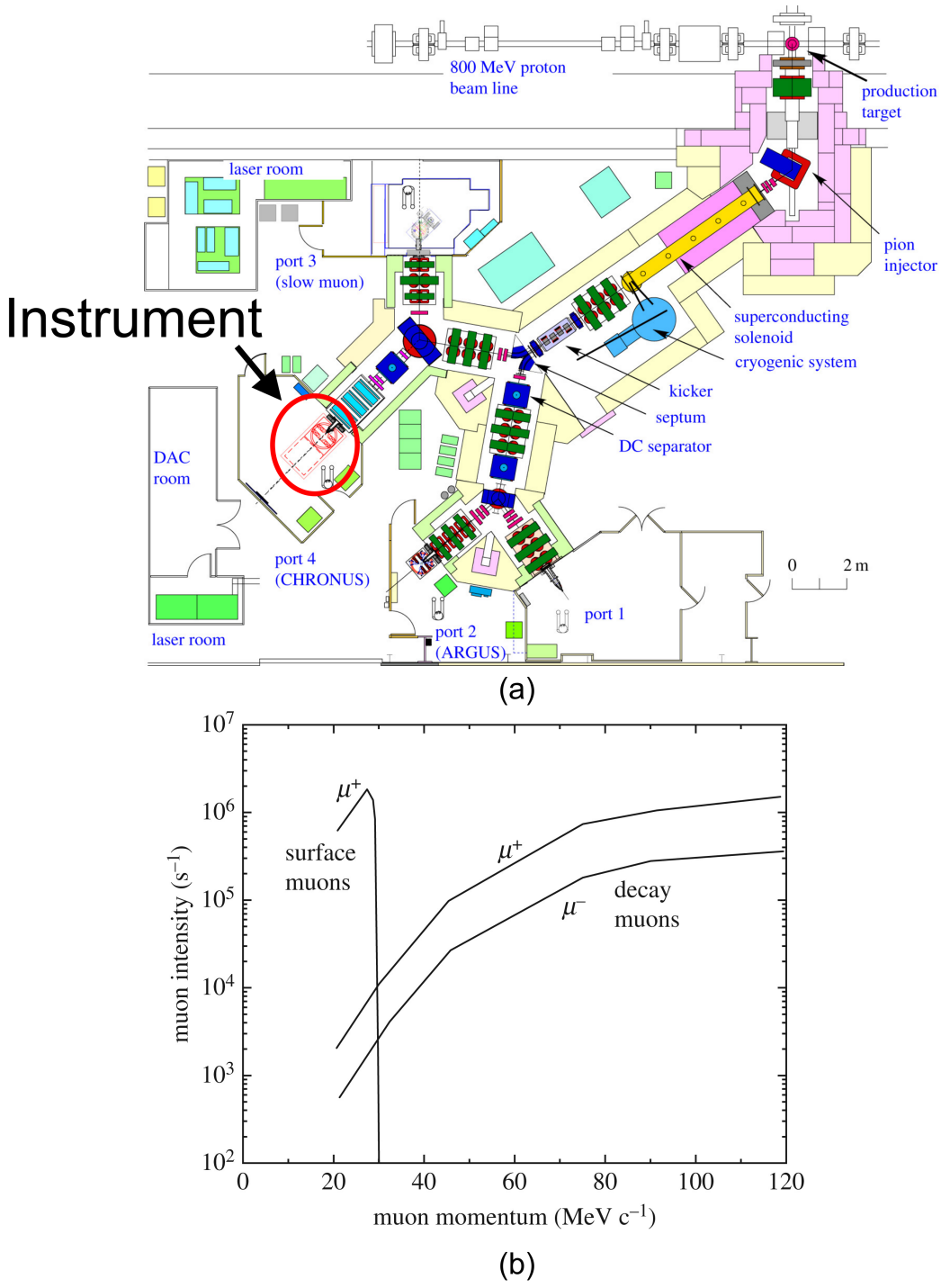

Figure 3.3: (a) The RIKEN-RAL facility at ISIS, Didcot, UK. All experiments in this thesis were carried out on Port 4/CHRONUS. (b) The muon intensity as a function of momentum on the RIKEN-RAL beamlines. Republished with permission of The Royal Society (U.K.), from A. D. Hillier *et al.*, "Muons at isis," *Philos. Trans. R. Soc. A.*, vol. 377, no. 2137, p. 20 180 064, 2019; permission conveyed through Copyright Clearance Center, Inc.

3.4.2 Compositional Analysis (μ^-)

The μ^- technique provides a method to analyse the composition of a material in a non-destructive way. In this technique [44], μ^-s are implanted into the sample where they interact locally with an ionic site. After muon capture onto the valence band, the μ^- cascades down the modified atomic orbitals, emitting a characteristic X-ray spectrum which allows the ionic site to be identified. This process is illustrated in Figure 3.4. Due to the larger mass of the μ^- (105.7 MeV/c^2), these muonic X-rays show less re-absorption by the material than if this experiment were carried out with electrons (0.5110 MeV/c^2). Furthermore, varying the momentum of the muon beam allows the implantation depth to be controlled, thus providing a method for depth dependent, non-destructive elemental analysis.

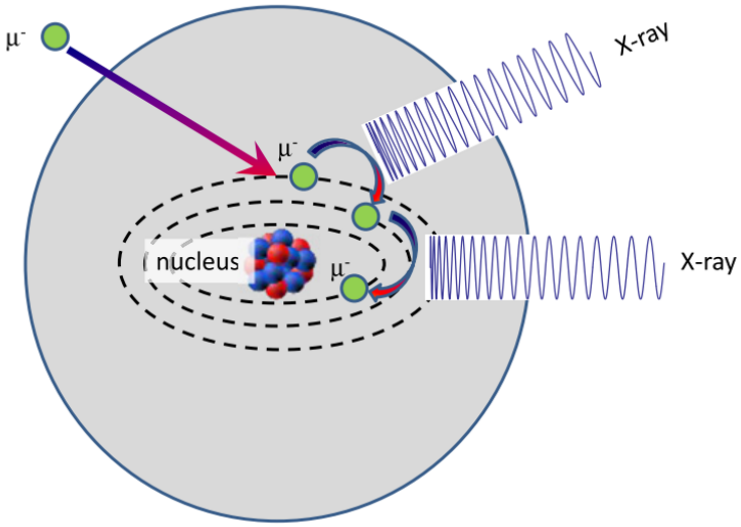

Figure 3.4: Illustration of the μ^- compositional analysis technique. Reprinted from A. D. Hillier *et al.*, "Probing beneath the surface without a scratch - bulk non-destructive elemental analysis using negative muons," *Microchem. J.*, vol. 125, p. 203, 2016, Copyright (2016), with permission from Elsevier.

The experimental setup consists of four Ge based ORTEC (Oak Ridge, TN, US) X-ray detectors, two upstream and two downstream, placed on a flat surface with the sample held in the centre. The four detectors are split into two pairs, low and high energy, with detection ranges of 3 keV - 1 MeV and 3 keV - 8 MeV respectively. One of each pair was placed upstream and downstream of the sample to increase the amount of solid angle covered. The four detectors are labelled in Figure 3.5. The details of the individual samples used in this thesis will be discussed in the relevant chapters but, in both experiments, these samples were held in an Al foil packet and suspended into the beam as illustrated in Figure 3.5. Due to the penetration depths required in this work, the incident muons have enough momentum to pass through the Al packet.

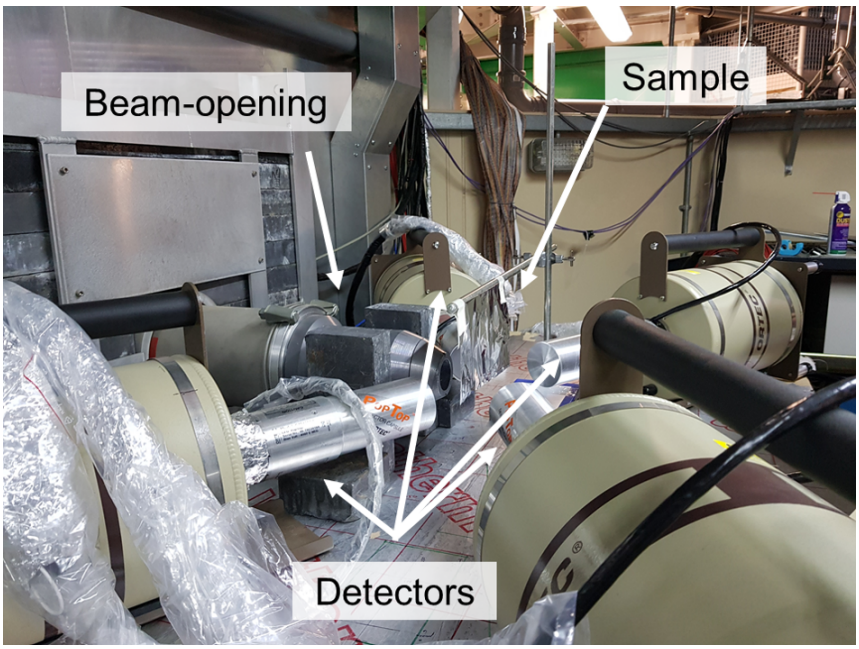

Figure 3.5: The experimental setup for μ^- experiments at ISIS.

3.4.3 Muon Spin Relaxation (μ^+)

Muon spin relaxation (μSR) is used to probe internal magnetic structures. It uses a polarised μ^+ beam which will show spin precession under a magnetic field. Upon generation, the muon beam at ISIS is polarised due to the parity-violating electroweak pion decay process. Furthermore, when the μ^+ subsequently decays into a positron, e^+, it is preferentially emitted along the direction of the spin, again due to an electroweak interaction. As the spin of a μ^+ will precess under the influence of a magnetic field, by detecting the angle of emission of the e^+, the precession can be measured. As the precession frequency is directly proportional to the field strength, this measurement can be used to determine the magnetic field at the site of muon implantation. The incident polarisation direction of the muon is known due to the polarised beam. This is illustrated in Figure 3.6

In a μSR experiment, the measured quantity, known as the asymmetry, A, is the normalised difference between the number of e^+ detected in the forward, F, and backwards, B, directions

$$A = \frac{F - \alpha B}{F + \alpha B}, \tag{3.48}$$

where the parameter α corrects for the difference in efficiency between the two detectors. This removes the characteristic decay curve of the muons which would otherwise be superimposed on the data. In this way, the asymmetry measures the polarisation of the muon beam and so allows the internal magnetic fields to be probed.

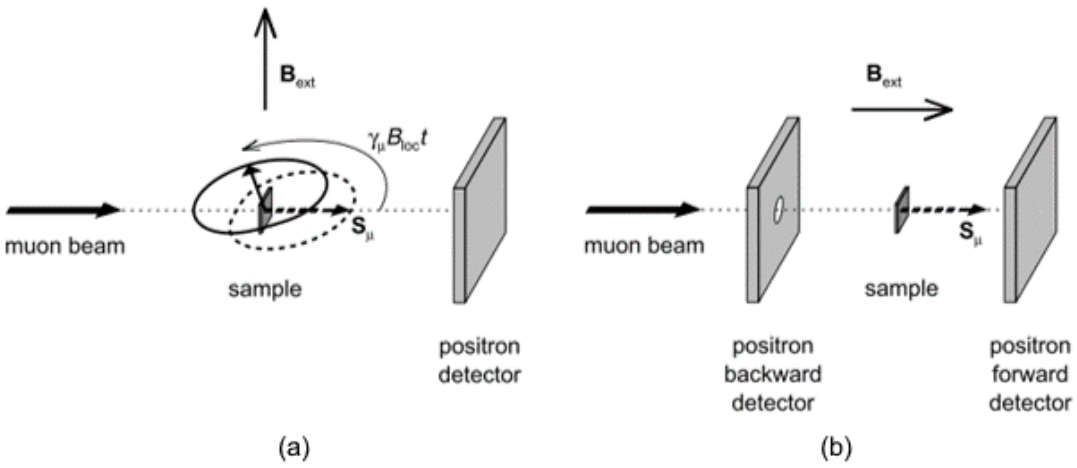

Figure 3.6: Illustration of the two μSR setups used in this thesis. (a) shows transverse field (TF) setup where the applied magnetic field is perpendicular to the initial muon spin polarisation. (b) shows longitudinal field (LF) setup where the applied magnetic field is aligned with the initial muon spin polarisation. This is also used for zero field (ZF) measurements. Republished with permission of IOP Publishing, Ltd., from P. Dalmas de Réotier *et al.*, "Muon spin rotation and relaxation in magnetic materials," *J. Phys.: Condens. Matter*, vol. 9, p. 9113, 1997; permission conveyed through Copyright Clearance Center, Inc.

References

[1] C. P. Burgess and G. D. Moore, *The Standard Model: A Primer*. Cambidge University Press, 2007, ch. 2, ISBN: 978-0-511-25485-7.

[2] J. Schwichtenberg, *Physics from Symmetry*, 2nd. Springer, 2018, ISBN: 978-3-319-66631-0.

[3] M. Robinson, *Symmetry and the Standard Model*. Springer, 2015, ch. 2, ISBN: 978-1-4419-8267-4.

[4] A. Quadt, *Top Quark Physics at Hadron Colliders*. Springer, 2007, ISBN: 978-3-540-71060-8.

[5] C. P. Burgess and G. D. Moore, *The Standard Model: A Primer*. Cambidge University Press, 2007, ch. 10, ISBN: 978-0-511-25485-7.

[6] C. G. Shull, "Early development of neutron scattering," in *Nobel Lectures, Physics 1991-1995*, Accessed online at `https://www.nobelprize.org/nobel_prizes/physics/laureates/1994/shull-lecture.html`. Accessed 16th April 2018, Singapore: World Scientific Publishing Co., 1997.

[7] J. Chadwick, "Possible existence of a neutron," *Nature*, vol. 129, p. 312, 1932. DOI: `10.1038/129312a0`.

[8] G. Shirane, S. Shapiro, and J. Tranquada, *Neutron Scattering with a Triple-Axis Spectrometer*. Cambridge University Press, 2004, ISBN: 9780511534881.

[9] Institut Laue-Langevin, *Technical Characteristics*, Accessed online at `https://www.ill.eu/reactor-and-safety/high-flux-reactor/technical-characteristics/`. Accessed 12th November 2021.

[10] G. Shirane, S. Shapiro, and J. Tranquada, *Neutron Scattering with a Triple-Axis Spectrometer*. Cambridge University Press, 2004, ch. 2, ISBN: 9780511534881.

[11] G. L. Squires, *Introduction to the Theory of Thermal Neutron Scattering*. Dover Publications Inc., 1978, ch. 2, ISBN: 0-486-69447-X.

[12] R. Loudon, *The Quantum Theory of Light*, 2nd. Oxford University Press, 1983, ch. 3, ISBN: 0-19-851155-8.

[13] R. Loudon, *The Quantum Theory of Light*, 2nd. Oxford University Press, 1983, ch. 4, ISBN: 0-19-851155-8.

[14] G. L. Squires, *Introduction to the Theory of Thermal Neutron Scattering*. Dover Publications Inc., 1978, ch. 2, ISBN: 0-486-69447-X.

[15] A. T. Boothroyd, *Principles of Neutron Scattering from Condensed Matter*. Oxford University Press, 2020, ch. 1, ISBN: 978-0-19-886231-4.

[16] S. W. Lovesey, *Theory of neutron scattering from condensed matter*. Oxford University Press, 1984, vol. 1, ch. 3, ISBN: 0-19-852015-8.

[17] D. S. Sivia, *Elementary Scattering Theory for X-Ray and Neutron Users*. Oxford University Press, 2011, ch. 3, ISBN: 978-0-19-922868-3.

[18] D. S. Sivia, *Elementary Scattering Theory for X-Ray and Neutron Users*. Oxford University Press, 2011, ch. 8, ISBN: 978-0-19-922868-3.

[19] C. Kittel, *Introduction to Solid State Physics*, 8th. John Wiley & Sons, Inc., 2005, ISBN: 0-471-41526-X.

[20] M. Blume, "Polarization effects in the magnetic elastic scattering of slow neutrons," *Phys. Rev.*, vol. 130, pp. 1670–1676, 5 1963. DOI: `10.1103/PhysRev.130.1670`.

[21] S. V. Maleev, V. G. Baryaktar, and R. A. Suris, *Sov. Phys. Solid State*, vol. 4, p. 2533, 1 1963.

[22] P. J. Brown, V. Nunez, F. Tasset, J. B. Forsyth, and P. Radhakrishna, "Determination of the magnetic structure of Mn_3Sn using generalized neutron polarization analysis," *J. Condens. Matter Phys.*, vol. 2, no. 47, pp. 9409–9422, 1990. DOI: `10.1088/0953-8984/2/47/015`.

[23] T. Chattopadhyay, P. Burlet, and P. J. Brown, "Magnetic structure of MnS_2: Single-k or multiple-k, collinear or helical spin density wave?" *J. Condens. Matter Phys.*, vol. 3, no. 29, pp. 5555–5561, 1991. DOI: 10.1088/0953-8984/3/29/009.

[24] P. J. Brown, J. B. Forsyth, E. Lelièvre-Berna, and F. Tasset, "Determination of the magnetization distribution in Cr_2O_3 using spherical neutron polarimetry," *J. Condens. Matter Phys.*, vol. 14, no. 8, pp. 1957–1966, 2002. DOI: 10.1088/0953-8984/14/8/323.

[25] E. E. Rodriguez *et al.*, "Noncollinear spin-density-wave antiferromagnetism in FeAs," *Phys. Rev. B*, vol. 83, p. 134 438, 13 2011. DOI: 10.1103/PhysRevB.83.134438.

[26] T. Frawley *et al.*, "Elucidation of the helical spin structure of FeAs," *Phys. Rev. B*, vol. 95, p. 064 424, 6 2017. DOI: 10.1103/PhysRevB.95.064424.

[27] C. Stock, J. A. Rodriguez-Rivera, K. Schmalzl, E. E. Rodriguez, A. Stunault, and C. Petrovic, "Single to multiquasiparticle excitations in the itinerant helical magnet $CeRhIn_5$," *Phys. Rev. Lett.*, vol. 114, p. 247 005, 24 2015. DOI: 10.1103/PhysRevLett.114.247005.

[28] D. M. Fobes *et al.*, "Low temperature magnetic structure of $CeRhIn_5$ by neutron diffraction on absorption-optimized samples," *J. Condens. Matter Phys.*, vol. 29, no. 17, 17LT01, 2017. DOI: 10.1088/1361-648x/aa6696.

[29] N. Qureshi, M. T. Fernández Díaz, L. C. Chapon, A. Senyshyn, W. Schweika, and W. Valldor, "Magnetic structure of the swedenborgite $CaBa(Co_3Fe)O_7$ derived by unpolarized neutron diffraction and spherical neutron polarimetry," *Phys. Rev. B*, vol. 97, p. 064 404, 6 2018. DOI: 10.1103/PhysRevB.97.064404.

[30] T. Honda *et al.*, "Coupled multiferroic domain switching in the canted conical spin spiral system Mn_2GeO_4," *Nat. Commun*, vol. 8, no. 1, p. 15 457, 2017. DOI: 10.1038/ncomms15457.

[31] L. D. Landau and E. M. Lifshitz, *Quantum Mechanics: Non- Relativistic Theory*, 2nd. Pergamon, 1965, ch. 17, ISBN: 978-0080291406.

[32] L. D. Landau and E. M. Lifshitz, *Quantum Mechanics: Non- Relativistic Theory*, 2nd. Pergamon, 1965, ch. 3, ISBN: 978-0080291406.

[33] L. Smith, *Linear Algebra*, 3rd ed. Springer-Verlag New York, 1998, ch. 2, ISBN: 978-1-4612-1670-4.

[34] P. J. Brown, "Spherical neutron polarimetry," in *Neutron Scattering from Magnetic Materials*, T. Chatterji, Ed., Elsevier Science, 2006, ch. 5, pp. 215–244, ISBN: 978-0-444-51050-1.

[35] J. A. Rodríguez-Velamazán, O. Fabelo, J. Campo, J. Rodríguez-Carvajal, N. Qureshi, and L. C. Chapon, "Switching of the chiral magnetic domains in the hybrid molecular/inorganic multiferroic $(ND_4)_2[FeCl_5(D_2O)]$," *Sci. Rep.*, vol. 8, no. 1, p. 10 665, 2018. DOI: 10.1038/s41598-018-28883-z.

[36] F. Tasset *et al.*, "Spherical neutron polarimetry with cryopad-ii," *Phys. B: Condens. Matter*, vol. 267-268, pp. 69–74, 1999. DOI: 10.1016/S0921-4526(99)00029-0.

[37] S. J. Blundell, "Spin-polarized muons in condensed matter physics," *Contemp. Phys.*, vol. 40, p. 175, 1999. DOI: 10.1080/001075199181521.

[38] P. Dalmas de Réotier and A. Yaouanc, "Muon spin rotation and relaxation in magnetic materials," *J. Phys.: Condens. Matter*, vol. 9, p. 9113, 1997. DOI: 10.1088/0953-8984/9/43/002.

[39] J. Y. Ueumura, "Probing spin glasses with zero-field μSR," *Hyperfine Interact.*, vol. 8, p. 739, 1981. DOI: 10.1007/BF01037554.

[40] G. Bonomi, P. Checchia, M. D'Errico, D. Pagano, and G. Saracino, "Applications of cosmic-ray muons," *Prog. Part. Nucl. Phys.*, vol. 112, p. 103 768, 2020. DOI: 10.1016/j.ppnp.2020.103768.

[41] G. H. Eaton *et al.*, "Commissioning of the rutherford appleton laboratory pulsed muon facility," *Nucl. Instrum. Methods Phys. Res. A*, vol. 269, p. 483, 1988. DOI: 10.1016/0168-9002(88)90124-6.

[42] C. P. Burgess and G. D. Moore, *The Standard Model: A Primer*. Cambidge University Press, 2007, ch. 5, ISBN: 978-0-511-25485-7.

[43] A. D. Hillier, J. S. Lord, K. Ishida, and C. Rogers, "Muons at isis," *Philos. Trans. R. Soc. A.*, vol. 377, no. 2137, p. 20 180 064, 2019. DOI: 10.1098/rsta.2018.0064.

[44] A. D. Hillier, D. M. Paul, and K. Ishida, "Probing beneath the surface without a scratch - bulk non-destructive elemental analysis using negative muons," *Microchem. J.*, vol. 125, p. 203, 2016. DOI: 10.1016/j.microc.2015.11.031.

Chapter 4

$Cu_3Nb_2O_8$

This chapter starts the presentation of results in this thesis. After putting the topic of material characterisation in context with regards to device applications, analysis of the multiferroic $Cu_3Nb_2O_8$ is presented. Its magnetic ground state is determined by polarised neutron scattering in order to provide clarity into the mechanism by which ferroelectricty arises as well as addressing an issue in the literature regarding the transition between ordered and disordered phases.

4.1 Chapter Introduction

Choosing the correct material is a key step in any device design process. Furthermore, accurate and reliable characterisation of the internal mechanisms of the materials allows the designer to make a much more informed decision. In this way, if the behaviour of the material understood can be understood at a fundamental level, this ultimately leads the way for new and innovative devices.

A real-world example of this process is the development of piezoelectric devices. These typically use ferroelectric materials and the introduction of new materials, such as relaxor-ferroelectric single crystals, has been shown to be capable of extending their use to novel applications. Typically, the characterisation of ferroelectric materials may be split into two parts:

Functional Characterisation

Functional characterisation of piezoelectric materials is a topic that has been in continual development over the past century. This is where the EPD matrix and other functional parameters such as k^2 are determined. The first document to collate equations, definition, and methods was the IRE piezoelectric standard in 1961 [1]. The method used here was the so-called 'resonance method' which uses the electrical impedance at resonance of known sample geometries, along with Mason's equivalent circuit model, to determine the full EPD matrix [2]. The latest version of this document is the 1987 IEEE standard which, whilst still citable, is no longer maintained [3].

However, this method was developed for materials with high energy conversion and Q_m, failing when the resonance is weak. It also uses multiple samples to determine all material properties. Whilst this is appropriate for mass-produced piezoceramics, the growth methods of single crystals make sample-to-sample variations almost impossible to avoid. This means that this 'standard' method, when applied to crystal materials, leads to a lack of self-consistency in the measured EPD matrix. With the rise of simulation, e.g. using finite element analysis (FEA), allowing virtual prototyping, self-consistent and accurate material properties are necessarily essential to obtain accurate results. Furthermore, the use of complex material properties to address material losses is not covered in these characterisation methods or many FEA packages, with more phenomenological approaches being taken.

Self-consistent and widely applicable functional characterisation is improving with more numerical methods being developed [4–8]. This includes the inclusion of complex material properties, reduction of sample numbers and iterative approaches. However, some of these come at the cost of more difficult measurement methodologies and, until recently, the problem of self-consistency remained. This is now being addressed though the development of 'inverse impedance spectroscopy' methods where roughly measured material properties, determined from wave velocities measured through ultrasonic time of flight measurement, are refined through a FEA simulation suite to match to a measured impedance curves [9, 10]. This method has shown to be effective at accurately determining the full EPD matrix from a single sample for both ceramic and single crystal samples [11, 12]. Furthermore, with the development of AI and machine learning, this method shows great promise.

Fundamental Characterisation

Where functional characterisation may be seen as concerned with determining 'useful' properties, fundamental characterisation is about the determination of material behaviour and mechanisms at a more microscopic level. For example, a device designer needs little knowledge of the microstructure of a piezoelectric material to adequately design a transducer which uses that material. However, it is also true to say that a good knowledge of fundamental behaviour will allow that designer to fully exploit their chosen material.

As fundamental characterisation probes deeper into the structure of the material, more elaborate methods are required. This includes but is not limited to the use of sub-atomic probes such as X-rays, neutrons and muons which interact at the correct length-scales to probe the atomic level of materials [13]. Furthermore, electron diffraction methods may also be used to study crystal structure and techniques such as 'electron energy loss spectroscopy' can be used to investigate composition. Electron microscopy can reveal structure on a range of length-scales including both the surfaces of samples, through scanning electron microscopy, and the bulk, through transmission electron microscopy [14]. Whilst these measurements are still sensitive to the 'useful' properties of functional characterisation such as elastic constants, they can be used

to investigate the microscopic mechanisms of the material.

This and the next two chapters present three studies in fundamental characterisation of ferroelectrics and multiferroics. It will be shown that the inclusion of multiple competing orders is capable of introducing novel mechanisms which may eventually allow device designers to exploit these materials in ways which suit a wide range of applications.

4.1.1 $Cu_3Nb_2O_8$

$Cu_3Nb_2O_8$ (CNO) has room temperature space group symmetry $P\bar{1}$ consisting of a primitive triclinic lattice which possesses a single inversion centre. It experiences two phase transitions at low temperatures magnetically ordering at $T_N \approx 26.5$ K with incommensurate propagation vector $\vec{k} = (0.4876, 0.2813, 0.2029)$ and developing an electric polarisation along the real space direction $[1,3,2]$ below $T_2 \approx 24$ K [15]. These two phases will be referred to as the MT and LT phases respectively. As the system possesses only two symmetry elements, it is easy to assign their breaking with the two transitions. The upper transition corresponds to the loss of time reversal symmetry (TRS) characterised by the onset of magnetic diffraction peaks. The lower transition reflects the breaking of the inversion centre, $P\bar{1} \rightarrow P1$, which allows both a chiral structure, as reported by Johnson *et al.*, and the emergence of the electric polarisation, following Neumann's principle. This is shown in Figure 4.1.

The nuclear structure as reported by Johnson *et al.* is shown in Figure 4.2. The two Cu sites are labelled using Wyckoff notation as 1*a* and 2*i*. Wyckoff special positions denote points which are left invariant by the application of the identity and at least one other symmetry operator. In this case 2*i* corresponds to a position which is invariant under the inversion centre and 1*a* denotes the origin. The 1*a* site has square-planar oxygen coordination while the 2*i* has a square-pyramidal coordination. The structure can be thought of as layers of Cu separated by layers of Nb along the *b* axis and the Cu sites form saw-tooth chains along the *a* axis. Whilst not a perovskite, CNO still provides an interesting study of a complex multiferroic and is able to shed light upon coupling in other materials.

Johnson *et al.* reported that the low temperature phase is generically helicoidal with all spins rotating in a common plane and the 1*a* site wholly out of phase with the two 2*i* sites which are slightly out of phase with each other. The term generic helicoid is used as an intermediary between the cases of a cycloid, where the propagation vector is contained within the rotation plane, and a helix, where the propagation vector is perpendicular to the rotation plane.

The low temperature dielectric polarisation observed in CNO is reported to be almost perpendicular to the rotation plane [15]. This is incompatible with the KNB model where this polarisation is required to be contained within the rotation plane of the spins [18]. In order to circumvent this, Johnson *et al.* proposed the phenomenological 'ferro-axial' model which couples the polarisation through a chiral term to a macroscopic axial vector, as allowed in certain crystals classes by symmetry. In $P\bar{1}$, there is no specified direction of this axial vector and so

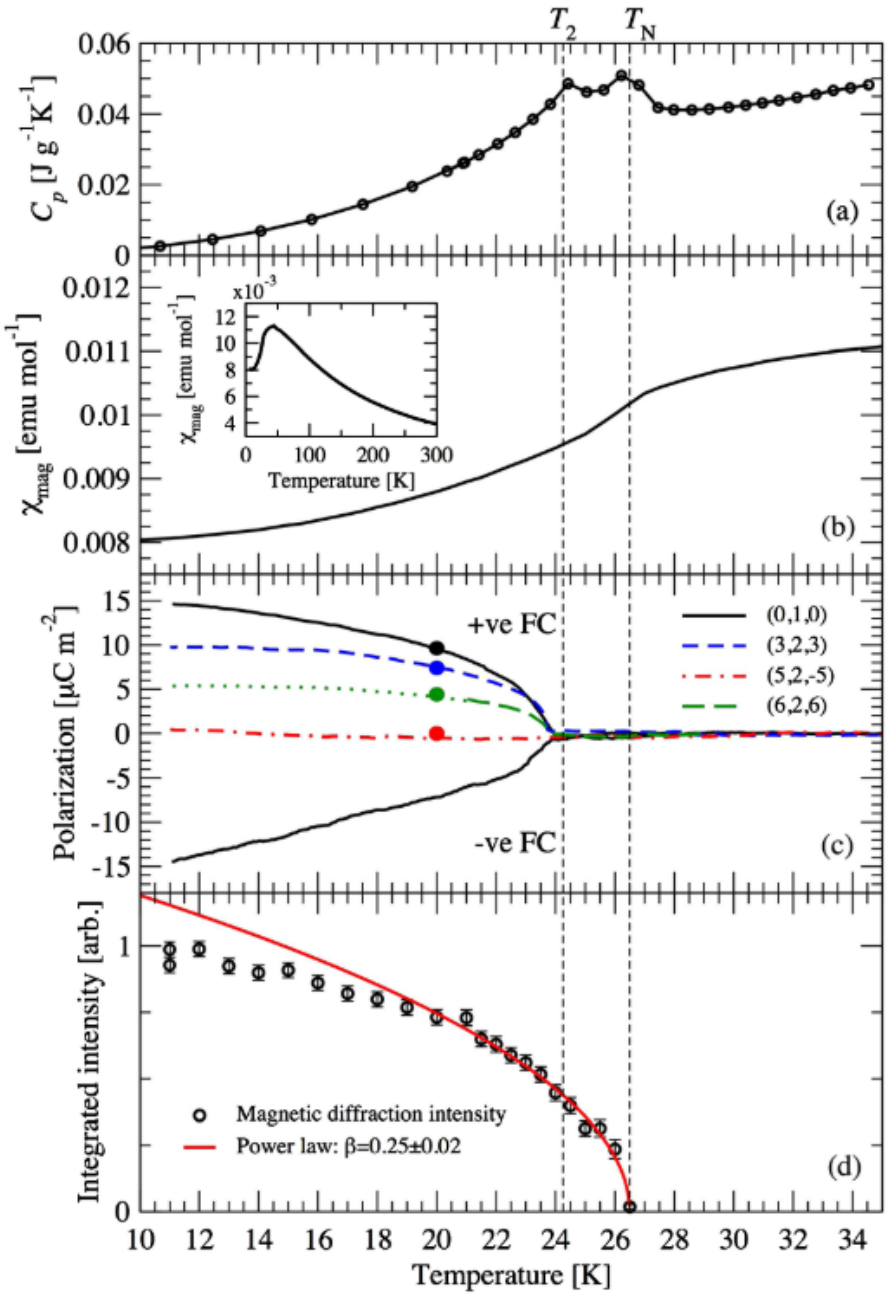

Figure 4.1: (a) The specific heat, (b) magnetic susceptibility, (c) electric polarisation and (d) neutron magnetic diffraction intensity from a powder study of CNO. The two transitions are clearly shown. The same phenomenology has been observed in single crystal samples [16]. Reprinted figure with permission from R. D. Johnson *et al.*, "$Cu_3Nb_2O_8$: A multiferroic with chiral coupling to the crystal structure," *Phys. Rev. Lett.*, vol. 107, p. 137 205, 13 2011. Copyright (2011) by the American Physical Society.

the polarisation may be along an arbitrary direction.

This model was supported by Sharma *et al.* [19]. However, Xiang *et al.* proposed a more general model of helical multiferroics [20] in which a polarisation is induced purely through the presence of a non-collinear magnetic structure. The polarisation results from non-collinear

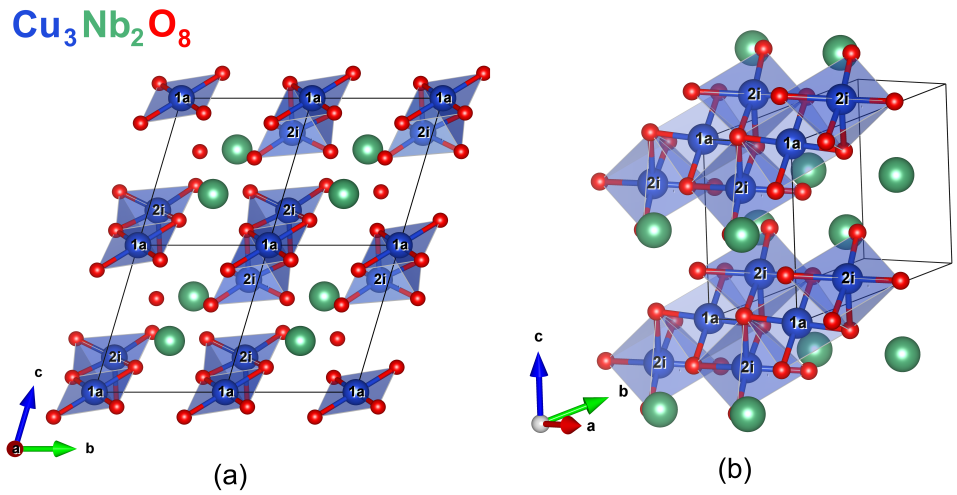

Figure 4.2: The nuclear structure of CNO. (a) shows a view along the *a* direction illustrating that the Cu sites are separated along *b* by layers of Nb. (b) shows the saw-tooth chains along a made by the Cu sites. The different Wyckoff sites occupied by Cu are labelled. Figure made in VESTA [17]. ©2020 APS

spin dimers, termed exchange pairs, and is expanded as a power series and the coefficients determined by first principles density functional field calculations. This model was found to explain the polarisation displayed by MnI_2 [20] and later extended to $CaMn_7O_{12}$ [21] where a noncentrosymmetric structure was considered. This model has also been applied to CNO [22] where it was concluded that the polarisation arises from exchange striction between Cu pairs, not spin-orbit coupling which the authors claim is in contradiction with the ferro-axial coupling mechanism. Furthermore, it is suggested that the small magnitude of the polarisation is due to the small phase difference between the Cu(2*i*) sites.

Given this, a conclusive method to classify the magnetic structure is required. In this study, the magnetic structure in a single crystal sample of CNO is reported as determined by SNP. There are two aims to this work: Firstly, to confirm the low temperature magnetic structure in a single crystal given the discussion surrounding the mechanism for ferroelectricity. Secondly, to investigate the unusual spin density wave phase and its relation to the two magnetic transitions. This is accomplished by reporting the magnetic structure in *both* ordered phases using SNP's sensitivity to individual components of the magnetic interaction vector. SNP involves measuring the polarisation matrix which contains information about how the sample interacts with the polarised neutron beam. Without the use of polarised neutrons, it is very difficult to distinguish between complex structures such as helicoidal or a spin density wave.

4.2 Results and Discussion

In order to unambiguously determine the magnetic structure of CNO, a review of the Blume-Maleev equations, presented in Section 3.3.4, allows comparison of these equations to the data

which shows several problems that can be accounted for by consideration of the systematic errors, given in Section 4.2.2. However, this theory can now be used to understand the neutron polarisation results from CNO. The refinement is described and some of the apparent inconsistencies between the data and the Blume-Maleev equations are reconciled. This is then applied to refine the magnetic structure.

4.2.1 Sample Details

The study in this chapter was carried out on a single crystal of CNO which is shown in Figure 4.3. This was grown at Rutgers University using the floating-zone technique whereby heat is used to melt a section of a vertically-mounted rod sample and this 'molten zone' is then moved along the sample to produce a single crystal [23].

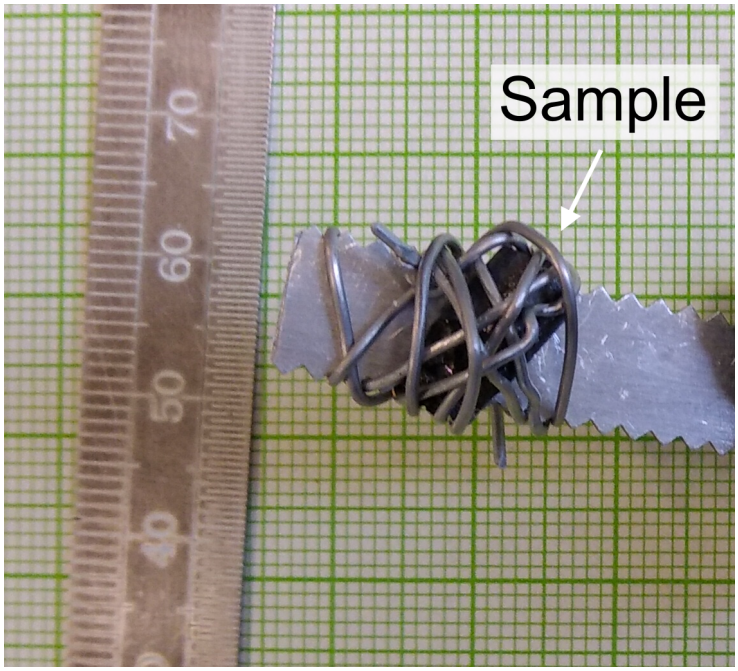

Figure 4.3: Single crystal sample of CNO shown attached to the mounting plate used for neutron scattering.

This single crystal sample has been shown to undergo the same transitions as are shown in the powder study by Johnson *et al.* and shown in Figure 4.1 [15]. Heat capacity measurements show the double-peak indicative of both the T_N and T_2 phase transitions and the emergence of electric polarisation and magnetisation have been confirmed [16]. Furthermore, the crystal structure has been confirmed with X-ray diffraction and the symmetry group with both X-ray and neutron Laue diffraction [16].

4.2.2 Full Matrix Refinement and Application of Systematic Errors

In order to determine the magnetic structure of CNO in both ordered phases, SNP was used to measure the polarisation matrix for multiple magnetic Bragg peaks. The experiment was performed using CRYOPAD on D3 (ILL, Grenoble, France; $\lambda = 0.85$ Å) which allows the polarisation matrix to be directly measured using the method detailed in Section 3.3.4. The full matrix was determined for multiple magnetic Bragg peaks in the LT phase, $T \approx 3.5$ K, and just below T_N in the MT phase, $T \approx 26.4$ K. The data-sets were refined in MAG2POL [24] and cross checked using the Blume-Maleev equations in MATLAB. Figures 4.4 and 4.5 show the outcome of the refinement in the LT and MT phase respectively. Also shown in Figure 4.6 are the refined matrix elements plotted against their measured counterparts for both phases. The overlaid linear pattern provides an indication that the refinement is of good quality.

The two Cu^{2+} ions occupying the Wyckoff position $2i$ are identical in all but the LT phase where the inversion centre is broken. This symmetry was taken into account in the MT phase by setting the moments of the $Cu(2i)$ sites to be identical. Constraints regarding the lengths of the moments were also implemented into MAG2POL refinement as SNP is not sensitive to the lengths of the moments unless there is nuclear-magnetic overlap [25]. This means that SNP cannot be used to determine the absolute length of the magnetic moments, only their relative size and directions. However, this usually provides sufficient information to ascertain the magnetic ground state, especially given published work refining the magnetic moment value [15].

There are two strict conditions on the polarisation matrix in the Blume-Maleev equation: the elements $\tilde{P}_{xx} \equiv -1$ and $\tilde{P}_{xy} = \tilde{P}_{xz} = 0$. From the matrix elements plotted in Figures 4.4 and 4.5, these two conditions do not seem to be obeyed with $\tilde{P}_{xx}$ consistently $\neq -1$ and $\tilde{P}_{xy} = \tilde{P}_{xz}$, though small, $\neq 0$. These two points will now be addressed in detail:

Due to the chiral nature of the LT structure, the option to refine using uncorrected matrix elements was implemented in MAG2POL (see Qureshi) [24]. The detector on D3 relies on a ^{3}He spin filter which, over time, will lose efficiency. This results in a reduced intensity of measurements [24] but can be corrected for in MAG2POL and so was taken into account for the refinement process. However, due to the presence of terms which do and don't depend on the initial polarisation, the correction process is computed only during the refinement. To quantify the goodness of the fit, the reduced χ^2 on the uncorrected matrix elements was calculated by MAG2POL [24] as $\chi^2_r = 37.98$ and $\chi^2_r = 36.69$ in the LT and MT phases respectively. This value for χ^2 is shown in Figures 4.4 and 4.5. However, the data were later corrected for spin filter efficiency and so Figures 4.4 and 4.5 show the *corrected* matrix elements. It is the correction resulting from the incomplete beam polarisation that is the dominant reason for the matrix element $\tilde{P}_{xx}$ deviating from -1 as will be demonstrated in Section 4.2.2.

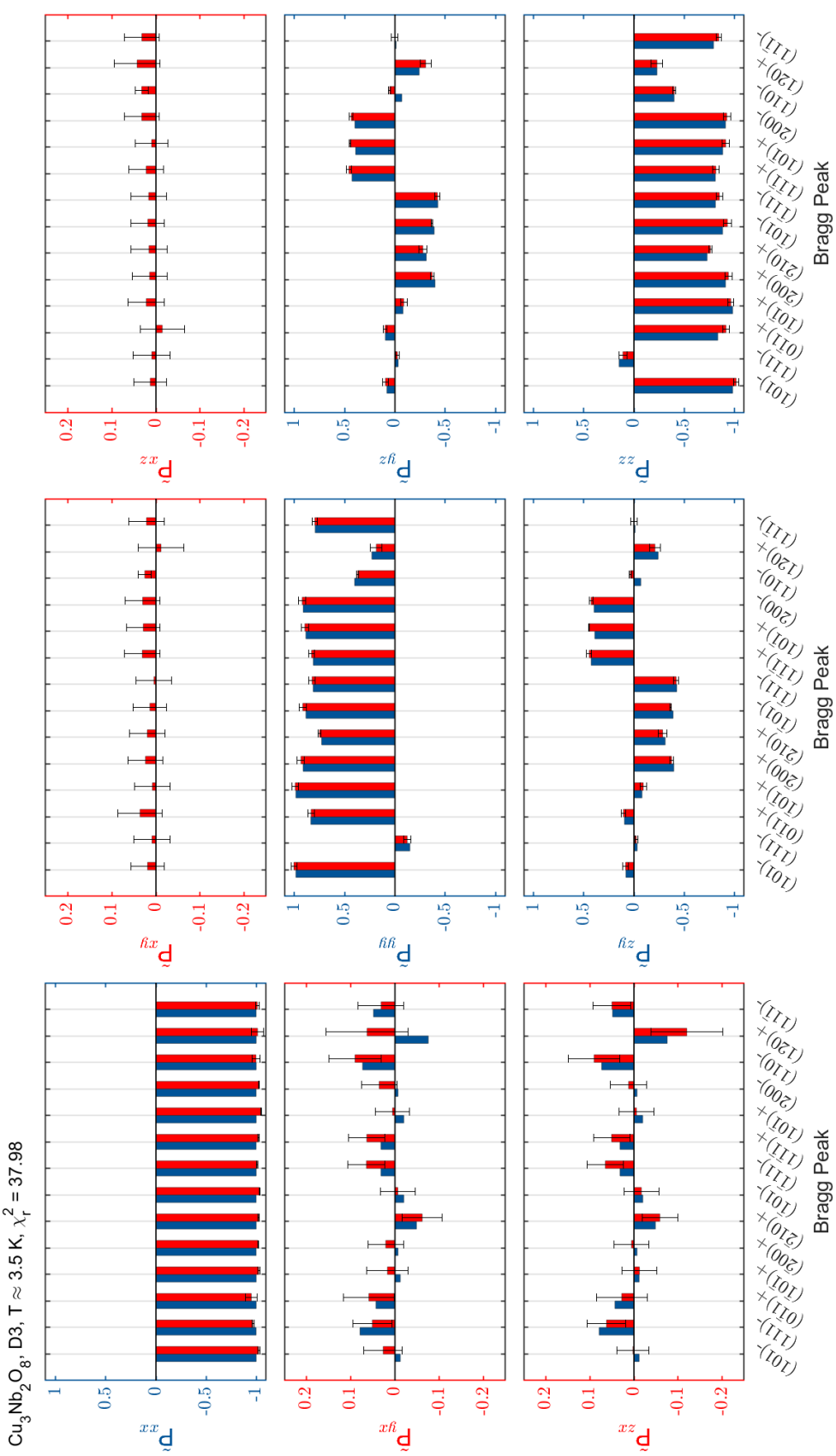

Figure 4.4: The refinement (in MAG2POL and confirmed in MATLAB) of the polarisation matrix at ≈ 3.5 K - LT phase. The bars show the refined matrix elements (left - blue) plotted for each magnetic Bragg peak against the measured matrix elements (right - red). Statistical and systematic experimental errors are shown in black (systematic errors due to instrument resolution were calculated in MATLAB). The plotted matrix elements are corrected for detector spin filter efficiency. For clarity, two different y scales are used and are displayed in different colours. Magnetic Bragg peaks are labelled as $(hkl)\pm$ meaning $(hkl) \pm \vec{k}$. ©2020 APS

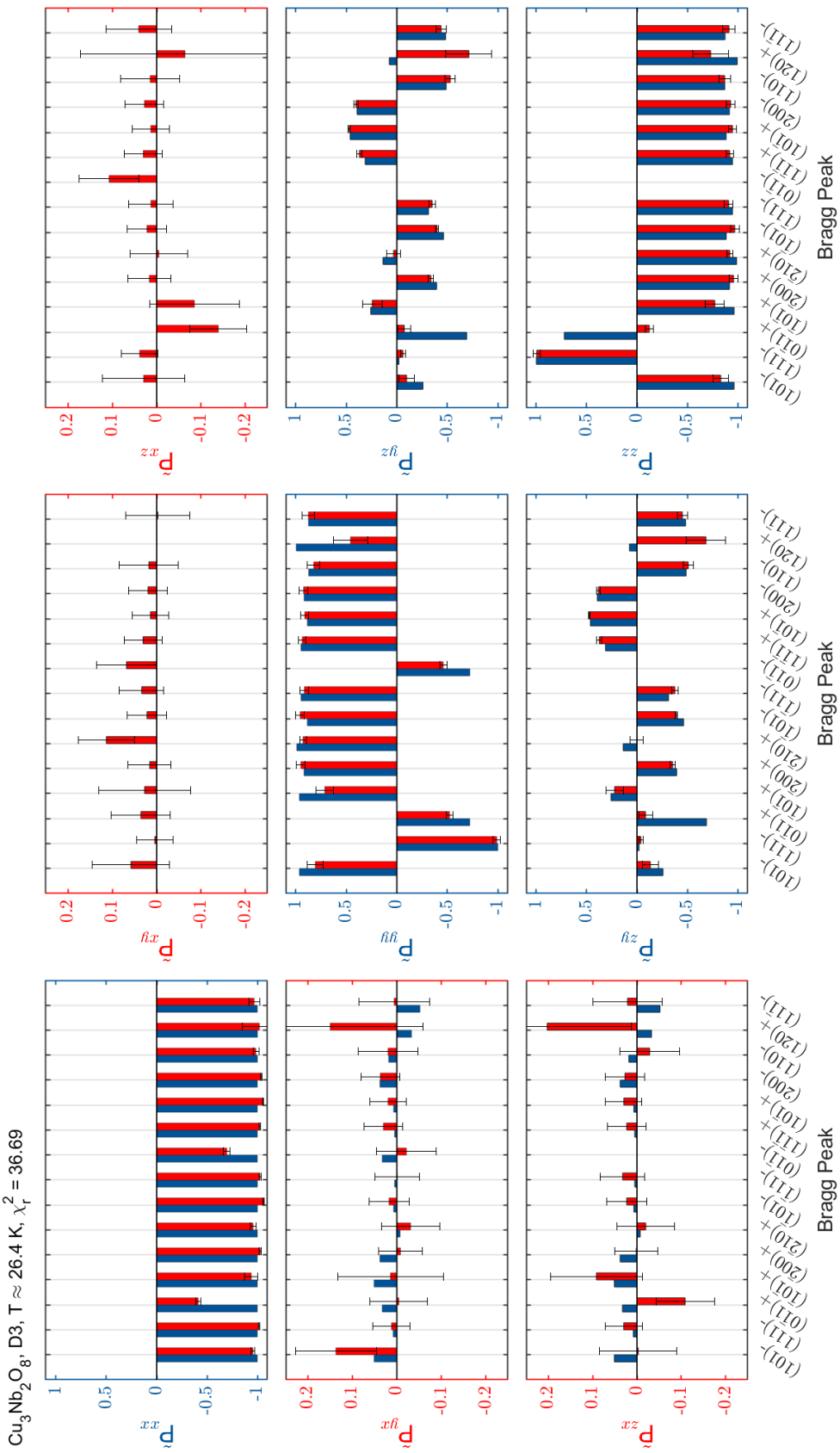

Figure 4.5: The refinement (in MAG2POL and confirmed in MATLAB) of the polarisation matrix at $\approx$ 26.4 K - MT phase. The bars show the refined matrix elements (left - blue) plotted for each magnetic Bragg peak against the measured matrix elements (right - red). Statistical and systematic experimental errors are shown in black (systematic errors due to instrument resolution were calculated in MATLAB). The plotted matrix elements are corrected for detector spin filter efficiency. For clarity, two different y scales are used and are displayed in different colours. Magnetic Bragg peaks are labelled as $(hkl)\pm$ meaning $(hkl) \pm \vec{k}$. ©2020 APS

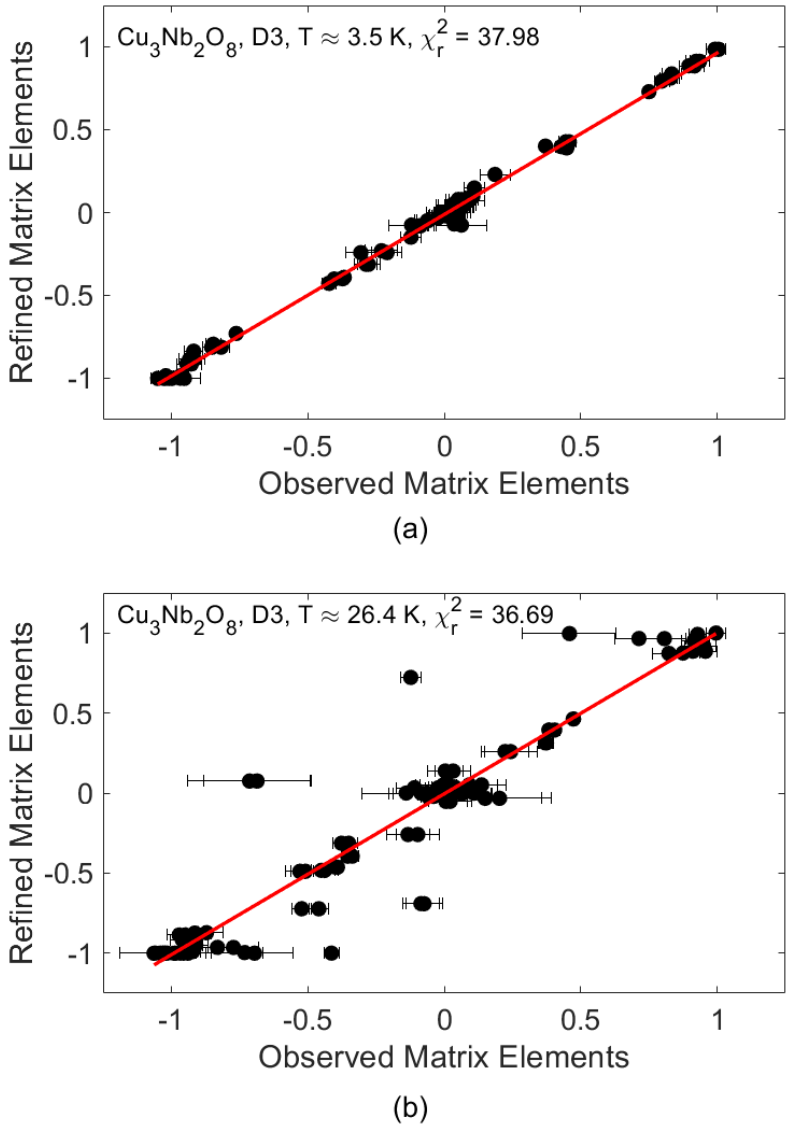

Figure 4.6: The refined (in MAG2POL and confirmed in MATLAB) elements of the polarisation matrix against those observed in (a) ≈ 3.5 K - LT phase and (b) ≈ 26.4 K - MT phase. The error bars shown are the systematic and statistical errors on the observed elements. ©2020 APS

The effects of the experimental setup can provide reason for the systematic $\neq 0$ values for the matrix elements $\tilde{P}_{xy}$ and $\tilde{P}_{xz}$. This is due to an imperfect initial polarisation of the neutron beam which can be due to two reasons: the monochromator used is not 100% effective, or the magnetic fields used to align the beam's polarisation to the desired direction have a finite resolution. Both of these effects are purely due to instrumental/sample alignment precision and are discussed more fully in Section 4.2.2. However, the non-zero values for $\tilde{P}_{xy}$ and $\tilde{P}_{xz}$ shown in Figure 4.4 and Figure 4.5 can be fully accounted for by an angular resolution of 2° as quoted in the literature [26]. This deviation only reduces the overall beam polarisation by 0.06%. As such, the actual systematic experimental errors should be considered larger than the statistical counting errors. The polarisation is known to be 93.5% on D3 so these effects can be assumed to have a non-negligible impact on the results. These errors were computed using custom code

implemented in MATLAB. Due to the nature of these errors, individual components of $\vec{M}_\perp$ were required to be calculated and used according to the equations given in the next section. The systematic errors are plotted in Figures 4.4 and 4.5 but were not taken into account in the calculation of χ_r^2.

Initial Polarisation Error Analysis

Systematic errors in a polarised neutron experiment can be attributed to two mechanisms:

1. Not all of the neutron beam is polarised - only a fraction $\zeta \approx 1$ - the rest remains unpolarised.

2. The polarisation vector is not exactly aligned to the specified direction, e.g. x, or some other *small* misalignment is present.

The causes of these mechanisms lay in the instrumental setup: The first case is consequent of a non-ideal monochromator crystal. Unlike muons, neutrons are generated in an unpolarised state and, so, must be aligned. However, this process may leave part of the beam unpolarised. The second is dependent on the apparatus used to align the polarisation vector of the neutron beam. On D3, this is a setup of a guide magnetic field and a magnetic nutator as shown in Figure 3.2. The nutator is a device which allows the polarisation to be rotated adiabatically towards a direction transverse to the beam through application magnetic fields up to 150 G [27]. The neutron then passes through a Meissner sheild where it encounters the second guide field, causing the spin to undergo precession. In this way, the combination of these two fields can orientate the neutron's spin in any direction.

Any *small* misalignment can be due to either the incoming/outgoing polarisation vector or the sample not being aligned correctly. This effects can all be included into an 'angular resolution' parameter θ and let, without loss of generality, the outgoing polarisation be taken as exact in this analysis.

The first mechanism may be treated using the density matrix formalism as a density matrix that represents this partially polarised 'mixed state' is easily constructed. This can be done by combining the density matrices that correspond to the separate 'pure states' multiplied by their respective population fraction in the beam:

$$\rho_{mixed} = \sum_i n_i \rho_i, \tag{4.1}$$

where i counts the number of pure states that are being combined and the population fractions $\{n_i\}$ sum to unity. The density matrix of the polarised fraction is given by Equation 3.26. The density matrix of the unpolarised fraction can be computed in two ways: either by setting $\vec{P}^I = 0$ in Equation 3.26, or from first principles. An unpolarised beam is made up of equal parts spin

up and down neutrons where the spin projection axis may be chosen as z. Hence, an unpolarised beam is also a 'mixed state' and so the density matrix is constructed according to

$$\rho_{unpol} = \frac{1}{2}\rho_{up} + \frac{1}{2}\rho_{down} = \frac{1}{2}\begin{pmatrix} 1 & 0 \\ 0 & 0 \end{pmatrix} + \frac{1}{2}\begin{pmatrix} 0 & 0 \\ 0 & 1 \end{pmatrix} = \frac{1}{2}\mathbb{I}. \tag{4.2}$$

This can be combined with 3.26 to write the full density matrix

$$\rho_1 = \zeta\rho_{pol} + (1-\zeta)\rho_{unpol} = \big[\frac{\zeta}{2}(\mathbb{I} + P_i^I\sigma_i)\big] + \frac{(1-\zeta)}{2}\mathbb{I} = \frac{1}{2}(\mathbb{I} + \zeta P_i^I\sigma_i). \tag{4.3}$$

Interestingly, this has the same form as Equation 3.26, except that the polarisation part has acquired a factor of ζ such that

$$\vec{P}^I \to \zeta\vec{P}^I, \tag{4.4}$$

must now used in the analysis. This can only affect the magnitude of the polarisation matrix elements and, therefore, the anomalous values of $\tilde{\mathsf{P}}_{xy}$ and $\tilde{\mathsf{P}}_{xz}$ must result from the second mechanism, which will now be considered.

Suppose that the alignment of the polarisation vector, with the direction $\hat{n}$, has an angular resolution of θ. This means a cone of angle θ may be constructed around $\hat{n}$, within which, the polarisation vector is expected to be contained. By considering the worse case, i.e the limit of the resolution, the polarisation vector must lie on the surface of this cone. In this case, its direction may be described using two angles: the angular deviation from $\hat{n}$, θ, and the azimuth angle at the base of the cone, ϕ. Therefore, in the general case, the polarisation vector of the incoming beam acquires components in the other two Cartesian directions perpendicular to $\hat{n}$. Hence, the final polarisation along the measurement direction will also contain terms which come from the scattering of these other components, and so this mechanism is able to change the form of the polarisation matrix. This effect is able to explain the observed non-zero value for $\tilde{\mathsf{P}}_{xy}$ and $\tilde{\mathsf{P}}_{xz}$. Furthermore, as the cause of the misalignment comes from the instrumentation, it should be consistent during a measurement, i.e. one matrix element, and will only be reset when either the initial polarisation vector direction changes or the sample is rotated. Hence, this mechanism adds a small, but non-zero, contribution to all matrix elements.

Allowing for both of these error mechanisms, the initial polarisation vector may be written as

$$\vec{P}^I \to \zeta(\vec{P}^I + \vec{\alpha}^{(i)}(\theta,\phi)), \tag{4.5}$$

where $\vec{\alpha}^{(i)}(\theta,\phi)$ contains the additional contribution from the non-zero angular resolution when the initial polarisation is in the ith direction. The error ε_{ij} in the polarisation matrix element $\tilde{\mathsf{P}}_{ij}$ may be written as

$$\varepsilon_{ij} = \max_{0<\phi<2\pi} \left| \left\langle \frac{\zeta \mathsf{P}_{jk}[P_k^I + \alpha_k^{(i)}(\theta,\phi)] + P_j'}{\zeta\cos(\theta)} \right\rangle - \tilde{\mathsf{P}}_{ij} \right|, \tag{4.6}$$

where care must be taken to use Equation 4.5 for the calculation of the cross-section inside the components of the polarisation tensor P_{jk} and the created polarisation vector $\vec{P}'$. The angled brackets indicate an average over domains. Furthermore, as the angle ϕ is attributed randomly due to the experimental precision, the maximum value of the function inside the absolute value sign should be taken to give the best estimate of the 'worst-case' error.

The vector $\vec{\alpha}^{(i)}(\theta,\phi)$ will be dependent on the initial polarisation direction and can be written as

$$\begin{aligned}
\vec{\alpha}^{(x)} =& [\cos(\theta)-1]\hat{x} + \sin(\theta)[\cos(\phi)\hat{y} + \sin(\phi)\hat{z}], \\
\vec{\alpha}^{(y)} =& [\cos(\theta)-1]\hat{y} + \sin(\theta)[\cos(\phi)\hat{z} + \sin(\phi)\hat{x}], \\
\vec{\alpha}^{(z)} =& [\cos(\theta)-1]\hat{z} + \sin(\theta)[\cos(\phi)\hat{x} + \sin(\phi)\hat{y}],
\end{aligned} \tag{4.7}$$

for an initial polarisation in the x, y and z direction respectively. These directions are in reference to the standard coordinate system.

Then the error terms can be computed as:

$$\varepsilon_{xx} = \left| \left\langle \frac{-\zeta|\vec{M}_\perp|^2\cos(\theta) - 2\mathcal{I}m\{M_{\perp y}M_{\perp z}^*\}}{\zeta\cos(\theta)\left\langle|\vec{M}_\perp|^2 + 2\zeta\cos(\theta)\mathcal{I}m\{M_{\perp y}M_{\perp z}^*\}\right\rangle} \right\rangle + 1 \right|, \tag{4.8}$$

$$\varepsilon_{xy} = \max_{0<\phi<2\pi} \left| tan(\theta) \frac{\left\langle [|\vec{M}_{\perp y}|^2 - |\vec{M}_{\perp z}|^2]\cos(\phi) + 2\mathcal{R}e\{M_{\perp y}M_{\perp z}^*\}\sin(\phi)\right\rangle}{\left\langle|\vec{M}_\perp|^2 + 2\zeta\cos(\theta)\mathcal{I}m\{M_{\perp y}M_{\perp z}^*\}\right\rangle} \right|, \tag{4.9}$$

$$\varepsilon_{xz} = \max_{0<\phi<2\pi} \left| tan(\theta) \frac{\left\langle 2\mathcal{R}e\{M_{\perp y}M_{\perp z}^*\}\cos(\phi) - [|\vec{M}_{\perp y}|^2 - |\vec{M}_{\perp z}|^2]\sin(\phi)\right\rangle}{\left\langle|\vec{M}_\perp|^2 + 2\zeta\cos(\theta)\mathcal{I}m\{M_{\perp y}M_{\perp z}^*\}\right\rangle} \right|, \tag{4.10}$$

$$\varepsilon_{yx} = \max_{0<\phi<2\pi} \left| \left\langle \frac{-\zeta|\vec{M}_\perp|^2\sin(\theta)\sin(\phi) - 2\mathcal{I}m\{M_{\perp y}M_{\perp z}^*\}}{\zeta\cos(\theta)\left\langle|\vec{M}_\perp|^2 + 2\zeta\sin(\theta)\sin(\phi)\mathcal{I}m\{M_{\perp y}M_{\perp z}^*\}\right\rangle} \right\rangle - \tilde{\mathsf{P}}_{yx} \right|, \tag{4.11}$$

$$\varepsilon_{yy} = \max_{0<\phi<2\pi} \left| \frac{\left\langle|\vec{M}_{\perp y}|^2 - |\vec{M}_{\perp z}|^2 + 2tan(\theta)\cos(\phi)\mathcal{R}e\{M_{\perp y}M_{\perp z}^*\}\right\rangle}{\left\langle|\vec{M}_\perp|^2 + 2\zeta\sin(\theta)\sin(\phi)\mathcal{I}m\{M_{\perp y}M_{\perp z}^*\}\right\rangle} - \tilde{\mathsf{P}}_{yy} \right|, \tag{4.12}$$

$$\varepsilon_{yz} = \max_{0<\phi<2\pi} \left| \frac{\left\langle 2\mathcal{R}e\{M_{\perp y}M_{\perp z}^*\} - [|\vec{M}_{\perp y}|^2 - |\vec{M}_{\perp z}|^2]tan(\theta)\cos(\phi)\right\rangle}{\left\langle|\vec{M}_\perp|^2 + 2\zeta\sin(\theta)\sin(\phi)\mathcal{I}m\{M_{\perp y}M_{\perp z}^*\}\right\rangle} - \tilde{\mathsf{P}}_{yz} \right|, \tag{4.13}$$

$$\varepsilon_{zx} = \max_{0<\phi<2\pi} \left| \left\langle \frac{-\zeta|\vec{M}_\perp|^2\sin(\theta)\cos(\phi) - 2\mathcal{I}m\{M_{\perp y}M^*_{\perp z}\}}{\zeta\cos(\theta)\left\langle|\vec{M}_\perp|^2 + 2\zeta\sin(\theta)\cos(\phi)\mathcal{I}m\{M_{\perp y}M^*_{\perp z}\}\right\rangle} \right\rangle - \tilde{\mathsf{P}}_{zx} \right|, \tag{4.14}$$

$$\varepsilon_{zy} = \max_{0<\phi<2\pi} \left| \frac{\left\langle tan(\theta)\sin(\phi)[|\vec{M}_{\perp y}|^2 - |\vec{M}_{\perp z}|^2] + 2\mathcal{R}e\{M_{\perp y}M^*_{\perp z}\}\right\rangle}{\left\langle|\vec{M}_\perp|^2 + 2\zeta\sin(\theta)\cos(\phi)\mathcal{I}m\{M_{\perp y}M^*_{\perp z}\}\right\rangle} - \tilde{\mathsf{P}}_{zy} \right|, \tag{4.15}$$

$$\varepsilon_{zz} = \max_{0<\phi<2\pi} \left| \frac{\left\langle 2tan(\theta)\sin(\phi)\mathcal{R}e\{M_{\perp y}M^*_{\perp z}\} - [|\vec{M}_{\perp y}|^2 - |\vec{M}_{\perp z}|^2]\right\rangle}{\left\langle|\vec{M}_\perp|^2 + 2\zeta\sin(\theta)\cos(\phi)\mathcal{I}m\{M_{\perp y}M^*_{\perp z}\}\right\rangle} - \tilde{\mathsf{P}}_{zz} \right|. \tag{4.16}$$

These equations explicitly show the additional terms which may arise from additional polarisation directions and all reduce to zero in the limit $\theta \to 0$. However, the presence of the azimuth angle ϕ in all errors, apart from Equation 4.8, allows Equations 4.8 - 4.16 to be plotted as a function of ϕ. These are shown in Figures 4.7 - 4.15 along with the measured value for the respective matrix element. These figures are produced using the reported [26] angular resolution and initial polarisation fraction, $\approx 2^\circ$ and 93.5% respectively, for CRYOPAD. This provided values for θ and ζ respectively in Equations 4.8 - 4.16 and allowed calculation of all errors ε_{ij} in MATLAB. The refined matrix elements were used for this calculation and these systematic errors were combined with the statistical counting errors.

The curves shown in Figures 4.7 - 4.15 graphically display the errors against the angle ϕ for both phases of CNO. The different panels show all magnetic Bragg peaks and, for clarity and consistency, the two different y scales are used are displayed in different colours. As stated above, the 'worst-case' error estimate is given by the maximum of the absolute value of these curves over the domain of ϕ and it can be seen in the case of the elements $\tilde{\mathsf{P}}_{xy}$ and $\tilde{\mathsf{P}}_{xz}$ (Figs. 4.8 and 4.9), that these error calculations are able to account for the systematic non-zero measured values in both phases. These curve amplitudes were calculated in MATLAB and the resultant errors were subsequently included in Figures 4.4 and 4.5.

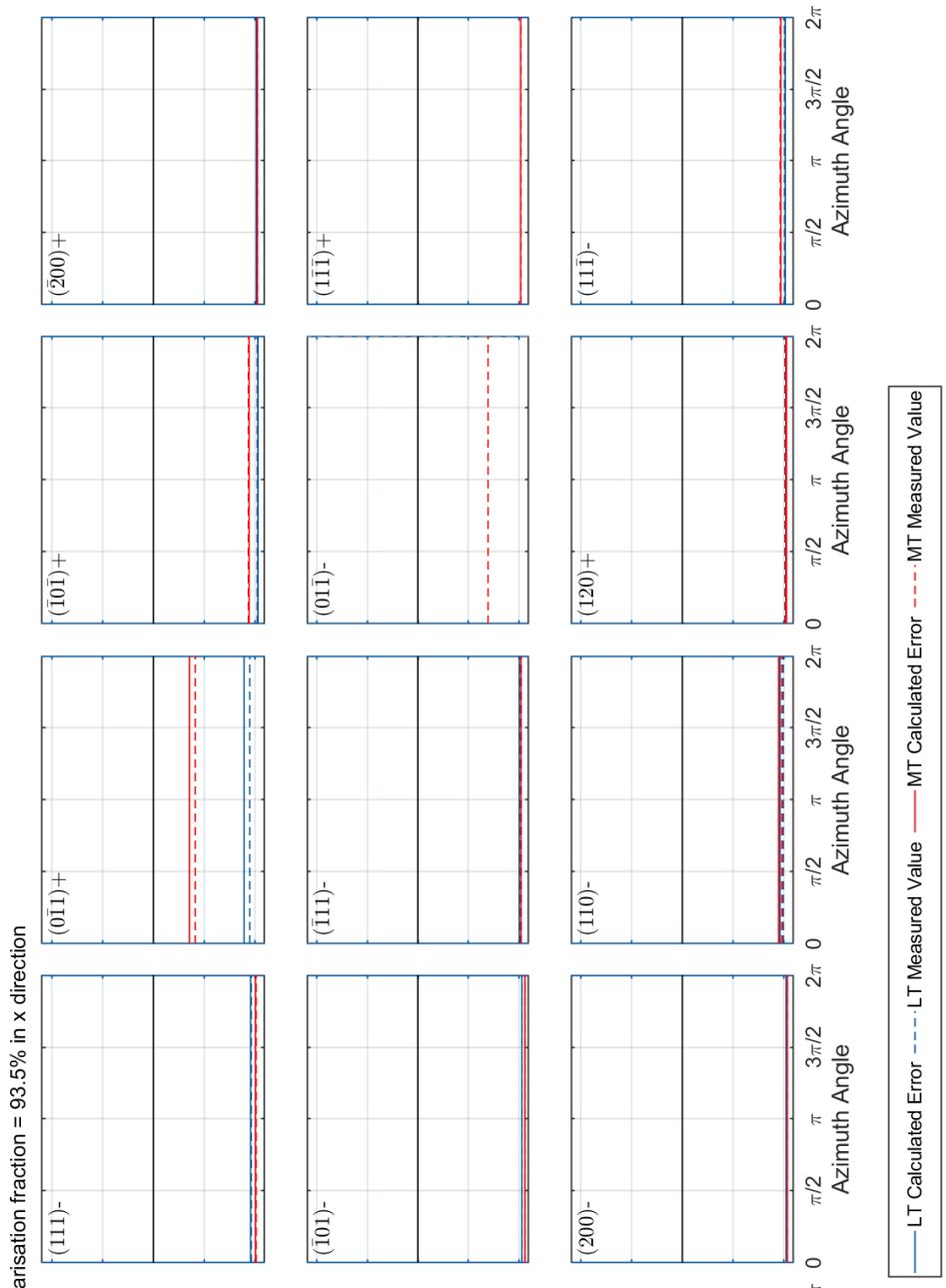

Figure 4.7: The calculated value of $\tilde{P}_{xx}$ when an angular resolution of 2° is assumed on the incident neutron polarisation. The panels correspond to the 15 Bragg peaks considered in this study. The solid curves indicate $\tilde{P}_{xx}$ against the azimuth angle ϕ so that the amplitude of these curves gives the 'worst-case' value for the error. The dashed lines show the measured value of $\tilde{P}_{xx}$ for each Bragg peak. LT phase is blue and MT phase is red. ©2020 APS

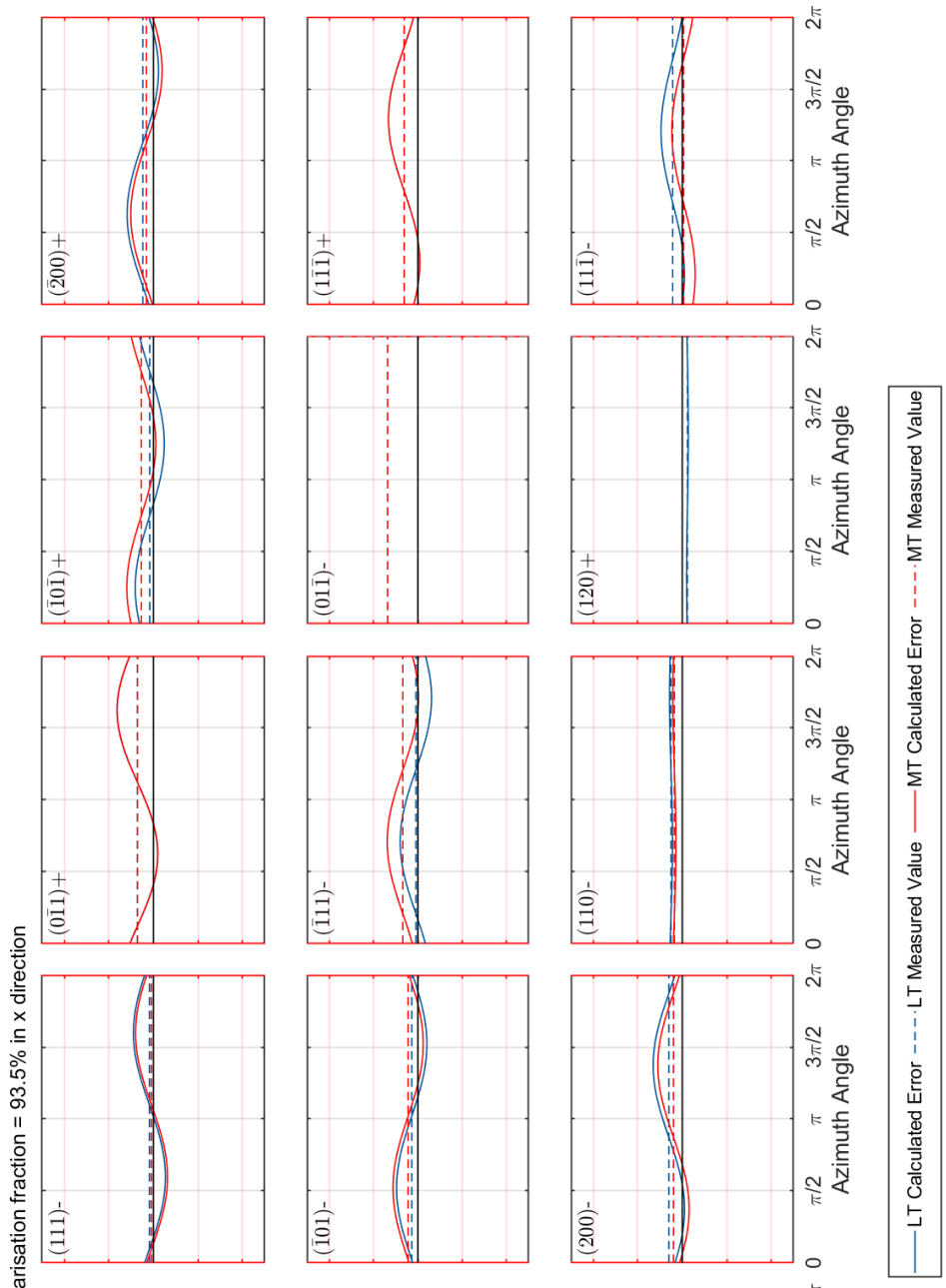

Figure 4.8: The calculated value of $\tilde{P}_{xy}$ when an angular resolution of 2° is assumed on the incident neutron polarisation. The panels correspond to the 15 Bragg peaks considered in this study. The solid curves indicate $\tilde{P}_{xy}$ against the azimuth angle ϕ so that the amplitude of these curves gives the 'worst-case' value for the error. The dashed lines show the measured value of $\tilde{P}_{xy}$ for each Bragg peak. LT phase is blue and MT phase is red. ©2020 APS

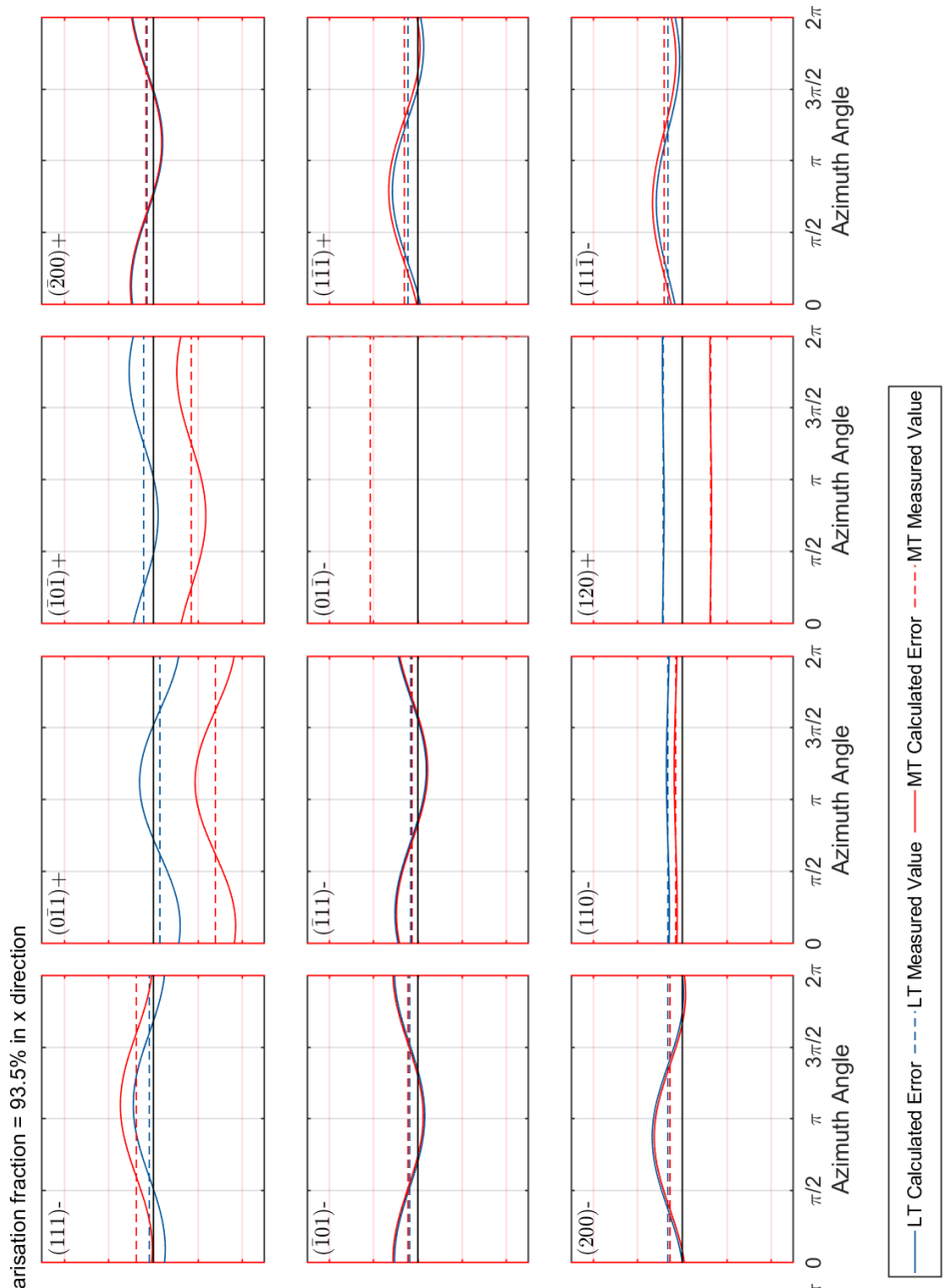

Figure 4.9: The calculated value of $\tilde{P}_{xz}$ when an angular resolution of 2° is assumed on the incident neutron polarisation. The panels correspond to the 15 Bragg peaks considered in this study. The solid curves indicate $\tilde{P}_{xz}$ against the azimuth angle ϕ so that the amplitude of these curves gives the 'worst-case' value for the error. The dashed lines show the measured value of $\tilde{P}_{xz}$ for each Bragg peak. LT phase is blue and MT phase is red. ©2020 APS

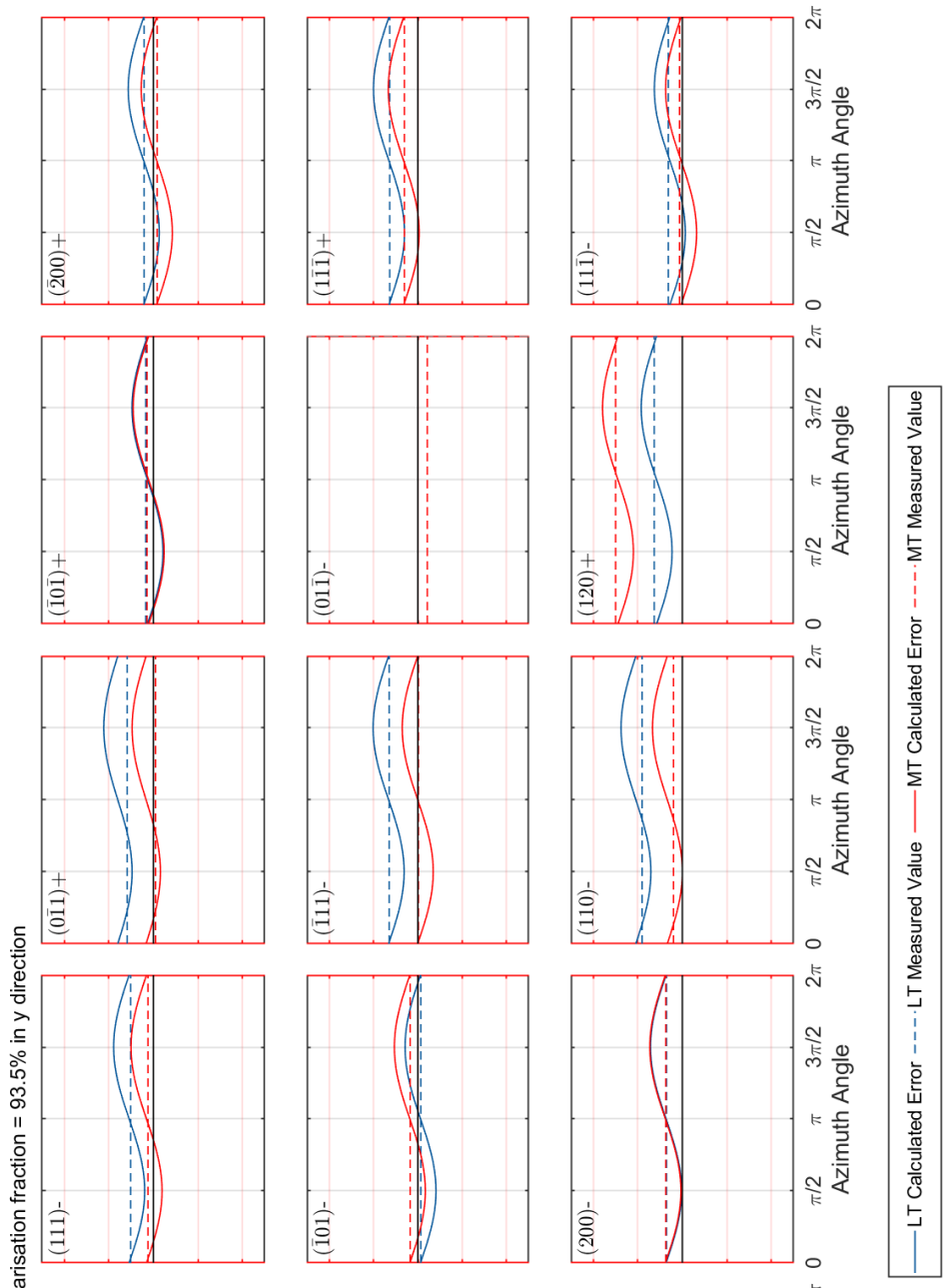

Figure 4.10: The calculated value of $\tilde{P}_{yx}$ when an angular resolution of 2° is assumed on the incident neutron polarisation. The panels correspond to the 15 Bragg peaks considered in this study. The solid curves indicate $\tilde{P}_{yx}$ against the azimuth angle ϕ so that the amplitude of these curves gives the 'worst-case' value for the error. The dashed lines show the measured value of $\tilde{P}_{yx}$ for each Bragg peak. LT phase is blue and MT phase is red. ©2020 APS

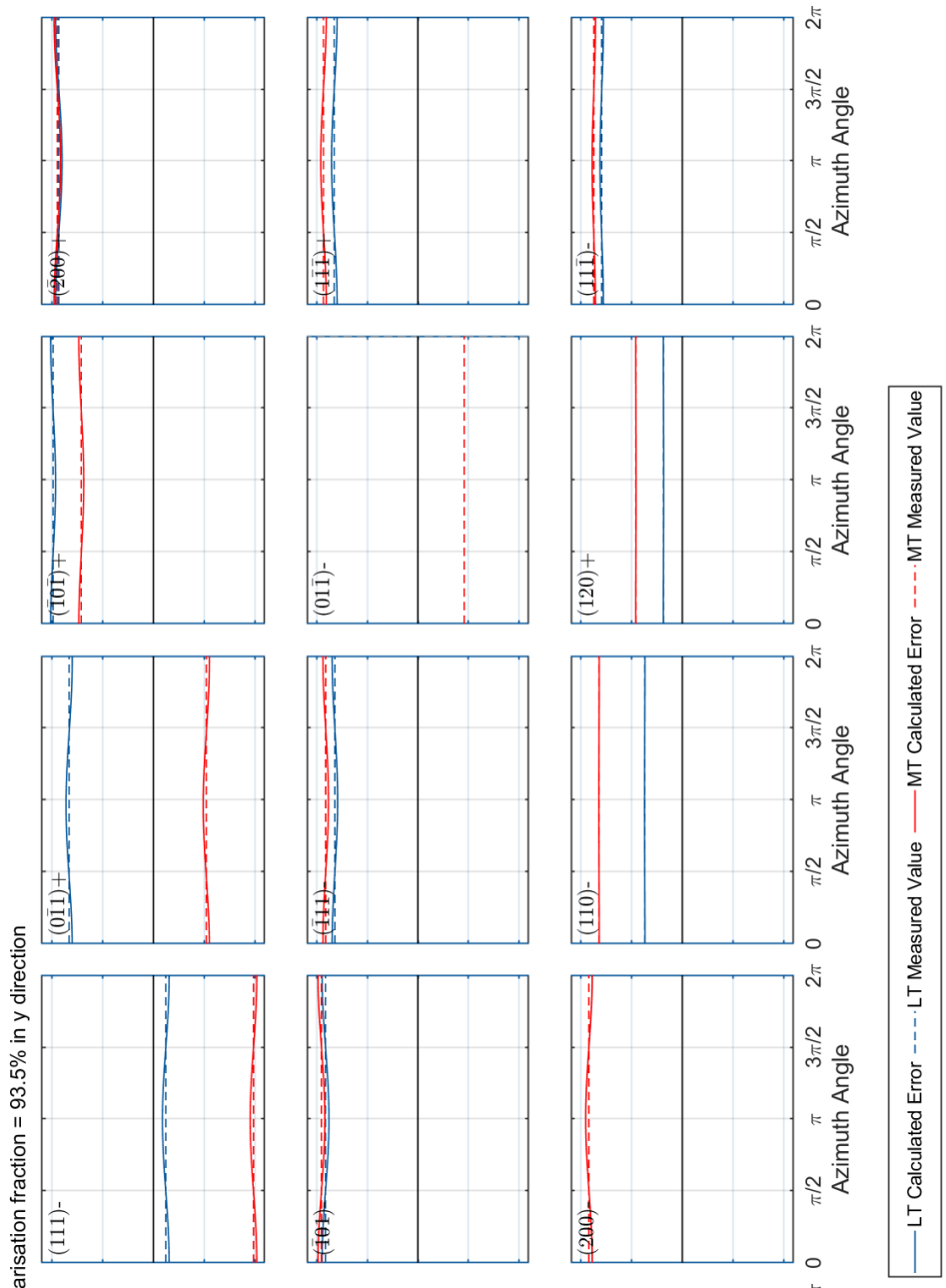

Figure 4.11: The calculated value of $\tilde{P}_{yy}$ when an angular resolution of 2° is assumed on the incident neutron polarisation. The panels correspond to the 15 Bragg peaks considered in this study. The solid curves indicate $\tilde{P}_{yy}$ against the azimuth angle ϕ so that the amplitude of these curves gives the 'worst-case' value for the error. The dashed lines show the measured value of $\tilde{P}_{yy}$ for each Bragg peak. LT phase is blue and MT phase is red. ©2020 APS

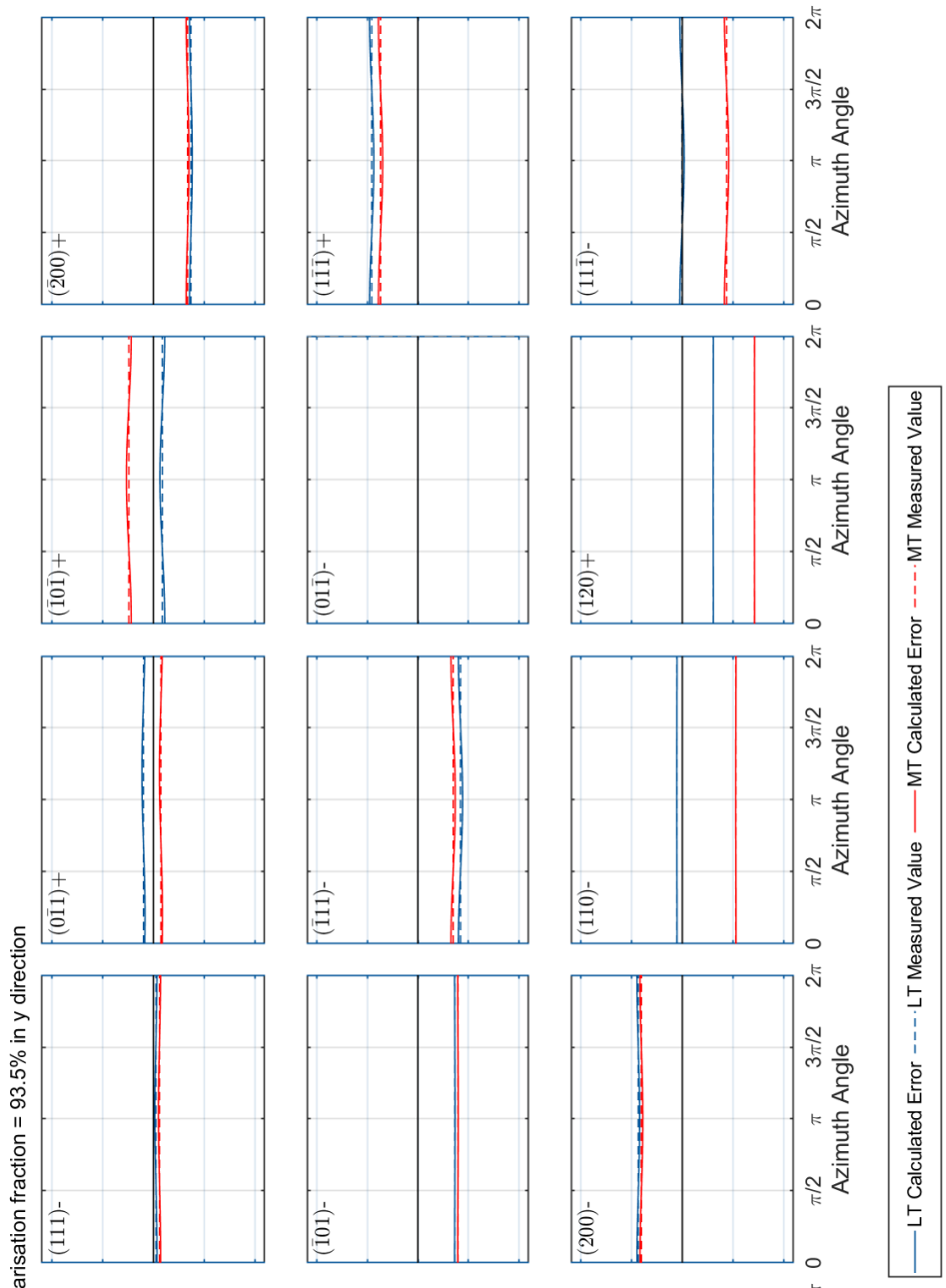

Figure 4.12: The calculated value of $\tilde{P}_{yz}$ when an angular resolution of 2° is assumed on the incident neutron polarisation. The panels correspond to the 15 Bragg peaks considered in this study. The solid curves indicate $\tilde{P}_{yz}$ against the azimuth angle ϕ so that the amplitude of these curves gives the 'worst-case' value for the error. The dashed lines show the measured value of $\tilde{P}_{yz}$ for each Bragg peak. LT phase is blue and MT phase is red. ©2020 APS

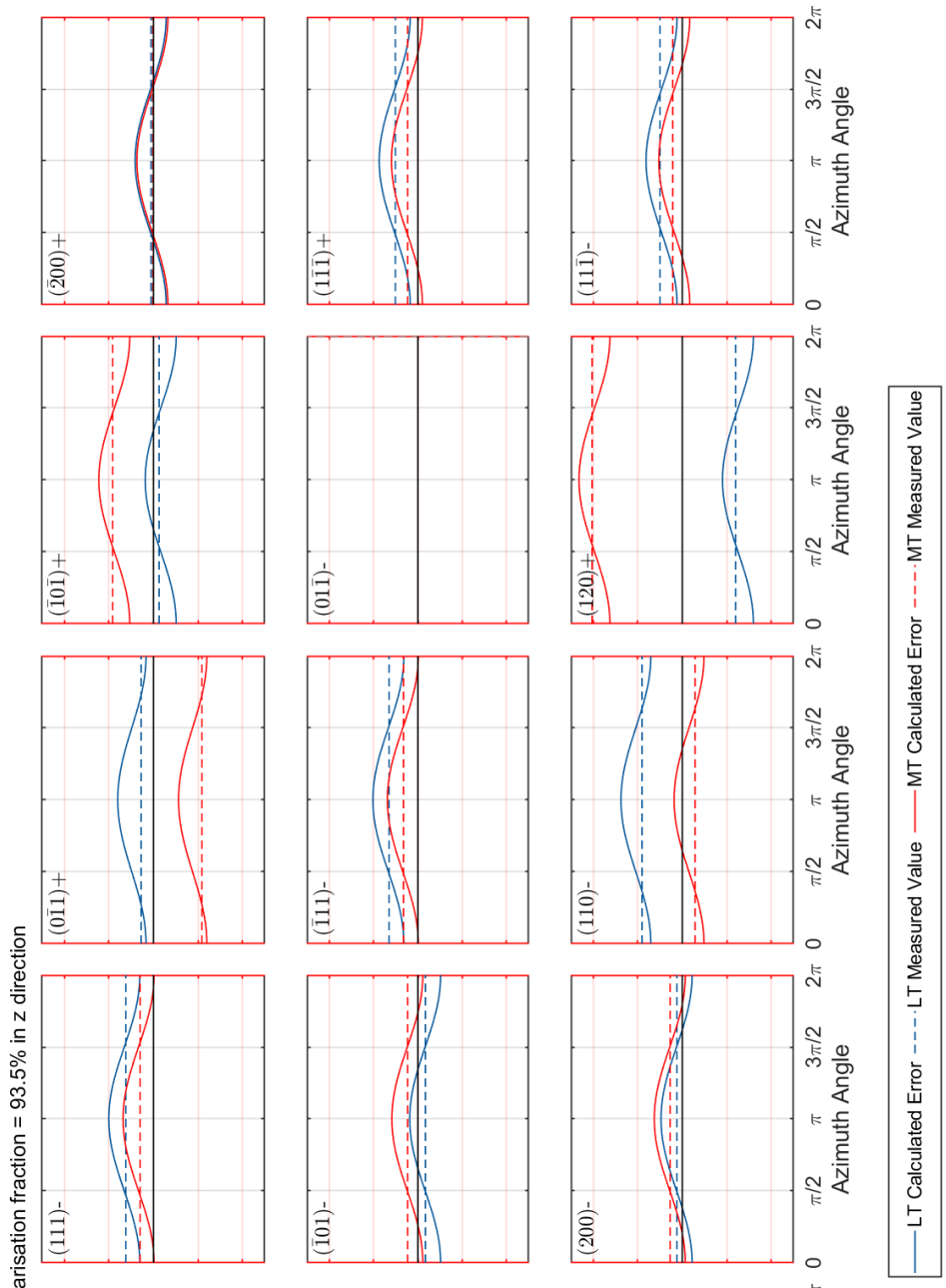

Figure 4.13: The calculated value of $\tilde{P}_{zx}$ when an angular resolution of 2° is assumed on the incident neutron polarisation. The panels correspond to the 15 Bragg peaks considered in this study. The solid curves indicate $\tilde{P}_{zx}$ against the azimuth angle ϕ so that the amplitude of these curves gives the 'worst-case' value for the error. The dashed lines show the measured value of $\tilde{P}_{zx}$ for each Bragg peak. LT phase is blue and MT phase is red. ©2020 APS

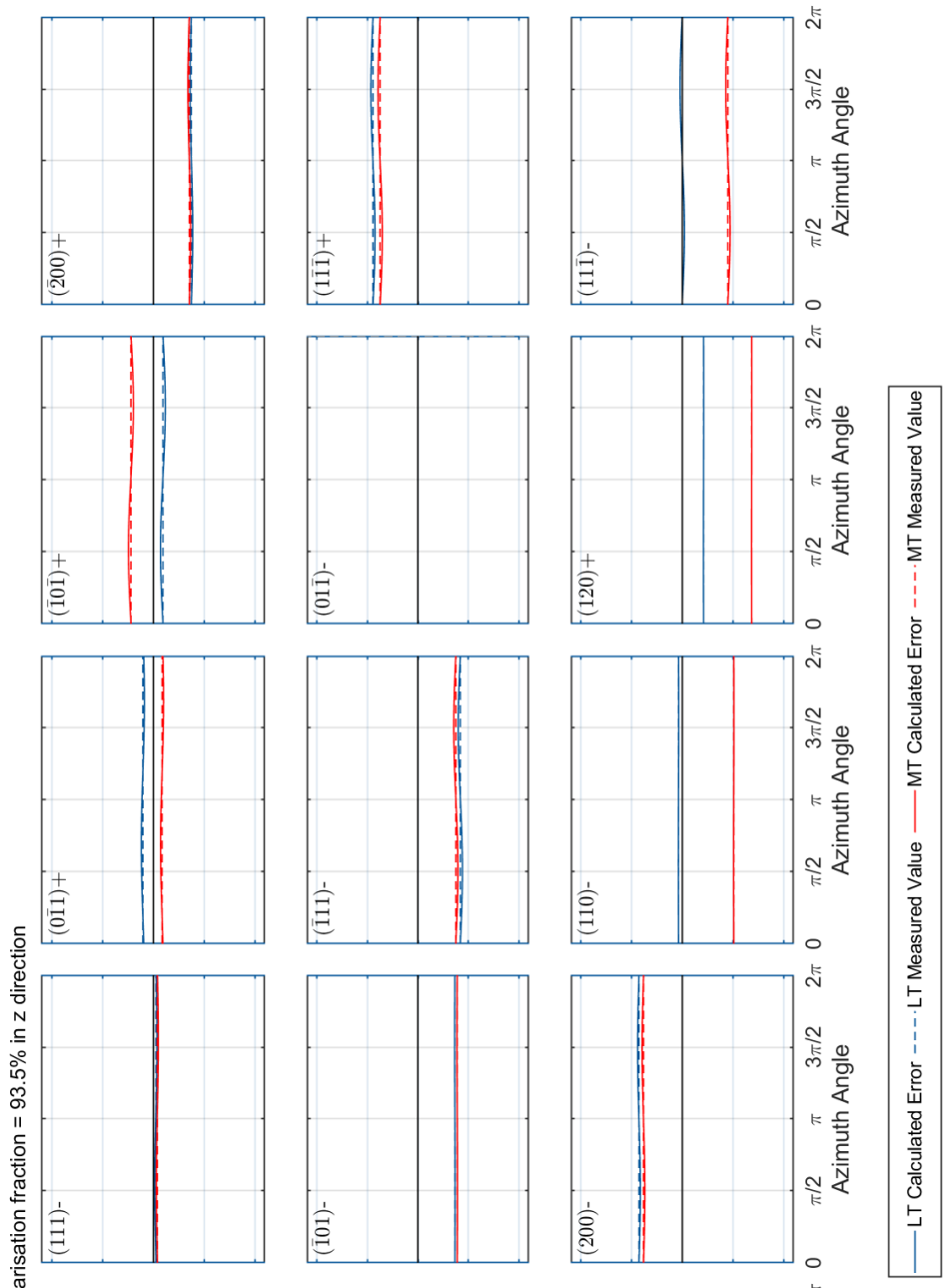

Figure 4.14: The calculated value of $\tilde{P}_{zy}$ when an angular resolution of 2° is assumed on the incident neutron polarisation. The panels correspond to the 15 Bragg peaks considered in this study. The solid curves indicate $\tilde{P}_{zy}$ against the azimuth angle ϕ so that the amplitude of these curves gives the 'worst-case' value for the error. The dashed lines show the measured value of $\tilde{P}_{zy}$ for each Bragg peak. LT phase is blue and MT phase is red. ©2020 APS

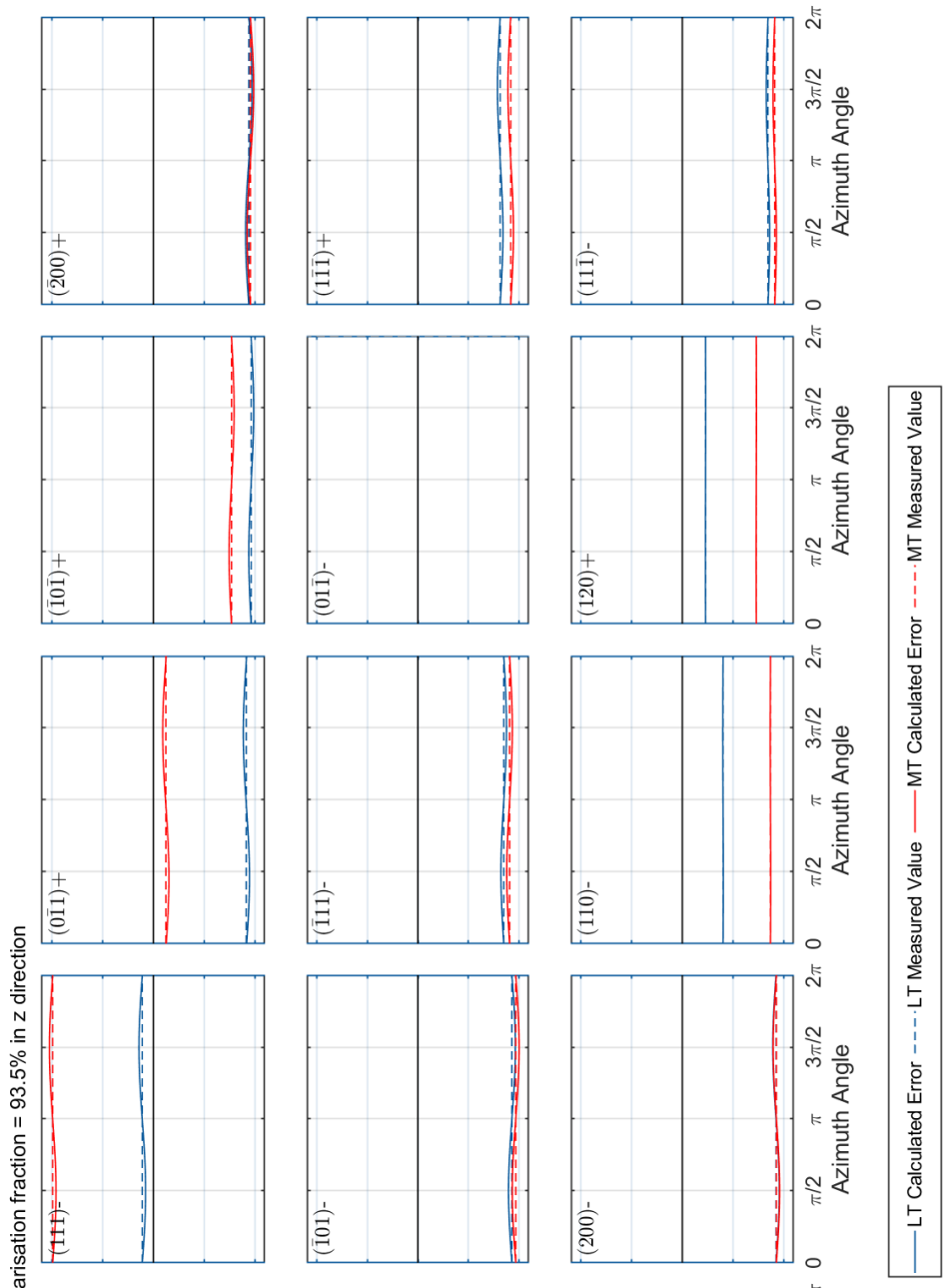

Figure 4.15: The calculated value of $\tilde{P}_{zz}$ when an angular resolution of 2° is assumed on the incident neutron polarisation. The panels correspond to the 15 Bragg peaks considered in this study. The solid curves indicate $\tilde{P}_{zz}$ against the azimuth angle ϕ so that the amplitude of these curves gives the 'worst-case' value for the error. The dashed lines show the measured value of $\tilde{P}_{zz}$ for each Bragg peak. LT phase is blue and MT phase is red. ©2020 APS

Having understood the matrix elements and deviations from some of the strict rules established by the Blume-Maleev equations, the results for the refined magnetic structures of CNO can be discussed.

4.2.3 Refined Magnetic Structure

The magnetic structures that result from the polarisation matrix refinements are detailed in Tables 4.1 and 4.2, and illustrated in Figures 4.16, 4.17, and 4.19. They can both be described by a rotating spin model:

$$S_i(\vec{L}) = \mathcal{R}_i \cos\left(\vec{k}\cdot\vec{L}+\Phi_i\right) + \mathcal{I}_i \sin\left(\vec{k}\cdot\vec{L}+\Phi_i\right), \tag{4.17}$$

where i labels the Cu sites and $\vec{L}$ is a real space lattice vector. Coordinates in this section are given with respect to a spherical polar coordinate system (r,ϕ,θ) constructed inside an orthonormal basis (x',y',z') where $x' \parallel a$ with b in the $x'-y'$ plane.

In the LT phase, the ground state of the system exhibits a generic helicoidal structure (Table 4.1, Figure 4.16). Here the spin rotation is confined to the plane spanned by the real and imaginary parts of $\vec{M}_\perp(\vec{Q})$. This plane can be wholly described by its normal direction which may be written in angular coordinates (ϕ,θ). In this study, a rotation plane whose normal has angular coordinates of $(59.73^\circ, 80.81^\circ)$ for the Cu$(1a)$ site and $(59.78^\circ, 81.00^\circ)$ for Cu$(2i)$ was refined. As noted in Section 3.3.4, CRYOPAD is not sensitive to the absolute moment value, but as shown in Table 4.1, the ratio of the Cu^{2+} moments on different sites is consistent with the unpolarised work giving a value of $|M_{Cu(1a)}/M_{Cu(2i)}| = 0.89\mu_B/0.69\mu_B$ [15].

Table 4.1: The refined magnetic structure at ≈ 3.5 K. Magnitudes are normalised. ©2020 APS

	$\lvert M\rvert$ (arb. units)	ϕ ($^\circ$)	θ ($^\circ$)	Φ (2π rad.)
$\mathcal{R}_1$	1	-43.62	35.01	0
$\mathcal{I}_1$	0.76	-23.93	124.32	
$\mathcal{R}_2$	0.78	-43.41	34.77	0.515
$\mathcal{I}_2$	0.59	-24.04	123.15	
$\mathcal{R}_3$	0.78	-43.41	34.77	0.525
$\mathcal{I}_3$	0.59	-24.04	123.15	

In this phase, the Cu^{2+} sites form ferromagnetic trimers which in turn form an antiferromagnetic saw-tooth chain along the a direction. This is illustrated in Figure 4.17. Two chiral domains, as reflected by the loss of the inversion centre, were permitted in the refinement and the populations were refined to be roughly equal (46%\54%). This accounts for the small value of $\tilde{P}_{yx}$ and $\tilde{P}_{zx}$ as these terms have the opposite sign in the two domains as discussed in the context of the Blume-Maleev equations.

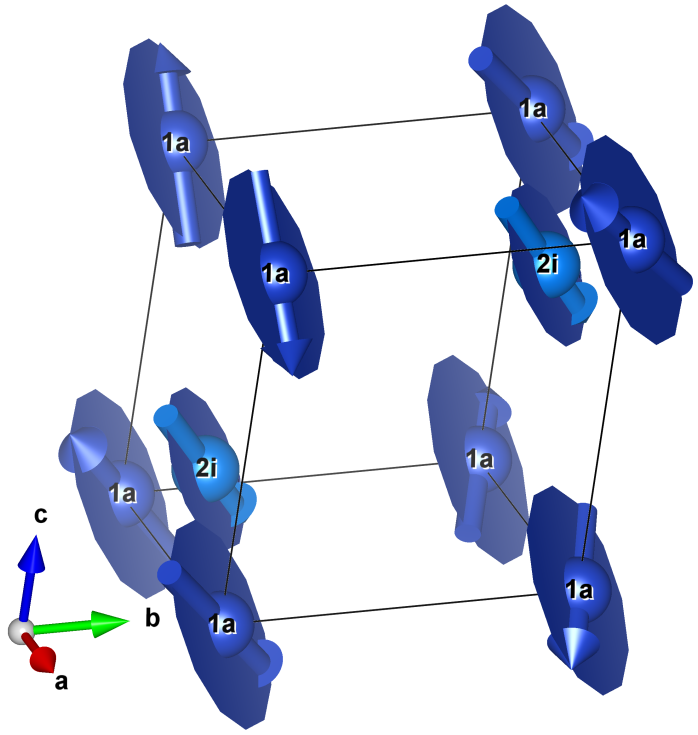

Figure 4.16: The refined magnetic structure of CNO in the LT phase. The Cu^{2+} magnetic moments are shown along with their rotational envelope. The two Wyckoff positions are labelled and shown in a different shade of blue for clarity. Figure made in VESTA [17]. ©2020 APS

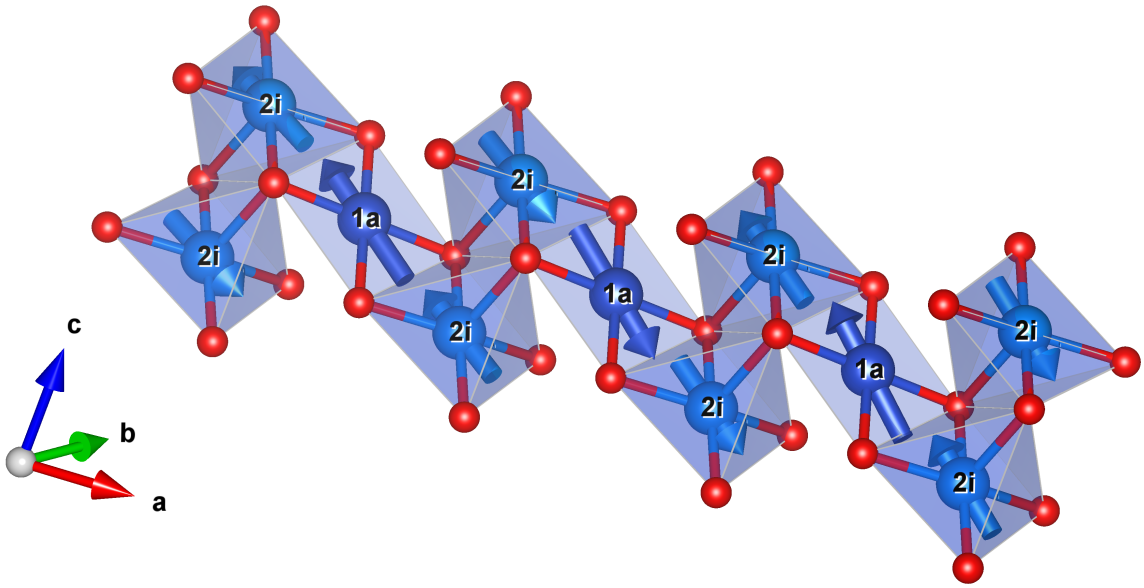

Figure 4.17: The Cu trimer saw-tooth chain. These trimers are ferromagnetically aligned but antiferromagnetically aligned with neighbouring trimers. The two Wyckoff positions are labelled and shown in a different shade of blue for clarity. Figure made in VESTA [17]. ©2020 APS

This structure is broadly in agreement with Johnson *et al.* who reported a plane normal of $(54.9^\circ, 75.5^\circ)$ [15]. This gives a discrepancy of $\approx 7^\circ$. Furthermore, whereas Johnson *et al.* reported a helicoidal structure with a circular rotation envelope from their powder sample, the best refinement of the SNP data from the single crystal results in an elliptical envelope. In the refinement presented in Figure 4.4, the length of the imaginary part of $M(\vec{Q})$ is 76% of the real part. This results in an elliptical rotation envelope with eccentricity of 0.65 compared to 0 from the circular structure reported by Johnson *et al.*

Whilst these differences may be attributed to the greater sensitivity of the SNP technique to the direction of the magnetic moments, a constraint was added into the refinement process in the LT phase such that the real and imaginary parts of $\vec{M}_\perp(\vec{Q})$ were of equal magnitude. Recalling Equation 4.17, if $\mathcal{R}_i$ and $\mathcal{I}_i$ have equal magnitude, then the rotation envelope becomes circular. This was to verify the elliptical fit. However, addition of this constraint produced a worse refinement than that presented in Section 4.2.3 with $\chi_r^2 = 62.40$ which is larger than the unconstrained fit ($\chi_r^2 = 37.98$). This refinement is shown in Figure 4.18, but the error bars only represent the purely statistical errors as this fit was not included in the systematic error calculations detailed in Section 4.2.2. However, this elliptical deviation can be expected to arise due to thermal fluctuations and, as this experiment was performed at finite temperature, it is possible the circular envelope is recovered as $T \to 0$.

In the structure reported here, the electric polarisation is still out of the rotation plane at $\approx 17^\circ$ to the plane normal. Moreover, although the phase difference of approximately π between the Cu$(1a)$ and Cu$(2i)$ sites strongly agrees with that reported by Johnson *et al.*, it is worth noting that the different coordinate systems used results in an overall $\approx 55^\circ$ phase factor.

In the MT phase, a spin density wave (SDW) structure is refined as the ground state (Table 4.2, Figure 4.19). SDW structures are typically found in metallic materials and are defined as a modulation of the local magnetic moment [28]. As in the LT case, the spin can be described by the rotating model with the rotation plane given by the real and imaginary parts of $M(\vec{Q})$. An SDW-like structure results when one of these becomes small compared to the other. In the refined structure, $\mathcal{I}m\{M_\perp(\vec{Q})\}$ becomes almost zero resulting in a highly elliptical rotational envelope which manifests as a modulation of the spins as can be seen in Figure 4.19(b) - (d). The polarisation of this SDW coincides with the LT rotation plane to within 2.5°. Also, all Cu^{2+} sites are now in phase. With the loss of TRS at T_N, 180° domains should be expected in this phase. However, as these will produce the same polarisation matrix, only one domain was included in the refinement.

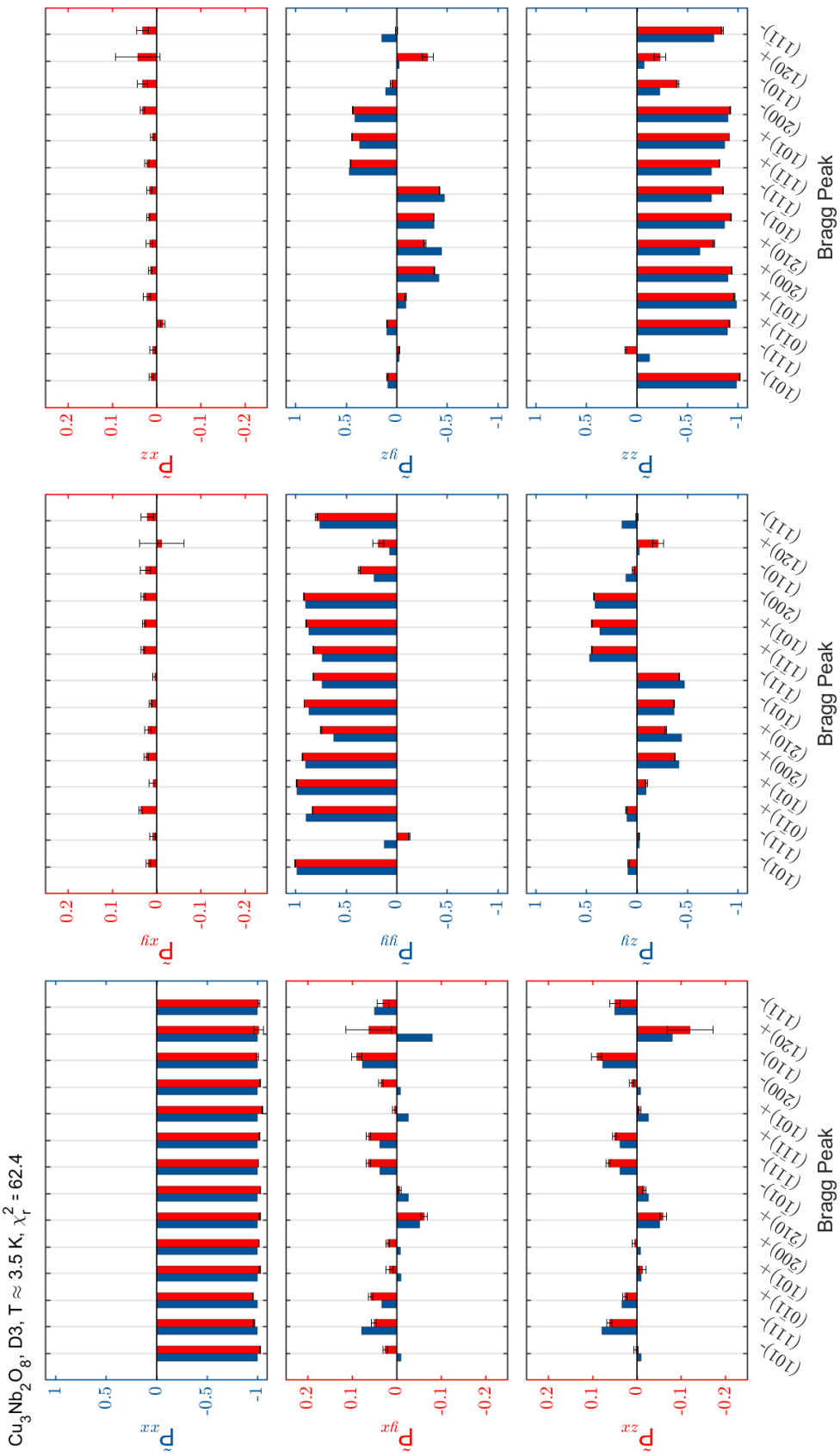

Figure 4.18: The refinement (in MAG2POL) of the polarisation matrix at ≈ 3.5 K - LT phase. This refinement is the result of constraining the rotational envelope of the Cu^{2+} moments to be circular. This produced a noticeably worse fit than that presented in the main text (section 4.2.3). The bars show the refined matrix elements (left - blue) plotted for each Bragg peak against the measured matrix elements (right - red). Statistical experimental errors *only* are shown in black. The plotted matrix elements are corrected for detector spin filter efficiency. For clarity, two different y scales are used and are displayed in different colours. ©2020 APS

Table 4.2: The refined magnetic structure at ≈ 26.4 K. Due to symmetry ($P\bar{1}$) $\mathcal{R}_2 = \mathcal{R}_3$ and $\mathcal{I}_2 = \mathcal{I}_3$ and so the latter are omitted from the table. Magnitudes are normalised. ©2020 APS

	$\lvert M\rvert$ (arb. units)	ϕ (°)	θ (°)	Φ (2π rad.)
$\mathcal{R}_1$	0.75	−43.00	30.60	0
$\mathcal{I}_1$	0.063	−154.36	80.46	
$\mathcal{R}_2$	1	−46.35	30.34	0.000
$\mathcal{I}_2$	0.036	−150.28	72.99	

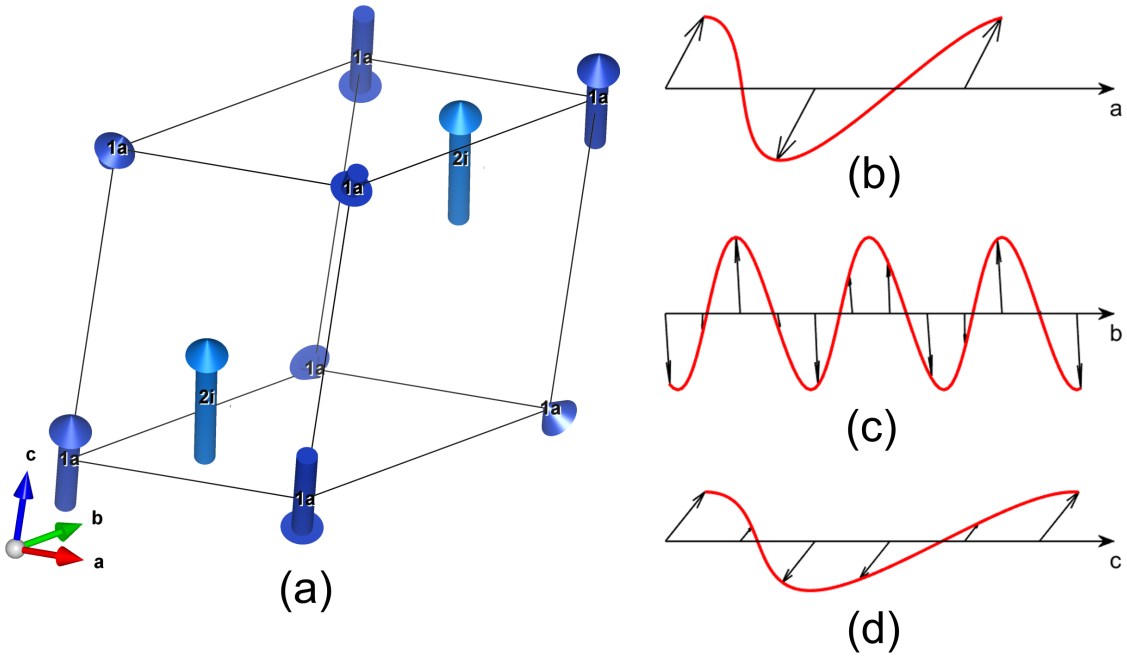

Figure 4.19: The refined magnetic structure of CNO in the MT phase. The Cu^{2+} magnetic moments in the context of the unit cell are shown in (a) whilst the in-plane oscillations along each crystal axis are shown in (b) - (d). As the propagation vector may be approximated as ($1/2$, $3/11$, $1/5$), approximately one complete oscillation along a should be contained within two unit cells, three complete oscillations along b contained within eleven unit cells and one complete oscillation along c contained within five unit cells. This is seen in the figure. The out-of-plane oscillations are much smaller in comparison and so are not plotted. This is due to $\mathcal{I}m\{M_\perp(\vec{Q})\} \ll \mathcal{R}e\{M_\perp(\vec{Q})\}$ in this phase. The two Wyckoff positions are labelled and shown in a different shade of blue for clarity. Figure (a) made in VESTA [17]. ©2020 APS

4.2.4 Temperature Dependence

The temperature dependence of the polarisation matrix was also measured. Figure 4.20 shows the element $\tilde{P}_{yz}$ measured on the Bragg peak $(\bar{2}10)+$ against temperature. A power law $|T - T_N|^{2\beta}$ was fitted with an exponent $\beta = 0.154$. The fact that this is centred on T_N reflects that $\tilde{P}_{yz}$ is indicative of magnetic ordering. This exponent is consistent with an Ising interpretation [29]. This can be motivated by considering the crystal field as the O polyhedra surrounding the Cu^{2+} are distorted by the crystal field which induces an anisotropy in a direction in which there is an energy cost associated with flipping a spin [30].

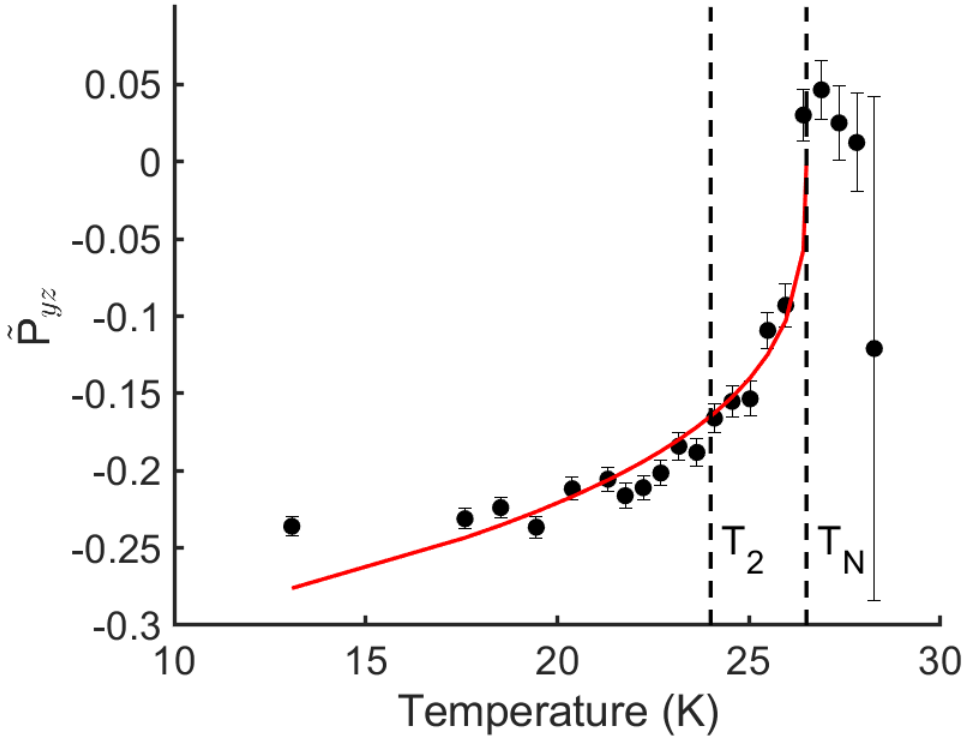

Figure 4.20: Plot of matrix element $\tilde{P}_{yz}$ against temperature. This was measured on the Bragg peak $(\bar{2}10)+$. The Néel temperature $T_N \approx 26.5$ K is indicated. The fit (solid line) shows a power law $|T - T_N|^{2\beta}$ with exponent $\beta = 0.154$. ©2020 APS

4.2.5 Multiferroic Mechanism

This subsection will address the interpretation of the refined structure and discuss the possible mechanisms behind the reported magnetic structure and, in particular, the presence of a SDW in the MT phase. Multiferroics, where one of the order parameters of interest is electric polarisation, are typically insulators [31–33]. Despite this, recently non-metallic systems have been reported where SDW-like structures have been found [34] to coexist with ferroelectricity. In a metallic material, a SDW arises due the presence of a nesting vector which links parts of the Fermi surface [28, 35, 36]. However, insulators lack such a surface and so these spin density

waves must be the product of a different mechanism.

Triclinic CNO is constrained by few symmetry elements with only an inversion centre in the paramagnetic phase and, as such, the magnetic free energy near T_N can, therefore, be expanded in symmetry-allowed even powers of the components of the site magnetisation $\vec{M}$ [37]

$$f_M(T) = f_0 + \alpha_x(T)|M_x|^2 + \alpha_y(T)|M_y|^2 + \alpha_z(T)|M_z|^2 + \beta_{ij}|M_i|^2|M_j|^2 + \cdots . \tag{4.18}$$

For the purpose of this simple illustration, any cross and gradient terms have been neglected. Owing to the lack of symmetry elements with only the presence of an inversion centre, there is no requirement that the α_i components are equal and a magnetic transition occurs when one of these goes to zero. However, even with the assumption that the magnitude of $\vec{M}$ must be fixed, the free energy can be written as

$$f_M(T) = f_0 + (\alpha_x(T) - \alpha_z(T))|M_x|^2 + (\alpha_y(T) - \alpha_z(T))|M_y|^2 + \alpha_z(T)|M|^2 + \beta_{ij}|M_i|^2|M_j|^2 + \cdots , \tag{4.19}$$

which preserves the fact that each component of the order parameter may have different temperature dependencies.

This description of the phase transition gives an anisotropy in the spatial structure of the real-space magnetism near the magnetic transition. However, it is not a SDW in the context of those observed in metallic systems owing to a nesting wave vector across an electronic Fermi surface [28, 35, 36]. This is corroborated by the temperature dependence of the off-diagonal term in the polarisation matrix $\tilde{P}_{yz}$ which shows little response to the second transition. Furthermore, if the structure did become a collinear SDW in this phase, all off diagonal terms in the polarisation matrix should go to zero - this is not observed in Figure 4.20. Therefore, it is concluded that the 'SDW' phase in CNO near the Néel transition is rather a manifestation of the symmetry-allowed decoupling of the different components of the order parameter.

In this way the decoupled magnetic structure destabilises the crystal structure to the point where it induces the structural chirality at T_2 due to the presence of critical fluctuations around T_N. This implies that the two transitions are indirectly coupled in an analogue with the Jahn-Teller effect where a structural distortion lifts the orbital degeneracy and lowers the symmetry. This allows magnetic ordering to occur at a lower temperature [38] *c.f.* MgV_2O_4, ZnV_2O_4 [39–42].

Microscopically this mechanism can be motivated from the inverse D.-M. effect whereby a magnetic structure with a helical component will induce structural chirality [43, 44]. Furthermore, it is compatible with ferro-axial coupling [15] and other symmetry considerations [45, 46]. The generic helicoidal structure is returned at low temperatures and is consistent with this study. Choosing the z direction to be component that that goes to zero at T_N, such that $\alpha_z(T) \propto |T - T_N|$, at a temperature below T_N one component of the magnetisation will dominate the free energy.

Terms in the free energy coupling magnetisation and structural order parameters will then allow it to become energetically favourable for the structure to distort when the transition from $P\bar{1} \rightarrow P1$ occurs, as observed in CNO.

Further analogy may be drawn with the nematic phase in Fe-based superconductors, i.e. the Fe pnictides [47]. Here it is argued the introduction of one type of ordering induces, via symmetry, others and thus the nematic order must be considered as resultant from "*correlation-driven electronic instabilities*" [47], which are likely driven by magnetic fluctuations. Similarly, in the case of $Fe_{1+x}Te$, a SDW structure is observed near the phase transition which is reported to be stabilised by magnetic fluctuations [48, 49].

Many of the 'SDW' phases reported in the literature for magnetic insulators may be speculated to arise due to the decoupling of the different components of the order parameter. In analogy with a fictitious force, whilst these 'SDW' phases appear genuine, they are simply the result of a deeper mechanism. Measuring the temperature dependence of the polarisation matrix is clearly important in understanding these transitions. Indeed, in the case of $Ni_3V_2O_8$ [34, 50], a similar mechanism has also been proposed in order to account for the presence of such a magnetic and ferroelectric structure where the ferroelectricity is due to a spin-induced symmetry breaking [51]. This has interesting consequences for the controlling of electric properties in these materials by applied magnetic fields which merits further study.

4.3 Chapter Conclusions

In conclusion, spherical neutron polarimetry was used to study the magnetic structure of CNO. The full polarisation matrix was determined in both low temperature phases for multiple magnetic Bragg peaks and the structure was refined to an apparent SDW below $T_N \approx 26.5$ K, which becomes generically helicoidal below $T_2 \approx 24$ K. The low temperature phase was found to be generally in agreement with the powder structure reported by Johnson *et al*. The temperature dependence of the matrix was also measured and the critical exponent extracted. A mechanism was proposed which could explain the presence of the SDW in this insulator. The structure, which manifests as an imitation of a SDW at finite temperatures, is actually reflective of the symmetry-allowed decoupling of the components of the order parameter allowing one to dominate the free energy. In turn, this then allows, through a coupling between magnetic and structural order parameters, the structural distortion and the manifestation of the electric polarisation.

References

[1] "Ire standards on piezoelectric crystals: Measurements of piezoelectric ceramics, 1961," *Proceedings of the IRE*, vol. 49, no. 7, pp. 1161–1169, 1961. DOI: 10.1109/JRPROC.1961.287860.

[2] W. P. Mason, *Electromechanical Transducers Wave Filters*. Van Nostrand, 1948, ISBN: 9780442051648.

[3] A. H. Meitzler, H. F. Tiersten, A. W. Warner, D. Berlincourt, G. A. Coquin, and F. S. Welsh, *An American National Standard: IEEE Standard on Piezoelectricity*, ANSI/IEEE Std 176-1987, 1987.

[4] S. Sherrit, H. D. Wiederick, and B. K. Mukherjee, "Non-iterative evaluation of the real and imaginary material constants of piezoelectric resonators," *Ferroelectrics*, vol. 134, no. 1, pp. 111–119, 1992. DOI: 10.1080/00150199208015574.

[5] S. Sherrit, H. D. Wiederick, and B. K. Mukherjee, "Complete characterization of the piezoelectric, dielectric, and elastic properties of motorola PZT 3203 HD, including losses and dispersion," *Proceedings spie 3037, Medical Imaging 1997: Ultrasonic Transducer Engineering*, vol. 3037, pp. 158–169, 1997. DOI: 10.1117/12.271326.

[6] C. Alemany, L. Pardo, B. Jimenez, F. Carmona, J. Mendiola, and A. M. González, "Automatic iterative evaluation of complex material constants in piezoelectric ceramics," *J. Phys. D: Appl. Phys.*, vol. 27, no. 1, pp. 148–155, 1994. DOI: 10.1088/0022-3727/27/1/023.

[7] M. Algueró, C. Alemany, L. Pardo, and A. M. González, "Method for obtaining the full set of linear electric, mechanical, and electromechanical coefficients and all related losses of a piezoelectric ceramic," *J. Am. Ceram. Soc.*, vol. 87, no. 2, pp. 209–215, 2004. DOI: 10.1111/j.1551-2916.2004.00209.x.

[8] L. Pardo, M. Algueró, and K. Brebøl, "A non-standard shear resonator for the matrix characterization of piezoceramics and its validation study by finite element analysis," *J. Phys. D: Appl. Phys.*, vol. 40, no. 7, pp. 2162–2169, 2007. DOI: 10.1088/0022-3727/40/7/046.

[9] A. M. González, Á. García, C. Benavente-Peces, and L. Pardo, "Revisiting the characterization of the losses in piezoelectric materials from impedance spectroscopy at resonance," *Materials*, vol. 9, no. 2, 2016. DOI: 10.3390/ma9020072.

[10] L. Tang and W. Cao, "Characterization of full set material constants and their temperature dependence for piezoelectric materials using resonant ultrasound spectroscopy," *J. Vis. Exp.*, e53461, 110 2016. DOI: doi:10.3791/53461.

[11] N. G. Fenu, N. Giles-Donovan, M. . R. Sadiq, and S. Cochran, "Full set of material properties of lead-free PIC 700 for transducer designers," *IEEE Trans. Ultrason. Ferroelectr. Freq. Contr.*, vol. 68, no. 5, pp. 1797–1807, 2021. DOI: 10.1109/TUFFC.2020.3044790.

[12] N. G. Fenu, "Investigation of piezoelectric materials for ultrasonic surgery," PhD thesis, University of Glasgow, 2021.

[13] C. Kittel, *Introduction to Solid State Physics*, 8th. John Wiley & Sons, Inc., 2005, ISBN: 0-471-41526-X.

[14] R. F. Egerton, *Electron Energy-Loss Spectroscopy in the Electron Microscope*, 3rd. Springer, 2011, ISBN: 978-1-4419-9583-4.

[15] R. D. Johnson *et al.*, "$Cu_3Nb_2O_8$: A multiferroic with chiral coupling to the crystal structure," *Phys. Rev. Lett.*, vol. 107, p. 137 205, 13 2011. DOI: 10.1103/PhysRevLett.107.137205.

[16] S.-W. Cheong, Private communication.

[17] K. Momma and F. Izumi, "VESTA*3* for three-dimensional visualization of crystal, volumetric and morphology data," *J. Appl. Crystallogr.*, vol. 44, no. 6, pp. 1272–1276, 2011. DOI: 10.1107/S0021889811038970.

[18] H. Katsura, N. Nagaosa, and A. V. Balatsky, "Spin current and magnetoelectric effect in noncollinear magnets," *Phys. Rev. Lett.*, vol. 95, p. 057 205, 5 2005. DOI: 10.1103/PhysRevLett.95.057205.

[19] G. Sharma, J. Saha, S. Kaushik, V. Siruguri, and S. Patnaik, "Improper ferroelectricity in helicoidal antiferromagnet $Cu_3Nb_2O_8$," *Solid State Commun.*, vol. 203, pp. 54–57, 2015. DOI: 10.1016/j.ssc.2014.11.016.

[20] H. J. Xiang, E. J. Kan, Y. Zhang, M.-H. Whangbo, and X. G. Gong, "General theory for the ferroelectric polarization induced by spin-spiral order," *Phys. Rev. Lett.*, vol. 107, p. 157 202, 15 2011. DOI: 10.1103/PhysRevLett.107.157202.

[21] X. Z. Lu, M.-H. Whangbo, S. Dong, X. G. Gong, and H. J. Xiang, "Giant ferroelectric polarization of $CaMn_7\mathbf{O}_{12}$ induced by a combined effect of dzyaloshinskii-moriya interaction and exchange striction," *Phys. Rev. Lett.*, vol. 108, p. 187 204, 18 2012. DOI: 10.1103/PhysRevLett.108.187204.

[22] Z.-L. Li, M.-H. Whangbo, X. G. Gong, and H. J. Xiang, "Helicoidal magnetic structure and ferroelectric polarization in $Cu_3Nb_2O_8$," *Phys. Rev. B*, vol. 86, p. 174 401, 17 2012. DOI: 10.1103/PhysRevB.86.174401.

[23] S. M. Koohpayeh, D. Fort, and J. S. Abell, "The optical floating zone technique: A review of experimental procedures with special reference to oxides," *Prog. Cryst. Growth Charact. Mater.*, vol. 54, no. 3, pp. 121–137, 2008. DOI: 10.1016/j.pcrysgrow.2008.06.001.

[24] N. Qureshi, "*Mag2pol*: A program for the analysis of spherical neutron polarimetry, flipping ratio and integrated intensity data," *J. Appl. Crystallogr.*, vol. 52, no. 1, pp. 175–185, 2019. DOI: 10.1107/S1600576718016084.

[25] P. J. Brown, "Spherical neutron polarimetry," in *Neutron Scattering from Magnetic Materials*, T. Chatterji, Ed., Elsevier Science, 2006, ch. 5, pp. 215–244, ISBN: 978-0-444-51050-1.

[26] F. Tasset *et al.*, "Spherical neutron polarimetry with cryopad-ii," *Phys. B: Condens. Matter*, vol. 267-268, pp. 69–74, 1999. DOI: 10.1016/S0921-4526(99)00029-0.

[27] E. Lelièvre-Berna *et al.*, "Advances in spherical neutron polarimetry with cryopad," *Phys. B: Condens. Matter*, vol. 356, no. 1, pp. 131–135, 2005. DOI: 10.1016/j.physb.2004.10.063.

[28] G. Grüner, *Density Waves in Solids*. Perseus, 1994, ISBN: 9780429501012.

[29] M. F. Collins, *Magnetic Critical Scattering*. Oxford University Press, 1989, ch. 5, ISBN: 9780195046007.

[30] K. Yosida, *Theory of Magnetism*. Springer, 1996, ISBN: 3-540-60651-3.

[31] P. W. Anderson and E. I. Blount, "Symmetry considerations on martensitic transformations: "ferroelectric" metals?" *Phys. Rev. Lett.*, vol. 14, pp. 217–219, 7 1965. DOI: 10.1103/PhysRevLett.14.217.

[32] Y. Shi *et al.*, "A ferroelectric-like structural transition in a metal," *Nat. Mater.*, vol. 12, no. 11, pp. 1024–1027, 2013. DOI: 10.1038/nmat3754.

[33] C. D. O'Neill, D. A. Sokolov, A. Hermann, A. Bossak, C. Stock, and A. D. Huxley, "Inelastic x-ray investigation of the ferroelectric transition in SnTe," *Phys. Rev. B*, vol. 95, p. 144 101, 14 2017. DOI: 10.1103/PhysRevB.95.144101.

[34] M. Kenzelmann *et al.*, "Field dependence of magnetic ordering in kagomé-staircase compound $Ni_3V_2O_8$," *Phys. Rev. B*, vol. 74, p. 014 429, 1 2006. DOI: 10.1103/PhysRevB.74.014429.

[35] A. W. Overhauser, "Spin density waves in an electron gas," *Phys. Rev.*, vol. 128, pp. 1437–1452, 3 1962. DOI: 10.1103/PhysRev.128.1437.

[36] Y. Feng *et al.*, "Incommensurate antiferromagnetism in a pure spin system via cooperative organization of local and itinerant moments," *Proc. Natl. Acad. Sci.*, vol. 110, no. 9, pp. 3287–3292, 2013. DOI: 10.1073/pnas.1217292110.

[37] J. C. Tolédano and P. Tolédano, *The Landau Theory of Phase Transitions*. World Scientific, 1987, ch. 2, ISBN: 978-981-3103-94-8.

[38] D. Khomskii, *Transition Metal Compounds*. Cambridge University Press, 2014, ISBN: 9781139096782.

[39] T. Weber *et al.*, "Transverse acoustic phonon anomalies at intermediate wave vectors in MgV_2O_4," *Phys. Rev. B*, vol. 96, p. 184 301, 18 2017. DOI: 10.1103/PhysRevB.96.184301.

[40] H. Mamiya, M. Onoda, T. Furubayashi, J. Tang, and I. Nakatani, "Structural and magnetic studies on vanadium spinel MgV_2O_4," *J. Appl. Phys.*, vol. 81, no. 8, pp. 5289–5291, 1997. DOI: 10.1063/1.364518.

[41] E. M. Wheeler *et al.*, "Spin and orbital order in the vanadium spinel MgV_2O_4," *Phys. Rev. B*, vol. 82, p. 140 406, 14 2010. DOI: 10.1103/PhysRevB.82.140406.

[42] M. Reehuis, A. Krimmel, N. Büttgen, A. Loidl, and A. Prokofiev, "Crystallographic and magnetic structure of ZnV_2O_4," *Eur. Phys. J. B*, vol. 35, pp. 311–316, 3 2003. DOI: 10.1140/epjb/e2003-00282-4.

[43] I. Dzyaloshinsky, "A thermodynamic theory of "weak" ferromagnetism of antiferromagnetics," *J. Phys. Chem. Solids*, vol. 4, no. 4, pp. 241–255, 1958. DOI: 10.1016/0022-3697(58)90076-3.

[44] T. Moriya, "Anisotropic superexchange interaction and weak ferromagnetism," *Phys. Rev.*, vol. 120, pp. 91–98, 1 1960. DOI: 10.1103/PhysRev.120.91.

[45] J. Hlinka, "Eight types of symmetrically distinct vectorlike physical quantities," *Phys. Rev. Lett.*, vol. 113, p. 165 502, 16 2014. DOI: 10.1103/PhysRevLett.113.165502.

[46] J. Hlinka, J. Privratska, P. Ondrejkovic, and V. Janovec, "Symmetry guide to ferroaxial transitions," *Phys. Rev. Lett.*, vol. 116, p. 177 602, 17 2016. DOI: 10.1103/PhysRevLett.116.177602.

[47] R. M. Fernandes, A. V. Chubukov, and J. Schmalian, "What drives nematic order in iron-based superconductors?" *Nat. Phys.*, vol. 10, pp. 97–104, 2 2014. DOI: 10.1038/nphys2877.

[48] D. Parshall *et al.*, "Competition between commensurate and incommensurate magnetic ordering in $Fe_{1+y}Te$," *Phys. Rev. B*, vol. 85, p. 140 515, 14 2012. DOI: 10.1103/PhysRevB.85.140515.

[49] C. Stock *et al.*, "Competing spin density wave, collinear, and helical magnetism in $Fe_{1+x}Te$," *Phys. Rev. B*, vol. 95, p. 144 407, 14 2017. DOI: 10.1103/PhysRevB.95.144407.

[50] G. Lawes *et al.*, "Competing magnetic phases on a kagomé staircase," *Phys. Rev. Lett.*, vol. 93, p. 247 201, 24 2004. DOI: 10.1103/PhysRevLett.93.247201.

[51] G. Lawes *et al.*, "Magnetically driven ferroelectric order in $Ni_3V_2O_8$," *Phys. Rev. Lett.*, vol. 95, p. 087 205, 8 2005. DOI: 10.1103/PhysRevLett.95.087205.

Chapter 5

$Pb(Fe_{1/2}Nb_{1/2})O_3$

This chapter presents the analysis through depth dependent muon techniques of the perovskite relaxor-ferroelectric $Pb(Fe_{1/2}Nb_{1/2})O_3$ (PFN). After a review of the contrasting previous studies of PFN, *negative* muon elemental analysis and zero field (ZF) *positive* muon spin relaxation results are presented. They confirm the absence of spatially long-range magnetic order and reveal a change near the surface concerning the magnetic ion Fe^{3+} and a two-state mechanism to account for this is discussed.

5.1 Chapter Introduction

Pb-based relaxor-ferroelectrics have challenged understanding of ferroelectric transitions in the presence of disorder, characteristically displaying a diffuse transition with a broadened, frequency dependent dielectric response [1–5]. Even with the diffuse nature of the paraelectric-ferroelectric transition, conventionally a single temperature scale is associated with this onset of ferroelectric order. However, two scales have been observed in relaxors [6]. Typically, a high temperature scale, defined by the Burns temperature and corresponding soft mode [7], introduces a root mean square (RMS) electric polarisation caused by short-range and dynamic correlations [8–10]. These so-called polar nano-region (PNR) have been directly observed in neutron and X-ray diffuse measurements and are characterised by momentum broadening [11–13]. The second, lower, temperature scale corresponds to when long-range ferroelectric correlations can be stabilised under an applied electric and when the PNRs become static [14, 15]. This is reflected by a large drop in the piezoelectric response [16].

This multiple-scale property of relaxors is also reflected in other domains with two length scales also being reported. Splitting of Bragg peaks indicate the introduction of a strain in the low temperature phases and this can be explained by the introduction of coexisting unit cell shapes such as rhombohedral and cubic phases observed [17]. Near-surface regions, where the unit cell shape seems to differ from the bulk, have been directly observed using diffraction techniques in relaxors such as PMN, PMN and their PT doped variants [17–22].

The cause behind this near-surface region is yet to be found but, in analogy to a similar effect observed in model magnets [23, 24], random field models are good candidates. These readily explain the two temperature scales in PMN and PZN based on random dipolar fields that result from the valence mismatch due to the B-site disorder [25–27].

5.1.1 $Pb(Fe_{1/2}Nb_{1/2})O_3$

$Pb(Fe_{1/2}Nb_{1/2})O_3$ (PFN) is a mixed perovskite relaxor-ferroelectric which has been reported to exhibit a coupling between magnetic and dielectric orders [28]. PFN contains a mixture of magnetic Fe^{3+}, with $S = 5/2$, $L = 0$, and non-magnetic Nb^{5+} on the B-site. Ferroelectric order has been observed below 400 K, evidenced by a corresponding recovery of a zone centre transverse optic soft mode [28]. PFN has been reported to show magnetoelectric coupling with anomalies reported in dielectric permittivity at the Néel temperature [29]. Unlike classic ferroelectrics [30, 31] and non-magnetic relaxors [25, 32], the energy of the polar soft mode in PFN deviates from the mean-field result at low temperatures. This has been suggested to correlate with the development of short-range magnetic correlations [28].

The magnetic structure of PFN is not well or consistently understood. It is reported to undergo two magnetic phase transitions with the first at $T_N \approx 140$ - 160 K [33] which supposedly corresponds to long-range ordering. Single crystal diffraction indicates that the system orders as an antiferromagnet with a momentum resolution-limited peak measured at $(1/2, 1/2, 1/2)$ [34], indicative of spatially long-range magnetic correlations. However, further anomalies were observed near 20 K in nuclear magnetic resonance (NMR) and magnetic susceptibility measurements indicating a second transition [35, 36]. This has now been interpreted as a transition to a spin glass structure [37] which coexists with the aforementioned long-range order [38, 39]. Neutron diffraction measurements have directly shown short and long-range order coexistence leading to models involving two phases defined by different Fe^{3+} clustering sizes [38].

However, Stock *et al.* reported a large single crystal sample which only shows short-range, glass ordering [28]. This will be referred to here as the size/order discrepancy as it may be correlated with the sample size: smaller and thinner samples have been found to display evidence for long-range magnetic ordering, whilst larger single crystals show only extremely short-range correlations [29, 39].

This study aims to address the question of the size/order discrepancy using depth dependent muon spectroscopy. In this way composition and magnetic properties can be probed over the near-surface region of the sample.

5.2 Results

Results are presented from two muon experiments that studied the near-surface composition, Section 5.2.2, and magnetic properties, Section 5.2.3. A discussion of both $\mu^{\pm}$ experiments will follow in Section 5.3.

5.2.1 Sample Details

For both muon experiments detailed in this chapter a single crystal sample of PFN was used with dimensions of $1\times1\times1$ cm^3. This is shown in Figure 5.1 and was grown at the Shanghai Institute of Ceramics using the modified-Bridgman method. This method is widely used in relaxor-ferroelectric crystal growth and is further reviewed in Chapter 6. The $\mu^{\pm}$ beam was incident onto a [100] crystallographic face. No sample preparation was required other than wrapping in foil and mounting the sample onto the experimental mount.

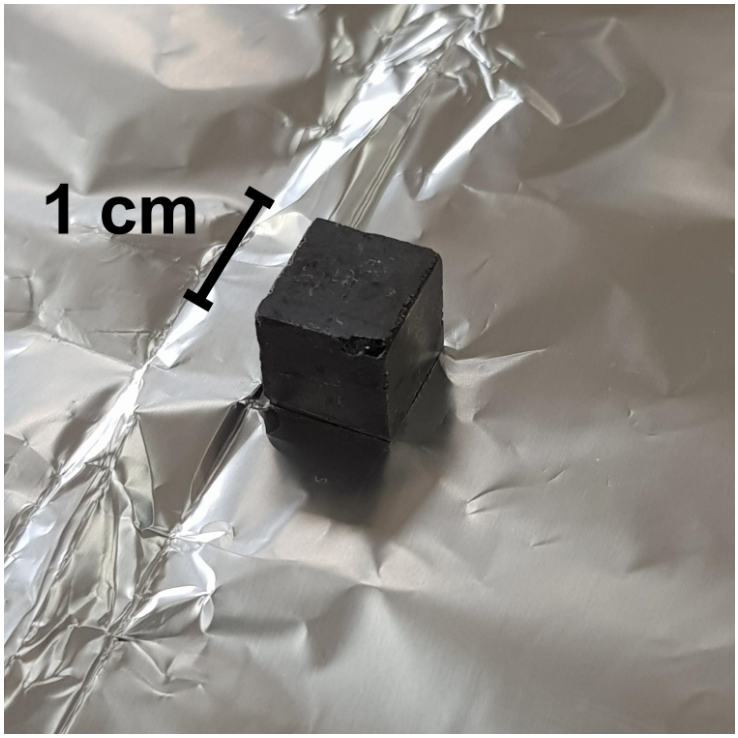

Figure 5.1: Single crystal sample of PFN.

This sample has be extensively characterised with neutron scattering [28, 40] and has previously been heated and cooled up to a maximum temperature of 500 K. These scattering experiments have confirmed the coupling between magnetic and ferroelectric orders [28] in agreement with the literature [29]. Furthermore, as described in the Section 5.1.1, these experiments have confirmed short-range order in this sample through diffuse scattering around both nuclear, as in non-magnetic relaxor-ferroelectrics such as PMN [11], and magnetic Bragg peaks [28, 40].

Table 5.1: Theoretical energies of the muonic transition lines of Pb, Fe and Nb that are relevant to this study [46].

Atom	Atomic	Transition	Energy (keV)
Pb	O	6h $\rightarrow$ 5g	233.7, 235
Fe	L	3d $\rightarrow$ 2p	265.7, 269.4
Nb	M	4f $\rightarrow$ 3d	231.4

These studies have also further confirmed the spatial B-site disorder in PFN where polarised neutrons were used to examine the nuclear scattering at $\vec{Q} = (1/2, 1/2, 1/2)$ [40]. Due to the equal fractions of Fe^{3+} and Nb^{5+}, structural ordering would establish a superlattice, as discussed in Chapter 2 in the compound $Pb(Sc_{1/2}Ta_{1/2})O_3$ [41, 42]. This superlattice would double the unit cell and so give rise to a Bragg peak at $(1/2, 1/2, 1/2)$. The lack of such a peak in this sample of PFN confirms the disorder of Fe^{3+} and Nb^{5+} ions in agreement with other studies [43, 44].

5.2.2 Compositional Analysis

First the composition near the surface was probed with the μ^- technique as detailed in Section 3.4.2. Six experimental runs, each at a different muon momentum corresponding to different implantation depths, allowed the relative concentration of Pb, Fe and Nb to be profiled with respect to depth. Stopping of the muons was simulated in SRIM/TRIM [45]. SRIM/TRIM calculates the stopping profile of ions in materials using statistical algorithms to simulate the collisions and other interactions in the stopping process. For the purpose of this simulation, the muon may be treated as a modified H^+ ion (the muon is approximately nine times lighter than the proton). In this simulation, the experimental setup was reconstructed which allowed the implantation depth of the muons to be determined for a given momenta. This involved measuring the 'layers' through which the muon will pass before implantation in the sample, i.e. air gap between the beam snout and the sample and the Al sample holder.

In this μ^- experiment, the range of muon momenta was 20 MeV/c - 35 MeV/c and the simulated stopping profiles for three of these momenta are shown in Fig. 5.2. This shows that 20 MeV/c corresponds to 'surface' implantation at ≈ 65 μm and 35 MeV/c to 'bulk' implantation at ≈ 570 μm, as indicated by the maxima of the distributions in Fig. 5.2. Also shown is the stopping distribution for 28 MeV/c to illustrate the shape of the intermediate profiles. This penetration range overlaps with the length-scales observed for the skin effect in non-magnetic relaxors ~ 100 μm [19, 22].

The main X-ray energy range of interest for this experiment is 220 - 280 keV and the emission lines contained within were tracked against implantation momentum. These peaks result from muonic X-ray emission by Nb, Pb and Fe and the energies and corresponding atomic transitions are detailed in Table 5.1 [46]. In this energy range, the observed transitions form part of the O series for Pb, the L series for Fe, and the M series for Nb [47].

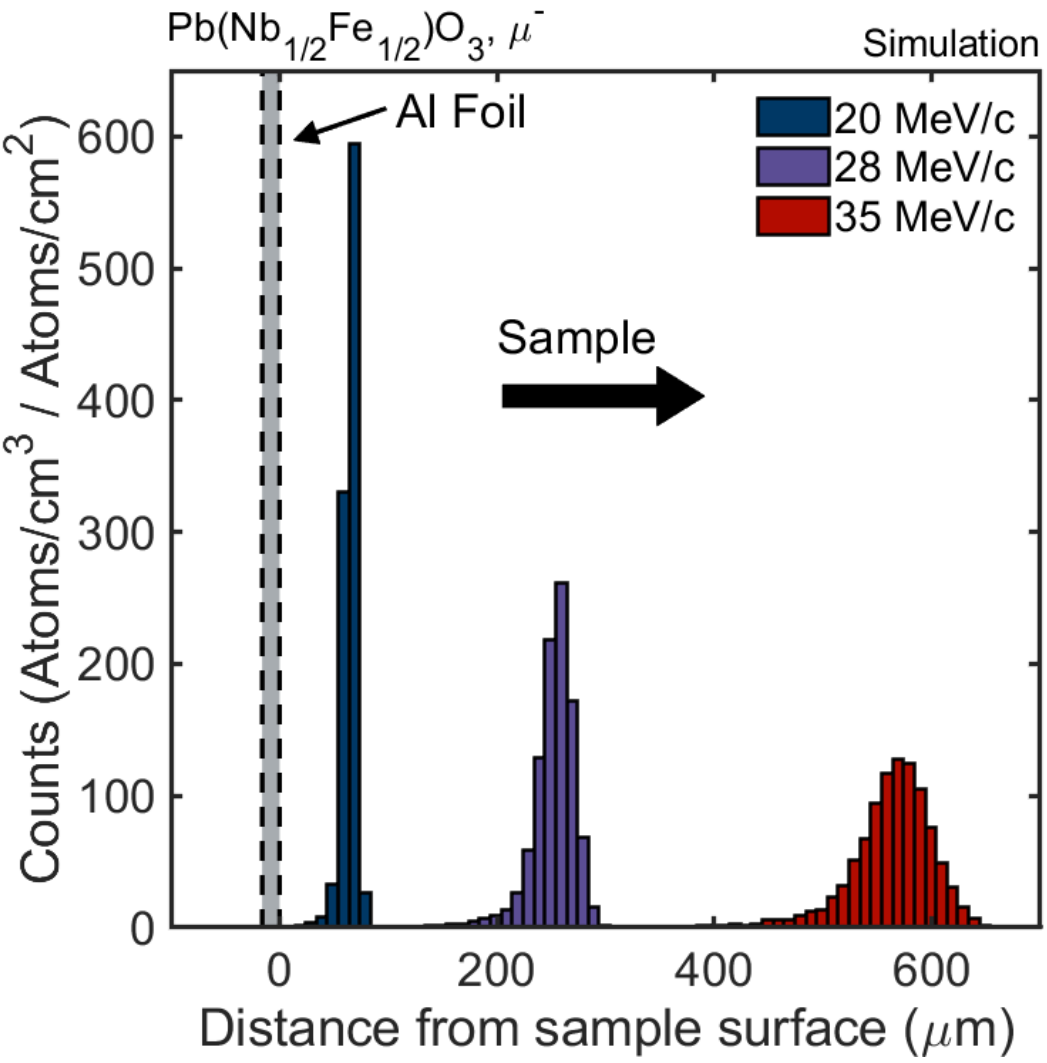

Figure 5.2: The results of a simulation in SRIM/TRIM [45] of μ^- implantation with momenta of 20 MeV/c, 28 MeV/c and 35 MeV/c. The peak of the distributions give the implantation depths as 65 μm, 260 μm and 570 μm respectively.

Figure 5.3 shows the five emission lines resulting from the transitions in Table 5.1 with each panel corresponding to a different momentum/depth. Gaussian fits are shown fitted to these five peaks and the overall fit is shown in red. A linear background term was also included determined by a least squares regression fit to the 'flat' portion of the spectrum between 240 keV and 260 keV. All fitting was carried out using MATLAB. The plots in Figure 5.3 have had this background term subtracted and are normalised to the fitted Pb peak at $\approx$ 233 keV which was assumed to be constant with depth. The issue of Pb vacancies was not specifically taken into account here as previous studies have reported little change in Pb with depth [48]. As the Pb atoms will have the least mobility, due to their relatively high mass, they are, therefore, assumed constant throughout the sample.

The normalised integrated intensity against depth for each peak is shown in Figure 5.4 and a simple linear fit is included as a guide to the eye. The width of each peak was found, within

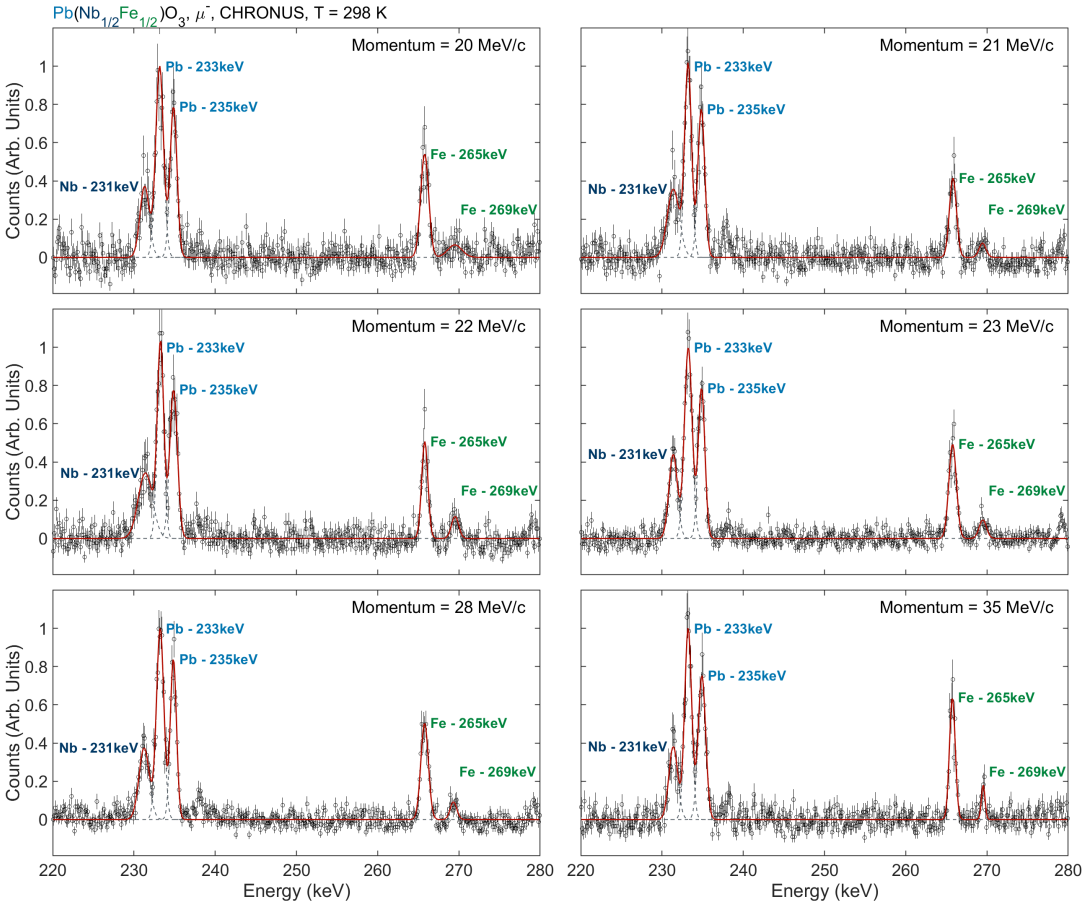

Figure 5.3: X-ray spectra resulting from μ^- implantation into the [001] face of PFN. The panels show different μ^- momenta corresponding to implantation depths between 65 μm (20 MeV/c) and 570 μm (35 MeV/c). The data were normalised to the Pb peak at $\approx$ 233 keV under the assumption that Pb is constant throughout the sample. This energy range clearly shows the emission lines in Table 5.1 for all momenta which allowed easy comparison. The red line shows the fit to the data and the linear background has been subtracted. Errors were estimated using Poisson/counting statistics. The small feature at $\approx$ 238 keV is likely to be another Nb emission line. However, it was not taken into account for this study as it is noticeably weaker than the line at $\approx$ 231 keV.

error, to be constant as a function of depth and so an average width was used for the integrated intensity calculation. This is indicative of broadening due to experimental mechanisms. Figure 5.4 appears to show a comparative deficiency of Fe near the surface of the sample and this will be discussed further in Section 5.3 in context of the μSR results. However, it would be advantageous to confirm this depth profile with other techniques. However, whilst methods such as energy dispersive X-ray spectroscopy or Rutherford backscattering are not inherently destructive and can be used to profile composition against depth, the preparation required can be. For example, in order to carry out energy dispersive X-ray spectroscopy in a scanning electron microscope, a cross-section of the sample must be made, typically through mechanical means such as grinding or cutting, which *is* destructive. This means that these sort of methods are not suited to rare, expensive or particularly interesting samples.

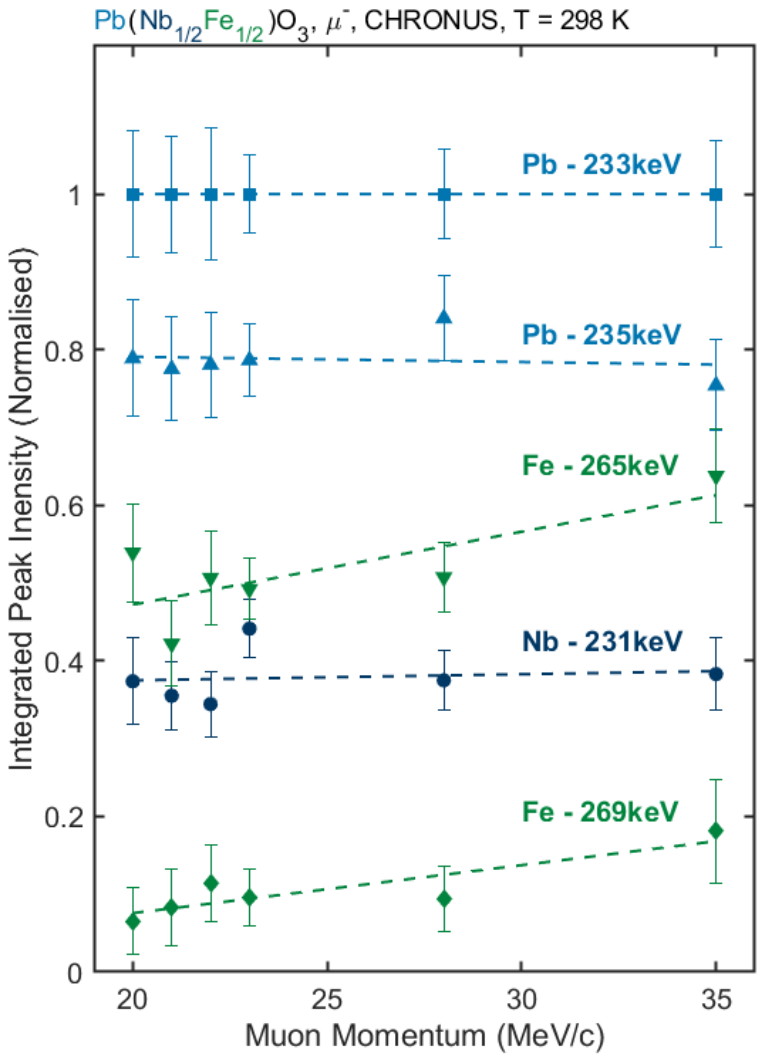

Figure 5.4: The integrated peak intensity of the muonic transition lines against momentum (depth). The range of depths probed is between 60 and 570 μm. The data are normalised to the Pb peaks at $\approx$ 233 keV. Straight lines are included as a guide to the eye. A deficiency in Fe appears to be shown near the surface of the sample and this can be correlated with the skin effect as measured in other relaxors.

5.2.3 Muon Spin Relaxation

To study the near-surface magnetic properties, the μSR technique with μ^+, as described in Section 3.4.3, was used. In this section, ZF μSR is first presented as a function of depth, tuned with incident muon momentum, followed by a temperature dependence study. All data are parameterised with a stretched exponential. Finally, the lack of magnetic order is confirmed using a longitudinal field (LF). The sample was wrapped in Ag foil and the experiment was carried out in a Janis dynamic He flow cryostat.

Depth Study

Firstly, four experimental runs at different momenta (implantation depths) were undertaken in order to allow the local magnetic properties to be profiled against depth. Muon implantation at a given momentum was again simulated in SRIM/TRIM [45]. The experimental setup distances were measured and reconstructed in the simulation in order to determine the stopping distance of the muons. The results of these calculations are shown in Figure 5.5(a) and it was found that 23 MeV/c corresponded best to a surface implantation depth of ≈ 5 μm as indicated by the maximum of the blue distribution in Figure 5.5(a). The maximum momentum of 27 MeV/c is also shown in red and corresponds to an implantation depth of ≈ 110 μm. As shown in Figure 3.3(b), any momentum above 27 MeV/c would require a change to decay muons in order to preserve the muon flux, although it still drops by two orders of magnitude. This change in the instrument settings was not feasible due to beam time constraints. Again, this penetration range overlaps with the length-scales observed for the skin effect in non-magnetic relaxors [19, 22].

Once the simulations had been run, the characterisation of the experimental setup could be carried out under a field of 20 G orientated transverse (TF) to the direction of spin polarisation, as standard. This allows the value of the forward-backward efficiency correction α and the initial values of the asymmetry to be estimated for each momentum. A relatively large TF ensures that there will be a strong muon precession signal and the amplitude of this gives a measure of the initial asymmetry. The results of this are shown in Figure 5.6. The full asymmetry on CHRONUS is $\approx 23\%$ and any dip in this value would indicate a reduced stopping of muons which is indicative of the surface of the sample. The measured values of α and initial asymmetry are plotted in Figure 5.5 (b) and (c) respectively against momentum. These are taken from the fits shown in Figure 5.6 in red. The drop-off in initial asymmetry clearly indicates that the surface is around 23 MeV/c, which agrees with the simulations. Based on these preliminary measurements, the momenta for the main experiment were chosen as 22.5 MeV/c, 23 MeV/c, 25 MeV/c and 27 MeV/c. All fitting was done using the WIMDA data analysis package [49].

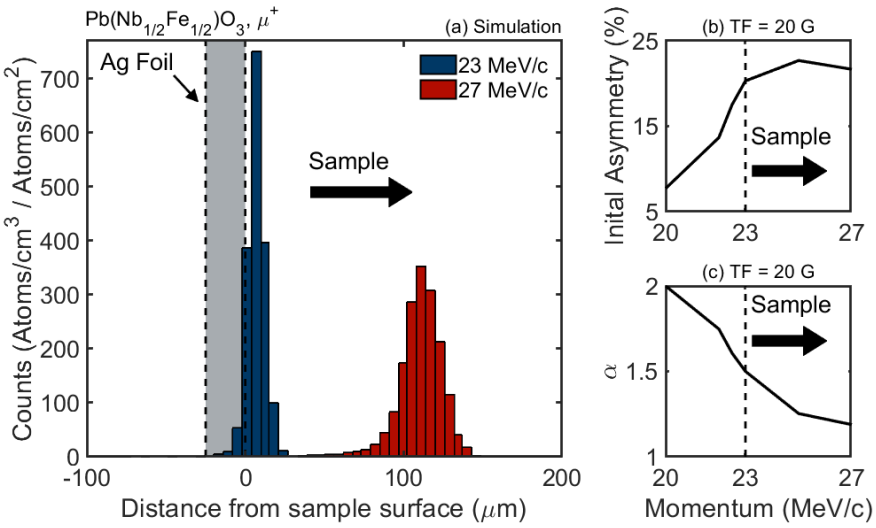

Figure 5.5: (a) Shows the results of a simulation in SRIM/TRIM [45] of μ^+ implantation with momenta of 23 MeV/c and 27 MeV/c. The peaks of the distributions give the implantation depths as ≈ 5 μm and ≈ 110 μm respectively. Also shown are (b) the measured initial asymmetry and (c) α values plotted against depth for a 20 G magnetic field orientated in the direction transverse to the muon spin polarisation measured on CHRONUS. The drop in asymmetry below 23 MeV/c indicates that the surface is near here which is in excellent agreement with the simulation.

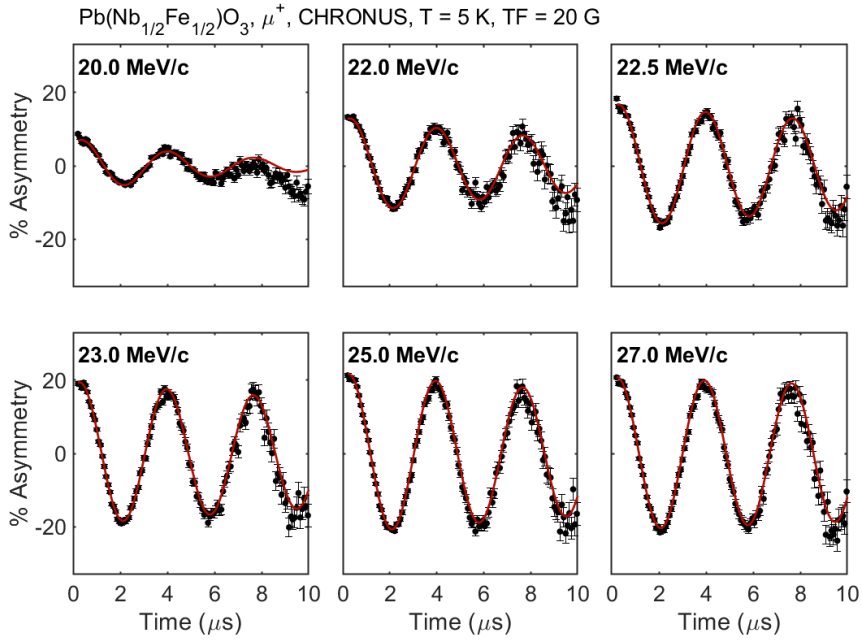

Figure 5.6: Muon asymmetry against time showing the μSR response under TF conditions against momentum (depth) for a field = 20 G. Oscillating fit is shown in red. The drop-off in amplitude below 23 MeV/c clearly indicates that this is the surface region in agreement with the simulations (Figure 5.5). For clarity, not all data points are plotted - a bunching factor (average) of 5 was used in WiMDA.

To study the spontaneous magnetic properties of the system, the main experiment was carried out under ZF conditions at a temperature of 5 K. The shallowest and deepest relaxation data are compared in Figure 5.7, where a slowing down of the relaxation with depth can be seen. These data were normalised using the initial symmetry values taken from the preliminary TF runs. The data were fitted using the stretched exponential function

$$A(t) = A_0 e^{-(\lambda t)^{\beta}}, \tag{5.1}$$

where A_0 is the normalised initial asymmetry, λ is the effective depolarisation rate and β is a power exponent. The use of this function will be discussed later, but it allows effective parameterisation of the asymmetry decay curve.

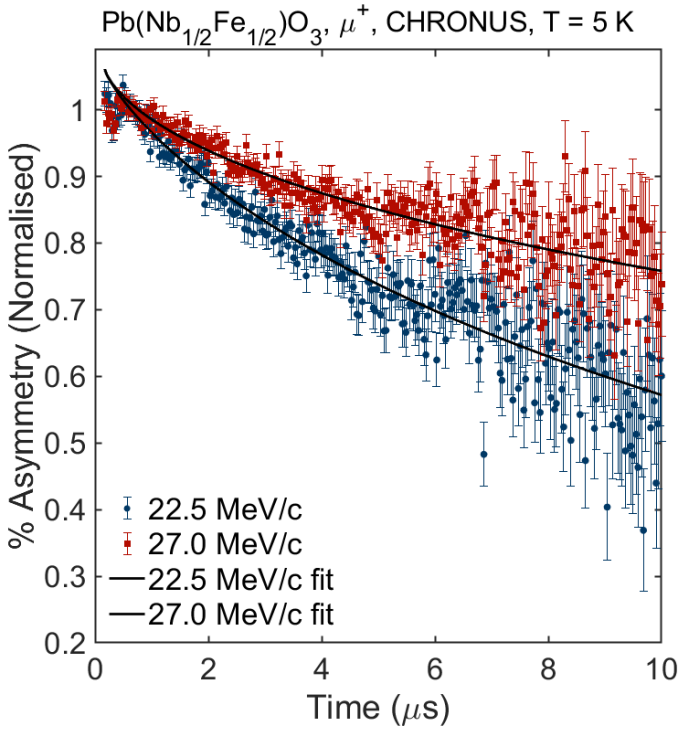

Figure 5.7: Muon asymmetry against time showing the μSR response under ZF conditions. Plotted are the shallowest ($\approx$ 5 μm, momentum = 22.5 MeV/c, blue) and deepest ($\approx$ 110 μm, momentum = 27 MeV/c, red) depths, to highlight the difference in the muon spin relaxation as a function of depth. Also plotted as solid lines are the stretched exponential fits that are discussed further in the main text.

The fitted values for these three parameters are plotted against muon momentum (depth) in Figure 5.8. It can be seen that both λ and β decrease with depth whilst A_0 remains roughly constant at near unity. This indicates that there is indeed a change in the magnetic properties as the depth is increased, which is consistent with the hypothesis that the change in Fe^{3+} near the surface impacts the magnetic structure. However, the constant $A_0 \approx 1$ implies that there is no long-range magnetic order in the sample. This is consistent with the measurements by Stock *et al.*, but in contradiction with the previous μSR of PFN.

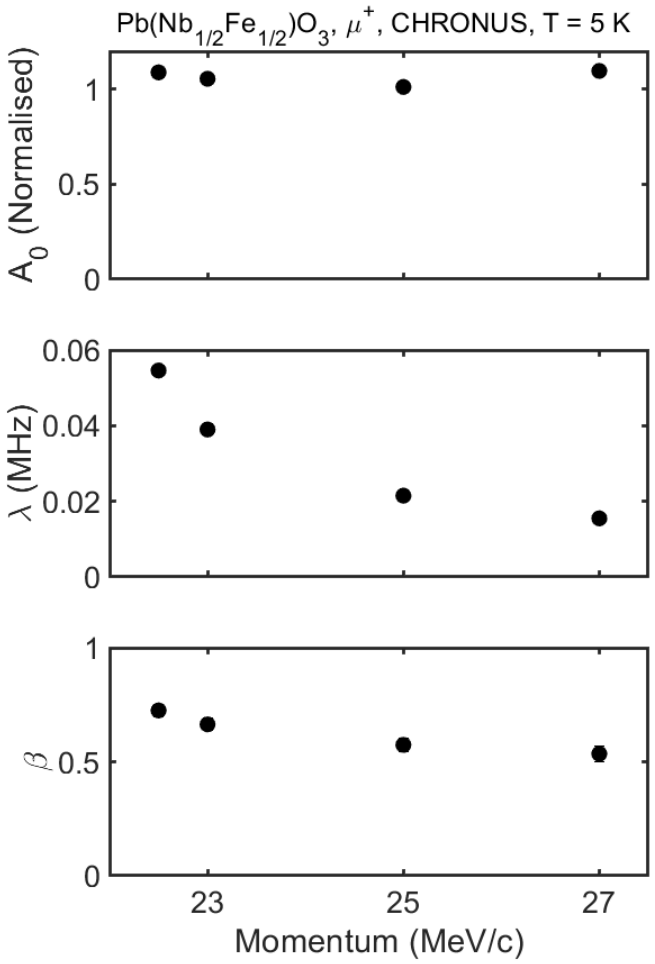

Figure 5.8: Values of normalised initial asymmetry, A_0, relaxation rate, λ, and exponent, β plotted against muon momentum (depth). A_0 remains roughly constant against depth at near unity whilst both λ and β decrease with depth. The error bars are smaller than the symbols used to plot the data.

Temperature Study

A ZF μSR experiment was also carried out to track the magnetic properties against temperature. In this way, magnetic transitions of the material could be identified. These measurements were done in the bulk, 27 MeV/c, as this momentum has the highest μ^+ flux.

Again, a stretched exponential was used to fit the data and the evolution of the fitting parameters is shown in Figure 5.9. A_0 remains near unity over the whole temperature range but a feature at $\approx$ 20 K may be seen in λ and β which coincides with the glassy transition identified through magnetic susceptibility measurements [29]. However, there is no clear sign of the second transition at $\approx$ 140 K to spatially long-range magnetic order which is consistent with $A_0 \approx 1$ further pointing to a lack of long-range order in this sample.

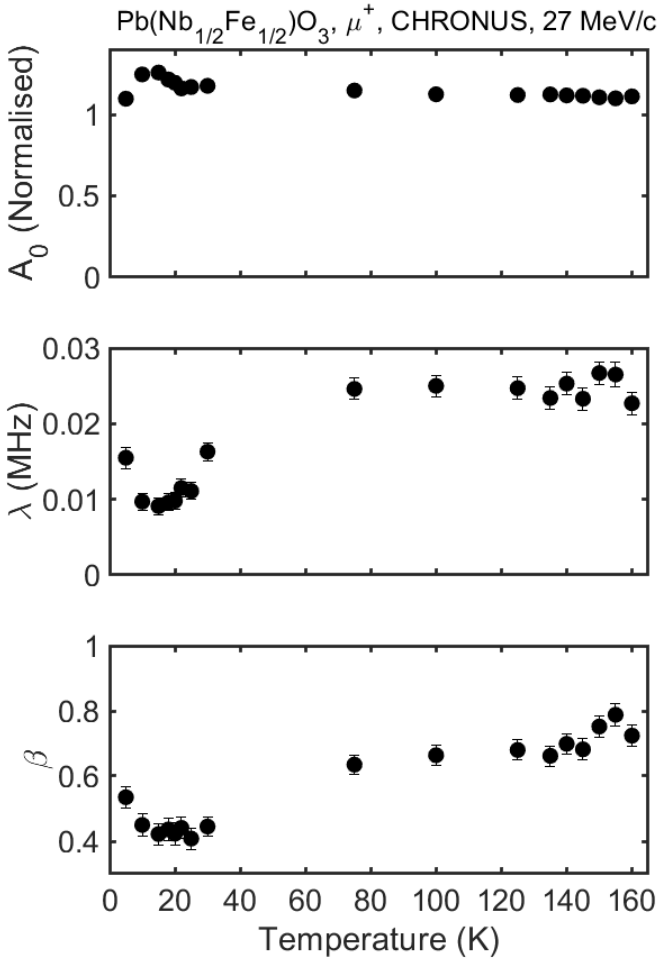

Figure 5.9: Values of normalised initial asymmetry, A_0, relaxation rate, λ, and exponent, β plotted against temperature. A_0 remains roughly constant against temperature at near unity. Both λ and β show a feature near 20 K which aligns with the glass transition reported by Rotaru *et al*. The exponent β softens near this transition but recovers as the temperature increases. λ also displays a minimum near the transition, which is unexpected. These trends are discussed in the main text. Some error bars are smaller than the symbols used to plot the data.

Longitudinal Field Study

With the absence of any observable long-range order in the ZF measurements, a LF study was used to determine the strength of the magnetic structure. Figure 5.10 shows the μSR relaxation under LF conditions for various μ^+ momenta. In this setup the magnetic field is orientated parallel to the initial μ^+ spin polarisation direction and so, under a large enough field, the spin of the μ^+ will align to this rather than the magnetic structure of the sample. This causes the asymmetry to remain near or above unity. At large enough fields, this response can also be due to the relaxation of nuclear moments which takes on more of a Gaussian signature. This can be seen in the 500 G curve at 22.5 MeV/c, i.e. near the surface.

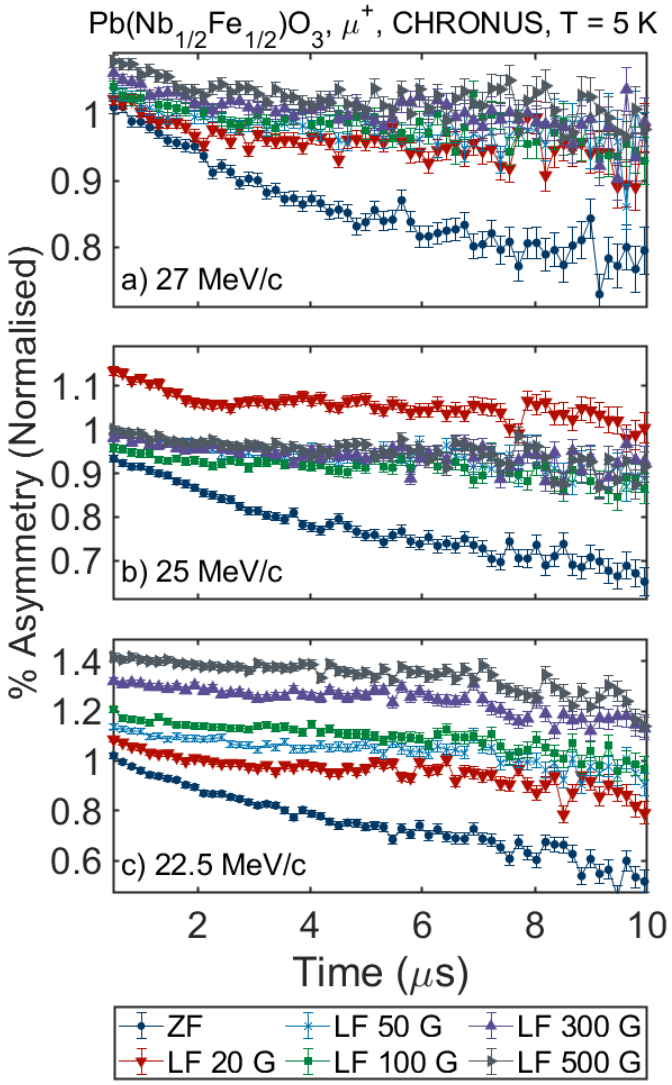

Figure 5.10: Muon asymmetry against time showing the μSR response under LF conditions at a momentum of 27 MeV/c. Magnetic field strengths from 0 G (ZF) to 500 G are shown. For clarity, not all data points are plotted - a bunching factor (average) of 5 was used in WiMDA.

The flattening of the relaxation above ZF shown in Figure 5.10 indicates that the μ^+ response decouples from the internal magnetic structure at low field strength. Fields up to 500 G were applied but no changes in the response were seen after 20 G with the asymmetry staying constant near unity. This was found to be consistent across all momenta (depths). The reason behind the anomalously high 20 G measurement at 25 MeV/c is unaccounted for but, even if this measurement is disregarded, a flattening trend is still shown across the other curves at this momentum. Overall, such a low decoupling threshold would indicate that the internal magnetic fields are weak. This agrees with the glassy behaviour seen in the ZF measurements.

5.3 Discussion

The negative muon data (Section 5.2.2) appears to show a deficiency of Fe near the surface of the sample. This provides evidence of a skin effect related to compositional inhomogeneity analogous to studies on other relaxor compounds such as PMN [48]. However, in this study, the inhomogeneity in Fe is supported by a change in the magnetic properties between the surface and the bulk seen with μSR in Section 5.2.3, as Fe^{3+} is the only magnetic species.

The random occupation of the B-site in relaxors has been shown to result in regions which are richer in one cation which arise though compositional fluctuations [10]. This is the basis for the Fe^{3+} cluster model proposed by Kleemann *et al.* [38]. Thus, if the proportion of Fe^{3+} decreases, it may be expected that these regions decrease in size and show larger separations. In the cluster model of PFN, the short-range spin-glass behaviour stems from small isolated clusters whereas the antiferromagnetic state exists within the larger exchange-coupled Fe^{3+} cluster. Hence, it should be expected that, if fewer isolated Fe^{3+} ions exist near the surface of the sample, the majority are contained within larger clusters.

The impact of this is seen in the ZF μ^+ depth study which showed is a difference in the local magnetic dynamics between the surface and the bulk as reflected in the changing relaxation. This data was parameterised using the stretched exponential function, i.e. Equation 5.1. The use of this function can be motivated by a general phenomenological argument: the muon spin experiences exponential relaxation e^{-st} with the relaxation rate s determined by the local magnetic field. This is due to the glassy nature of the magnetic fields in PFN and is a typical response to dynamics [50, 51]. However, the B-site disorder means that the total μSR signal will correspond to the spatial average of relaxation rates. Hence, the overall relaxation may be modelled stochastically, averaged over a probability distribution $H_{\lambda,\beta}(s)$ based on the implantation site, which mathematically corresponds to the stretched exponential [52]

$$e^{-(\lambda t)^{\beta}} = \int_0^{\infty} ds H_{\lambda,\beta}(s) e^{-st}. \tag{5.2}$$

An integral representation for $H_{\lambda,\beta}(s)$ was first obtained by Pollard [53] using contour integration

$$H_{\lambda,\beta}(s) = \frac{1}{\pi\lambda} \int_0^{\infty} du e^{-\frac{su}{\lambda}} e^{-u^{\beta}\cos(\beta\pi)} \sin\left[u^{\beta}\sin(\beta\pi)\right]. \tag{5.3}$$

A complementary form

$$H_{\lambda,\beta}(s) = \frac{1}{\pi\lambda} \int_0^{\infty} dy e^{-y^{\beta}\cos\left(\frac{\beta\pi}{2}\right)} \cos\left[y^{\beta}\sin\left(\frac{\beta\pi}{2}\right) - \frac{sy}{\lambda}\right], \tag{5.4}$$

was also derived by Berberan-Santos *et al.* [54] and this derivation is reproduced below. The equivalence of Equations 5.3 and 5.4 is explicitly shown. These integrals are only solvable in terms of standard functions for the cases where $\beta = 1$ or $\beta = \frac{1}{2}$ [55]. Finally, a series form for

$H_{\lambda,\beta}(s)$ is also derived following Humbert and is convergent for all s [56]. It provides an easy computation method and was used to tabulate the distributions for various values of λ and β by Dishon *et al.* [57]. The normalisation of $H_{\lambda,\beta}$ is guaranteed by the assumption that the relaxing asymmetry is likewise normalised - i.e. it starts from unity.

As shown in Equation 5.2, the stretched exponential function $e^{-(\lambda t)^\beta}$ can be motivated as an average over individual exponential relaxations e^{-st} with the relaxation rate s drawn from a distribution $H_{\lambda,\beta}(s)$ [52]. The dependence of the effective relaxation rate λ can be removed but introducing the variables $T = \lambda t$ and $S = \frac{s}{\lambda}$ so that

$$e^{-T^\beta} = \int_0^\infty dS G_\beta(S) e^{-ST}, \tag{5.5}$$

where the function $G_\beta(S) = \lambda H_{\lambda,\beta}(s)$ is the scaled distribution. Clearly, this integral amounts to a Laplace transform [58] and so $G_\beta(S)$ may be calculated by performing the inverse Laplace transform of e^{-T^β} [54] which may be inverted by the Bromwich integral

$$G_\beta(S) = \lim_{\gamma\to 0} \frac{1}{2\pi i} \int_{\gamma-i\infty}^{\gamma+i\infty} dT e^{-T^\beta + ST}, \tag{5.6}$$

where the customary γ allows the integration contour to be shifted away from $T = 0$ where the integrand has a branch point. Taking the branch cut along the negative real axis, the integration variable may be split into real and imaginary components $T = \gamma + iy$. Furthermore, a polar representation of T may also be implemented where $T = Re^{i\theta}$ and this will be used in the following to show that the imaginary part of the integral vanishes due to symmetry. Combining these representations gives $R = \frac{\gamma}{\cos\theta}$ and $T = \frac{\gamma e^{i\theta}}{\cos\theta} = \gamma\big[1 + i\tan\theta\big]$. Substitution into Equation 5.6 then gives an integral purely in terms of the angle θ

$$G_\beta(S) = \lim_{\gamma\to 0} \frac{1}{2\pi} \int_{-\frac{\pi}{2}}^{\frac{\pi}{2}} d\theta \frac{\gamma}{\cos^2\theta} \exp\Big\{ -\Big(\frac{\gamma}{\cos\theta}\Big)^\beta \big[\cos(\beta\theta) + i\sin(\beta\theta)\big] + S\gamma(1 + i\tan\theta)\Big\}. \tag{5.7}$$

After some manipulation using trigonometric identities, this may be rewritten as

$$G_\beta(S) = \lim_{\gamma\to 0} \frac{1}{2\pi} \int_{-\frac{\pi}{2}}^{\frac{\pi}{2}} d\theta \frac{\gamma}{\cos^2\theta} \exp\Big\{ -\Big(\frac{\gamma}{\cos\theta}\Big)^\beta \cos(\beta\theta) + S\gamma\Big\} \times \big[\cos\phi - i\sin\phi\big], \tag{5.8}$$

where $\phi = \Big(\frac{\gamma}{\cos\theta}\Big)^\beta \sin(\beta\theta) - S\gamma\tan\theta$.

Observing that ϕ is an odd function of θ, together with the fact that the other terms in the integrand are even, means that the real part of Equation 5.8 is totally even and the imaginary part is totally odd. Hence, since the limits of the integral are symmetric, the odd part must vanish due to symmetry. This leaves

$$G_\beta(S) = \lim_{\gamma\to 0}\frac{1}{\pi}\int_0^{\frac{\pi}{2}} d\theta \frac{\gamma}{\cos^2\theta}\exp\Big\{-\Big(\frac{\gamma}{\cos\theta}\Big)^\beta \cos(\beta\theta)+S\gamma\Big\}\cos\phi, \tag{5.9}$$

where the symmetry has also been used to reduce the integration range to positive angles. Reintroducing the variable $y = \gamma\tan\theta$ transforms the integral to

$$G_\beta(S) = \lim_{\gamma\to 0}\frac{1}{\pi}\int_0^{\infty} dy \exp\Big\{S\gamma-(\gamma^2+y^2)^{\frac{\beta}{2}}\cos\big(\beta\theta(y)\big)\Big\}\cos\Big[(\gamma^2+y^2)^{\frac{\beta}{2}}\sin\big(\beta\theta(y)\big)-Sy\Big]. \tag{5.10}$$

The final steps in order to arrive at Equation 5.4 are to impose the limit $\gamma\to 0$ and counteract the scaling of the distribution. As $y=\gamma\tan\theta$, in order for y to remain finite as $\gamma\to 0$, $\theta\to\frac{\pi}{2}$ should also be imposed so that the tangent becomes large. This ensures that the integration contour is wholly in the imaginary direction. Hence, in order to fully account for this limit $\gamma\to 0$ *and* $\theta\to\frac{\pi}{2}$ must be set in Equation 5.10 to give

$$G_\beta(S) = \frac{1}{\pi}\int_0^{\infty} dy e^{-y^\beta\cos\left(\frac{\beta\pi}{2}\right)}\cos\Big[y^\beta\sin\Big(\frac{\beta\pi}{2}\Big)-Sy\Big]. \tag{5.11}$$

This is equal to Equation 5.4 once the scaling of S is removed. However, Pollard first derived an alternative integral form, again using contour integration [53] and the equivalence of Equations 5.4 and 5.3 will now be shown. Observe that Equation 5.4 maybe be rewritten as

$$\begin{aligned} H_{\lambda,\beta}(s) =& \mathcal{R}e\left\{\frac{1}{\pi\lambda}\int_0^{\infty} dy e^{-y^\beta\cos\left(\frac{\beta\pi}{2}\right)}e^{i\left[y^\beta\sin\left(\frac{\beta\pi}{2}\right)-\frac{sy}{\lambda}\right]}\right\} \\ =& \mathcal{R}e\left\{\frac{1}{\pi\lambda}\int_0^{\infty} dy e^{-\left(ye^{\frac{-i\pi}{2}}\right)^\beta}e^{-\frac{isy}{\lambda}}\right\}. \end{aligned} \tag{5.12}$$

This more compact representation may be motivated as the zero imaginary part has already been shown. Performing a rotation in the complex plane, let $u=iy$ to give

$$\begin{aligned} H_{\lambda,\beta}(s) =& \mathcal{R}e\left\{\frac{-i}{\pi\lambda}\int_0^{\infty} du e^{-\left(ue^{-i\pi}\right)^\beta}e^{-\frac{su}{\lambda}}\right\} \\ =& \mathcal{I}m\left\{\frac{1}{\pi\lambda}\int_0^{\infty} du e^{-\left(ue^{-i\pi}\right)^\beta}e^{-\frac{su}{\lambda}}\right\}. \end{aligned} \tag{5.13}$$

Finally, expanding the complex exponentials gives

$$\begin{aligned} H_{\lambda,\beta}(s) =& \mathcal{I}m\left\{ \frac{1}{\pi\lambda} \int_0^\infty du e^{-u^\beta \cos(\beta\pi)+iu^\beta \sin(\beta\pi)} e^{-\frac{su}{\lambda}} \right\} \\ =& \frac{1}{\pi\lambda} \int_0^\infty du e^{-\frac{su}{\lambda}} e^{-u^\beta \cos(\beta\pi)} \mathcal{I}m\left\{ e^{iu^\beta \sin(\beta\pi)} \right\}, \end{aligned} \tag{5.14}$$

which, when the imaginary part is taken, gives Equation 5.3. As noted by Berberan-Santos *et al.*, these two integral representations are actually complementary with Equation 5.3 being easier to compute numerically at large s whilst Equation 5.4 is hard to compute at large s due to the large oscillations of the integrand [54].

As these integrals are difficult to compute, a series representation of $H_{\lambda,\beta}(s)$ is desired. Returning to Equation 5.13, a series form may be derived by alternatively Taylor expanding the first exponential

$$H_{\lambda,\beta}(s) = \mathcal{I}m\left\{ \frac{1}{\pi\lambda} \int_0^\infty du \sum_{n=0}^\infty \frac{1}{n!} \left[-u^\beta e^{-i\beta\pi} \right]^n e^{-\frac{su}{\lambda}} \right\}. \tag{5.15}$$

Integrating term by term, permitted since the power series is convergent, this gives

$$H_{\lambda,\beta}(s) = \mathcal{I}m\left\{ \frac{1}{\pi\lambda} \sum_{n=0}^\infty \frac{e^{-i\beta n\pi}}{n!} (-1)^n \int_0^\infty du u^{\beta n} e^{-\frac{su}{\lambda}} \right\}, \tag{5.16}$$

which, along with the substitution $x = \frac{su}{\lambda}$ allows recognition of the integral form of the gamma function

$$\begin{aligned} H_{\lambda,\beta}(s) =& \mathcal{I}m\left\{ \frac{1}{\pi\lambda} \sum_{n=0}^\infty \frac{e^{-i\beta n\pi}}{n!} (-1)^n \left(\frac{\lambda}{s}\right)^{\beta n+1} \int_0^\infty dx x^{\beta n} e^{-x} \right\} \\ =& \mathcal{I}m\left\{ \frac{1}{\pi\lambda} \sum_{n=0}^\infty \frac{e^{-i\beta n\pi}}{n!} (-1)^n \left(\frac{\lambda}{s}\right)^{\beta n+1} \Gamma(1+\beta n) \right\}. \end{aligned} \tag{5.17}$$

Lastly, apart from the complex exponential, the whole expression is real and so, taking the imaginary part simply transforms this exponential to a sine function. Then, the odd property of sine may be used along with the fact that $\sin 0 = 0$, meaning that $n = 0$ term in the series correspondingly vanishes, to give the series form for the distribution $H_{\lambda,\beta}(s)$:

$$H_{\lambda,\beta}(s) = \frac{1}{\pi\lambda} \sum_{n=1}^\infty \frac{\sin(\beta n\pi)}{n!} (-1)^{n+1} \left(\frac{\lambda}{s}\right)^{\beta n+1} \Gamma(1+\beta n). \tag{5.18}$$

This series was first derived by Humbert and is convergent for all s [56]. It is this form that was used by Dishon *et al.* to tabulate $H_{\lambda,\beta}(s)$ [57], the values of which were used in this work.

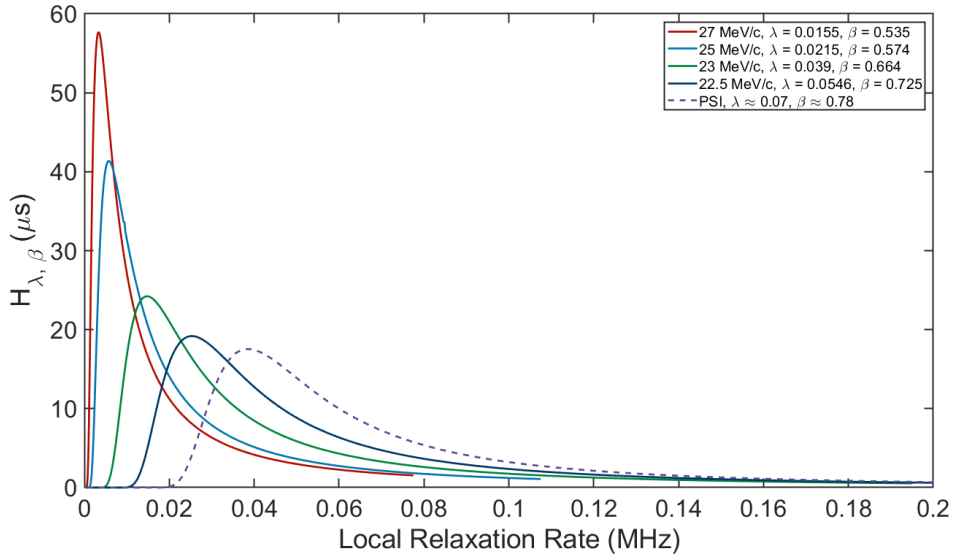

Figure 5.11: Distribution of relaxation rates $H_{\lambda,\beta}$ that, when averaged, produces the observed stretched exponential relaxation from the ZF measurements at 5 K. All depths are shown, along with the distribution that produces the relaxation observed at PSI by Rotaru *et. al* [39]. As the penetration depth increases, the distribution narrows and slows.

Figure 5.11 shows the distribution of local relaxation rates that produce the observed relaxation of the muon polarisation under ZF conditions for all momenta (depths). These distributions were computed using Equation 5.18 and values from the tables by Dishon *et al.* [57]. It clearly shows that the distribution narrows with depth into the sample and that the peak moves left indicating that the relaxation slows in the bulk. The frequency distribution near the surface indicates a broadening of the relaxation presumably due to the greater inter-cluster distances near the surface - larger separation means that the coupling between neighbouring regions will be weaker and this will lead to a larger spread of responses.

In order to put this into context, the results reported here may be compared to the study performed at PSI by Rotaru *et. al* [39]. Also parameterising their decay with a stretched exponential, two discrepancies are seen and are summarised in Table 5.2.

Table 5.2: Comparison of the muon relaxation parameterisation for the extreme depths in this study with the literature values taken from Rotaru *et. al* [39].

		A_0	λ (MHz)	β
Rotaru *et. al* ('Bulk') [39]		$\approx 1/3$	≈ 0.05	≈ 0.8
This study	Bulk (27 MeV/c)	1.09(1)	0.016(1)	0.54(3)
	Surface (22.5 MeV/c)	1.08(1)	0.055(1)	0.73(3)

Firstly, the PSI study's relaxing asymmetry begins at $1/3$ whereas the relaxation in this study begins from unity. This can be attributed to the lack of long-range order in this sample as, with antiferromagnetic order as reported by Rotaru *et. al*, the experiment will only effectively be sensitive to one out of three component of the relaxation. This is supported by the μSR temperature study presented in Section 5.2.3 which observed no evidence of the Néel transition at $\approx$ 140 - 160 K.

Secondly, the two relaxation parameters of the PSI study can be seen to agree much more closely with this study's surface measurements than the bulk as should be expected. The distribution resulting in the PSI relaxation was back-calculated and is also plotted with a dashed line in Figure 5.11. This graphically illustrates the similarity between that study and our surface measurements and shows that the PSI response contains a much broader range of frequencies. When taken into context with the size difference between the two samples, Rotaru *et al.* used a small single crystal sample, this comparison would indicate that this larger sample is able to stabilise a bulk phase which is different from that probed in smaller samples.

Additionally, the shape of these distributions may be linked to the presence of random fields with Fe^{3+} being particularly susceptible to their influence due to a lack of an orbital degree of freedom. A narrowing and slowing of the distribution would indicate that the random fields are stronger in the bulk. It is well-known that the random occupation of the B-site results in an ionic charge disorder that produces random electric fields [59]. It is proposed that the mixing of Nb^{5+} and Fe^{3+} results too in frustrated random magnetic fields. Random field models also provide the current best description of phenomena such as the skin effect [23, 24, 60].

Consider a Fe^{3+} cluster near the surface. Due to the compositional gradient, it may be expected that it is relatively isolated and, within this region, that the antiferromagnetic superexchange mechanism is likely to be dominant. However, this order will be frustrated due to the presence of Nb^{5+}, which will alter the molecular field. As the cation distribution is random, these fields may also be considered as such.

However, moving into the bulk of the sample, the Fe^{3+} clusters will grow and start to couple which introduces a further frustration mechanism. Being in different Nb^{5+} molecular fields, any intra-cluster order will be destroyed by the interaction of these random fields. This can be seen as the frequency response narrows in the bulk.

It is proposed that this provides a solution to the size/order discrepancy in PFN as the bulk structure present here, and absent from smaller samples, disrupts the long-range magnetic order. This structure can be expected to have larger random fields due to the B-site disorder.

5.4 Chapter Conclusions

In conclusion, depth dependent muon spectroscopy was used to probe the near-surface properties of the multiferroic relaxor-ferroelectric PFN. This was done in order to investigate the skin effect which is well-reported in relaxors. However, the driving force behind the skin effect is implicated to be due to random fields arising from B-site disorder but this is still not well-understood and so requires further study.

Negative muon elemental analysis showed that there appears to be a deficiency of Fe near the surface of PFN in agreement with studies in non-magnetic relaxors. Furthermore, ZF μSR experiments showed that this compositional gradient is correlated with a change in the magnetic properties over this region. This supports inhomogeneity in Fe as this is the only magnetic species.

By parameterising the relaxing muon asymmetry in terms of a phenomenologically motivated stretched exponential, a solution to the size/order discrepancy was proposed. The parametrisation allows the change in the magnetic dynamics to be quantified and compared to literature measurements. The B-site disorder causes the development of random fields and this model has been successful in describing other relaxor properties. Here in PFN, it has been shown that the 'bulk' response observed in small samples is in agreement with the surface measurements of this larger sample. This implies that the presence of a bulk structure, characterised by a slowing of the muon relaxation, disrupts the long-range order causing it to be absent from the large sample. This has been seen by neutron measurements and is confirmed here.

References

[1] S.-E. Park and T. R. Shrout, "Ultrahigh strain and piezoelectric behavior in relaxor based ferroelectric single crystals," *J. Appl. Phys.*, vol. 82, p. 1804, 1997. DOI: 10.1063/1.365983.

[2] D. Viehland, J. F. Li, S. J. Jang, L. E. Cross, and M. Wuttig, "Dipolar-glass model for lead magnesium niobate," *Phys. Rev. B*, vol. 43, pp. 8316–8320, 10 1991. DOI: 10.1103/PhysRevB.43.8316.

[3] D. Viehland, S. J. Jang, L. E. Cross, and M. Wuttig, "Deviation from curie-weiss behavior in relaxor ferroelectrics," *Phys. Rev. B*, vol. 46, pp. 8003–8006, 13 1992. DOI: 10.1103/PhysRevB.46.8003.

[4] R. Pirc, R. Blinc, and V. Bobnar, "Dynamics of relaxor ferroelectrics," *Phys. Rev. B*, vol. 63, p. 054 203, 5 2001. DOI: 10.1103/PhysRevB.63.054203.

[5] R. Pirc and R. Blinc, "Vogel-fulcher freezing in relaxor ferroelectrics," *Phys. Rev. B*, vol. 76, 020101(R), 2 2007. DOI: 10.1103/PhysRevB.76.020101.

[6] R. A. Cowley, "The phase transition of strontium titanate," *Philos. Trans. Royal Soc. A*, vol. 354, no. 1720, pp. 2799–2814, 1996. DOI: 10.1098/rsta.1996.0130.

[7] S. B. Vakhrushev and S. M. Shapiro, "Direct evidence of soft mode behavior near the burns temperature in the $PbMg_{1/3}Nb_{2/3}O_3$ relaxor ferroelectric," *Phys. Rev. B*, vol. 66, p. 214 101, 21 2002. DOI: 10.1103/PhysRevB.66.214101.

[8] G. Burns and F. H. Dacol, "Polarization in the cubic phase of $BaTiO_3$," *Solid State Commun.*, vol. 42, pp. 9–12, 1 1982. DOI: 10.1016/0038-1098(82)91018-3.

[9] G. Burns and F. H. Dacol, "Glassy polarization behavior in ferroelectric compounds $Pb(Mg_{1/3}Nb_{2/3})O_3$ and $Pb(Zn_{1/3}Nb_{2/3})O_3$," *Solid State Commun.*, vol. 48, no. 10, pp. 853–856, 1983. DOI: 10.1016/0038-1098(83)90132-1.

[10] L. E. Cross, "Relaxor ferroelectrics," *Ferroelectrics*, vol. 76, pp. 241–267, 1 1987. DOI: 10.1080/00150198708016945.

[11] C. Stock *et al.*, "Evidence for anisotropic polar nanoregions in relaxor $Pb(Mg_{1/3}Nb_{2/3})O_3$: A neutron study of the elastic constants and anomalous TA phonon damping in PMN," *Phys. Rev. B*, vol. 86, no. 10, pp. 1–18, 2012. DOI: 10.1103/PhysRevB.86.104108.

[12] K. Hirota, Z.-G. Ye, S. Wakimoto, P. M. Gehring, and G. Shirane, "Neutron diffuse scattering from polar nanoregions in the relaxor $Pb(Mg_{1/3}Nb_{2/3})O_3$," *Phys. Rev. B*, vol. 65, p. 104 105, 2002. DOI: 10.1103/PhysRevB.65.104105.

[13] T. R. Welberry *et al.*, "Single-crystal neutron diffuse scattering and monte carlo study of the relaxor ferroelectric $PbZn_{1/3}Nb_{2/3}O_3$ (PZN)," *J. Appl. Crystallogr.*, vol. 38, no. 4, pp. 639–647, 2005. DOI: 10.1107/S0021889805015918.

[14] Z.-G. Ye and H. Schmid, "Optical, dielectric and polarization studies of the electric field-induced phase transition in $Pb(Mg_{1/3}Nb_{2/3})O_3$ [PMN]," *Ferroelectrics*, vol. 145, p. 83, 1993. DOI: 10.1080/00150199308222438.

[15] C. Stock *et al.*, "Neutron and x-ray diffraction study of cubic [111] field-cooled $Pb(Mg_{1/3}Nb_{2/3})O_3$," *Phys. Rev. B*, vol. 76, p. 064 122, 2007. DOI: 10.1103/PhysRevB.76.064122.

[16] F. Li *et al.*, "The origin of ultrahigh piezoelectricity in relaxor-ferroelectric solid solution crystals," *Nat. Commun*, vol. 7, p. 13 807, 2016. DOI: 10.1038/ncomms13807.

[17] P. M. Gehring, W. Chen, Z.-G. Ye, and G. Shirane, "The non-rhombohedral low-temperature structure of PMN–10% PT," *J. Condens. Matter Phys.*, vol. 16, no. 39, pp. 7113–7121, 2004. DOI: 10.1088/0953-8984/16/39/042.

[18] G. Xu, D. Viehland, J. F. Li, P. M. Gehring, and G. Shirane, "Evidence of decoupled lattice distortion and ferroelectric polarization in the relaxor system PMN - xPT," *Phys. Rev. B*, vol. 68, p. 212 410, 21 2003. DOI: 10.1103/PhysRevB.68.212410.

[19] G. Xu, Z. Zhong, Y. Bing, Z.-G. Ye, C. Stock, and G. Shirane, "Ground state of the relaxor ferroelectric $PbZn_{1/3}Nb_{2/3}O_3$," *Phys. Rev. B*, vol. 67, p. 104 102, 10 2003. DOI: 10.1103/PhysRevB.67.104102.

[20] G. Xu, H. Hiraka, G. Shirane, and K. Ohwada, "Dual structures in (1-x)$PbZn_{1/3}Nb_{2/3}O_3$-x$PbTiO_3$ ferroelectric relaxors," *Appl. Phys. Lett.*, vol. 84, no. 20, pp. 3975–3977, 2004. DOI: 10.1063/1.1751216.

[21] C. Stock *et al.*, "Strong influence of the diffuse component on the lattice dynamics in $Pb(Mg_{1/3}Nb_{2/3})O_3$," *J. Phys. Soc. Jpn.*, vol. 74, no. 11, pp. 3002–3010, 2005. DOI: 10.1143/JPSJ.74.3002.

[22] K. H. Conlon *et al.*, "Direct observation of the near-surface layer in $Pb(Mg_{1/3}Nb_{2/3})O_3$ using neutron diffraction," *Phys. Rev. B*, vol. 70, p. 172 204, 17 2004. DOI: 10.1103/PhysRevB.70.172204.

[23] J. P. Hill, T. R. Thurston, R. W. Erwin, M. J. Ramstad, and R. J. Birgeneau, "Transition to long-range order in the three-dimensional random-field ising model," *Phys. Rev. Lett.*, vol. 66, pp. 3281–3284, 25 1991. DOI: 10.1103/PhysRevLett.66.3281.

[24] Q. Feng, Q. J. Harris, R. J. Birgeneau, and J. P. Hill, "Neutron and x-ray scattering studies of field-cooled ordering in the three-dimensional random-field ising model," *Phys. Rev. B*, vol. 55, p. 370, 1 1997. DOI: 10.1103/PhysRevB.55.370.

[25] C. Stock *et al.*, "Universal static and dynamic properties of the structural transition in $Pb(Zn_{1/3}Nb_{2/3})O_3$," *Phys. Rev. B*, vol. 69, p. 094 104, 2004. DOI: 10.1103/PhysRevB.69.094104.

[26] V. Westphal, W. Kleemann, and M. D. Glinchuk, "Diffuse phase transitions and random-field-induced domain states of the "relaxor" ferroelectric $PbMg_{1/3}Nb_{2/3}O_3$," *Phys. Rev. Lett.*, vol. 68, p. 847, 1992. DOI: 10.1103/PhysRevLett.68.847.

[27] R. Fisch, "Random-field models for relaxor ferroelectric behavior," *Phys. Rev. B*, vol. 67, p. 094 110, 2003. DOI: 10.1103/PhysRevB.67.094110.

[28] C. Stock, S. R. Dunsiger, R. A. Mole, X. Li, and H. Luo, "Coupled short-range ferroelectric and magnetic order in $Pb(Fe_{1/2}Nb_{1/2})O_3$," *Phys. Rev. B*, vol. 88, p. 094 105, 2013. DOI: 10.1103/PhysRevB.88.094105.

[29] Y. Yang, J.-M. Liu, H. B. Huang, W. Q. Zou, P. Bao, and Z. G. Liu, "Magnetoelectric coupling in ferroelectromagnet $Pb(Fe_{1/2}Nb_{1/2})O_3$ single crystals," *Phys. Rev. B*, vol. 70, p. 132 101, 13 2004. DOI: 10.1103/PhysRevB.70.132101.

[30] G. Shirane, J. D. Axe, J. Harada, and J. P. Remeika, "Soft ferroelectric modes in lead titanate," *Phys. Rev. B*, vol. 2, p. 155, 1970. DOI: 10.1103/PhysRevB.2.155.

[31] M. Kempa, J. Hlinka, J. Kulda, P. Bourges, A. Kania, and J. Petzelt, "Lattice dynamics of cubic $PbTiO_3$ by inelastic neutron scattering," *Phase Transit.*, vol. 79, p. 351, 2006. DOI: 10.1080/01411590600892021.

[32] S. Wakimoto *et al.*, "Ferroelectric ordering in the relaxor $Pb(Mg_{1/3}Nb_{2/3})O_3$ as evidenced by low-temperature phonon anomalies," *Phys. Rev. B*, vol. 65, p. 172 105, 17 2002. DOI: 10.1103/PhysRevB.65.172105.

[33] V. A. Bokov, I. E. Mylnikova, and G. A. Smolenskii, *Soviet Physics JETP-USSR*, vol. 15, p. 447, 1962.

[34] B. Howes, M. Pelizzone, P. Fischer, C. Tabares-Munoz, J.-P. Rivera, and H. Schmid, "Characterisation of some magnetic and magnetoelectric properties of ferroelectric $Pb(Fe_{1/2}Nb_{1/2})O_3$," *Ferroelectrics*, vol. 54, no. 1, pp. 317–320, 1984. DOI: 10.1080/00150198408215879.

[35] V. V. Bhat, K. V. Ramanujachary, S. E. Lofland, and A. M. Umarji, "Tuning the multiferroic properties of $Pb(Fe_{1/2}Nb_{1/2})O_3$ by cationic substitution," *J. Magn. Magn. Mater.*, vol. 280, p. 221, 2004. DOI: 10.1016/j.jmmm.2004.03.016.

[36] R. Blinc, V. V. Laguta, B. Zalar, B. Zupančič, and M. Itoh, "^{17}O and ^{93}Nb nmr investigation of magnetoelectric effect in $Pb(Fe_{1/2}Nb_{1/2})O_3$," *J. Appl. Phys.*, vol. 104, p. 084 105, 2008. DOI: 10.1063/1.2957077.

[37] A. Kumar, R. S. Katiyar, C. Rinaldi, S. G. Lushnikov, and T. A. Shaplygina, "Glasslike state in $Pb(Fe_{1/2}Nb_{1/2})O_3$ single crystal," *Appl. Phys. Lett.*, vol. 93, p. 232 902, 2008. DOI: 10.1063/1.3043686.

[38] W. Kleemann, V. V. Shvartsman, P. Borisov, and A. Kania, "Coexistence of antiferromagnetic and spin cluster glass order in the magnetoelectric relaxor multiferroic $PbFe_{0.5}Nb_{0.5}O_3$," *Phys. Rev. Lett.*, vol. 105, p. 257 202, 25 2010. DOI: 10.1103/PhysRevLett.105.257202.

[39] G. M. Rotaru *et al.*, "Spin-glass state and long-range magnetic order in $Pb(Fe_{1/2}Nb_{1/2})O_3$ seen via neutron scattering and muon spin rotation," *Phys. Rev. B*, vol. 79, p. 184 430, 18 2009. DOI: 10.1103/PhysRevB.79.184430.

[40] C. Stock *et al.*, "From paramagnetic to glassy dynamics in $Pb(Fe_{1/2}Nb_{1/2})O_3$ - (2) neutron scattering," *Phys. Rev. B*, Submitted.

[41] N. Setter and L. E. Cross, "The role of B-site cation disorder in diffuse phase transition behavior of perovskite ferroelectrics," *J. Appl. Phys.*, vol. 51, no. 8, pp. 4356–4360, 1980. DOI: 10.1063/1.328296.

[42] C. G. F. Stenger, F. L. Scholten, and A. J. Burggraaf, "Ordering and diffuse phase transitions in $Pb(Sc_{0.5}Ta_{0.5})O_3$ ceramics," *Solid State Commun.*, vol. 32, no. 11, pp. 989–992, 1979. DOI: 10.1016/0038-1098(79)90812-3.

[43] N. Lampis, P. Sciau, and A. G. Lehmann, "Rietveld refinements of the paraelectric and ferroelectric structures of $PbFe_{0.5}Nb_{0.5}O_3$," *J. Condens. Matter Phys.*, vol. 11, no. 17, pp. 3489–3500, 1999. DOI: 10.1088/0953-8984/11/17/307.

[44] S. B. Majumder, S. Bhattacharyya, R. S. Katiyar, A. Manivannan, P. Dutta, and M. S. Seehra, "Dielectric and magnetic properties of sol-gel-derived lead iron niobate ceramics," *J. Appl. Phys.*, vol. 99, no. 2, p. 024 108, 2006. DOI: 10.1063/1.2158131.

[45] J. F. Ziegler, M. D. Ziegler, and J. P. Biersack, "SRIM - the stopping and range of ions in matter (2010)," *Nucl. Instrum. Methods Phys. Res. B*, vol. 268, p. 1818, 2010. DOI: 10.1016/j.nimb.2010.02.091.

[46] R. Engfer, H. Schneuwly, J. L. Vuilleumier, H. K. Walter, and A. Zehnder, "Charge-distributed parameters, isotope shifts, isomer shifts, and magnetic hyperfine constants from muonic atoms," *At. Data Nucl. Data Tables*, vol. 14, pp. 509–597, 5,6 1974. DOI: 10.1016/S0092-640X(74)80003-3.

[47] C. Briancon *et al.*, *Mesoroentgen Spectra Catalogue*, Accessed online at http://muxrays.jinr.ru/. Accessed 17th November 2021.

[48] K. L. Brown *et al.*, "Depth dependant element analysis of $Pb(Mg_{1/3}Nb_{2/3})O_3$ using muonic x-rays," *J. Phys. Condens. Matter*, vol. 30, p. 125 703, 2018. DOI: 10.1088/1361-648X/aaade3.

[49] F. L. Pratt, "WIMDA: A muon data analysis program for the windows PC," *Phys. B: Condens. Matter*, vol. 289-290, p. 710, 2000. DOI: 10.1016/S0921-4526(00)00328-8.

[50] C. P. Slichter, *Principles of Magnetic Resonance*. Harper & Row Publishers, New York, 1963, ISBN: 9781258476250.

[51] J. Y. Ueumura, "Probing spin glasses with zero-field μSR," *Hyperfine Interact.*, vol. 8, p. 739, 1981. DOI: 10.1007/BF01037554.

[52] R. Kohlrausch, "Theorie des elektrischen rückstandes in der leidener flasche," *Ann. Phys.*, vol. 167, p. 56, 1854. DOI: 10.1002/andp.18541670103.

[53] H. Pollard, "The representation of $e^{-x^{\lambda}}$ as a laplace integral," *Amer. Math. Soc.*, vol. 52, p. 908, 1946. DOI: 10.1090/S0002-9904-1946-08672-3.

[54] M. N. Berberan-Santos, E. N. Bodunov, and B. Valeur, "Mathematical functions for the analysis of luminescence decays with underlying distributions 1. kohlrausch decay function (stretched exponential)," *Chem. Phys.*, vol. 315, p. 171, 2005. DOI: 10.1016/j.chemphys.2005.04.006.

[55] B. D. Wagner and W. R. Ware, "Recovery of flourescence lifetime distributions: Application to förster transfer in rigid and viscous media," *J. Phys. Chem.*, vol. 94, p. 3489, 1990. DOI: 10.1021/j100372a600.

[56] C. P. Humbert, *Bull. Soc. Math France*, vol. 69, p. 121, 1945.

[57] M. Dishon, J. T. Bendler, and G. H. Weiss, "Tables of the inverse laplace transform of the function e^{-s^β}," *J. Res. Natl. Inst. Stand. Technol.*, vol. 95, p. 433, 1990. DOI: 10.6028/jres.095.036.

[58] K. F. Riley, M. P. Hobson, and S. J. Bence, *Mathematical Methods for Physics and Engineering*, 3rd. Cambridge University Press, 2006, ch. 13, ISBN: 978-0-521-67971-8.

[59] M. Glinchuk, "Relaxor ferroelectrics: From cross superparaelectric model to random field theory," *British Ceramic Transactions*, vol. 103, pp. 76–82, 2 2004. DOI: 10.1179/096797804225012792.

[60] Y. Imry and S.-K. Ma, "Random-field instability of the ordered state of continuous symmetry," *Phys. Rev. Lett.*, vol. 35, pp. 1399–1401, 21 1975. DOI: 10.1103/PhysRevLett.35.1399.

Chapter 6

Mn-Modified Relaxor-PT Single Crystals

This chapter reports the investigation into the chemical valence of Mn in modified relaxor-ferroelectric piezocrystals. This was done using the negative muon technique and the chapter starts with a comprehensive examination of the muonic X-ray emission lines in several Mn oxides - MnO, Mn_2O_3 and MnO_2 - with each having a different valence on the Mn site. The different spectra were compared to search for any differences which would suggest that the technique is sensitive to this. This is followed by a study of the feasibility of using this method in a sample of Mn:PIN-PMN-PT to study the dopant valence with the aim of providing insight into the doping process and the behaviour of the Mn.

6.1 Chapter Introduction

Mn-modified relaxor-ferroelectric piezocrystals, i.e. Mn:PIN-PMN-PT, have shown great promise for applications requiring high power ultrasound [1–3]. However, the mechanism by which the Mn is doped into PIN-PMN-PT is not fully understood, and any segregation may affect the performance of these crystals [4]. In order to fully exploit Mn:PIN-PMN-PT and other doped materials, these effects should be understood. It is, therefore, desirable to study the distribution of Mn ions throughout the crystal. Another feature of interest is the valence state of Mn in these piezocrystals which is difficult to determine non-destructively in bulk crystalline samples.

Thus, this chapter aims to establish the feasibility of using negative muons (μ^-) to determine the valence of Mn in Mn:PIN-PMN-PT. Furthermore, as with PFN, by changing the momentum of the muons, this study can be performed as a function of depth, providing a way to measure any segregation of the Mn.

6.2 Brief Review of Crystal Growth Methods

As segregation of components is a major issue in relaxor-PT single crystal, the growth process will now be briefly reviewed. Various methods of crystal growth have been developed [5, 6], but one of the most relevant to this thesis is the Bridgman method [7]. This has been used extensively to grow single crystal piezoelectric materials [8–11].

The Bridgman method originally used a vertically mounted furnace which was heated to above the melting point of the charge i.e. the source materials to be crystallised. The material was then lowered out of the bottom of the furnace, causing a thermal gradient along the sample and inducing a gradual crystallisation along its height. This method was later modified by Stockbarger to include two co-axial furnaces such that the sample was now lowered into a lower temperature zone, with the high temperature zone still above the charge's melting point [12]. This setup is illustrated in Figure 6.1 and is known as the modified-Bridgman method.

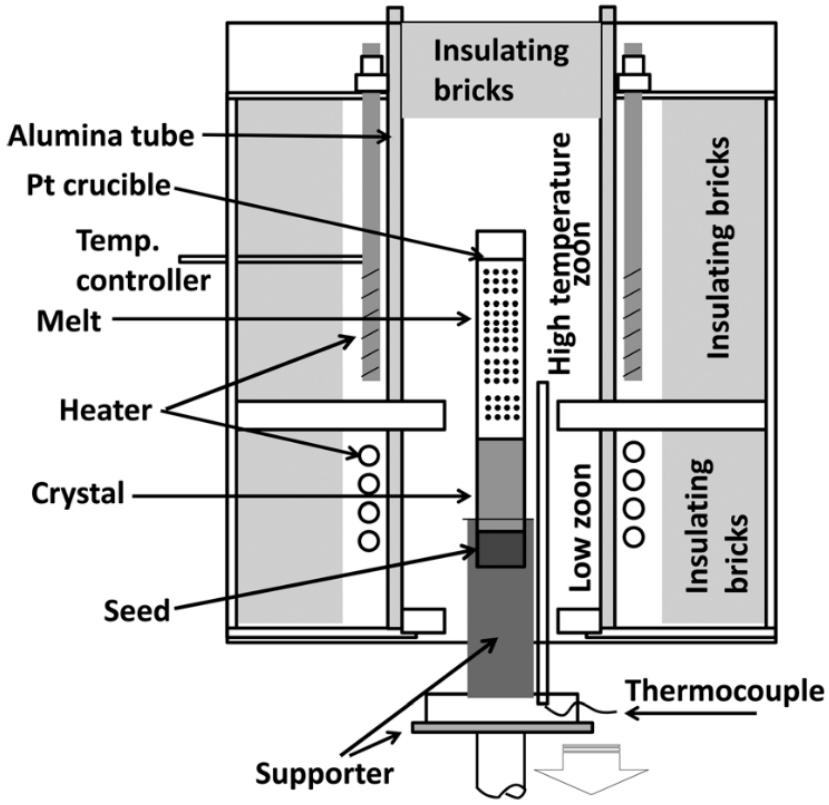

Figure 6.1: Schematic of a modified-Bridgman furnace set-up. Reprinted from S. Zhang *et al.*, "High performance ferroelectric relaxor-$PbTiO_3$ single crystals: Status and perspective," *J. Appl. Phys.*, vol. 111, p. 031 301, 3 2012, with the permission of AIP Publishing.

PMN-PT grown with the modified-Bridgman method was first reported in 1997, after previous techniques such as flux growth proved to have unsuitably slow growth rates [14–16]. Modified-Bridgman has now become the standard method for commercial manufacturing of

relaxor-ferroelectric single crystals [13]. However, due to congruent melting, segregation is present in the boule. This is most easily seen in the case of PMN-PT where the concentration of the PT component varies along the crystal boule [17, 18]. This can lead to high sample-to-sample variation and means that large samples are difficult to grow; both of which are a problem for ultrasonic device applications [19]. Furthermore, this variation can lead to differing phases in the boule, which means that some material has to be discarded. This is not cost effective and so presents a barrier to commercialisation [20].

Alternative methods have been developed [21]; the most notable is the solid-state conversion method where a small seed crystal is used to convert the grains in a dense polycrystalline matrix after a long annealing period [22, 23]. However, this has proved difficult to replicate and has gained no commercial acceptance. As such, no alternatives have yet replaced modified-Bridgman in commercial manufacturing.

6.3 Relaxor-PT Single Crystals

The currently best performing piezoelectric materials in terms of large piezoelectric coefficients, d, and large electromechanical coupling, k^2, are the relaxor-PT single crystal class. Although PMN had been reported to possess large dielectric permittivity, it retains an averagely cubic structure down to low temperatures [24]. However, if doped with a small amount of PT, the transition to a ferroelectric state can be increased to a useful temperature [25] and, therefore, applications of relaxor-ferroelectrics use these mixed compositions.

Whereas attempts to grow single crystal PZT were unsuccessful, there are many systems that have been grown as single crystals. These have been studied extensively since the 1990s [9, 20]. A comparison of the properties of each generation is included in Table 6.1 along with the reference of PZT. For the appropriate use case, relaxor-PT materials are far superior to PZT [26].

6.3.1 Development of Relaxor-PT Single Crystals

For convenience, the development of relaxor-PT single crystals is split into three generations [20] and these are now reviewed in turn:

First Generation Relaxor-PT Single Crystals

The first generation consists of binary compounds, where the relaxor-ferroelectric component is mixed with PT. These binary mixtures were first studied in the 1970s and 80s in ceramic form [27]. Whilst pure PMN showed no piezoelectric behaviour at room temperature, it did display a large electrostrictive coefficient [28], which was further improved upon the addition of PT [29]. The phase diagram for the binary mixture $Pb(Mg_{1/3}Nb_{2/3})O_3$ - $PbTiO_3$ (PMN-PT) was mapped by the late 1980s and a MPB was identified at $\approx$ 30% PT [30]. Similar work was

also carried out for $Pb(Zn_{1/3}Nb_{2/3})O_3$ - $PbTiO_3$ (PZN-PT) in 1981, with the MPB being now at $\approx 9\%$ PT [31]. These phase diagrams are shown in Figure 6.2.

Table 6.1: Table comparing material properties for various relaxor-PT single crystal compositions against PZT. (Data compiled from [9, 13, 20])

Material	**Properties**						
	ε_{33}^T [ε_0]	T_{lim}* [°C]	E_C [kV/cm]	d_{33} [pC/N]	k_{33}	$\tan\delta$ [%]	Q_{m}
Ceramic							
PZT4	1300	328	14.2	300	0.70	0.4	500
PZT8	1000	300	18.7	230	0.64	0.4	1000
Piezocrystal - Generation I							
PMN-0.29PT	5400	96	2.3	1540	0.91	-	150
PMN-0.33PT	8200	70	2.8	2800	0.95	-	100
PZN-0.08PT	6000	95	3	2500	0.93	-	-
Piezocrystal - Generation II							
PIN-PMN-PT (MPB)	7241	96	5.5	2740	0.95	0.2	120
PIN-PMN-PT	4400	70	5	1510	0.92	0.2	180
PMN-PZ-PT	4850	144	4.5	1530	0.92	0.5	100
Piezocrystal - Generation III							
Mn:PIN-PMN-PT	3700	119	6.0	1120	0.90	0.4	810
Mn:PMN-PZ-PT	3410	141	6.3	1140	0.92	0.2	1050

* T_{lim} is the upper phase transition temperature that limits the materials usage. For ceramic this corresponds to the Curie temperature T_C but for the various piezocrystal materials, this corresponds to another ferroelectric-ferroelectric phase transition such as T_{RT}.

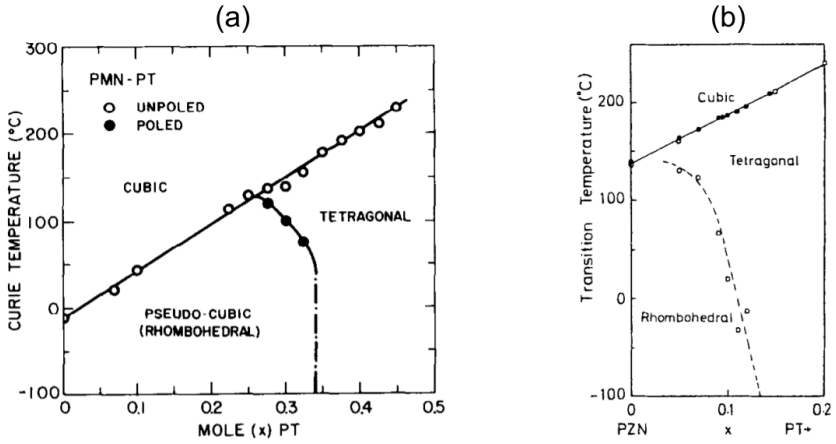

Figure 6.2: Phase diagram of PMN-PT (a) and PZN-PT (b). Curvature of the MPB can clearly be seen in both diagrams. (a) Reprinted from S. W. Choi *et al.*, "Morphotropic phase boundary in $Pb(Mg_{1/3}Nb_{2/3})O_3$-$PbTiO_3$ system," *Mater. Lett.*, vol. 8, no. 6, pp. 253–255, 1989, Copyright (1989), with permission from Elsevier. (b) Reproduced with permission from J. Kuwata *et al.*, "Phase transitions in the $Pb(Zn_{1/3}Nb_{2/3})O_3$-$PbTiO_3$ system," *Ferroelectrics*, vol. 37, no. 1, pp. 579–582, 1981.

The promising electrostrictive and dielectric performance of these ceramics, combined with the identification of a MPB, led to renewed interest in the materials which intensified when Kuwata *et al.* reported PZN-PT single crystals with $d_{33} > 1500$ pm/V [32]. MPB composition PZN-PT ceramic had been hard to manufacture but it could readily be grown as a single crystal. Furthermore, its large piezoelectric coupling was measured in crystals which were not poled along the polar direction. Specifically, the crystals were measured to be in the rhombohedral phase, which has polar direction along $[111]$, but the best performing crystals were poled along $[001]$. This highlights one of the main advantages of single crystal materials over polycrystalline: their ability to form domain engineered samples. This is where the macroscopic polarisation direction differs from the spontaneous, microscopic, one as allowed by symmetry. This is possible because of the pronounced crystal anisotropy, compared to ceramics [33]. A detailed review of the development of Gen. I single crystal materials, with a focus on PMN-PT, is given by Luo *et al.* [10].

Gen. I material has been reported to have a very large electromechanical coupling factor, $k_{33} \approx 0.9$, which far exceeds PZT, $k_{33} \approx 0.7$. This has allowed it to be commercialised in medical imaging [11, 19, 34]. The FOMs for many ultrasonic applications are reviewed by Zhang *et al.*; in this case, the correct FOM is simply the electromechanical coupling factor. This ensures that the medical imaging device will have high resolution and power efficiency as well as a broad bandwidth [20]. Hence, the superior k of relaxor-PT single crystals makes them very applicable in this case [35]. Furthermore, Gen. I's low mechanical quality factor, $Q_\mathrm{m} \approx 100$, aids the broad bandwidth requirement. This is because, as stated in Section 2.4.8, Q_m may be linked to the sharpness of the resonance and antiresonance. A poor Q_m produces broad resonance and antiresonance features in the electrical impedance, and so give large bandwidths.

Despite these advantages, binary compositions have some drawbacks. Unlike in PZT, where the MPB is largely temperature independent, as seen in Figure 2.3, PMN-PT and PZN-PT both show a curved MPB, as can clearly been seen in Figure 6.2. The region beneath the MPB is now thought to contain a monoclinic phase which likely contributes towards the high piezoelectric performance here [36]. However, this curvature means that, for compositions near the MPB, upon heating, they will encounter a ferroelectric-ferroelectric phase transition below the 'Curie' temperature. Commonly between rhombohedral and tetragonal phases, and referred to accordingly as T_RT, this temperature represents the upper temperature limit in many use cases as the piezoelectric performance is unstable across this transition and device behaviour will suffer as a result. Unfortunately, in MPB composition PMN-PT, $T_\mathrm{RT} \approx 80$ - $100\ ^\circ$C [10] which severely reduces the use window of Gen. I materials, especially in high-power and SONAR applications. This is compounded by Gen. I material's low Q_m which indicates that it has high losses and will suffer from self-heating.

Second Generation Relaxor-PT Single Crystals

Second generation materials are ternary mixtures, where a binary Gen. I crystal is doped with a third relaxor. An example is $Pb(In_{1/2}Nb_{1/2})O_3$ - $Pb(Mg_{1/3}Nb_{2/3})O_3$ - $PbTiO_3$ (PIN-PMN-PT) where In is doped into PMN-PT by the addition of the relaxor component $Pb(In_{1/2}Nb_{1/2})O_3$ (PIN). PIN-PMN-PT was first reported in the early 2000s and shares much of the phenomenology with Gen. I materials, such as the presence of a MPB which results in very high dielectric and piezoelectric coefficients [37]. Furthermore, it shows great promise for improving the applicability of relaxor-PT materials for two main reasons [38–40]:

Firstly, T_{RT} is raised to $\approx$ 115 - 135 °C [8]. This gives a much larger use window for high-power applications. Moreover, this gain does not come at the expense of any loss in the piezoelectric coefficient or electromechanical coupling factor [8], as shown in table 6.1.

Secondly, PIN-PMN-PT also shows a higher coercive field, on the order of 4.5 - 5.6 kV/cm, a two to three fold increase over Gen. I PMN-PT [8]. This greater stability diminishes the risk of an electric field induced transition, and allows the material to be driven with larger voltages - key in high-power ultrasound.

However, as shown in Table 6.1, PIN-PMN-PT still displays relatively low Q_m which, regardless of the previously mentioned improvements, limits its use in high-power and SONAR applications, where Q_m is linked to both the device electro-acoustic efficiency, FOM: k^2Q_m, and the device surface's vibration velocity amplitude, FOM: dQ_m [20].

Third Generation Relaxor-PT Single Crystals and Beyond

The continued low Q_m in Gen. II materials has motivated further experimentation with doping which had been found to be a good mechanism to tune material properties in PZT [41, 42]. Hence, doped ternary compositions make up the third generation of relaxor-ferroelectric materials.

The 'classic' Gen. III material is Mn-modified PIN-PMN-PT, written as Mn:PIN-PMN-PT. The addition of Mn has been reported to increase Q_m by four to five times compared to Gens. I and II [1, 43] and the same effect has been seen in Mn-modified PMN-PZ-PT [3]. Again, this increase comes almost 'free' as the electromechanical coupling and piezoelectric constants are not significantly impacted. Indeed, these materials defy the inverse trend between k_{33} and Q_m seen in PZT as illustrated in Figure 6.3 [9]. This means that materials, such as Mn:PIN-PMN-PT, may be produced with simultaneously high k_{33} and Q_m, hence, greatly increasing the suitability for high-power and underwater SONAR devices [20].

Whilst the positive effects of Mn modification are clear, the reason behind this is not well-understood. A proposed mechanism by which the Mn increases Q_m is through the formation of defect dipoles which, by creating internal bias fields, hinder the extrinsic loss mechanism of domain wall movement [44]. However, this applies only if the Mn substitutes as Mn^{2+} on the perovskite B-site [45], replacing a more positively charged ion e.g. Ti^{4+} or Nb^{5+}. As the

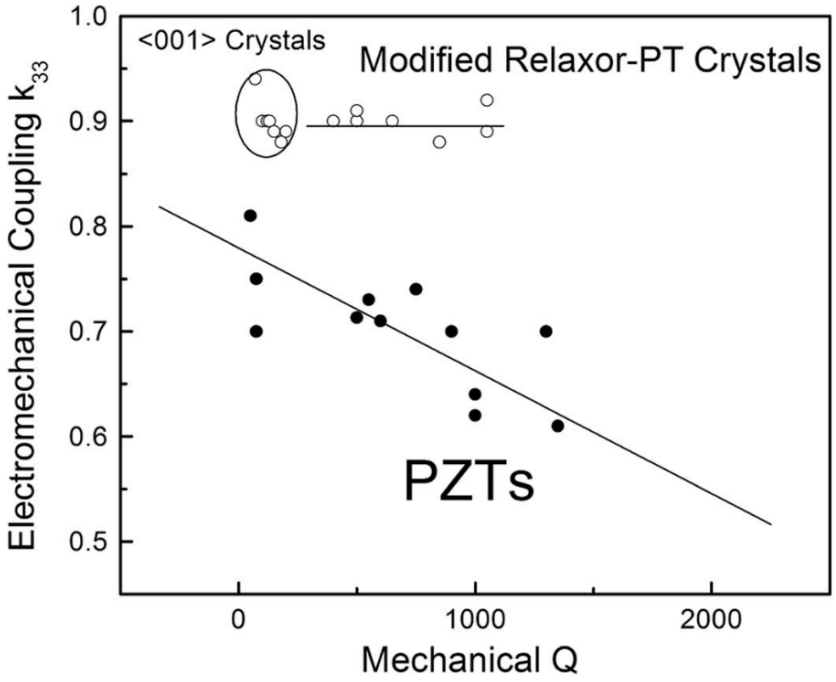

Figure 6.3: The inverse relationship between k_{33} and Q_{m} seen in PZT. This trend is not seen in Mn-modified relaxor-PT single crystals, suggesting as possible materials with simultaneously high k and Q_{m}. Reproduced from S. Zhang *et al.*, "Relaxor-PT single crystals: Observations and developments," *IEEE Trans. Ultrason. Ferroelectr. Freq. Contr.*, vol. 57, no. 10, pp. 2138–2146, 2010. ©2010 IEEE

valence and dopant site of the Mn have been reported to be variable [46, 47], a more general mechanism may be present. Furthermore, it is believed that material processing conditions may also impact this variability [48].

Another doped composition that has attracted recent attention is Sm doped PMN-PT [49]. This material has shown huge piezoelectric coefficients with d_{33} in the range 3400 - 4100 pC/N, and much higher dielectric permittivity. However, it also shows an increase in dielectric losses and much lower $T_{\mathrm{RT}} \approx 60$ °C [50], both of which need to be addressed for it to have any real impact.

6.3.2 Piezoelectric Mechanisms

This section briefly reviews some proposed mechanisms to account for the large piezoelectric behaviour in relaxor-PT single crystals.

The first is domain engineering: where multiple symmetry-related domains are combined to create a state with a different macroscopic symmetry [51]. This is typically achieved by poling the crystal along a non-polar axis which, so as to minimise the angle to this poling direction, favours certain symmetry-related domains. The different configurations are reviewed by Zhang *et al.* [20]. This effect was first reported by Kuwata *et al.* when they observed higher piezo-

electric coupling in crystals which were not poled along the polar direction [32]. The domains, in turn, induce other phenomena such as the domain wall motion, which has been implicated in the high performance of these materials. This is one of the dominant extrinsic mechanisms but can also lead to increased losses [52]. Furthermore, domain engineering enables, through the creation of new macroscopic symmetries, exploitation of novel resonance modes such as the face-shear, d_{36}, and length-thickness extensional, d_{32}, modes [20].

The impact of the MPB and its link to high material property values has also been studied. Following its discovery in PZT [53], monoclinic phases were also soon reported in relaxor-ferroelectrics such as PMN-PT [54] and PZN-PT [55]. Near the MPB, the free energies of the different phases are naturally similar, and so the appearance of the monoclinic phase permits a new rotation path between the tetragonal and rhombohedral phases which classically sit on either side of the MPB [56]. This polarisation rotation was shown by Fu and Cohen to be a viable mechanism behind the 'ultrahigh' piezoelectric responses in relaxor-ferroelectrics [57]. This is a so-called 'intrinsic' mechanism and is believed to be dominant in multi-domain relaxor-PT single crystals and behind their strong uniaxial piezoelectric activity, i.e. d_{33} [13]. However, as with domain wall motion, easy polarisation rotation has also been linked to higher losses due to rotationally-induced torques [58].

Lastly, there is the contribution of PNRs. These have been linked to the large dielectric and piezoelectric responses shown in relaxor-PT materials and have been implicated in flattening the free energy profile near the MPB, which facilitates the polarisation rotation mechanism, through phase-field simulations [59]. It has been suggested by Li *et al.* that this is corroborated by measurements, showing that the PNR contribution can be frozen out at cryogenic temperatures [60]. This is illustrated in Figure 6.4, where the large jump is seen in relaxor-PT materials only. The authors attribute this to the unlocking of the dynamic nature of the PNRs as it is unable to be accounted for by any long range phenomena.

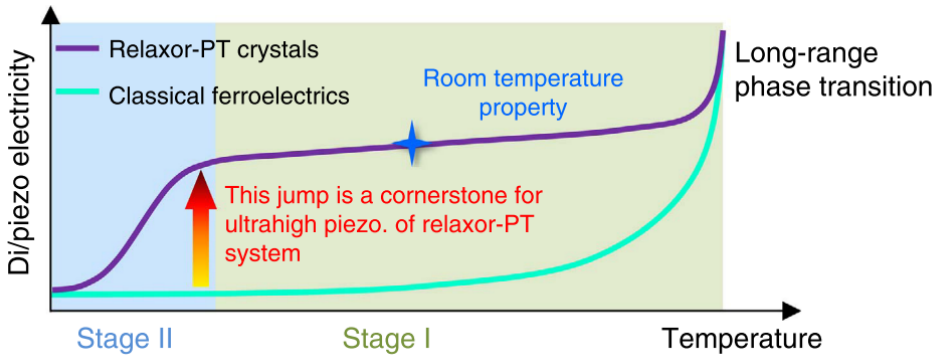

Figure 6.4: Schematic plot comparing the temperature dependence of the dielectric and piezoelectric properties in normal and relaxor-PT ferroelectric crystals. Figure reproduced under the terms of the Creative Commons CC BY license from F. Li *et al.*, "The origin of ultrahigh piezoelectricity in relaxor-ferroelectric solid solution crystals," *Nat. Commun*, vol. 7, p. 13 807, 2016.

To the contrary, Shepley *et al.* argue that this contribution is a result of domain wall motion and not PNRs [61]. They report that the large dielectric relaxation seen in Figure 6.4 is present only when the sample is poled and is more prominent in multi-domain samples. They argue that, if this contribution were purely PNR based, as suggested by Li *et al.*, then it should be universally present. Furthermore, they cast doubt upon the freezing nature of this behavioural 'transition' and conclude that no current mechanism can fully account for the observed behaviour. This dilemma leaves many unanswered questions as to what is behind the low temperature behaviour of the materials, providing motivations for further cryogenic studies.

If the large piezoelectric effect is due to domain wall motion, it is unclear how the pinning of these domain walls in Mn:PIN-PMN-PT, responsible for their simultaneous large Q_{m}, is consistent. This provides further motivation for studying the Mn content and, as such, this chapter will discuss a feasibility study for determining the Mn content and valence using the negative muon technique.

6.4 Mn Valence Study

Given that the chemistry of Mn:PIN-PMN-PT is complicated, the first step was to characterise the change in muonic emission between samples with different, known Mn oxidation states. Whilst the use of μ^- implantation as a means of chemical analysis in relaxor-ferroelectrics has been established both in the literature [62] and here in Chapter 5, the aim of the present study was to explore whether this technique can be used to determine valence states of Mn. Given that the exact mechanisms by which the Mn increases Q_{m} are still not entirely understood, a method to non-destructively determine the Mn valence in a sample would be invaluable.

Previous theoretical and experimental studies have provided evidence that the muon capture may be dependent on valence. The Fermi-Teller 'Z law', postulated in 1947, states that the stopping cross-section for μ^-s is proportional to the number of electrons [63]. This is based on the assumption that the primary mechanism for slowing the μ^-s is through electron collisions. Further analysis confirmed that the cross-section is sensitive to the electronic structure of the atom [64]. The Z law has since been refined, with many muon capture models being developed subsequently [65, 66], culminating in the more general muon-cascade model [67].

Recently, the μ^- technique has been used to investigate local chemistry. Previously this was achieved using methods such as X-ray absorption spectroscopy (XAS) and X-ray emission spectroscopy (XES) [68] but these are not suited to low atomic number (Z) materials due to the high rates of soft photon reabsorption. The larger mass of the μ^-, can overcome this problem with muonic X-rays, as these have higher energy, and can pass through condensed matter with little reabsorption.

Muonic X-rays have been shown to be sensitive to the density of both gases [69] and carbon-based solid-state materials [70] but, only recently, has evidence been presented to show their

sensitivity to electronic structure solidifying the link with the Fermi-Teller and muon-cascade models [71]. The intensities of muonic X-rays from Fe oxides and the mixed-hydride system $Ca(BH_4)_2$-Mg_2NiH_4 were used to determine the electronic structure and a variation was found in the ratio of doublet Kα emission lines ($2p \rightarrow 1s$) of FeO, Fe_3O_4 and Fe_2O_3 which decreased with Fe oxidation number, and a similar shift was observed in iron halides.

This evidence suggests that the μ^- technique should be able to distinguish between the different valences of Mn. In order to verify this, a series of measurements on MnO - Mn(II); Mn_2O_3 - Mn(III); and MnO_2 - Mn(IV) were performed to test whether there is a measurable change in the muonic X-ray emission either through a change in their intensity or energy.

6.4.1 Sample Preparation

Powders of MnO, Mn_2O_3 and MnO_2 (Sigma-Aldrich, Merck KGaA, Darmstadt, Germany) were ground and pressed into pellets for the beamline experiment. These pellets were 32 mm in diameter and 10 mm in thickness with their weights as follows: MnO - 10.42 g; Mn_2O_3 - 10.71 g; and MnO_2 - 40.33 g. The three oxides have different crystal structures with MnO adopting a rock salt lattice, Mn_2O_3 a bixbyite structure, and MnO_2 a rutile structure. However, in the case of the powders used here, these structures have not been independently confirmed and were assumed based on the quoted compositions. As with PFN, the pellets were wrapped in an Al foil packet, illustrated in Figure 6.5, which was suspended in the μ^- beam.

The larger weight of the MnO_2 pellet was aimed at increasing the muon count rate. However, this was juxtaposed with issues with the detector efficiency. In order to ensure that X-ray detectors are not saturated, care must be taken to reduce the number of photons detected to a suitable level. This arises because of the finite reaction time of the detector and so saturation may result in a so-called 'double peak' where a false splitting is observed. Though this can be overcome by using a larger number of detectors, each covering a smaller solid angle, only four detectors were used in the measurements described here, and a detuning of the μ^- beam was necessary. The μ^- beam is focused and steered through the beam guide by a series of superconducting magnets as illustrated in Figure 3.3(a). To reduce the μ^- flux slightly, the first two focussing quadrupole magnets were set to 90% efficiency but this was reduced to 85% for the larger pellet.

6.4.2 Emission Lines

The theory of muonic atoms is well-characterised and so both theoretical and experimental atomic transition levels are extensively documented both in the literature [72] and in other resources such as the Mesoroentgen Spectra Catalogue website [73], the latter compiled over many years by scientists using instruments at both the PSI (Villigen, Switzerland) and MuSIC (Osaka, Japan) muon sources. Hence, the expected emission lines for Mn and O are listed in Tables 6.2 and 6.3.

Figure 6.5: A pressed pellet of MnO_2 shown (a) before and (b) after wrapping in Al foil.

Table 6.2: Theoretical energies of the muonic emission lines of Mn [72, 73].

Atomic Transition		Energy (keV)
K	2p → 1s	1170.6, 1174.2
	3p → 1s	1419.3
	4p → 1s	1505.3
L	3d → 2p	245.5, 248.8
	4d → 2p	331.2, 334.7
M	4f → 3d	85.1
	5f → 3d	125
	6f → 3d	146.6
	7f → 3d	159.1
	8f → 3d	168
	9f → 3d	173.6

Table 6.3: Theoretical energies of the muonic emission lines of O [72, 73].

Atomic Transition		Energy (keV)
K	2p → 1s	133.5
	3p → 1s	158.4
	4p → 1s	167.1
	5p → 1s	171.1
	6p → 1s	173.3

6.4.3 Results

This section presents the emission spectra from the three oxides. All samples were measured at room temperature on Port 4 of the RIKEN-RAL beamline at ISIS. The counting time was approximately 24 hours per sample. A μ^- momentum of 30 MeV/c was used to ensure sufficient penetration into the samples. Two regions of interest are considered here: 80 keV - 350 keV, encompassing the M and L lines of Mn and the K lines of O, and 1100 keV - 1550 keV, encompassing the K lines of Mn.

Also observed in the spectra were several spurious peaks that could not be identified as resulting from a muonic transition. However, once the muon has completed its cascade, it can be captured into the nucleus in a process analogous to electron capture. This results in an excited nucleus of reduced Z, which undergoes gamma decay. In this case, the μ^- is captured into the Mn nucleus (Z = 25), producing an excited isotope of Cr (Z = 24). The resulting gamma emission is of sufficient energy to be detected in this experiment. This effect was observed in all oxides and has been labelled accordingly in Figures 6.9, 6.12 and 6.15.

Data Analysis

As detailed in Chapter 3, the four Ge based X-ray detectors were split into two pairs, low and high energy, with detection ranges of 3 keV - 1 MeV and 3 keV - 8 MeV respectively. In this experiment, due to the relatively small samples, all four detectors could be used, and so, the counts from the upstream and downstream detectors were added in both energy ranges. Errors in these measurements were estimated as the square root of the counts, according to the Poisson statistics which apply to counting experiments [74, 75]. These errors were appropriately propagated through the analysis [76].

A background was fitted and subtracted from the raw count data. Inclusion of a background term accounts for phenomena such as the low energy profile of the photoelectric absorption and inelastic Compton scattering [71]. Assuming, over the energy regions of interest, that this background is linear, a least squares fit was performed to the sections of the spectra without discernable peaks. In the low energy region of interest, a piecewise fit of two linear polynomials was required due to the more pronounced curvature of the measured background over this larger range. This is illustrated in Figure 6.6, with an error in this background was estimated from the 95% confidence interval for the fitting procedure.

In order to fit the observed emission lines, a Gaussian profile was assumed. This is justified due to the broadening being caused by the experimental energy resolution, limited by the detector. This allowed an amplitude and energy to be estimated for each line and these are detailed in the subsections that follow.

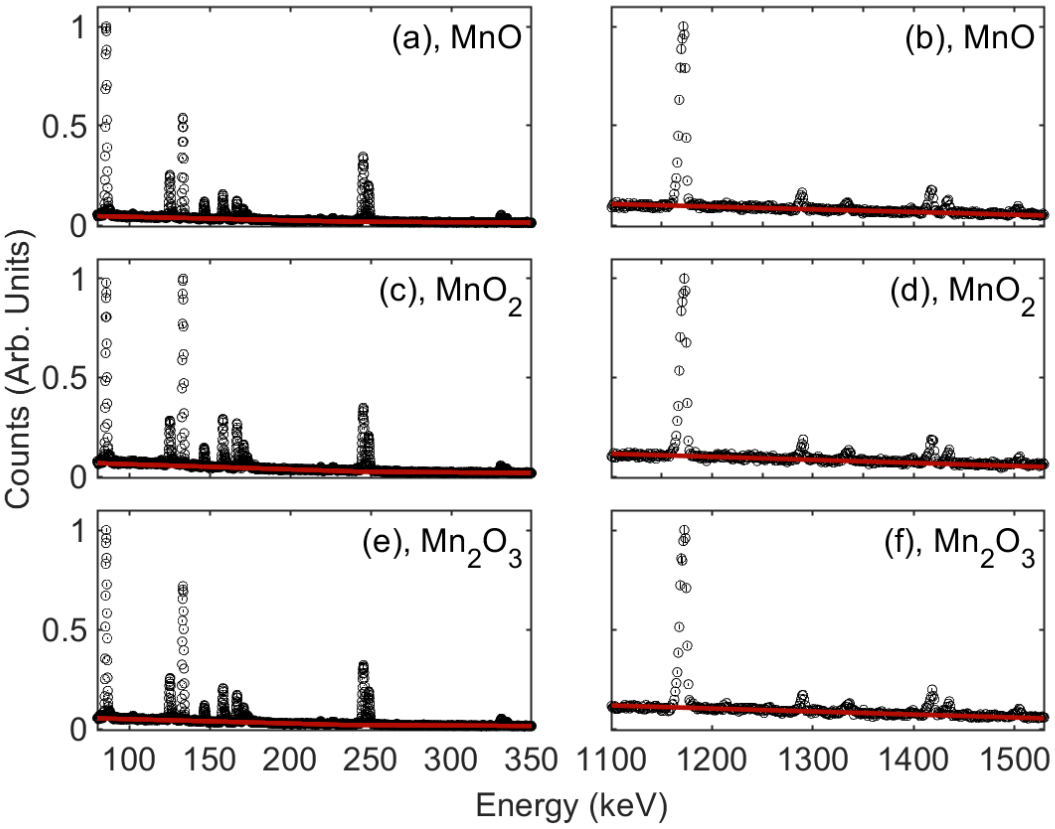

Figure 6.6: The fitted background (red) to the two regions of interest for the three samples.

MnO - Mn(II)

The first powder to be studied was MnO. As oxygen has an oxidation number of 2-, the one-to-one stoichiometry in MnO ensures that Mn also has a valence of 2. Sections of the emission spectra are shown in Figures 6.7 - 6.9. All of the expected Mn and O lines were identified in accordance with Tables 6.2 and 6.3. The fitted Mn values for both peak amplitude and energy are shown in Table 6.4. Good agreement is shown with the expected emission lines.

Table 6.4: Fitted values for the measured muonic emission lines of Mn in MnO.

Atomic Transition		Fitted Amplitude	Fitted Energy (keV)
K	2p $\rightarrow$ 1s	1385 $\pm$ 172	1168.1 $\pm$ 0.2
		2273 $\pm$ 132	1172.0 $\pm$ 0.2
	3p $\rightarrow$ 1s	305 $\pm$ 39	1417.2 $\pm$ 0.3
	4p $\rightarrow$ 1s	93 $\pm$ 35	1503 $\pm$ 1.2
L	3d $\rightarrow$ 2p	2744 $\pm$ 414	245.3 $\pm$ 0.1
		1552 $\pm$ 435	248.7 $\pm$ 0.2
	4d $\rightarrow$ 2p	301 $\pm$ 398	331 $\pm$ 1
		182 $\pm$ 423	334 $\pm$ 2
M	4f $\rightarrow$ 3d	8335 $\pm$ 218	85.57 $\pm$ 0.01
	5f $\rightarrow$ 3d	1844 $\pm$ 196	125.16 $\pm$ 0.07
	6f $\rightarrow$ 3d	697 $\pm$ 200	146.6 $\pm$ 0.2
	7f $\rightarrow$ 3d	326 $\pm$ 455	159 $\pm$ 3
	8f $\rightarrow$ 3d	127 $\pm$ 1247	167 $\pm$ 15
	9f $\rightarrow$ 3d	119 $\pm$ 1792	173 $\pm$36

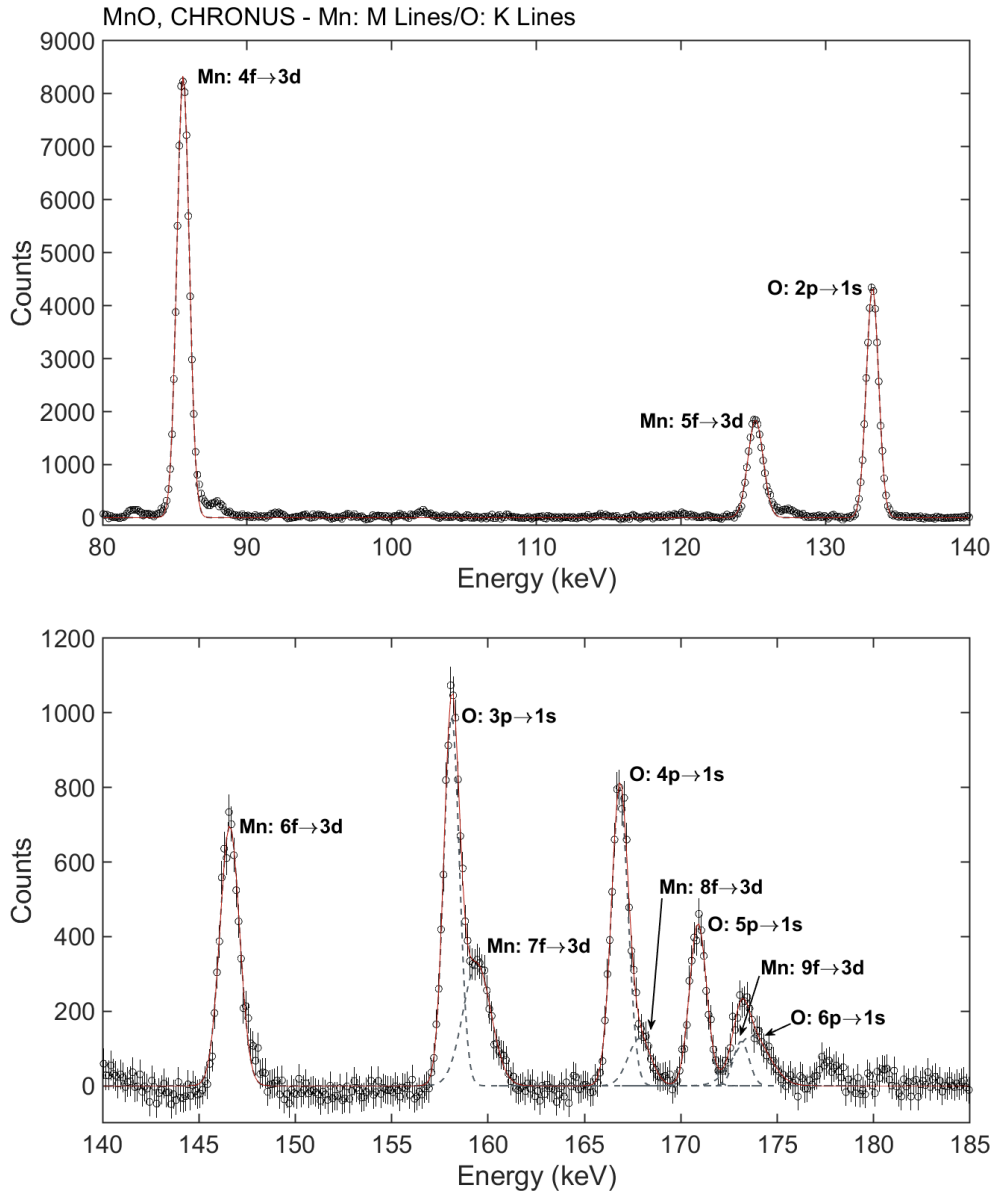

Figure 6.7: X-ray spectra resulting from μ^- implantation into a powder sample of MnO, showing the M lines of Mn (nf $\rightarrow$ 3d) and the K lines of O (np $\rightarrow$ 1s). Errors were estimated using Poisson/counting statistics. A linear background has been subtracted.

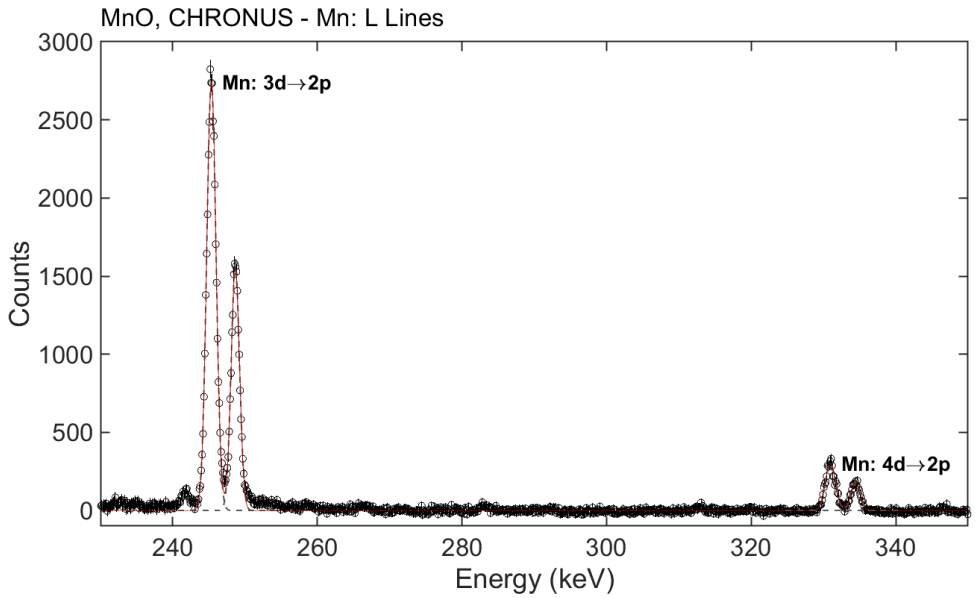

Figure 6.8: X-ray spectra resulting from μ^- implantation into a powder sample of MnO, showing the L lines of Mn (nd $\rightarrow$ 2p). The absence of a line at $\approx$ 346 keV indicates that the μ^- were correctly stopping in the sample rather than in the Al foil coating. Errors were estimated using Poisson/counting statistics. A linear background has been subtracted.

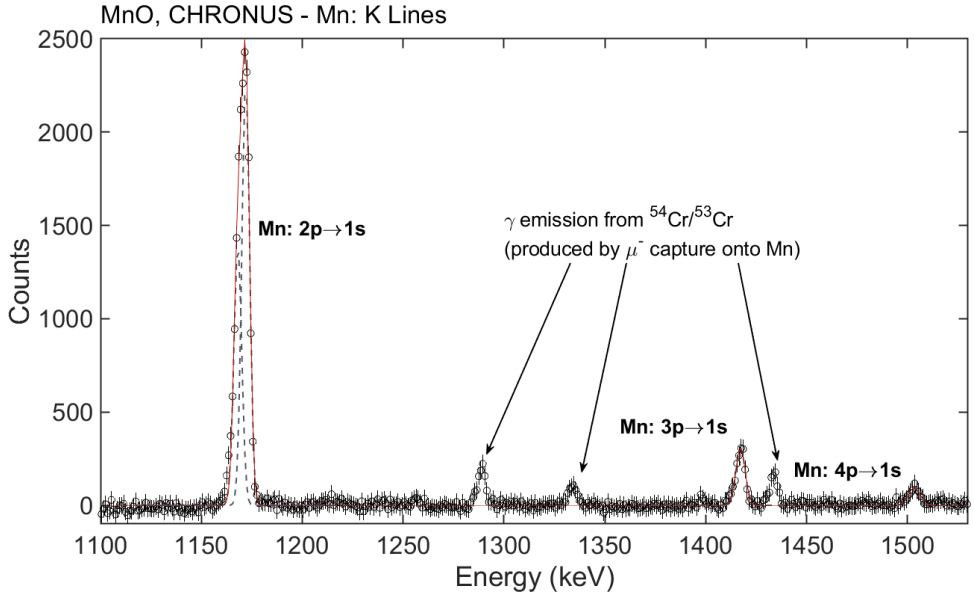

Figure 6.9: X-ray spectra resulting from μ^- implantation into a powder sample of MnO, showing the K lines of Mn (np $\rightarrow$ 1s). Also labelled are the γ emission signals from ^{54}Cr/^{53}Cr formed as a product of muon capture by the Mn nucleus. Errors were estimated using Poisson/counting statistics. A linear background has been subtracted.

Mn_2O_3 - Mn(III)

Mn_2O_3 was studied next with sections of the emission spectra shown in Figures 6.10 - 6.12. In this compound, Mn has a valence of 3. Again, all expected Mn and O lines were identified and fitted Mn values are given in Table 6.5. Good agreement is shown with Tables 6.2 and 6.3.

Table 6.5: Fitted values for the measured muonic emission lines of Mn in Mn_2O_3.

Atomic Transition		Fitted Amplitude	Fitted Energy (keV)
K	2p → 1s	1570 ± 177	1168.7 ± 0.2
		2422 ± 145	1172.9 ± 0.2
	3p → 1s	309 ± 43	1418 ± 0.4
	4p → 1s	104 ± 38	1504 ± 1.4
L	3d → 2p	2737 ± 467	245.5 ± 0.1
		1500 ± 478	248.8 ± 0.2
	4d → 2p	313 ± 447	331 ± 1
		179 ± 453	334 ± 2
M	4f → 3d	8370 ± 236	85.60 ± 0.02
	5f → 3d	1906 ± 212	125.22 ± 0.07
	6f → 3d	706 ± 219	146.7 ± 0.2
	7f → 3d	384 ± 735	159 ± 5
	8f → 3d	165 ± 3111	167 ± 25
	9f → 3d	225 ± 17462	173 ± 6

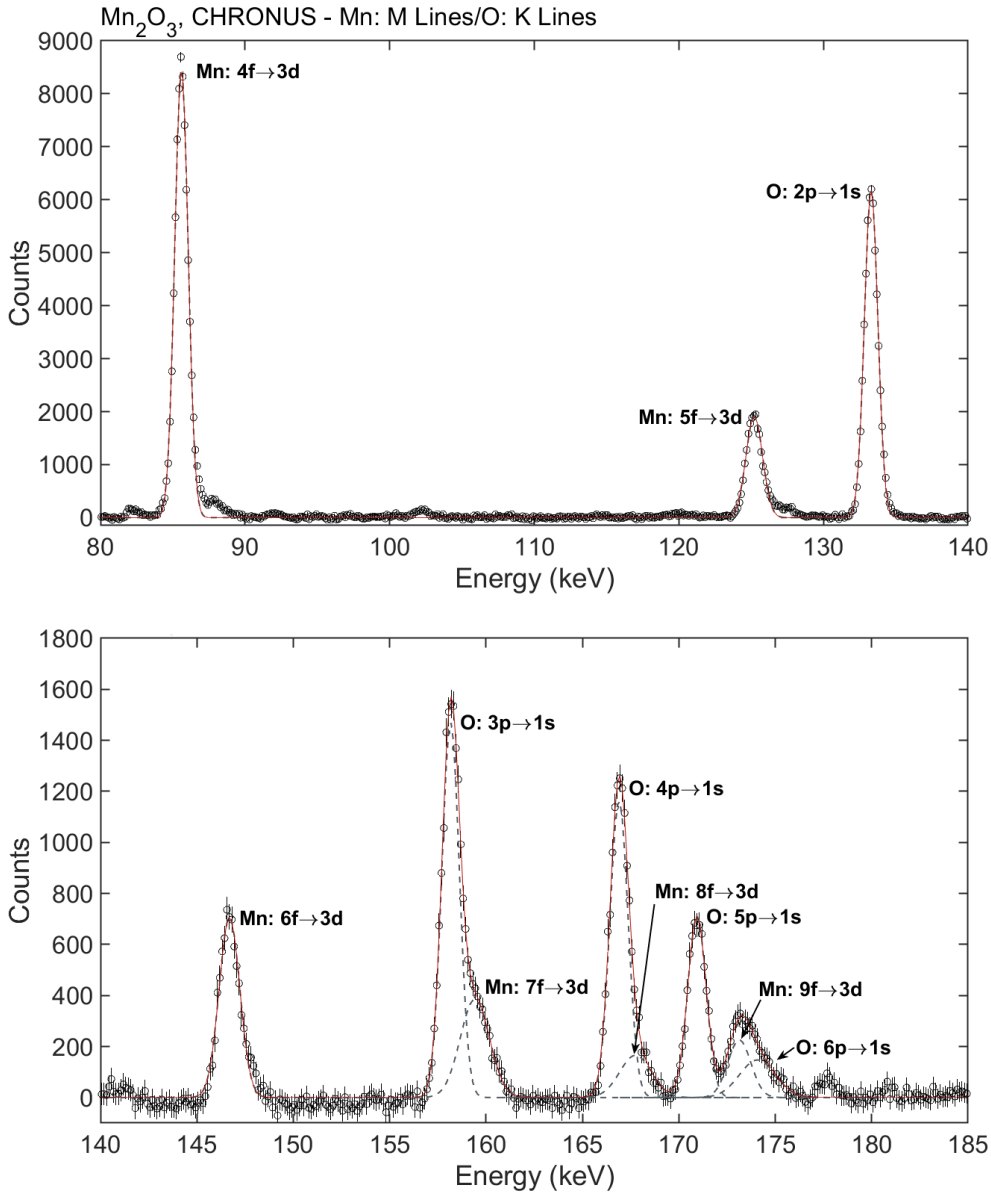

Figure 6.10: X-ray spectra resulting from μ^- implantation into a powder sample of Mn_2O_3, showing the M lines of Mn (nf $\rightarrow$ 3d) and the K lines of O (np $\rightarrow$ 1s). Errors were estimated using Poisson/counting statistics. A linear background has been subtracted.

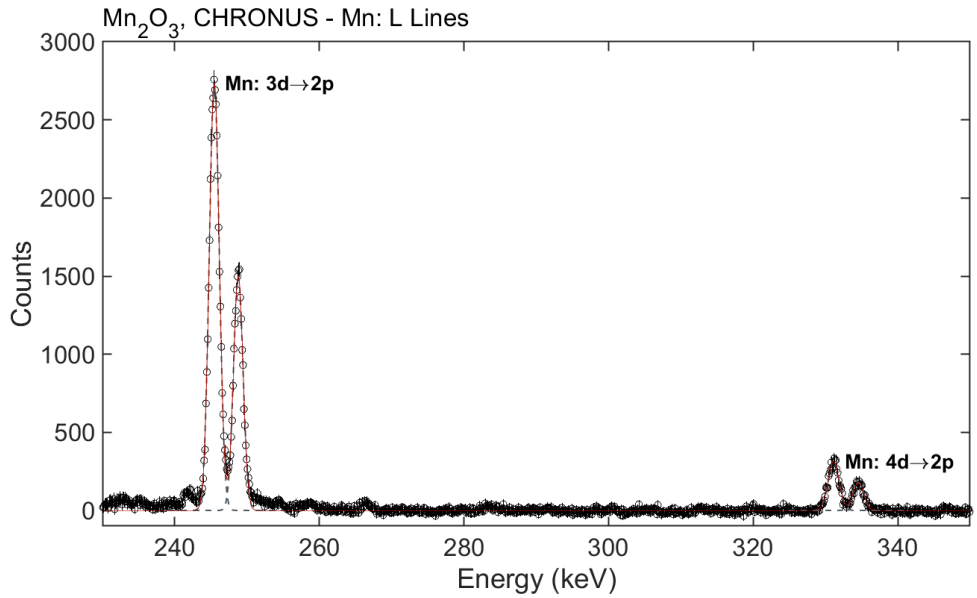

Figure 6.11: X-ray spectra resulting from μ^- implantation into a powder sample of Mn_2O_3, showing the L lines of Mn (nd $\rightarrow$ 2p). The absence of a line at $\approx$ 346 keV indicates that the μ^- were correctly stopping in the sample rather than in the Al foil coating. Errors were estimated using Poisson/counting statistics. A linear background has been subtracted.

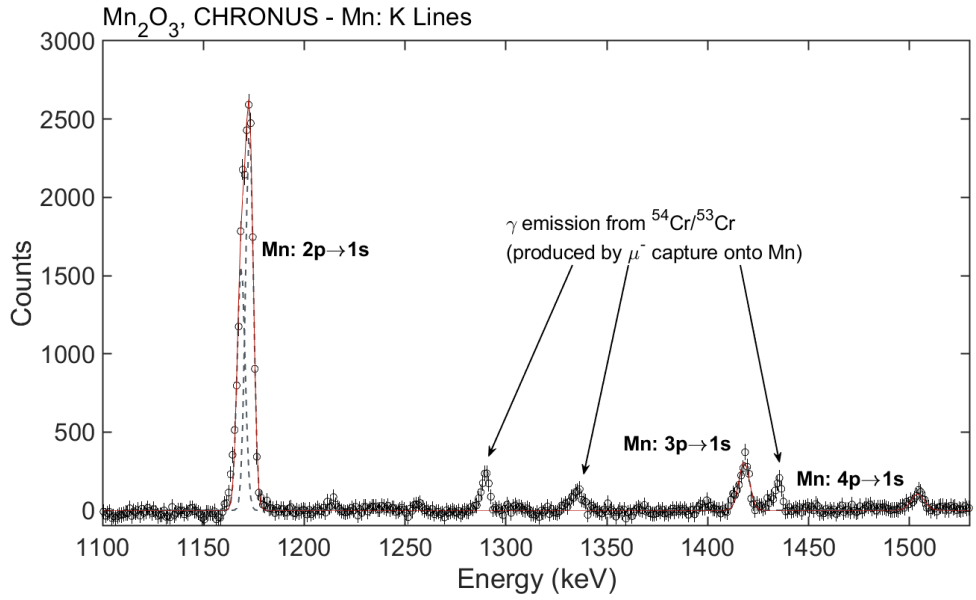

Figure 6.12: X-ray spectra resulting from μ^- implantation into a powder sample of Mn_2O_3, showing the K lines of Mn (np $\rightarrow$ 1s). Also labelled are the γ emission signals from ^{54}Cr/^{53}Cr formed as a product of muon capture by the Mn nucleus. Errors were estimated using Poisson/counting statistics. A linear background has been subtracted.

MnO_2 - Mn(IV)

Finally, MnO_2 (Mn valence of 4) completed the study. Relevant sections of the emission spectra are shown in Figures 6.13 - 6.15 and the Mn and O lines were identified with fitted Mn values given in Table 6.5. Again, good agreement is shown to the theoretical lines.

Table 6.6: Fitted values for the measured muonic emission lines of Mn in MnO_2.

Atomic Transition		Fitted Amplitude	Fitted Energy (keV)
K	2p $\rightarrow$ 1s	1235 $\pm$ 127	1168.8 $\pm$ 0.2
		1872 $\pm$ 105	1172.8 $\pm$ 0.1
	3p $\rightarrow$ 1s	268 $\pm$ 37	1417.9 $\pm$ 0.4
	4p $\rightarrow$ 1s	61 $\pm$ 24	1504 $\pm$ 2.5
L	3d $\rightarrow$ 2p	1907 $\pm$ 349	245.4 $\pm$ 0.1
		1058 $\pm$ 356	248.7 $\pm$ 0.2
	4d $\rightarrow$ 2p	213 $\pm$ 336	331 $\pm$ 1
		132 $\pm$ 345	334 $\pm$ 2
M	4f $\rightarrow$ 3d	5317 $\pm$ 187	85.57 $\pm$ 0.02
	5f $\rightarrow$ 3d	1345 $\pm$ 157	125.21 $\pm$ 0.08
	6f $\rightarrow$ 3d	547 $\pm$ 168	146.6 $\pm$ 0.2
	7f $\rightarrow$ 3d	312 $\pm$ 468	159 $\pm$ 4
	8f $\rightarrow$ 3d	218.6 $\pm$ 2508	167 $\pm$ 7
	9f $\rightarrow$ 3d	224 $\pm$ 1837	173 $\pm$ 1

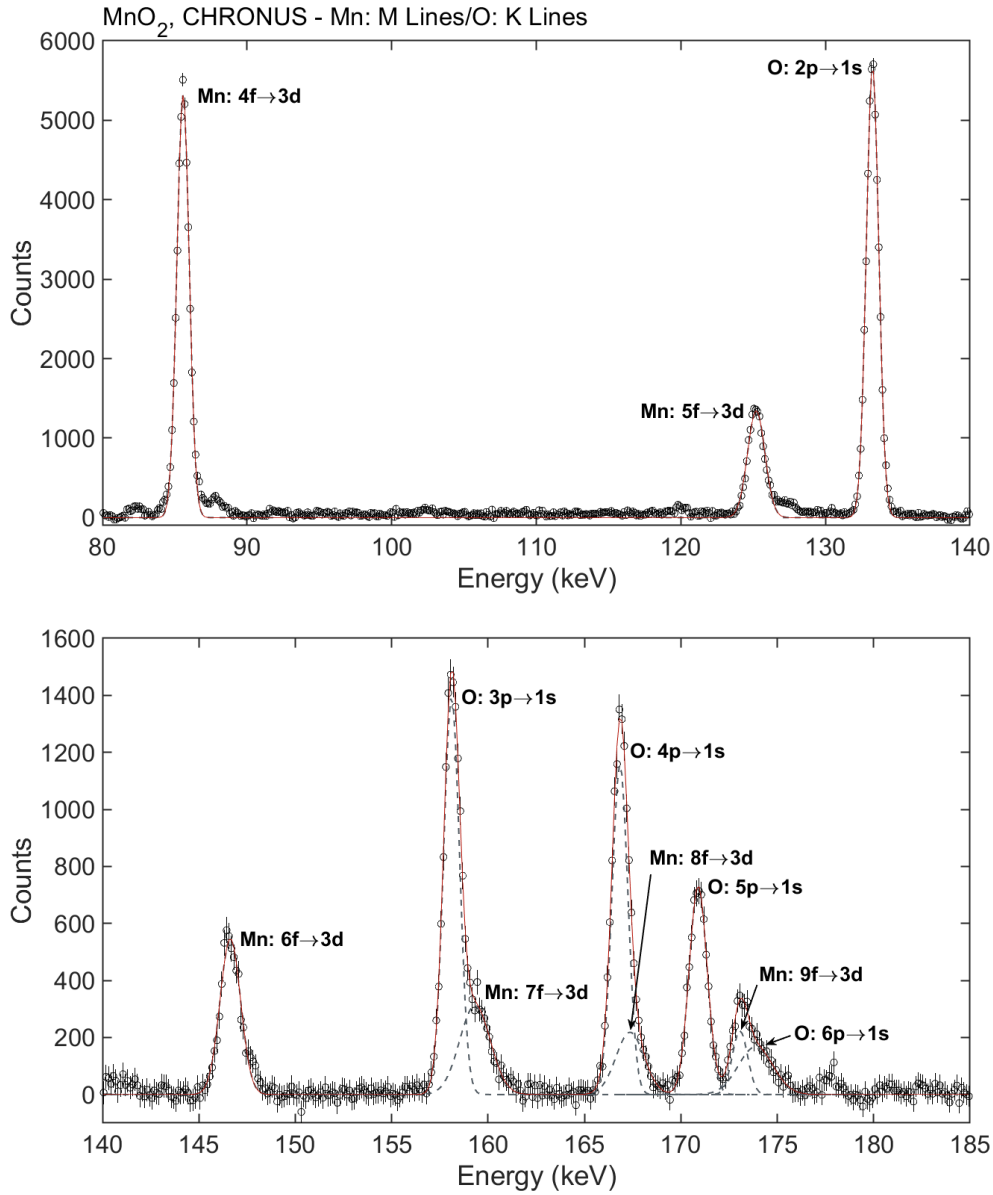

Figure 6.13: X-ray spectra resulting from μ^- implantation into a powder sample of MnO_2, showing the M lines of Mn (nf $\rightarrow$ 3d) and the K lines of O (np $\rightarrow$ 1s). Errors were estimated using Poisson/counting statistics. A linear background has been subtracted.

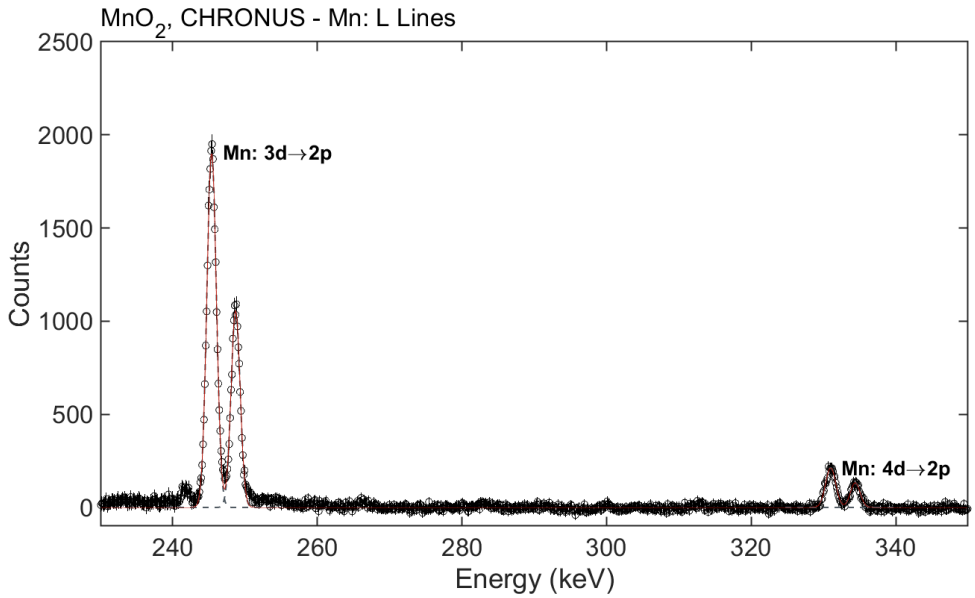

Figure 6.14: X-ray spectra resulting from μ^- implantation into a powder sample of MnO_2, showing the L lines of Mn (nd $\rightarrow$ 2p). The absence of a line at $\approx$ 346 keV indicates that the μ^- were correctly stopping in the sample rather than in the Al foil coating. Errors were estimated using Poisson/counting statistics. A linear background has been subtracted.

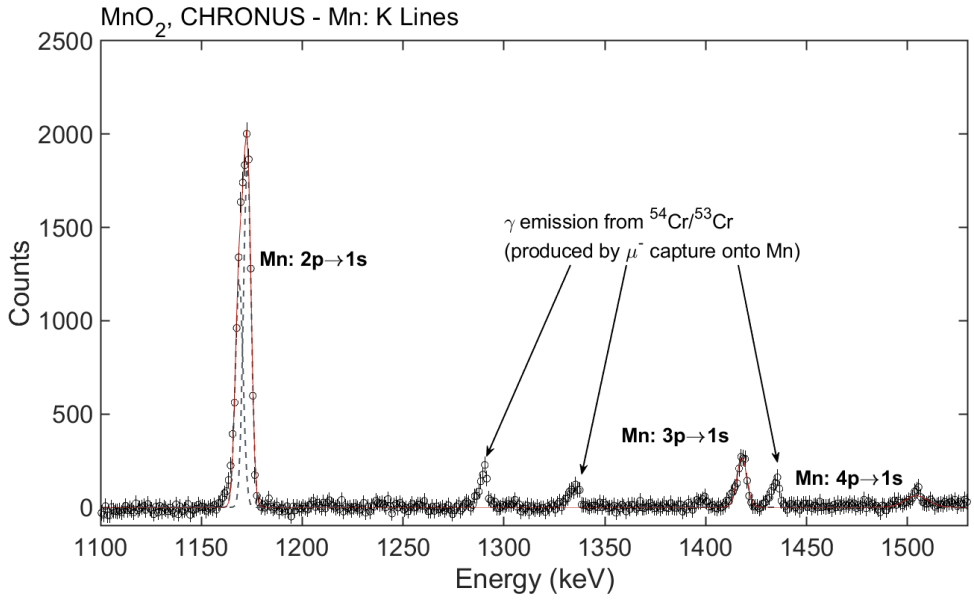

Figure 6.15: X-ray spectra resulting from μ^- implantation into a powder sample of MnO_2, showing the K lines of Mn (np $\rightarrow$ 1s). Also labelled are the γ emission signals from ^{54}Cr/^{53}Cr formed as a product of muon capture by the Mn nucleus. Errors were estimated using Poisson/counting statistics. A linear background has been subtracted.

6.4.4 Discussion

According to Fermi/Teller and others, the muon capture process should be dependent on the number of electrons and the emission spectra from the different Mn oxides should thus be different. Furthermore, due to the differing electronic structures, it is logical to assume that the change in valence should affect both emission line energy and intensity.

The lowest K lines are usually easily identified and may be expected to show the largest change, as they are both high in energy and of sufficient intensity. These are typically denoted as Kα_1 and Kα_2 corresponding to the transitions $2p_{3/2} \rightarrow 1s_{1/2}$ and $2p_{1/2} \rightarrow 1s_{1/2}$ respectively, with Kα_1 being the higher in energy. The subscript refers to the angular momentum of the state, with the splitting being induced by fine structure corrections such as spin-orbit coupling. These two peaks are compared using the fitted data. Whilst the splitting is not strong enough nor the instrument of sufficient resolution to fully, separate Kα_1 and Kα_2, the resulting peak shape is well-fitted with two constituent Gaussian profiles as shown in Figures 6.9, 6.12 and 6.15.

Figure 6.16 shows the combined Kα_1/Kα_2 2p $\rightarrow$ 1s peak for Mn, in arbitrary units, for all three oxides. A shift can clearly be seen between the MnO peak, shown in black, and the other two. In order to discount any systematic shift, the combined Kα_1/Kα_2 2p $\rightarrow$ 1s peak for O, in arbitrary units, is also compared in Figure 6.17 and no such effect is observed. The fitted peak energies are compared in Table 6.7.

Table 6.7: Comparison of the fitted energies of the muonic 2p $\rightarrow$ 1s muonic emission line for Mn and O in various Mn oxides.

Element	Atomic Transition		MnO	Mn_2O_3	MnO_2
Mn	2p $\rightarrow$ 1s	Kα_1	1172.0 ± 0.2	1172.9 ± 0.2	1172.8 ± 0.1
		Kα_2	1168.1 ± 0.2	1168.7 ± 0.2	1168.8 ± 0.2
O	2p $\rightarrow$ 1s	Kα	133.25 ± 0.2	133.30 ± 0.2	133.26 ± 0.2

The ratio of the Mn Kα_1 and Kα_2 peaks was calculated and is plotted against valence in Figure 6.18(a). Previous studies had measured a systematic decrease in this ratio against valence [71] and a similar pattern is observed here. However, it should be noted that the change is within the error bar and so further measurements may required to verify this trend.

This previous study also compared the ratio of the first L lines [71]. Unable to observe the splitting of Lα, they compared the combined Lα to Lβ. However, in the case of Mn oxides presented here, this splitting is clear and the two peaks of Lα_1 and Lα_2 are discernable. Their ratio is plotted in Figure 6.18(b) but no real trend was observed. Again, the error bars are so large that further measurements are desirable to verify this result.

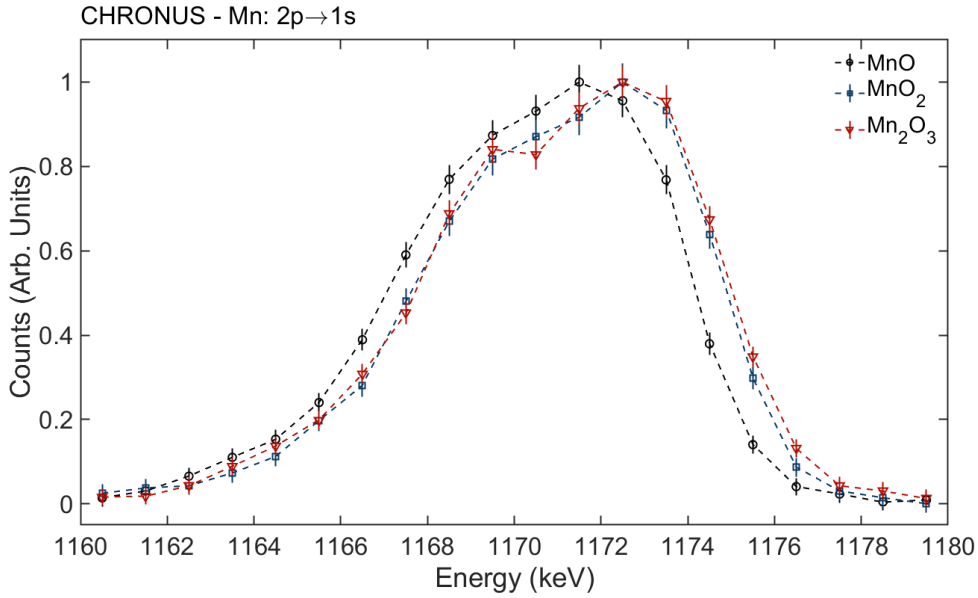

Figure 6.16: Comparison of the muonic Mn 2p $\rightarrow$ 1s Kα_1/Kα_2 emission line for various Mn oxides. Errors were estimated using Poisson/counting statistics.

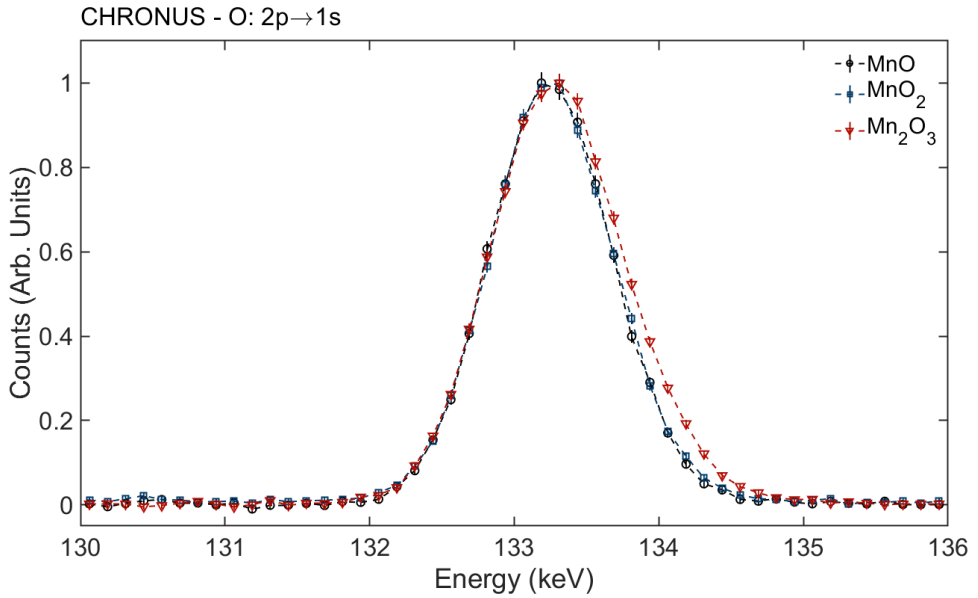

Figure 6.17: Comparison of the muonic O 2p $\rightarrow$ 1s Kα emission line for various Mn oxides. Errors were estimated using Poisson/counting statistics.

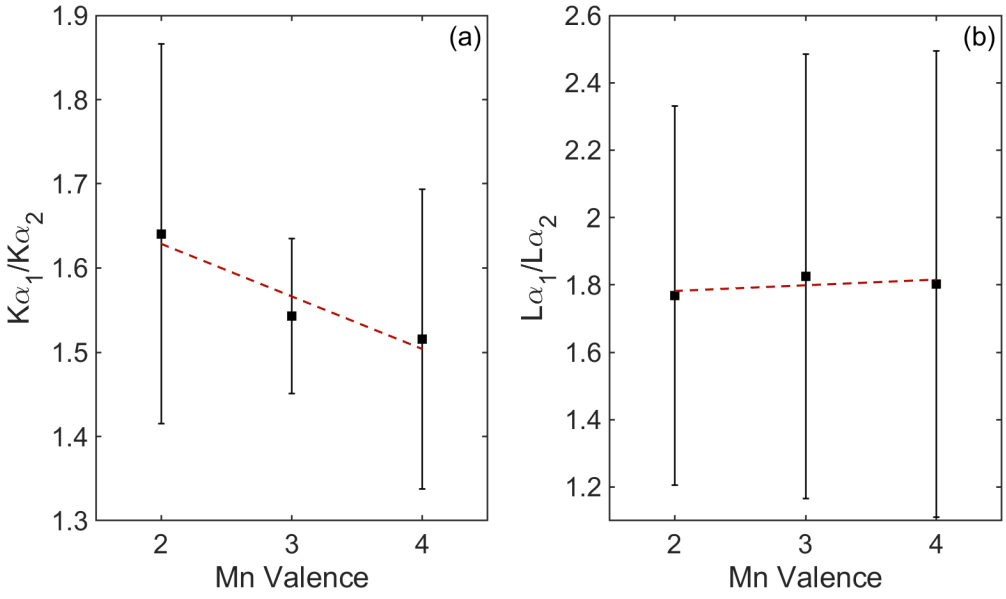

Figure 6.18: Comparison of the ratios of the Mn muonic emission lines (a) Kα_1 and Kα_2 and (b) Lα_1 and Lα_2. Straight lines are included as a guide to the eye.

6.5 Extension to Mn-Modified Single Crystal

With the distinction between Mn oxidation states observable in Mn oxides, the next step was to test the feasibility of applying this method to a single crystal sample and see whether the marginal changes are observable with the ultimate goal being a non-destructive way to determine valence of Mn.

6.5.1 Sample Preparation

A disk of Mn:PIN-PMN-PT crystal (Innovia Materials Co., Ltd., Shanghai, China), with a nominal doping level of 5%, was cut straight from the boule with a diameter of $\approx$ 6 cm. It is shown in Figure 6.19. This disk was not a single crystal, having been grown with multiple orientations. As can be seen in Figure 6.19, a large, single grain, portion of the wafer is orientated along the [011] direction. However, the rest of the sample is visibly split into other domains. However, this multi-component structure is irrelevant because the muon is a local probe and so is sensitive only to the implantation site.

As with the Mn oxide powders, the wafer was wrapped in Al foil, as seen in Figure 6.19, and placed in the muon beamline.

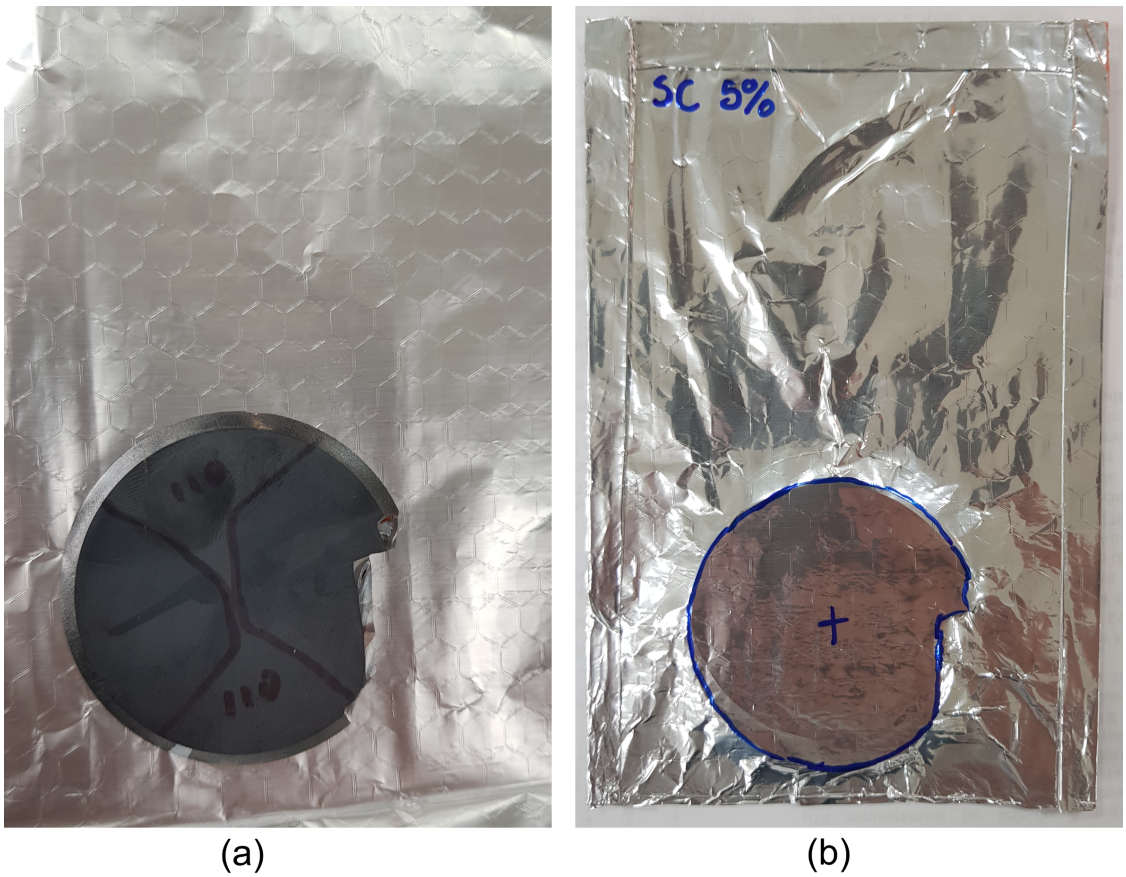

Figure 6.19: Crystal sample of Mn:PIN-PMN-PT (a) before and (b) after wrapping in Al foil. The multi-grain structure of the sample is clearly visible.

6.5.2 Emission Lines

The study focused on two regions of the emission spectra - the range of K lines, 900 keV - 1500 keV, and of L lines, 225 keV - 350 keV, of Mn. As only a small quantity of Mn is added to the crystal, it should be expected that the Mn lines are very weak. This is further complicated by the large quantity of other elements in the crystal. Emission lines of other element in these two regions are given in Table 6.8.

6.5.3 Results and Discussion

The sample was again measured at room temperature on Port 4, RIKEN-RAL, ISIS. However, unlike the powder experiment, two μ^- momenta were tested here, 30 MeV/c and 40 MeV/c. This was to ascertain any changes with depth as the issue of Mn segregation is well-known [4, 48]. Due to beam time constraints, the counting time was only approximately 12 hours per sample. Due to the anticipated weakness of the Mn lines, the data analysis has been concentrated in the energy ranges containing the K and L Mn lines as these were observed to be the strongest in the powder experiment.

Table 6.8: Theoretical energies of the muonic emission lines of Mg, Nb, In, Pb and O that occur in the ranges of K and L lines of Mn [72, 73].

Element	Atomic Transition		Energy (keV)
Mg	K	2p → 1s	296.5
Nb	M	4f → 3d	231.4, 238.3
In	L	3d → 2p	941.9, 947.6, 982.9
	M	4f → 3d	331.3, 335.6
Pb	M	4f → 3d	936.7, 970.7
		5f → 3d	1365.0, 1403.8
	O	6h → 5g	233.7, 235

The data analysis method was the same as for the powder samples; the outputs of same-energy detectors were summed and a linear background was fitted. Figures 6.20 - 6.23 show the emission spectra in the two regions of interest for both muon momenta with Figures 6.20 and 6.21 at 30 MeV/c and Figures 6.22 and 6.23 at 40 MeV/c.

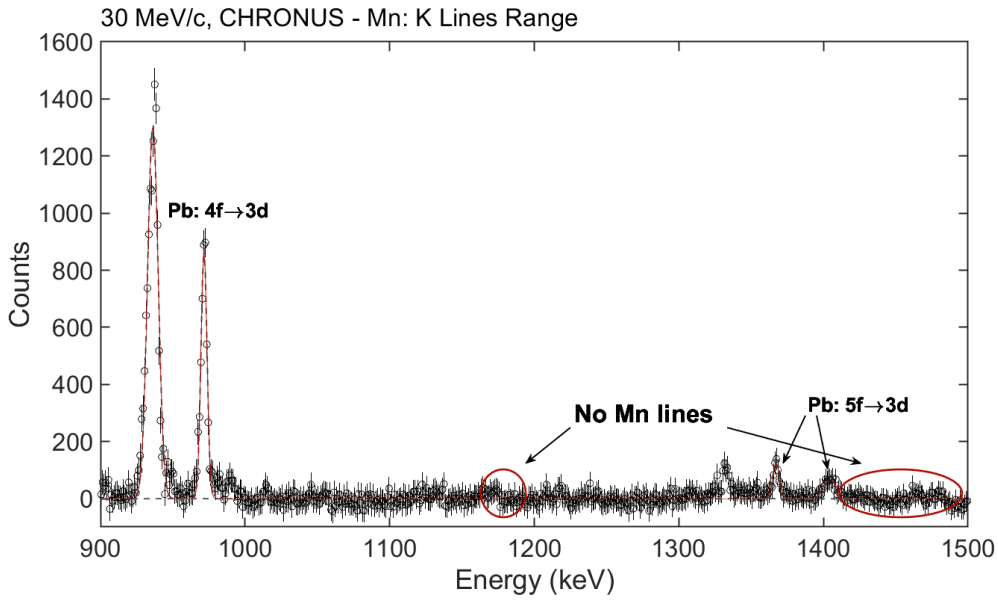

Figure 6.20: X-ray spectra resulting from μ^- implantation into a crystal sample of Mn:PIN-PMN-PT for a muon momentum of 30 MeV/c, showing the energy range in which the K lines of Mn, np → 1s, should be present. However, no Mn lines were observed. The fit (red) shows the Pb lines. Errors were estimated using Poisson/counting statistics. A linear background has been subtracted.

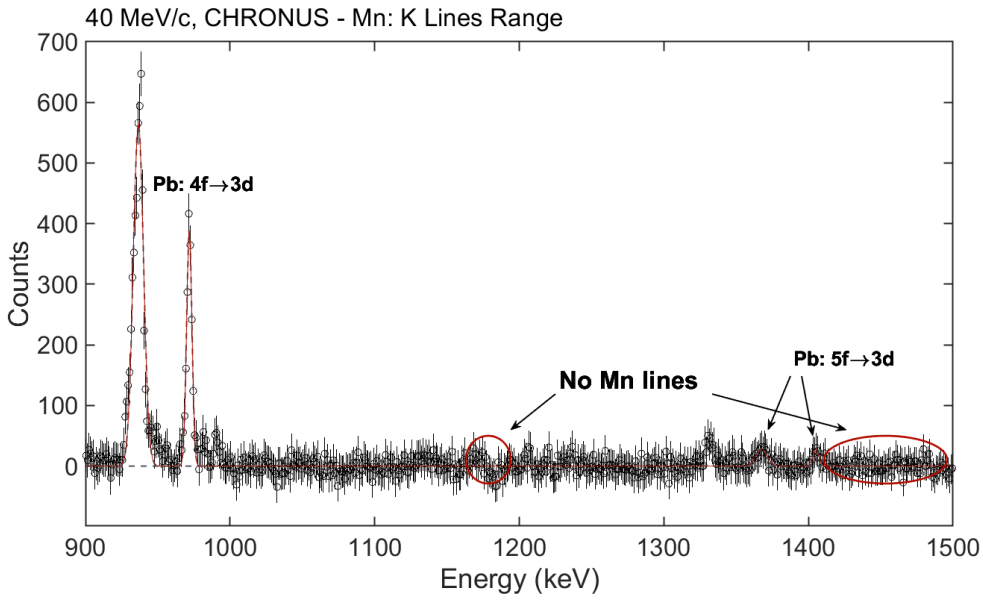

Figure 6.21: X-ray spectra resulting from μ^- implantation into a crystal sample of Mn:PIN-PMN-PT for a muon momentum of 40 MeV/c, showing the energy range in which the K lines of Mn, np $\rightarrow$ 1s, should be present. However, no Mn lines were observed. The fit (red) shows the Pb lines. Errors were estimated using Poisson/counting statistics. A linear background has been subtracted.

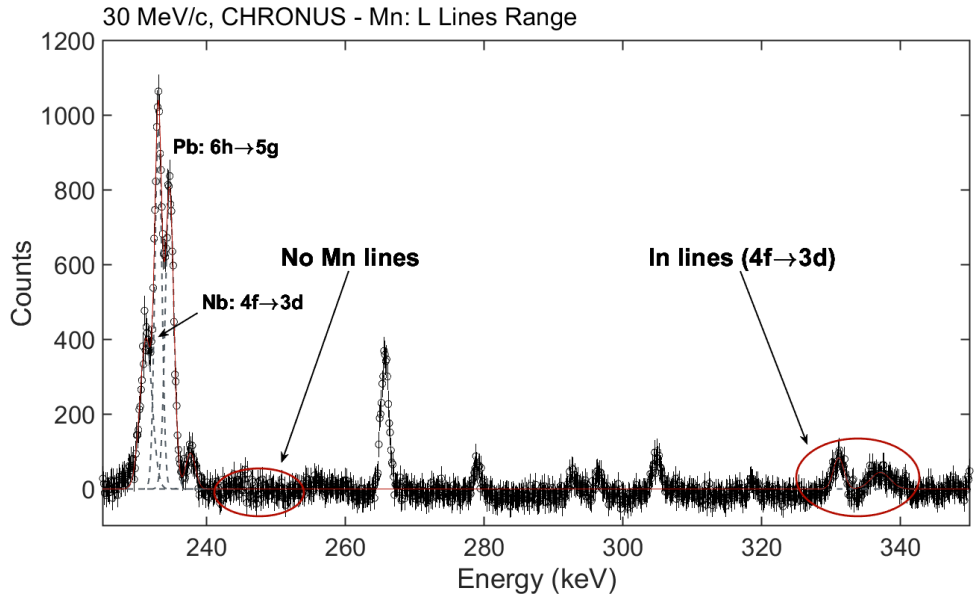

Figure 6.22: X-ray spectra resulting from μ^- implantation into a crystal sample of Mn:PIN-PMN-PT for a muon momentum of 30 MeV/c, showing the energy range in which the L lines of Mn, nd $\rightarrow$ 2p, should be present. However, no Mn lines were observed. The fit (red) shows the Pb, Nb and In lines. Errors were estimated using Poisson/counting statistics. A linear background has been subtracted.

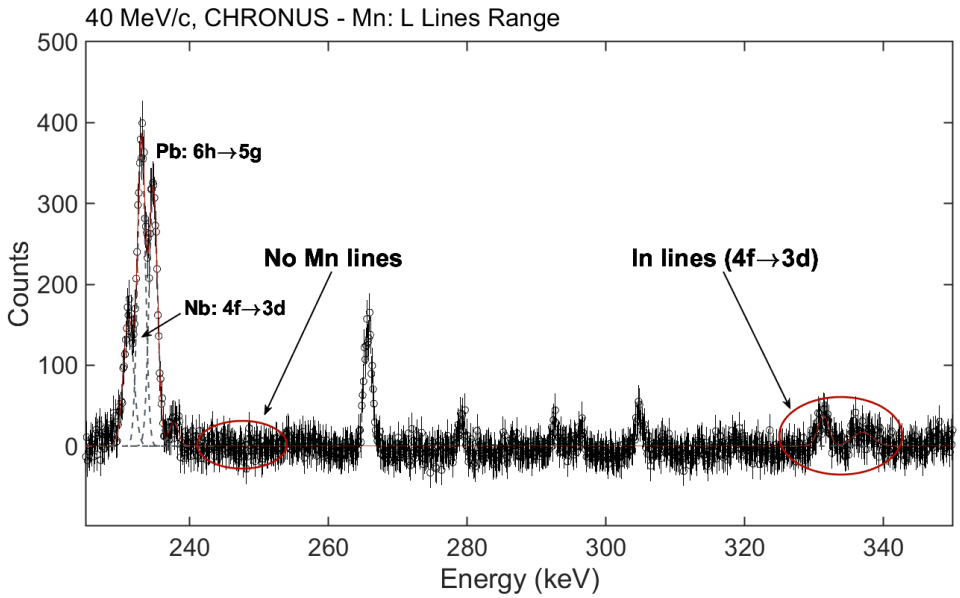

Figure 6.23: X-ray spectra resulting from μ^- implantation into a crystal sample of Mn:PIN-PMN-PT for a muon momentum of 40 MeV/c, showing the energy range in which the L lines of Mn, nd $\rightarrow$ 2p, should be present. However, no Mn lines were observed. The fit (red) shows the Pb, Nb and In lines. Errors were estimated using Poisson/counting statistics. A linear background has been subtracted.

The clearest identified lines result from Pb transitions. This is expected as Pb is the most abundant element in the sample. A fit of the Pb lines is shown in red in Figures 6.20 - 6.21; the fit in Figures 6.22 - 6.23 also incorporates the Nb and In lines. However, it appears that this fit alone cannot describe the observed counting pattern, e.g. as seen for the M Pb lines at 936.7/970.7 keV. It should be noted, with reference to Table 6.8, that these transitions overlap with the In 3d $\rightarrow$ 2p triplet, and so, this may be assumed to account for any discrepancies. Other In lines were identified, i.e. the doublet at 331.3/335.6 keV, but these were also quite weak. Whilst they result from a higher energy transition then those at $\approx$ 930/970 keV, and may thus be assumed to be naturally softer, this is a good indication that the small discrepancy in the Pb lines may be attributed to the overlap of the In lines. Additionally, the In doublet at 331.3/335.6 keV completely obscures the L Mn doublet, with energies of 331.2/334.7 keV. Hence, this energy range cannot be used to analyse Mn transitions.

A number of lines in Figures 6.20 - 6.23 remain unidentified. These are likely from another reaction present in the sample space. A good candidate for this is gamma decay resulting from muon capture, as observed in the powder experiment. Whilst most of these lines are weak, the peak at $\approx$ 265 keV warrants attention for its relative strength. This has not been linked to any specific decay or transition, but a similar, yet still unidentified line, appears in the Pb spectra measured by the Mesoroentgen Spectra Catalogue website [73]. It is suggested that the line in the spectra measured here arises through the same, unidentified, mechanism.

Mn Content

When considering Figures 6.20 - 6.23, no Mn lines are discernible, within error, above the background. Some possible reasons for this are now discussed.

First, the Mn content is very low; the manufacturer-specified dopant level in the crystal is 5% Mn. However, even at '5%', some evidence of the Mn should be seen. Given that no lines were observed, this might point to the Mn content being lower than specified. PIN-PMN-PT undergoes a colour change when Mn is added, changing from yellow to black. Given that the sample shown in Figure 6.19 is black, there is certainly a non-zero amount of Mn added. This question requires further study, possibly through techniques such as X-ray fluorescence (XRF).

Another, somewhat linked, point is that the spectra of Mn:PIN-PMN-PT is very crowded. This was touched on when discussing the Pb peaks at $\approx$ 930/970 keV. Tables 6.2 and 6.8 show many emission lines which are close in energy and, due to experimental broadening, will subsequently overlap in the measured spectra. This can make identification of individual lines difficult. Whilst some Mn lines are masked by others, thankfully, the Kα and Lα lines are unobscured and so the lack of lines can be analysed properly.

This leads on to the last point for discussion: instrument details such as resolution, detector setup and counting time can severely impact the data. A higher X-ray count can produce a much clearer spectra. This would also proportionately reduce the error, given by the square root of counts. This would allow time for more muon implantation events, which would increase the likelihood that a significant number of muons land on the, rare, Mn sites. A simple way to increase the count is to increase the experiment time but this can be restricted by beam time requirements, as was the case here.

However, if the counting rate, i.e. events recorded per second, could be increased, this would serve the same end. A higher counting rate may be achieved in two ways: The first would be to increase the muon flux. However, due to the momentum tuning apparatus and the need for decay muons, the RIKEN-RAL facility can only support one instrument at a time when being used in μ^- mode. This means that Port 4 already receives the full double pulse of muons. Furthermore, given that the quantity of muons had to be reduced in this experiment to avoid saturating the detectors, any increase in flux would most likely not be usable with the current setup. The other way to improve the counting rate, is to improve the detector setup. One weakness of the current setup is that only four X-ray detectors are used, leaving a lot of solid angle uncovered. By increasing not only the number, but also the spread of detectors, more X-rays could be counted in the same time.

Another method that could be used to improve data analysis is the inclusion of better peak detection algorithms, possible including machine learning. Here, the data were analysed using bespoke MATLAB scripts and simple Gaussian fits were made.

However, whilst it is possible that a more sophisticated analysis routine might improve the process and allow the Mn peaks to be identified, the present spectra were simply too noisy. In all cases, the background subtracted counts in the energy ranges of the Mn lines was zero *to within experimental error*.

6.6 Chapter Conclusions

In conclusion, powder samples of three Mn oxides and a multi-grain crystal of Mn:PIN-PMN-PT were studied using the negative muon technique. The aim was to study the valence of Mn in a non-destructive way with possible future application in characterising relaxor-ferroelectric single crystals. Being the strongest lines, the Kα muonic X-ray emission lines were investigated and a difference was seen with a shift in energy in MnO. The ratio of the constituent peaks in the Kα doublet was also calculated against depth and a decrease was observed against valence in agreement with literature [71]. However, the change is technically within error but still merits further study as, whilst the technique might be sensitive to oxidation states, better instrumentation should be able to verify this.

The feasibility of using this technique to study the Mn distribution in Mn:PIN-PMN-PT was also considered and, without significant detector upgrades, was also found to be impractical. None of the Mn emission lines could be identified in the measured spectra, let alone any of the small effects observed from the powder experiments.

Strategies to improve the data collection rate and analysis were discussed. It is argued that the primary method of improvement is to increase the X-ray detector coverage by the development of a new instrument setup. This will allow further study of this topic and potential future experiments are outline in Section 8.2.1.

References

[1] E. Sun, R. Zhang, F. Wu, B. Yang, and W. Cao, "Influence of manganese doping to the full tensor properties of 0.24Pb($In_{1/2}Nb_{1/2}$)O_3-0.47Pb($Mg_{1/3}Nb_{2/3}$)O_3-0.29$PbTiO_3$ single crystals," *J. Appl. Phys.*, vol. 113, no. 7, p. 074 108, 2013. DOI: 10.1063/1.4792600.

[2] R. Sahul, "Effect of manganese doping on PIN-PMN-PT single crystals for high power applications," PhD thesis, Pennsylvania State University, 2014.

[3] H.-T. Oh, J.-Y. Lee, and H. Y. Lee, "Mn-Modified PMN-PZT [Pb($Mg_{1/3}Nb_{2/3}$)O_3-Pb(Zr,Ti)O_3] Single Crystals for High Power Piezoelectric Transducers," *J. Korean Ceram. Soc.*, vol. 54, no. 2, pp. 150–157, 2017. DOI: 10.4191/kcers.2017.54.2.03.

[4] E. Sun and W. Cao, "Relaxor-based ferroelectric single crystals: Growth, domain engineering, characterization and applications," *Prog. Mater. Sci.*, vol. 65, pp. 124–210, 2014. DOI: 10.1016/j.pmatsci.2014.03.006.

[5] K.-W. Benz and W. Neumann, *Introduction to Crystal Growth and Characterization*. John Wiley & Sons, Inc., 2014, ch. 3, ISBN: 978-3-527-68436-6.

[6] P. Rudolph, Ed., *Handbook of Crystal Growth: Bulk Crystal Growth*, 2nd. Elsevier, 2015, vol. 2, ISBN: 978-0-444-63303-3.

[7] P. W. Bridgman, "Certain physical properties of single crystals of tungsten, antimony, bismuth, tellurium, cadmium, zinc, and tin," *Proc. Am. Acad. Arts Sci.*, vol. 60, no. 6, pp. 305–383, 1925.

[8] J. Luo, W. Hackenberger, S. Zhang, and T. R. Shrout, "Elastic, piezoelectric and dielectric properties of PIN-PMN-PT crystals grown by bridgman method," *2008 IEEE Int. Ultrason. Symp.*, pp. 261–264, 2008. DOI: 10.1109/ULTSYM.2008.0064.

[9] S. Zhang and T. R. Shrout, "Relaxor-PT single crystals: Observations and developments," *IEEE Trans. Ultrason. Ferroelectr. Freq. Contr.*, vol. 57, no. 10, pp. 2138–2146, 2010. DOI: 10.1109/TUFFC.2010.1670.

[10] L. Luo, X. Zhao, and H. Luo, "Single crystal pzn-pt, pmn-pt, psn-pt and pin-pt-based piezoelectric materials," in *Advanced Piezoelectric Materials*, K. Uchino, Ed., Woodhead Publishing, 2017, ch. 7, pp. 271–318, ISBN: 978-0-08-102135-4. DOI: 10.1016/B978-0-08-102135-4.00001-1.

[11] J. Tian and P. Han, "Growth and Characterization on PMN-PT-Based Single Crystals," *Crystals*, vol. 4, no. 3, pp. 331–341, 2014. DOI: 10.1007/978-3-319-93659-8_36.

[12] D. C. Stockbarger, "The production of large single crystals of lithium fluoride," *Rev. Sci. Instrum.*, vol. 7, no. 3, pp. 133–136, 1936. DOI: 10.1063/1.1752094.

[13] S. Zhang and F. Li, "High performance ferroelectric relaxor-$PbTiO_3$ single crystals: Status and perspective," *J. Appl. Phys.*, vol. 111, p. 031 301, 3 2012. DOI: 10.1063/1.3679521.

[14] X. Le, H. Luo, G. Shen, P. Wang, and Z. Yin, "Study of new piezoelectric material - relaxor ferroelectric single crystals," *J. Inorg. Mater.*, vol. 12, no. 5, pp. 768–768, 1997. [Online]. Available: http://www.jim.org.cn/EN/abstract/article_11650.shtml.

[15] Z. Yin, H. Luo, P. Wang, and G. Xu, "Growth, characterization and properties of relaxor ferroelectric PMN-PT single crystals," *Ferroelectrics*, vol. 229, no. 1, pp. 207–216, 1999. DOI: 10.1080/00150199908224341.

[16] H. Luo, G. Xu, P. Wang, and Z. Yin, "Growth and characterization of relaxor ferroelectric PMNT single crystals," *Ferroelectrics*, vol. 231, no. 1, pp. 97–102, 1999. DOI: 10.1080/00150199908014518.

[17] A. Benayad *et al.*, "Segregation study and segregation modeling of Ti in $Pb[Mg_{1/3}Nb_{2/3})_{0.60}Ti_{0.40}]O_3$ single crystal grown by bridgman method," *Mater. Res. Bull.*, vol. 41, no. 6, pp. 1069–1076, 2006. DOI: 10.1016/j.materresbull.2005.11.012.

[18] K. T. Zawilski *et al.*, "Segregation during the vertical bridgman growth of lead magnesium niobate–lead titanate single crystals," *J. Cryst. Growth*, vol. 258, no. 3, pp. 353–367, 2003. DOI: 10.1016/S0022-0248(03)01552-5.

[19] Y. Chen *et al.*, "High performance relaxor-based ferroelectric single crystals for ultrasonic transducer applications," *Sensors*, vol. 14, no. 8, pp. 13 730–13 758, 2014. DOI: 10.3390/s140813730.

[20] S. Zhang, F. Li, X. Jiang, J. Kim, J. Luo, and X. Geng, "Advantages and challenges of relaxor-$PbTiO_3$ ferroelectric crystals for electroacoustic transducers - a review," *Prog. Mater. Sci.*, vol. 68, pp. 1–66, 2015. DOI: 10.1016/j.pmatsci.2014.10.002.

[21] K. T. Zawilski, R. C. DeMattei, and R. S. Feigelson, "Zone leveling of lead magnesium niobate-lead titanate crystals using rf heating," *J. Cryst. Growth*, vol. 277, no. 1, pp. 393–400, 2005. DOI: 10.1016/j.jcrysgro.2005.01.090.

[22] T. Yamamoto and T. Sakuma, "Fabrication of barium titanate single crystals by solid-state grain growth," *J. Am. Ceram. Soc.*, vol. 77, no. 4, pp. 1107–1109, 1994. DOI: 10.1111/j.1151-2916.1994.tb07281.x.

[23] K. H. Brosnan, G. L. Messing, R. J. M. Jr., and M. D. Vaudin, "Texture measurements in <001> fiber-oriented PMN–PT," *J. Am. Ceram. Soc.*, vol. 89, no. 6, pp. 1965–1971, 2006. DOI: 10.1111/j.1551-2916.2006.01049.x.

[24] D. Phelan *et al.*, "Phase diagram of the relaxor ferroelectric (1 - *x*) $Pb(Mg_{1/3}Nb_{2/3})O_3$ + *x*$PbTiO_3$ revisited: A neutron powder diffraction study of the relaxor skin effect," *Phase Transit.*, vol. 88, no. 3, pp. 283–305, 2015. DOI: 10.1080/01411594.2014.989226.

[25] M. Davis, "Phase transitions, anisotropy and domain engineering: The piezoelectric properties of relaxor-ferroelectric single crystals," PhD thesis, École Polytechnique Fédérale de Lausanne, 2006.

[26] S. Zhang, F. Li, J. Luo, R. Sahul, and T. R. Shrout, "Relaxor-$PbTiO_3$ single crystals for various applications," *IEEE Trans. Ultrason. Ferroelectr. Freq. Contr.*, vol. 60, pp. 1572–1580, 8 2013.

[27] B. Jaffe, W. J. Cook, and H. Jaffe, *Piezoelectric Ceramics*, 3rd. London: Academic Press, 1971, ISBN: 978-0-12-379550-2.

[28] K. Uchino, S. Nomura, L. E. Cross, S. J. Jang, and R. E. Newnham, "Electrostrictive effect in lead magnesium niobate single crystals," *J. Appl. Phys.*, vol. 51, no. 2, pp. 1142–1145, 1980. DOI: 10.1063/1.327724.

[29] S. J. Jang, K. Uchino, S. Nomura, and L. E. Cross, "Electrostrictive behavior of lead magnesium niobate based ceramic dielectrics," *Ferroelectrics*, vol. 27, no. 1, pp. 31–34, 1980. DOI: 10.1080/00150198008226059.

[30] S. W. Choi, T. R. Shrout, S. J. Jang, and A. S. Bhalla, "Morphotropic phase boundary in $Pb(Mg_{1/3}Nb_{2/3})O_3$-$PbTiO_3$ system," *Mater. Lett.*, vol. 8, no. 6, pp. 253–255, 1989. DOI: 10.1016/0167-577X(89)90115-8.

[31] J. Kuwata, K. Uchino, and S. Nomura, "Phase transitions in the $Pb(Zn_{1/3}Nb_{2/3})O_3$-$PbTiO_3$ system," *Ferroelectrics*, vol. 37, no. 1, pp. 579–582, 1981. DOI: 10.1080/00150198108223490.

[32] J. Kuwata, K. Uchino, and S. Nomura, "Dielectric and piezoelectric properties of $0.91Pb(Zn_{1/3}Nb_{2/3})O_3$-$0.09PbTiO_3$ single crystals," *Jpn. J. Appl. Phys.*, vol. 21, no. Part 1, No. 9, pp. 1298–1302, 1982. DOI: 10.1143/jjap.21.1298.

[33] D. Damjanovic, M. Budimir, M. Davis, and N. Setter, "Piezoelectric anisotropy: Enhanced piezoelectric response along nonpolar directions in perovskite crystals," *J. Mater. Sci.*, vol. 41, pp. 65–76, 1 2006. DOI: 10.1007/s10853-005-5925-5.

[34] D. Zhou *et al.*, "Fabrication and performance of endoscopic ultrasound radial arrays based on PMN-PT single crystal/epoxy 1-3 composite," *IEEE Trans. Ultrason. Ferroelectr. Freq. Contr.*, vol. 58, pp. 477–484, 2 2011. DOI: 10.1109/TUFFC.2011.1825.

[35] S.-E. Park and T. R. Shrout, "Ultrahigh strain and piezoelectric behavior in relaxor based ferroelectric single crystals," *J. Appl. Phys.*, vol. 82, p. 1804, 1997. DOI: 10.1063/1.365983.

[36] B. Noheda, D. E. Cox, G. Shirane, J. Gao, and Z.-G. Ye, "Phase diagram of the ferroelectric relaxor $(1-x)PbMg_{1/3}Nb_{2/3}O_3 - xPbTiO_3$," *Phys. Rev. B*, vol. 66, p. 054 104, 5 2002. DOI: 10.1103/PhysRevB.66.054104.

[37] J. A. Gallagher, J. Tian, and C. S. Lynch, "Composition dependence of electro-mechanical properties and field induced phase transformations in $[001]_C$ PIN–PMN–PT single crystals," *Smart Mater. Struct.*, vol. 23, no. 9, p. 095 031, 2014. DOI: 10.1088/0964-1726/23/9/095031.

[38] Y. Guo, H. Luo, T. He, and Z. Yin, "Peculiar properties of a high curie temperature $Pb(In_{1/2}Nb_{1/2})O_3$-$PbTiO_3$ single crystal grown by the modified bridgman technique," *Solid State Commun.*, vol. 123, no. 9, pp. 417–420, 2002. DOI: 10.1016/S0038-1098(02)00311-3.

[39] G. Xu, K. Chen, D. Yang, and J. Li, "Growth and electrical properties of large size $Pb(In_{1/2}Nb_{1/2})O_3$-$Pb(Mg_{1/3}Nb_{2/3})O_3$-$PbTiO_3$ crystals prepared by the vertical bridgman technique," *Appl. Phys. Lett.*, vol. 90, no. 3, p. 032 901, 2007. DOI: 10.1063/1.2431706.

[40] J. Tian, P. Han, X. Huang, H. Pan, J. F. Carroll, and D. A. Payne, "Improved stability for piezoelectric crystals grown in the lead indium niobate–lead magnesium niobate–lead titanate system," *Appl. Phys. Lett.*, vol. 91, no. 22, p. 222 903, 2007. DOI: 10.1063/1.2817743.

[41] K. Carl and K. H. Hardtl, "Electrical after-effects in Pb(Ti, Zr)O_3 ceramics," *Ferroelectrics*, vol. 17, no. 1, pp. 473–486, 1978. DOI: 10.1080/00150197808236770.

[42] S. Takahashi, "Effects of impurity doping in lead zirconate-titanate ceramics," *Ferroelectrics*, vol. 41, no. 1, pp. 143–156, 1982. DOI: 10.1080/00150198208210617.

[43] J. Luo, W. Hackenberger, S. Zhang, and T. R. Shrout, "A high Q_m relaxor ferroelectric single crystal: Growth and characterization," *2010 IEEE Int. Ultrason. Symp.*, pp. 68–71, 2010. DOI: 10.1109/ULTSYM.2010.5935675.

[44] X. Li *et al.*, "Microstructure and dielectric relaxation of dipolar defects in Mn-doped (1-*x*)$Pb(Mg_{1/3}Nb_{2/3})O_3$-*x*$PbTiO_3$ single crystals," *Scr. Mater.*, vol. 69, no. 5, pp. 377–380, 2013. DOI: 10.1016/j.scriptamat.2013.05.018.

[45] L.-X. He and C.-E. Li, "Effects of addition of MnO on piezoelectric properties of lead zirconate titanate," *J. Mater. Sci.*, vol. 35, pp. 2477–2480, 10 2000. DOI: 10.1023/A:1004717702149.

[46] Y. Hou *et al.*, "Effect of MnO_2 addition on the structure and electrical properties of $Pb(Zn_{1/3}Nb_{2/3})_{0.20}(Zr_{0.50}Ti_{0.50})_{0.80}O_3$ ceramics," *J. Am. Ceram. Soc.*, vol. 87, no. 5, pp. 847–850, 2004. DOI: 10.1111/j.1551-2916.2004.00847.x.

[47] K. Carl and K. H. Hardtl, "Electrical after-effects in Pb(Ti, Zr)O_3 ceramics," *Ferroelectrics*, vol. 17, no. 1, pp. 473–486, 1977. DOI: 10.1080/00150197808236770.

[48] L. A. Stoica, "Relaxor-$PbTiO_3$ single crystals and polycrystals: Processing, growth and characterisation," PhD thesis, University of Leeds, 2016.

[49] F. Li *et al.*, "Giant piezoelectricity of Sm-doped $Pb(Mg_{1/3}Nb_{2/3})O_3$-$PbTiO_3$ single crystals," *Science*, vol. 364, no. 6437, pp. 264–268, 2019. DOI: 10.1126/science.aaw2781.

[50] F. Li *et al.*, "Supplementary materials for giant piezoelectricity of Sm-doped $Pb(Mg_{1/3}Nb_{2/3})O_3$-$PbTiO_3$ single crystals," *Science*, vol. 364, no. 6437, pp. 264–268, 2019. DOI: 10.1126/science.aaw2781.

[51] D. M. Hatch, H. T. Stokes, and W. Cao, "Allowed mesoscopic point group symmetries in domain average engineering of perovskite ferroelectric crystals," *J. Appl. Phys.*, vol. 94, no. 8, pp. 5220–5227, 2003. DOI: 10.1063/1.1611634.

[52] D. Damjanovic, "Contributions to the piezoelectric effect in ferroelectric single crystals and ceramics," *J. Am. Ceram. Soc.*, vol. 88, pp. 2663–2676, 10 2005. DOI: 10.1111/j.1551-2916.2005.00671.x.

[53] B. Noheda, D. E. Cox, G. Shirane, J. A. Gonzalo, L. E. Cross, and S.-E. Park, "A monoclinic ferroelectric phase in the $Pb(Zr_{1-x}Ti_x)O_3$ solid solution," *Appl. Phys. Lett.*, vol. 74, no. 14, pp. 2059–2061, 1999. DOI: 10.1063/1.123756.

[54] Z.-G. Ye, B. Noheda, M. Dong, D. E. Cox, and G. Shirane, "Monoclinic phase in the relaxor-based piezoelectric/ferroelectric $Pb(Mg_{1/3}Nb_{2/3})O_3-PbTiO_3$ system," *Phys. Rev. B*, vol. 64, p. 184 114, 18 2001. DOI: 10.1103/PhysRevB.64.184114.

[55] B. Noheda, D. E. Cox, G. Shirane, S.-E. Park, L. E. Cross, and Z. Zhong, "Polarization rotation via a monoclinic phase in the piezoelectric 92% $PbZn_{1/3}Nb_{2/3}O_3$-8% $PbTiO_3$," *Phys. Rev. Lett.*, vol. 86, pp. 3891–3894, 17 2001. DOI: 10.1103/PhysRevLett.86.3891.

[56] H. Liu *et al.*, "Critical role of monoclinic polarization rotation in high-performance perovskite piezoelectric materials," *Phys. Rev. Lett.*, vol. 119, p. 017 601, 1 2017. DOI: 10.1103/PhysRevLett.119.017601.

[57] H. Fu and R. E. Cohen, "Polarization rotation mechanism for ultrahigh electromechanical response in single-crystal piezoelectrics," *Nature*, vol. 403, pp. 281–283, 6767 2000. DOI: 10.1038/35002022.

[58] G. Liu, S. Zhang, W. Jiang, and W. Cao, "Losses in Ferroelectric Materials," *Mater. Sci. Eng. R Rep.*, vol. 89, pp. 1–48, 2015. DOI: 10.1016/j.mser.2015.01.002.

[59] F. Li, S. Zhang, Z. Xu, and L.-Q. Chen, "The contributions of polar nanoregions to the dielectric and piezoelectric responses in domain-engineered relaxor-$PbTiO_3$ crystals," *Adv. Funct. Mater*, vol. 27, no. 18, p. 1 700 310, 2017. DOI: 10.1002/adfm.201700310.

[60] F. Li *et al.*, "The origin of ultrahigh piezoelectricity in relaxor-ferroelectric solid solution crystals," *Nat. Commun*, vol. 7, p. 13 807, 2016. DOI: 10.1038/ncomms13807.

[61] P. M. Shepley, L. A. Stoica, Y. Li, G. Burnell, and A. J. Bell, "Effects of poling and crystallinity on the dielectric properties of $Pb(In_{1/2}Nb_{1/2})O_3$-$Pb(Mg_{1/3}Nb_{2/3})O_3$-$PbTiO_3$ at cryogenic temperatures," *Sci. Rep.*, vol. 9, p. 2442, 1 2019. DOI: 10.1038/s41598-019-38995-9.

[62] K. L. Brown *et al.*, "Depth dependant element analysis of $Pb(Mg_{1/3}Nb_{2/3})O_3$ using muonic x-rays," *J. Phys. Condens. Matter*, vol. 30, p. 125 703, 2018. DOI: 10.1088/1361-648X/aaade3.

[63] E. Fermi and E. Teller, "The capture of negative mesotrons in matter," *Phys. Rev.*, vol. 72, pp. 399–408, 5 1947. DOI: 10.1103/PhysRev.72.399.

[64] V. G. Zinov, A. D. Konin, and A. I. Mukhin, *Sov. J. Nucl. Phys.*, vol. 2, p. 613, 1966.

[65] H. Daniel, "Formation of mesonic atoms in condensed matter," *Phys. Rev. Lett.*, vol. 35, pp. 1649–1651, 24 1975. DOI: 10.1103/PhysRevLett.35.1649.

[66] H. Schneuwly, V. I. Pokrovsky, and L. I. Ponomarev, "On coulomb capture ratios of negative mesons in chemical compounds," *Nuclear Physics A*, vol. 312, no. 3, pp. 419–426, 1978. DOI: 10.1016/0375-9474(78)90601-2.

[67] F. Kottmann, "The exotic-atom cascade," in *Muonic Atoms and Molecules*, Birkhäuser Basel, 1993, pp. 157–165, ISBN: 978-3-0348-7271-3.

[68] J. A. Van Bokhoven and C. Lamberti, *X-Ray Absorption and X-Ray Emission Spectroscopy: Theory and Applications*. Wiley, 2016, ISBN: 978-1-118-84423-6.

[69] K. Ninomiya *et al.*, "Negative muon capture on nitrogen oxide molecules," *J. Korean Phys. Soc.*, vol. 59, no. 4, pp. 2917–2920, 1 2011. DOI: 10.3938/jkps.59.2917.

[70] J. D. Knight *et al.*, "Chemical effects in negative muon capture in some ionic and covalent solids and ionic aqueous solutions," *Phys. Rev. A*, vol. 13, pp. 43–53, 1 1976. DOI: 10.1103/PhysRevA.13.43.

[71] M. Aramini *et al.*, "Using the emission of muonic x-rays as a spectroscopic tool for the investigation of the local chemistry of elements," *Nanomaterials*, vol. 10, no. 7, 2020. DOI: 10.3390/nano10071260.

[72] R. Engfer, H. Schneuwly, J. L. Vuilleumier, H. K. Walter, and A. Zehnder, "Charge-distributed parameters, isotope shifts, isomer shifts, and magnetic hyperfine constants from muonic atoms," *At. Data Nucl. Data Tables*, vol. 14, pp. 509–597, 5,6 1974. DOI: 10.1016/S0092-640X(74)80003-3.

[73] C. Briancon *et al.*, *Mesoroentgen Spectra Catalogue*, Accessed online at http://muxrays.jinr.ru/. Accessed 17th November 2021.

[74] L. Kirkup, *Experimental Methods*. John Wiley & Sons Australia Ltd., 1994, ch. 5, ISBN: 978-0-471-33579-5.

[75] G. L. Squires, *Practical Physics*, 4th. Cambridge University Press, 2001, ch. Appendix D, ISBN: 0-521-77940-5.

[76] L. Kirkup, *Experimental Methods*. John Wiley & Sons Australia Ltd., 1994, ch. 4, ISBN: 978-0-471-33579-5.

Chapter 7

Energy Density

In Chapter 6, various comparative FOMs were noted for piezocrystals. However, these did not provide a means of fundamental material comparison, with the use of k being particularly concerning. This chapter, therefore, develops a method to quantify, in a meaningful way, the energy density of piezoelectric material in order to provide a universal and comparable metric, thus allowing raw material performance to be benchmarked.

First, the concept of energy density in a piezoelectric material is reviewed, with the example of the length extensional bar used for illustration. This is followed by the derivation of a generalised electromechanical coupling factor which is verified *in silico* and applied to two test cases - comparison of relaxor-PT single crystal materials with piezoceramic standards and the potential of Pb-free materials.

7.1 Chapter Introduction

The motivation for studying Gen. III relaxor-PT single crystals is their superior piezoelectric performance. However, there is a conflation between a material's performance and a specific use case in any FOM by design. Typically, comparisons are done using parameters such as piezoelectric charge constants, d, electromechanical coupling factors, k^2, and the effective Curie temperature, T_C. With the new vibrational modes unlocked by Pb-based relaxor-ferroelectric single crystal materials, powered by different crystal symmetries, a more generalised measure is sought which can determine the piezoelectric performance of a material based purely on its material properties, i.e. the EPD matrix.

Furthermore, due to safety concerns over the continued use of Pb in electrical equipment [1], Pb-free piezoelectric materials are also a subject of interest, though still to be fully commercialised [2]. Similarly, a generalised metric would enable the progress of Pb-free material to be tracked away from any single application.

In both cases, comparison between different materials can be difficult and are usually restricted to specific use cases. For example, underwater SONAR and high power ultrasonic

devices require simultaneous high d, k_{33}^2 and mechanical quality factor, Q_m, to ensure good electro-acoustic efficiency and large vibration velocity at the transducer's surface. This contrasts with the requirement for medical imaging devices which have no restrictions on Q_m; instead the focus is on high k^2 to ensure a broad bandwidth and good ultrasonics energy conversion [3]. These different requirements can lead to disparate results when comparing materials, with the potential to bias decisions relating to specific use cases.

To circumvent this, a universal method is sought to support unbiased comparison. A good candidate is the energy density of the material i.e. the material's ability to store energy and convert from mechanical to dielectric and *vice-versa*. This is usually quantified by k^2 but still lacks generality as k^2 is linked to a resonant mode e.g. k_{33} or k_t for length-extensional or thickness-extensional modes respectively. This link is very much central to standard material characterisation methods [4].

Hence, in this chapter, a generalised k^2 is developed to better represent the pure piezoelectric response of the material without being obscured by any resonance behaviour. Developing such a metric also provides insight into the different energy conversion mechanisms at play in the material and how these influence its response.

7.2 Calculating Energy Density

The energy density of a piezoelectric material is related to the quantity of work converted per unit work input with energy conversion linked to the electromechanical coupling factor, k^2, which defines the proportion of work instantaneously converted by the material from electrical to mechanical energy, or *vice versa* [5]. Before considering conversion in detail, the different types of energy density and how they can flow in and out of a material are reviewed.

7.2.1 Types of Energy Density

Typically, energy density in a piezoelectric material is considered as four types [6]:

1. **Kinetic**: $T = \frac{\rho}{2}\frac{\partial u_i}{\partial t}\frac{\partial u_i}{\partial t}$
2. **Elastic**: $U^{(E)} = \frac{1}{2}c^E_{\mu\nu}S_\mu S_\nu$
3. **Dielectric**: $U^{(D)} = \frac{1}{2}\varepsilon^S_{ij}E_iE_j$
4. **Piezoelectric**: $U^{(P)} = \frac{1}{2}e_{i\mu}E_iS_\mu$

where ρ is the density, $\frac{\partial u}{\partial t}$ is the velocity, c^E is the stiffness, S is the strain, ε^S is the dielectric permittivity at constant strain, E is the electric field and e is the piezoelectric stress constant. These last three together make up the total 'potential' energy density U. It may be easily verified that these four terms have dimensions of Jm^{-3} and so indeed correspond to energy *densities*.

Then, to find the energy contained with a specific type, the relevant density must be integrated over the material volume.

7.2.2 Poynting's Theorem

Similarly to the more familiar case of electromagnetism, Poynting's theorem defines the flow of energy in and out of a volume. In order to derive Poynting's theorem for a piezoelectric material, one may start at Equation 2.6 (which is reproduced here for convenience):

$$dU = \sigma_\mu dS_\mu + E_i dD_i. \tag{7.1}$$

This follows from the combination of mechanical and electric energy densities and provides a function equivalent to the first law of thermodynamics in a piezoelectric material. As it clearly expresses the natural variables of U as S_μ and D_i, an expression for the time derivative of U is

$$\frac{\partial U}{\partial t} = \sigma_\mu \frac{\partial S_\mu}{\partial t} + E_i \frac{\partial D_i}{\partial t}. \tag{7.2}$$

This can also be found by 'dividing' Equation 2.6 by dt.

Equation 7.2 then gives the total change in time of the potential energy stored within the material [7]. Following Yang and suspending Voigt notation, upon introduction of the definition of strain, this becomes

$$\begin{aligned} \frac{\partial U}{\partial t} &= \sigma_{ij} \frac{\partial}{\partial t}\left[\frac{1}{2}\left(\frac{\partial u_i}{\partial x_j} + \frac{\partial u_j}{\partial x_i}\right)\right] + E_i \frac{\partial D_i}{\partial t} \\ &= \sigma_{ij} \frac{\partial^2}{\partial t \partial x_i} u_j + E_i \frac{\partial D_i}{\partial t} \end{aligned} \tag{7.3}$$

where the second equality is due to the symmetry of the stress tensor. Then, by using the product rule of partial differentiation and introducing the quasi-static electric potential, this can be rewritten as

$$\begin{aligned} \frac{\partial U}{\partial t} &= \sigma_{ij} \frac{\partial^2}{\partial t \partial x_i} u_j - \frac{\partial \phi}{\partial x_i} \frac{\partial D_i}{\partial t} \\ &= \frac{\partial}{\partial x_i}\left(\sigma_{ij} \frac{\partial u_j}{\partial t}\right) - \frac{\partial u_j}{\partial t} \frac{\partial \sigma_{ij}}{\partial x_i} - \frac{\partial}{\partial x_i}\left(\phi \frac{\partial D_i}{\partial t}\right) + \phi \frac{\partial^2 D_i}{\partial t \partial x_i}. \end{aligned} \tag{7.4}$$

Using Newton's second law (Equation 2.42), Gauss' Law (Equation 2.43) and rearranging terms, this becomes

$$\frac{\partial U}{\partial t} = \frac{\partial}{\partial x_i}\left(\sigma_{ij} \frac{\partial u_j}{\partial t} - \phi \frac{\partial D_i}{\partial t}\right) - \frac{\partial u_j}{\partial t}\left(\rho \frac{\partial^2 u_j}{\partial t^2} - f_j\right) + \phi \frac{\partial \rho_e}{\partial t}, \tag{7.5}$$

which may be immediately rewritten as

$$\frac{\partial U}{\partial t} = -\frac{\partial}{\partial x_i}\left(\phi\frac{\partial D_i}{\partial t} - \sigma_{ij}\frac{\partial u_j}{\partial t}\right) - \frac{\partial}{\partial t}\left(\frac{\rho}{2}\frac{\partial u_j}{\partial t}\frac{\partial u_j}{\partial t}\right) + \frac{\partial u_j}{\partial t}f_j + \phi\frac{\partial \rho_e}{\partial t}. \tag{7.6}$$

Finally, recognising the third term as the kinetic energy density, T, allows an expression for the time derivative of the total internal energy to be written as

$$\frac{\partial}{\partial t}\left(U+T\right) = -\frac{\partial}{\partial x_i}\left(\phi\frac{\partial D_i}{\partial t} - \sigma_{ij}\frac{\partial u_j}{\partial t}\right) + \frac{\partial u_j}{\partial t}f_j + \phi\frac{\partial \rho_e}{\partial t}. \tag{7.7}$$

Equation 7.7 is then a continuity equation with two energy sources, one corresponding to mechanical stimulation though the external force density, f_i, and the other to electric stimulation through the external charge density, ρ_e. The other term of the right hand side is then the piezoelectric Poynting vector, $S_i^{(P)}$, which contains information about energy flow in the material [8]. In the absence of external forces or charges, Poynting's theorem then states

$$\frac{\partial}{\partial t}\left(U+T\right) = -\frac{\partial}{\partial x_i}\left(\phi\frac{\partial D_i}{\partial t} - \sigma_{ij}\frac{\partial u_j}{\partial t}\right) = -\frac{\partial S_i^{(P)}}{\partial x_i}. \tag{7.8}$$

7.3 Analysis of a Length Extensional Bar

One of the simplest piezoelectric geometries is the length extensional (LE) bar, in which the length is 10 times each width, Figure 2.4(a). Assuming the bar is poled through its length direction, then it will resonate in the LE mode. Consider the case where this material is driven in 'transmit' mode with a DC signal and has mechanically free surfaces, S, which can be defined as the electroded, S_e, and un-electroded, S_u, such that $S = S_e \cup S_u$. In this case, the input energy is purely electrical, no mechanical work can be extracted, and all converted energy is stored. Hence this case can be used to study k^2.

7.3.1 Analytic Treatment

More specifically, this is a boundary value problem (BVP), which is defined by a system of differential equations along with suitable boundary conditions [9]. In this case, the differential equations are the piezoelectric equations of motion, Equations 2.44 and 2.45, and the boundary conditions are:

- Mechanically free: $\sigma_{ij} = 0$ on S
- Electrical continuity: $\vec{D}\cdot\hat{n} = 0$ on S_u
- Driving voltage: $\phi(z=h) - \phi(z=-h) = V\Theta(t-t_s)$ on S_e, where V is the amplitude of the DC voltage, Θ is the Heaviside step function defined as zero for $t < t_s$ and unity for $t > t_s$, and t_s is the time the voltage is switched on.

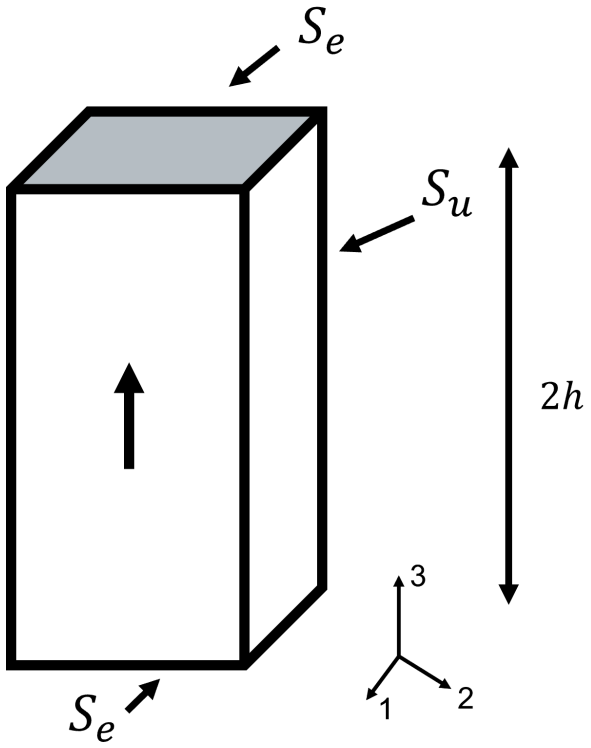

Figure 7.1: A schematic diagram showing the length extensional bar BVP setup. The electroded and non-electroded surfaces, S_e and S_u respectively, are labelled, as is the height of the bar $= 2h$.

These boundary conditions are illustrated in Figure 7.1 and allow the behaviour to be completely solved. As only DC voltage is considered, the solution is likewise static. In addition to being simpler to solve, the standard electromechanical coupling factor calculations are derived under quasi-static conditions so this approach does not stray too far from the standard approach. Under these conditions, the equations of motion may be rewritten as

$$c^E_{ijkl}\frac{\partial^2}{\partial x_j \partial x_k}u_l + e_{kij}\frac{\partial^2}{\partial x_j \partial x_k}\phi = 0, \tag{7.9}$$

$$\varepsilon^S_{ij}\frac{\partial^2}{\partial x_i \partial x_j}\phi - e_{ijk}\frac{\partial^2}{\partial x_i \partial x_j}u_k = 0, \tag{7.10}$$

where all time dependence may now be ignored. As stated above, Newton's 2nd law now reads

$$\frac{\partial \sigma_{ij}}{\partial x_j} = 0. \tag{7.11}$$

Combined with the boundary conditions, this implies that the whole bar is stress free and allows proposition of the following *ansatz*

$$\begin{aligned} u_1 &= u_1(x), \\ u_2 &= u_2(y), \\ u_3 &= u_3(z), \\ \phi &= \phi(z). \end{aligned} \tag{7.12}$$

Mechanically, this form is justified as no shear strains can arise from an electric field in the 3 direction due to the material symmetry, e.g. $4mm$ but true for most piezoelectric symmetries. In terms of the electrical potential, the induced electric field should behave in a similar way due to the uniformity of the driving voltage and the electroded surface in the x-y plane. Furthermore, taken with the electric continuity boundary condition, this specifies that the components E_1 and E_2 should be zero.

The equations of motion, Equations 7.9 and 7.10, may then be expanded as

$$c_{11}^E \frac{\partial^2 u_1(x)}{\partial x^2} = 0, \tag{7.13}$$

$$c_{11}^E \frac{\partial^2 u_2(y)}{\partial y^2} = 0, \tag{7.14}$$

$$\frac{\partial^2}{\partial z^2}\left(c_{33}^E u_3(z) + e_{33}\phi(z)\right) = 0, \tag{7.15}$$

$$\frac{\partial^2}{\partial z^2}\left(\varepsilon_{33}^S \phi(z) - e_{33}u(z)\right) = 0, \tag{7.16}$$

which may trivially be solved by solutions of the form

$$u_1 = A_1 x + B_1, \tag{7.17}$$

$$u_2 = A_2 y + B_2, \tag{7.18}$$

$$u_3 = A_3 z + B_3, \tag{7.19}$$

$$\phi = A_4 z + B_4, \tag{7.20}$$

where the eight constants of integration must be fixed by the boundary conditions.

First, the $\{B\}$ coefficients may all be set to zero as, in the case of the displacements, they correspond to translations which can be fixed in this way without loss of generality. In the remaining case, it is standard that a constant term in a potential may be disregarded.

The remaining $\{A\}$ constants are now fixed from the boundary conditions at a time after t_s

$$u_1 = \frac{V}{2h}\left[e_{31}(s^E_{11}+s^E_{12})+e_{33}s^E_{13}\right]x = \frac{V}{2h}d_{31}x, \tag{7.21}$$

$$u_2 = \frac{V}{2h}\left[e_{31}(s^E_{11}+s^E_{12})+e_{33}s^E_{13}\right]y = \frac{V}{2h}d_{31}y, \tag{7.22}$$

$$u_3 = \frac{V}{2h}\left[2e_{31}s^E_{13}+e_{33}s^E_{33}\right]z = \frac{V}{2h}d_{33}z, \tag{7.23}$$

$$\phi = \frac{V}{2h}z. \tag{7.24}$$

Two points must be addressed here. The first is that the electric field, i.e. the first derivative of ϕ, is just the voltage divided by the bar length. This is as expected and it also shows that the axial strains, i.e. first derivatives of the displacements, indeed follow $S_\mu = d_{i\mu}E_i$, again as expected. Whilst this is a simple example, it shows that much information can be gained.

7.3.2 Input Energy Density

From Poynting's theorem, the input energy between times t_0 and t_1 is given by

$$\begin{aligned}\Delta W &= -\oint_S dS_i \int_{t_0}^{t_1}\left(\phi\frac{\partial D_i}{\partial t}-\sigma_{ij}\frac{\partial u_j}{\partial t}\right)\\ &= -\int_{S_e} dS\int_{t_0}^{t_1}\phi\frac{\partial \vec{D}\cdot\hat{n}}{\partial t}-\int_{S_u} dS\int_{t_0}^{t_1}\phi\frac{\partial \vec{D}\cdot\hat{n}}{\partial t}+\int_S dS\int_{t_0}^{t_1}\sigma_{ij}\hat{n}_i\frac{\partial u_j}{\partial t},\end{aligned} \tag{7.25}$$

where the first term corresponds to dielectric energy flow in the electrodes, the second to dielectric energy flow over the non-electroded surface and the third to the mechanical energy flow over the whole surface. As the second and third terms are zero due to the electrical continuity and mechanically free boundary conditions respectively

$$\Delta W = -\int_{S_e} dS\int_{t_0}^{t_1}\phi\frac{\partial \vec{D}\cdot\hat{n}}{\partial t}. \tag{7.26}$$

For the LE bar, the normal vector to the electrodes is in the 3 direction so $\vec{D}\cdot\hat{n} = \pm D_3$ for the top and bottom electrodes, S_t and S_b respectively, to give

$$\Delta W = -\int_{t_0}^{t_1}\left(\int_{S_t} dS\phi(z=h)\frac{\partial D_3}{\partial t}-\int_{S_b} dS\phi(z=-h)\frac{\partial D_3}{\partial t}\right). \tag{7.27}$$

Gauss's law states $\partial D_3/\partial z = 0$. Hence D_3 is independent of z and is the same at both ends of the bar. Therefore,

$$\begin{aligned}\Delta W &= -\int_{t_0}^{t_1}(\phi(z=h)-\phi(z=-h))\int_{S_t} dS\frac{\partial D_3}{\partial t} \\ &= -\varepsilon_{33}^{\sigma}\int_{t_0}^{t_1} V\Theta(t-t_s)\frac{\partial}{\partial t}\int_{S_t} dSE_3,\end{aligned} \tag{7.28}$$

where the electrical driving boundary condition and the constitutive equation, Equation 2.22, were used in the second equality. Furthermore, the electric field can be substituted by differentiating Equation 7.24 and multiplying by the Heaviside function

$$\begin{aligned}\Delta W &= -\varepsilon_{33}^{\sigma}\int_{t_0}^{t_1} V\Theta(t-t_s)\frac{\partial}{\partial t}\int_{S_t} dS\frac{V}{2h}\Theta(t-t_s), \\ &= -\frac{V^2}{2h}A\varepsilon_{33}^{\sigma}\int_{t_0}^{t_1}\Theta(t-t_s)\frac{\partial\Theta(t-t_s)}{\partial t}.\end{aligned} \tag{7.29}$$

As the electric field is non-zero only in the 3 direction and is uniform in the cross-section, the surface integral can be trivially performed to obtain the cross-sectional area, A. The remaining time integral can be evaluated using integration by parts to arrive at

$$\Delta W = -\frac{V^2}{2h}A\varepsilon_{33}^{\sigma}\left[\frac{\Theta^2(t-t_s)}{2}\right]_{t_0}^{t_1}, \tag{7.30}$$

which gives

$$\Delta W = \begin{cases} -\frac{1}{2}\frac{V^2}{2h}A\varepsilon_{33}^{\sigma} & \text{if} \quad t_0 < t_s < t_1 \\ 0 & \text{if} \quad t_s < t_0 \quad \text{or} \quad t_s > t_1, \end{cases} \tag{7.31}$$

where the negative sign shows that energy is flowing into the bar and can be ignored further. This expression also shows that the energy only really flows at time t_s, meaning that the energy is introduced only when the source is switched on. This follows as t_s is the only time when the internal electric field, and hence the internal energy, will change.

Assuming $t_0 < t_s < t_1$, the input energy is

$$\begin{aligned}W_{\text{input}} &= \frac{1}{2}\frac{V}{2h}\frac{V}{2h}\varepsilon_{33}^{\sigma}2Ah \\ &= \frac{1}{2}E_3D_3\Omega,\end{aligned} \tag{7.32}$$

where Ω is the volume of the bar. As E_2, $E_3 \approx 0$, this verifies that the input energy density, denotes by a lower case w, is then

$$w_{\text{input}} = \frac{1}{2}D_iE_i. \tag{7.33}$$

Although focussing on the LE bar geometry, the arguments presented also apply to many of the quasi-static conditions under which the electromechanical coupling factor is defined, given that the excitation is in the 3 direction. This section has therefore built up and verified many of the relations that will be used to generalise the electromechanical coupling factor.

7.4 The Electromechanical Coupling Factor Revisited

As introduced in Section 2.4.7, the electromechanical coupling factor quantifies the proportion of work stored by the piezoelectric material. It is defined as

$$k^2 = \frac{\text{Converted/Stored energy}}{\text{Input energy}}. \tag{7.34}$$

7.4.1 Energy Storage vs. Transmission vs. Efficiency

Whilst it is conceptually useful sometimes to interpret k^2 as piezoelectric efficiency, this is not strictly the case. As such, the distinction should be made between the energy converted and stored by a material, converted and transmitted by a material, and the 'true' piezoelectric efficiency. By definition, k^2 gives the energy converted and stored within the material relating to storing energy within the different parts of the potential energy density defined above. However, energy transmission requires a different, though related, constant. Not all energy that is stored can be extracted and this depends on the external conditions. For example, Equation 7.8 shows that without stress, no mechanical work can flow out of the material. In this case a second constant must be defined, the maximal electromechanical energy transmission coefficient:

$$\lambda_{\max} = \frac{\text{Output energy}}{\text{Input energy}}. \tag{7.35}$$

For simple geometries and with materials with small k^2, it can be shown that $\lambda_{\max} \approx k^2/4$. However, $\lambda_{\max} \approx k^2/2$ for large k^2 and $\lambda_{\max} \approx k^2$ for the case of $k \gg 0.95$ [5].

Importantly, in the case of both conversion and storage/transmission, the unconverted energy is not lost, merely stored inaccessibly within the material [5]. This creates a distinction with the final constant, η, which is the efficiency in the proper sense, i.e. taking into account losses. η can be defined over a work cycle and accounts for losses in the electrical circuit, the mechanical coupling and the piezoelectric material itself, as set out in Section 2.4.8. However, if the material losses are small, most of the energy is retained within the system and $\eta \approx \lambda_{max}$.

7.4.2 The Generalised Coupling Factor

Now that the energy conversion nomenclature has been clarified, the quantification of the energy density can be considered. As this is concerned with the conversion ability of the material and

should not be dependent on any external loads, apart from the driving one, the correct constant to focus on is indeed the electromechanical coupling factor, k^2.

Specific equations for k^2 have been derived for use in specific cases [4], and are listed in Table 2.3, but, to use k^2 as a generalised metric, a generalised equation needs to be derived.

The coupling factor is defined under quasi-static conditions [4] and so the result of Section 7.3.2 may be used: under static electrical stimulation, the input energy density may be written as

$$w_{\text{input}} = \frac{1}{2} D_i E_i = \frac{1}{2} \left(\varepsilon_{ij}^S E_i E_j + e_{i\mu} E_i S_\mu \right), \tag{7.36}$$

where the driving voltage will be contained within the electric field. Taking this discussion at zero frequency ensures that no resonance effects are present. Now, the two terms in Equation 7.36 may be recognised as the purely dielectric energy density and the energy density resulting from piezoelectric coupling respectively. Hence the electromechanical coupling factor is

$$k^2 = \frac{\int dV e_{i\mu} E_i S_\mu}{\int dV \left(\varepsilon_{ij}^S E_i E_j + e_{i\mu} E_i S_\mu \right)}, \tag{7.37}$$

where the energy densities must be integrated over the material volume due to k^2 being defined in terms of energies. Furthermore, electromechanical coupling factors are typically derived under static or quasi-static conditions and so the equation of motion is $\nabla \cdot \sigma = 0$, meaning that there is no stress, σ, present in the material. In the absence of stress, the strain results purely from the piezoelectric effect, $S_\mu = d_{i\mu} E_i$ where d is the piezoelectric charge coefficient. Substituting this form of strain and writing e in terms of d, Equation 2.35:

$$\begin{aligned} k^2 =& \frac{(d_{i\nu} c_{\nu\mu}^E) \int_V dV (d_{j\mu} E_j) E_i}{\varepsilon_{kl}^S \int_V dV E_k E_l + (d_{k\rho} c_{\rho\sigma}^E) \int_V dV (d_{l\sigma} E_l) E_k} \\ =& \frac{d_{i\nu} c_{\nu\mu}^E d_{j\mu} \int_V dV E_i E_j}{(\varepsilon_{kl}^S + d_{k\rho} c_{\rho\sigma}^E d_{l\sigma}) \int_V dV E_k E_l} \\ =& \frac{d_{i\nu} c_{\nu\mu}^E d_{j\mu} \int_V dV E_i E_j}{\varepsilon_{kl}^\sigma \int_V dV E_k E_l}, \end{aligned} \tag{7.38}$$

where the material properties may be taken to be spatially independent and so are removed from the integral. Now, under an electric field assumed purely in the poling direction, $E_1 = E_2 = 0$, the strain can be rewritten as $S_\mu = d_{3\mu} E_3$ which allows the volume integral of the square of E_3 to cancel from the numerator and denominator in Equation 7.38. This assumption is implemented by setting $i, j, k, l = 3$ in Equation 7.38, hence

$$k^2 \approx \frac{d_{3\nu} c^E_{\nu\mu} d_{3\mu} \int_V dV (E_3)^2}{\varepsilon^\sigma_{33} \int_V dV (E_3)^2}. \tag{7.39}$$

This means that the generalised coupling factor can be expressed as

$$k^2_{\mathrm{G}} = \frac{d_{3\mu} c^E_{\mu\nu} d_{3\nu}}{\varepsilon^\sigma_{33}}, \tag{7.40}$$

where ε^σ is the dielectric permittivity at constant stress.

The inclusion of the summations fully incorporates the material anisotropy and ensures this expression quantifies all conversion mechanisms allowed by symmetry for a given electric field. Importantly, as no assumptions have been made regarding the dimensions of the material, k^2_{G} should be universally applicable, achieving the aim to provide a useful comparison between materials.

7.4.3 Expansion of the Generalised Coupling Factor for *4mm* Symmetry

k^2_{G} may be explored for 4*mm* symmetry first by expanding the Einstein sums in Equation 7.40 to give

$$k^2_{\mathrm{G}} = \frac{d^2_{33} c^E_{33}}{\varepsilon^\sigma_{33}} + 4\frac{d_{31} c^E_{13} d_{33}}{\varepsilon^\sigma_{33}} + 2\frac{d^2_{31}(c^E_{11} + c^E_{12})}{\varepsilon^\sigma_{33}}. \tag{7.41}$$

Now, from matrix inversion, the stiffness constant c^E_{33} can be expressed as

$$c^E_{33} = \frac{1}{s^E_{33}} - \frac{2(c^E_{13})^2}{c^E_{11} + c^E_{12}}, \tag{7.42}$$

which allows k^2_{G} to be expanded fully as

$$k^2_{\mathrm{G}} = \frac{d^2_{33}}{s^E_{33}\varepsilon^\sigma_{33}} + 2\frac{d^2_{33}}{\varepsilon^\sigma_{33}}\frac{(c^E_{13})^2}{(c^E_{11} + c^E_{12})} + 2\frac{d^2_{31}(c^E_{11} + c^E_{12})}{\varepsilon^\sigma_{33}} + 4\frac{d_{31} c^E_{13} d_{33}}{\varepsilon^\sigma_{33}}. \tag{7.43}$$

The four terms in this expansion can be broken down as follows: the first is recognised as the standard LE coupling factor, k^2_{33}; the second arrives as a mathematical artefact of the matrix nature of c^E i.e. from Equation 7.42; the third term arises from energy conversion in the lateral direction and the forth term as a cross-coupling of that lateral energy conversion with the thickness motion. The numerical coefficients of the terms arise from the four-fold symmetry.

It is the three additional terms, missing from the conventional analysis of the LE bar, that allow a generalisation of the coupling factor. In the remainder of this thesis they will be collectively grouped together as

$$\lambda \equiv 2\frac{d^2_{33}}{\varepsilon^\sigma_{33}}\frac{(c^E_{13})^2}{(c^E_{11} + c^E_{12})} + 2\frac{d^2_{31}(c^E_{11} + c^E_{12})}{\varepsilon^\sigma_{33}} + 4\frac{d_{31} c^E_{13} d_{33}}{\varepsilon^\sigma_{33}}. \tag{7.44}$$

The value of this correction is shown in Table 7.1 for some common materials, along with k_{33}^2 for comparison. The value of λ is small though not negligible, which reinforces the conclusion that the LE or any other thickness mode is a dominant one. This is mainly due to the large value of d_{33} typically seen in Pb-based piezoelectric materials.

Table 7.1: Comparison the LE coupling factor, k_{33}, with the expanded correction term, λ, in the generalised coupling factor, k_G.

Material	k_{33}^2	λ
PZT4	0.4556	0.0527
PMN-PT	0.8355	0.0169
Mn:PIN-PMN-PT	0.8295	0.0270

7.5 *In Silico* Verification

In order to verify Equation 7.40, finite element analysis (FEA) was chosen as it allows simulation of complete samples. FEA is very much a standard tool today in the field of piezoelectrics with many packages available. The software used in this study was OnScale (previously PZFlex, Redwood City, CA, USA).

FEA allows computation of solutions of boundary value, initial value and eigenvalue problems by discretisation of the problem domain effectively to reduce it to a finite set of coupled differential equations defined on a lattice of nodes. Approximate solutions to the problem are then constructed on this lattice, allowing practical and reliable evaluation of complex behaviour [10].

The simulation here was applied to a material sample which was excited along the 3 direction with a DC voltage of 1 V. Once the steady state had been reached, the four energy densities were calculated across the whole sample. As any transient effects were allowed to dissipate, the energy densities are spatially constant across the whole sample with any deviation interpreted as arising from numerical error in the simulation. As such, an average over the sample was taken and the error estimated as the standard error on this mean.

Due to the summation present in k_G^2, a full set of material properties is required for calculation. This coincides with the requirement for a full EPD matrix for FEA. Full and self-consistent sets of material properties are rare in the literature especially for single crystal materials. For this reason, two specific use cases were chosen to explore the application of Equation 7.40.

7.5.1 Application to Piezocrystal

The first application was chosen to show the superior performance of relaxor-ferroelectric piezocrystal over piezoceramics. Four materials were compared, each representing a differ-

ent stage in the development of Pb-based piezoelectrics. The first is [001]-poled piezoceramic, PZT4, used as a reference, with the properties taken from the internal OnScale material database. The second is, Gen. I [001]-poled piezocrystal, PMN-PT, representing the broad class of single crystal materials already commercialised. Properties were taken from the crystal manufacturer's (TRS Technologies, State College, PA, USA) datasheet. Finally two sets of Mn:PIN-PMN-PT were used to represent the most advanced piezocrystals. The first is [001]-poled and was characterised using a single sample method [11, 12] and the second is a domain engineered, [011]-poled sample taken from the literature [13]. The different poling means that the material has a different symmetry which allows excitation and exploitation of new modes. This is exemplified by the introduction of the '32' mode which is usually degenerate with the LTE, '31' mode in 4*mm* symmetry due to the four-fold rotation axis. However, [011]-poled samples have *mm*2 symmetry and so allow the 32 mode to manifest. This mode has both a high k^2_{32} and Q_m, making it of interest to many fields.

Table 7.2 shows the calculated and simulated values for k^2_G, with excellent agreement being shown. Both the calculated and *in silico* values of k^2_G are invariant under different geometries for all materials. It can be seen that the piezocrystal materials possess a much higher k^2_G than the piezoceramic. This was expected as high electromechanical coupling is a reported property of piezocrystal. However, it is interesting to note that the generalised coupling does not increase much between Gens. I and III materials, indicative of the fact that development of Gen. II and Gen. III materials was driven by other factors, namely the poor Q_m and T_RT shown by PMN-PT.

7.5.2 Application to Pb-Free Materials

The second application was chosen to explore the performance of Pb-free materials. This study compares three Pb-free materials, $LiNbO_3$ (LNO) and $LiTaO_3$ (LTO) with properties from Smith and Welsh [14], and PIC 700 - $Bi_{1/2}Na_{1/2}TiO_3$ (BNT) - properties from Fenu *et al.* [12]. The two Li compounds admit a 3*m* symmetry and the properties were measured from single crystal samples through a mixture of ultrasonic phase-velocity measurements, the resonant and antiresonant frequencies of a single length-extensional bar resonator, and low-frequency capacitance measurements. PIC 700 is a piezoceramic and so admits ∞*mm* symmetry. The full EPD matrix from a single sample was obtained using a hybrid approach combining resonant ultrasound spectroscopy with an optimisation algorithm [12].

Table 7.3 shows the calculated and simulated values for k^2_G. Excellent agreement is evident. LNO and LTO display very low values, attributed to their weak piezoelectric effect, with d_{33} = 6 pC/N and 5.7 pC/N respectively [14]. PIC 700 has a larger piezoelectric effect (d_{33} = 101.3 pC/N) and, correspondingly, shows an improved k^2_G. Whilst this is not too dissimilar from PZT4 (d_{33} = 253.3 pC/N), and so these materials display k^2_G values that differ only by a factor of ~ 2.5, this is still quite a large gap in the context of applications.

Undoubtedly, the large $d_{33} > 1500$ pC/N of the Pb-based piezocrystals is mainly responsible

for their very large k_G^2. However, d is not the only parameter that will influence k_G^2. For example, if the increase in piezoelectric coefficients alone was responsible for the change in k_G^2, then a ~ 200-fold increase should be expected between LNO and PIC 700 but this is clearly unphysical and was not observed. Instead the increase is tempered to a reasonable level by the changes in the permittivity and stiffness, showing that the value of k_G^2 is set by a delicate interplay of many material properties.

Again both the calculated and *in silico* values of k_G^2 are invariant under different geometries, seen after simulating. Classically, a LE bar will be characterised by k_{33} and TE plate by k_t. These are linked through the relation [6]

$$k_t^2 = \frac{k_{33}^2}{1+k_{33}^2}, \tag{7.45}$$

derived in Chapter 2, implying that the LE mode is better able to convert and store energy than the TE mode. This stems from a combination of two factors: the inherent material response and resonance effects. The invariance of k_G^2 indicates that it is indeed free of any influence of a resonance mode, as expected, and provides strong evidence that k_G^2 quantifies purely the material response.

Furthermore, as k_G^2 encompasses all energy conversion mechanisms for a given field, it may be interpreted as a maximum electromechanical coupling value. Interestingly, the value of k_{33}^2 in PIC 700 matches closely that of k_G^2 indicating that this an 'efficient' mode in which to use this material. The Li compounds on the other hand, show a small gap. This means the 'efficiency' of the LE mode is poorer and is instead representative of energy being lost to other motion (i.e. d_{31}).

Table 7.2: Comparison of energy density for Pb-based piezocrystals quantified by the generalised electromechanical coupling factor, k^2_{G}. Also included as reference is piezoceramic, PZT4.

Material	**Symmetry**	**Geometry**		**Conventional Mode k^2_{ij}**	**Generalised k^2_{G}**	
		Mode	**Dimensions (mm^3)**		**Calculated**	***in Silico***
PZT4	∞mm	LE	1×1×10	$k^2_{33} = 0.456$	0.4631597	0.463165(5)
		-	1×1×1	-		0.463165(1)
		LTE	10×3×1	$k^2_{31} = 0.0886$		0.4631652(2)
PMN-PT	4*mm*	LE	1×1×10	$k^2_{33} = 0.836$	0.8380994	0.8381021(5)
		-	1×1×1	-		0.838102(2)
Mn:PIN-PMN-PT A	4*mm*	LE	1×1×10	$k^2_{33} = 0.830$	0.8380056	0.83800(1)
		-	1×1×1	-		0.838008(4)
		TE	10×10×1	$k^2_{\mathrm{t}} = 0.453$		0.8380102(9)
		LTE	10×3×1	$k^2_{31} = 0.245$		0.8380081(4)
		Ring	t=2, r_O=10, r_I=5	-		0.838(8)
Mn:PIN-PMN-PT B	*mm*2	LE	1×1×10	$k^2_{33} = 0.808$	0.8506829	0.85067(1)
		LTE	10×3×1	$k^2_{31} = 0.504$		0.8506851(3)
		32	3×10×1	$k^2_{32} = 0.810$		0.8506849(3)

Table 7.3: Comparison of energy density for three Pb-free materials, LNO, LNO and PIC 700, quantified by the generalised electromechanical coupling factor k_G^2. Also included as reference is piezoceramic, PZT4, high performance piezocrystal, PMN-PT, and cutting-edge Mn-modified piezocrystal, Mn:PIN-PMN-PT.

Material	**Symmetry**	**Geometry**		**Conventional Mode k_{ij}^2**	**Generalised k_G^2**	
		Mode	**Dimensions (mm^3)**		**Calculated**	***in Silico***
LNO	3*m*	LE	1×1×10	$k_{33}^2 = 0.0283$	0.0298867	0.0298873(8)
		-	1×1×1	-		0.0298873(1)
		TE	10×10×1	$k_t^2 = 0.0275$		0.02988670(7)
LTO	3*m*	LE	1×1×10	$k_{33}^2 = 0.0115$	0.0142683	0.0142686(6)
		-	1×1×1	-		0.0142686(4)
		TE	10×10×1	$k_t^2 = 0.0114$		0.01426880(4)
PIC 700	∞*mm*	LE	1×1×10	$k_{33}^2 = 0.2066$	0.2066128	0.206616(1)
		-	1×1×1	-		0.2066164(6)
		TE	10×10×1	$k_t^2 = 0.1712$		0.2066164(6)
PZT4	∞*mm*	LE	1×1×10	$k_{33}^2 = 0.456$	0.4631597	0.463165(5)
PMN-PT	4*mm*	LE	1×1×10	$k_{33}^2 = 0.836$	0.8380994	0.8381021(5)
Mn:PIN-PMN-PT	4*mm*	LE	1×1×10	$k_{33}^2 = 0.830$	0.8380056	0.83800(1)

7.6 Impact of Losses

The discussion of the generalised electromechanical coupling factor here has, necessarily, been conducted without consideration of material losses. However, if this method is to be applied to real world materials, then the inclusion of losses is unavoidable. Losses may simply be incorporated into Equation 7.40 by allowing the material properties to become complex, with the imaginary parts accounting for the losses. This would lead to the coupling factor becoming complex, with its imaginary part corresponding to the overall loss in the transduction process [15]. In this way, if the dielectric, mechanical and piezoelectric loss tangents could be determined for all material properties present in k_G^2, the impact of losses on transduction may be further examined in general without relying on resonance-determined quality factors.

However, for the static case considered here, losses have little impact. This is due to the fact that, once the steady state is reached, the energy is necessarily balanced and so loss terms can safely be ignored. This is not the case for dynamic driving where such a balance cannot be assumed. Further discussion of the case of dynamic driving is included in Section 8.2.3.

7.7 Chapter Conclusions

A generalised electromechanical coupling factor, k_G^2, defined at zero frequency, was developed in order to allow unbiased comparison of piezoelectric materials. This coupling factor includes all conversion mechanisms allowed by symmetry and so is not restricted to a single resonance mode or application. The coupling factor was verified *in silico* using FEA and excellent agreement was found between the calculations and simulations.

This new metric was then applied to two cases where comparison between materials is difficult to separate from specific use cases. Firstly, the superiority of relaxor-PT single crystal materials over the piezoceramic standard PZT4 was shown. As expected, k_G^2 calculated for all generations of crystal was almost double that of PZT4, quantifying the piezocrystal's better transduction capability. Secondly, k_G^2 was shown to be useful for the comparison of Pb-free LNO, LTO, and PIC 700. Poor performance of Pb-free piezoelectrics is a major barrier to their commercialisation and so an unbiased metric by which their transduction can be tracked is desirable. In this study, the Pb-free materials were compared against the standard PZT4 and high performance, cutting-edge piezocrystal PMN-PT and Mn:PIN-PMN-PT. Classic materials such as LNO and LTO showed very low k_G^2 whereas the more recent composition, PIC 700, displayed a value which was an order of magnitude higher.

These two applications show that the generalised electromechanical coupling factor is able to quantify the pure material transduction of many piezoelectric materials. By decoupling transduction from a resonance mode or specific material geometry, a more rounded and fundamental comparison may be made.

References

[1] A. J. Bell and O. Deubzer, "Lead-free piezoelectrics-the environmental and regulatory issues," *MRS Bull.*, vol. 43, no. 8, pp. 581–587, 2018. DOI: 10.1557/mrs.2018.154.

[2] J. Koruza, A. J. Bell, T. Frömling, K. G. Webber, K. Wang, and J. Rödel, "Requirements for the transfer of lead-free piezoceramics into application," *J. Materiomics*, vol. 4, no. 1, pp. 13–26, 2018. DOI: 10.1016/j.jmat.2018.02.001.

[3] S. Zhang, F. Li, X. Jiang, J. Kim, J. Luo, and X. Geng, "Advantages and challenges of relaxor-$PbTiO_3$ ferroelectric crystals for electroacoustic transducers - a review," *Prog. Mater. Sci.*, vol. 68, pp. 1–66, 2015. DOI: 10.1016/j.pmatsci.2014.10.002.

[4] A. H. Meitzler, H. F. Tiersten, A. W. Warner, D. Berlincourt, G. A. Coquin, and F. S. Welsh, *An American National Standard: IEEE Standard on Piezoelectricity*, ANSI/IEEE Std 176-1987, 1987.

[5] K. Uchino, "The development of piezoelectric materials and the new perspective," in *Advanced Piezoelectric Materials*, K. Uchino, Ed., Woodhead Publishing, 2017, ch. 1, pp. 1–92, ISBN: 978-0-08-102135-4. DOI: 10.1016/B978-0-08-102135-4.00001-1.

[6] J. Yang, *An Introduction to the Theory of Piezoelectricity*. Springer, 1985, ISBN: 0-387-23546-9.

[7] J. Yang, *An Introduction to the Theory of Piezoelectricity*. Springer, 1985, ch. 2, ISBN: 0-387-23546-9.

[8] J. F. Havlice, W. L. Bond, and L. B. Wigton, ""elastic" poynting vector in a piezoelectric medium," *IEEE Trans. Sonics Ultrason.*, vol. 17, no. 4, pp. 246–248, 1970. DOI: 10.1109/T-SU.1970.29573.

[9] K. F. Riley, M. P. Hobson, and S. J. Bence, *Mathematical Methods for Physics and Engineering*, 3rd. Cambridge University Press, 2006, ch. 21, ISBN: 978-0-521-67971-8.

[10] E. Madenci and I. Guven, *The Finite Element Method and Applications in Engineering Using ANSYS*, 2nd. Springer, 2015, ISBN: 978-1-4899-7550-8.

[11] N. G. Fenu, "Investigation of piezoelectric materials for ultrasonic surgery," PhD thesis, University of Glasgow, 2021.

[12] N. G. Fenu, N. Giles-Donovan, M. . R. Sadiq, and S. Cochran, "Full set of material properties of lead-free PIC 700 for transducer designers," *IEEE Trans. Ultrason. Ferroelectr. Freq. Contr.*, vol. 68, no. 5, pp. 1797–1807, 2021. DOI: 10.1109/TUFFC.2020.3044790.

[13] R. Sahul, "Effect of manganese doping on PIN-PMN-PT single crystals for high power applications," PhD thesis, Pennsylvania State University, 2014.

[14] R. T. Smith and F. S. Welsh, "Temperature dependence of the elastic, piezoelectric, and dielectric constants of lithium tantalate and lithium niobate," *J. Appl. Phys.*, vol. 42, no. 6, pp. 2219–2230, 1971. DOI: 10.1063/1.1660528.

[15] A. V. Mezheritsky, "Elastic, dielectric, and piezoelectric losses in piezoceramics: How it works all together," *IEEE Trans. Ultrason. Ferroelectr. Freq. Contr.*, vol. 51, no. 6, pp. 695–707, 2004. DOI: 10.1109/TUFFC.2004.1304268.

Chapter 8

Conclusions and Future Work

This chapter presents the conclusion of the thesis. The main findings of each chapter are reviewed and assessed against the aims and objectives as set out in the introduction. Following this, some suggestions for ways in which the work may be taken forward are laid out.

8.1 Conclusions

This thesis aimed to advance the fundamental understanding of complex ferroelectric and multiferroic oxides.

The first way reported (Chapter 4) was through the use of spherical neutron polarimetry to characterise the magnetic ground state of $Cu_3Nb_2O_8$ (CNO). This addressed issues in the literature relating to the nature of the magnetic structure in both low temperature phases and the mechanism by which the ferroelectric polarisation emerges.

By determining the full polarisation matrix for multiple magnetic Bragg peaks, the magnetic structure in both low temperature phases was found to be a generic helicoid in the low temperature phase (LT: $T < 24$ K), in agreement with the powder structure reported by Johnson *et al* [1], and an apparent spin density wave in the intermediate phase (MT: 24 K $< T <$ 26.5 K). However, the temperature dependence of the off-diagonal polarisation matrix elements revealed that it is not a true spin density wave. Therefore, a mechanism was proposed by which the magnetic ground state of the MT phase mimics a spin density wave at finite temperatures but really stems from the decoupling of the components of the order parameter, as allowed in CNO due to its lack of strong symmetry. This magnetic structure then induces a structural distortion which allows the ferroelectric order to develop. This mechanism alleviates the constraints on the polarisation imposed by classical models, i.e. the KNB model [2], yet is still consistent with others such as ferro-axial model [1].

The competition between order parameters in CNO creates a situation which, superficially, displays simple phenomenology but hides a more complex and subtle mechanism revealed using sensitive neutron techniques. A similar situation occurs in the multiferroic relaxor-ferroelectric

$Pb(Fe_{1/2}Nb_{1/2})O_3$ (PFN) (Chapter 5) with contrasting magnetic results reported in multiple samples with magnetic Bragg peaks [3], momentum broadened correlations [4], and cluster glass dynamics [5]. Here depth dependent muon techniques were adopted to study the near-surface region.

Relaxor-ferroelectrics have been shown to exhibit a skin effect (e.g. in PMN [6, 7]) where the near-surface structure seems to differ from the bulk, but the mechanism is still not well-understood although random field models are good candidates. Previous muon studies have linked this skin region to compositional heterogeneity [8] and this was probed here for the first time in the magnetoelectric relaxor-ferroelectric PFN. A deficiency of Fe^{3+} was seen near the surface using the μ^- elemental analysis method supported by μ^+ μSR experiments which showed a change in the magnetic properties through this region. As Fe^{3+} is the only magnetic ion present, this supports the link to compositional heterogeneity. Furthermore, μSR results in the literature [3] agree more closely with the near-surface relaxation than in the bulk, but these results used a small sample. A larger sample was studied here and the bulk showed a slowing down of the relaxation and a tightening of the frequency distribution, which was linked to the presence of random fields induced by the compositional disorder of Fe^{3+}. It was posited that the presence of this 'bulk' structure disrupts the long-range magnetic order seen in smaller samples.

Another application of the negative muon technique to characterise relaxor-ferroelectrics was in the study of Mn modification (Chapter 6). Third generation relaxor-ferroelectric single crystals are a promising candidate for high power ultrasonics including SONAR and ultrasound actuated surgical tools [9]. However, the Mn doping mechanism is not well understood with Mn segregation reported [10]. Furthermore, being a transition metal, Mn may take on many oxidation states and this can affect material properties. Hence the μ^- technique was used with the aim of both identifying the Mn oxidation state and allowing it to be tracked in a crystal sample of Mn:PIN-PMN-PT. The muonic X-ray spectra is sensitive to valence state as the muon stopping interaction is dependent on the number of electrons [11], and three Mn oxide powder samples were used to verify this. Difference was seen between the energies of the Kα emission lines of the three oxide samples confirming the μ^-'s sensitivity.

A further feasibility study was carried out using the μ^- technique to investigate the Mn distribution in a multi-domain crystal of Mn:PIN-PMN-PT. None of the Mn emission lines were able to be identified in the measured spectra, and it was concluded that significant detector upgrades would be needed to detect the small effects observed from the Mn oxide powder experiments.

As the performance of Mn:PIN-PMN-PT remains of interest for ultrasonic devices, a method was developed (Chapter 7) by which electromechanical performance may be measured. The fundamental characterisation carried out in the preceding chapters provides the base for understanding of the complex mechanisms present in these materials but, without a practical end, there is little to guide their development. Hence, the comparison of electromechanical coupling

factor (k) is essential if new materials are to be developed to fulfil specific purposes.

Present comparisons between candidate materials rely on figures of merit for specific use cases. However, a universal metric for unbiased comparison would allow more general discussion of material performance.

In this thesis, a generalised electromechanical coupling factor k_G^2 was developed. k_G^2 includes all symmetry-allowed conversion mechanisms for a given electric field and thus is not restricted to a single resonance mode or use case. FEA was carried out to verify this method *in silico* and excellent agreement was shown.

Two case studies were detailed for k_G^2. The first related to the already introduced superior performance of Pb-based relaxor-ferroelectric single crystals which were shown to well outperform standard piezoelectric ceramic. k_G^2 was then calculated for Pb-free piezoelectric materials. Whilst their performance was found to be significantly lower than Pb-based materials by the measure of k_G^2, the comparison illustrates the effectiveness of this method and its applicability to a range of materials and symmetries.

Overall, this thesis presents fundamental characterisation of complex ferroelectric and multiferroic oxides, with context provided by ultrasonic device applications. Device designers do not need to understand the microscopic mechanisms at play but it is only through understanding of these mechanisms that new materials may be developed, in turn unlocking novel device designs and future applications.

8.2 Future Work

The contributions to knowledge made by this thesis address the overall aims and objectives set out, and suggest further avenues of research.

8.2.1 Further Study of Mn Valence and Distribution in Mn:PIN-PMN-PT

Given that the μ^- technique was able to distinguish between Mn oxidation state in oxide powders, it was disappointing that a similar result was not found in a crystal sample of Mn:PIN-PMN-PT. However, as no Mn lines were observed, the change is likely simply to be below the noise floor of the experiment. Better instrument resolution should be able to combat this absence of signal and a repeat measurement is warranted at such time as the instrument is improved.

8.2.2 Cryogenic Measurements

Temperature was considered only occasionally in this thesis, but it offers a way to explore further the behaviour of materials, especially in the cryogenic regime [12, 13]. An ultra-low vibration cryogenic measurement system is now available at the University of Glasgow which is suited

to study of electromechanical properties in relaxor-ferroelectric materials with the following experiments suggested:

Dielectric Measurements

Through use of an LCR bridge, dielectric measurements may be performed as a function of temperature. Given the temperature broadening effects in relaxor-ferroelectrics, an instrument with a large temperature range is indicated. A low vibration interface will make it additionally suitable for sensitive capacitance measurements through which phase transitions may be monitored.

Piezoelectric Measurements and Conventional Characterisation

Once an ultrasonic device is assembled, temperature effects may affect performance. These can stem from self-heating due to losses, e.g. power ultrasonics applications, or ambient conditions, such as in extraterrestrial applications. Hence, investigation of the influence of temperature on piezoelectric mode shapes, probed through conventional material characterisation techniques or with laser Doppler vibrometry, is of great interest. A cryostat with a heating capability is able to simulate almost any operating conditions with regards to temperature and can provide real-world applicable information.

Non-Contact Material Characterisation

Accurate material characterisation is critical to modern ultrasonics device design due to the role played by FEA. This is true for single crystal materials, where sample-to-sample variation reduces the accuracy of standard characterisation mechanisms, and also for characterisation of extremely small piezoelectric samples where the coupling introduced by the measurement procedure itself can affect the results. To circumvent this issue, all-optical, non-contact characterisation with laser generated ultrasound can be used [14]. A low vibration cryogenic measurement system enables non-contact ultrasonic characterisation as a function of temperature, further extending the range of this promising technique.

8.2.3 Extension of Generalised Electromechanical Coupling Factor

Whilst k_G^2 (Chapter 7) is able to provide unbiased comparison between materials, some extensions may be considered.

Experimental Verification

Experimental verification of the values of k_G^2 is desirable. However, this may run into issues with material property consistency. It is well-known, especially with single crystal samples,

that, when characterised with methods such as the IEEE standard, the set of material properties obtained may be internally inconsistent. This can be overcome by single-sample methods, e.g. [15]. This consistency problem did not affect the present study because, if the properties used for both the calculations and simulations match, the results will do so too, regardless of how well the material properties actually relate to a real sample.

Incorporation of Other Electric Field Directions

Another avenue concerns an extension to k_{G}^2 to incorporate additional behaviour. This is most clearly seen in the case of the Pb-free comparison: the LE associated constants of the Li based materials are weak but the shear coefficients, e.g. d_{15}, are strong. This behaviour is not fully captured by k_{G}^2 because of the assumption that the electric field is only uniaxial, in the 3 direction. The method developed in Chapter 7 is compatible with an electric field in a different direction and inclusion of all electric field directions is desirable for a comprehensive metric.

Dynamic Driving

An area for further study of k_{G}^2 is an extension to AC driving. By considering the dynamic case, it should be possible to link the material's inherent performance as quantified by the static k_{G}^2 and resonant behaviour used in ultrasonic devices.

One approach to achieve this is to reintroduce the stress term in Equation 7.38 through utilisation of the full constitutive equation. Recall, the stress was neglected based on the static equation of motion, $\nabla \cdot \sigma = 0$. This is not the case in a general dynamic situation where the strain is $S_\mu = s^E_{\mu\nu}\sigma_\nu + d_{i\mu}E_i$. Substituting this into Equation 7.37 and again taking the electric field to be uniaxial in the 3 direction,

$$k_D^2 = \frac{d_{3\mu}\int_V dV\,\sigma_\mu E_3 + d_{3\mu}c^E_{\mu\nu}d_{3\nu}\int_V dV\,(E_3)^2}{d_{3\mu}\int_V dV\,\sigma_\mu E_3 + \varepsilon^\sigma_{33}\int_V dV\,(E_3)^2}. \tag{8.1}$$

With some algebraic manipulation, this can be rewritten as

$$k_{\mathrm{D}}^2 = \frac{\mu[V] + \frac{d_{3\mu}c^E_{\mu\nu}d_{3\nu}}{\varepsilon^\sigma_{33}}}{\mu[V]+1} = 1 + \frac{k_{\mathrm{G}}^2 - 1}{1+\mu[V]}, \tag{8.2}$$

where

$$\mu[V] = \frac{d_{3\mu}\int_V dV\,\sigma_\mu E_3}{\varepsilon^\sigma_{33}\int_V dV\,(E_3)^2}, \tag{8.3}$$

with k_{G}^2 the static, generalised coupling factor.

Through the functional $\mu[V]$, this dynamic coupling factor depends not only on material properties but also on the material dimensions, through the integrals in $\mu[V]$, and the driving

conditions, as the stress and electric field are present in $\mu[V]$. However, upon *in silico* verification, unphysical effects were seen. Over the frequency domain, k_D^2 displayed negative values with magnitude greater than unity. This behaviour was correlated to frequency regions where the stress and electric field were out of phase rendering the piezoelectric coupling energy density negative. Again, this is clearly unphysical and so an alternative approach, inclusive of losses and which reduces to k_G^2 for DC excitation, is required.

References

[1] R. D. Johnson *et al.*, "$Cu_3Nb_2O_8$: A multiferroic with chiral coupling to the crystal structure," *Phys. Rev. Lett.*, vol. 107, p. 137 205, 13 2011. DOI: 10.1103/PhysRevLett.107.137205.

[2] H. Katsura, N. Nagaosa, and A. V. Balatsky, "Spin current and magnetoelectric effect in noncollinear magnets," *Phys. Rev. Lett.*, vol. 95, p. 057 205, 5 2005. DOI: 10.1103/PhysRevLett.95.057205.

[3] G. M. Rotaru *et al.*, "Spin-glass state and long-range magnetic order in $Pb(Fe_{1/2}Nb_{1/2})O_3$ seen via neutron scattering and muon spin rotation," *Phys. Rev. B*, vol. 79, p. 184 430, 18 2009. DOI: 10.1103/PhysRevB.79.184430.

[4] C. Stock, S. R. Dunsiger, R. A. Mole, X. Li, and H. Luo, "Coupled short-range ferroelectric and magnetic order in $Pb(Fe_{1/2}Nb_{1/2})O_3$," *Phys. Rev. B*, vol. 88, p. 094 105, 2013. DOI: 10.1103/PhysRevB.88.094105.

[5] W. Kleemann, V. V. Shvartsman, P. Borisov, and A. Kania, "Coexistence of antiferromagnetic and spin cluster glass order in the magnetoelectric relaxor multiferroic $PbFe_{0.5}Nb_{0.5}O_3$," *Phys. Rev. Lett.*, vol. 105, p. 257 202, 25 2010. DOI: 10.1103/PhysRevLett.105.257202.

[6] C. Stock *et al.*, "Strong influence of the diffuse component on the lattice dynamics in $Pb(Mg_{1/3}Nb_{2/3})O_3$," *J. Phys. Soc. Jpn.*, vol. 74, no. 11, pp. 3002–3010, 2005. DOI: 10.1143/JPSJ.74.3002.

[7] K. H. Conlon *et al.*, "Direct observation of the near-surface layer in $Pb(Mg_{1/3}Nb_{2/3})O_3$ using neutron diffraction," *Phys. Rev. B*, vol. 70, p. 172 204, 17 2004. DOI: 10.1103/PhysRevB.70.172204.

[8] K. L. Brown *et al.*, "Depth dependant element analysis of $Pb(Mg_{1/3}Nb_{2/3})O_3$ using muonic x-rays," *J. Phys. Condens. Matter*, vol. 30, p. 125 703, 2018. DOI: 10.1088/1361-648X/aaade3.

[9] S. Zhang, F. Li, X. Jiang, J. Kim, J. Luo, and X. Geng, "Advantages and challenges of relaxor-$PbTiO_3$ ferroelectric crystals for electroacoustic transducers - a review," *Prog. Mater. Sci.*, vol. 68, pp. 1–66, 2015. DOI: 10.1016/j.pmatsci.2014.10.002.

[10] L. A. Stoica, "Relaxor-$PbTiO_3$ single crystals and polycrystals: Processing, growth and characterisation," PhD thesis, University of Leeds, 2016.

[11] E. Fermi and E. Teller, "The capture of negative mesotrons in matter," *Phys. Rev.*, vol. 72, pp. 399–408, 5 1947. DOI: 10.1103/PhysRev.72.399.

[12] F. Li *et al.*, "The origin of ultrahigh piezoelectricity in relaxor-ferroelectric solid solution crystals," *Nat. Commun*, vol. 7, p. 13 807, 2016. DOI: 10.1038/ncomms13807.

[13] P. M. Shepley, L. A. Stoica, Y. Li, G. Burnell, and A. J. Bell, "Effects of poling and crystallinity on the dielectric properties of $Pb(In_{1/2}Nb_{1/2})O_3$-$Pb(Mg_{1/3}Nb_{2/3})O_3$-$PbTiO_3$ at cryogenic temperatures," *Sci. Rep.*, vol. 9, p. 2442, 1 2019. DOI: 10.1038/s41598-019-38995-9.

[14] N. G. Fenu, N. Giles-Donovan, P. Prentice, and S. Cochran, "Potential of all-optical piezocrystal characterization for fea simulation," in *International Workshop on Acoustic Transduction Materials and Devices (IWATMD)*, State College, PA, USA, 2019.

[15] N. G. Fenu, N. Giles-Donovan, M. . R. Sadiq, and S. Cochran, "Full set of material properties of lead-free PIC 700 for transducer designers," *IEEE Trans. Ultrason. Ferroelectr. Freq. Contr.*, vol. 68, no. 5, pp. 1797–1807, 2021. DOI: 10.1109/TUFFC.2020.3044790.